PSL
UNIVERSITÉ PARIS

UNIVERSITAS ISLANDIAE SIGILLUM

UNIVERSITY OF ICELAND
FACULTY OF EARTH SCIENCES

THÈSE DE DOCTORAT
DE L'UNIVERSITÉ PSL

Préparée à l'Ecole Normale Supérieure (Paris)
Dans le cadre d'une cotutelle avec l'Université d'Islande

Propriétés électriques des roches volcaniques altérées: observations et interprétations basées sur des mesures en laboratoire, terrain et forage au volcan Krafla, Islande

Electrical properties of hydrothermally altered rocks: observations and interpretations based on laboratory, field and borehole studies at Krafla volcano, Iceland

Soutenue par
Léa LEVY
Le 15 février 2019

Ecole doctorale n° 560
STEP'UP

Spécialité
Sciences de la Terre

Composition du jury :

Lee, SLATER Professeur, Rutgers University, Newark NJ	*Rapporteur*
Jean-François, GIRARD Professeur, Université de Strasbourg	*Rapporteur*
Sophie, VIOLETTE Maître de conférence, Sorbonne Université	*Examinateur*
Philippe, COSENZA Professeur, Université de Poitiers	*Président du jury*
Ólafur G., FLÓVENZ Directeur, ÍSOR – Iceland GeoSurvey	*Examinateur*
Pierre, BRIOLE DR2, Ecole Normale Supérieure	*Directeur de thèse*
Freysteinn, SIGMUNDSSON Professeur, University of Iceland	Co-*Directeur de thèse*
Benoit, GIBERT Maître de conférence, Géosciences Montpellier	*Invité*
Gylfi Páll, HERSIR Ingénieur, ÍSOR – Iceland GeoSurvey	*Invité*

1794
ENS
ÉCOLE NORMALE SUPÉRIEURE

PREFACE

"Les plus belles âmes sont celles qui ont plus de variété et de souplesse."

— Montaigne, Book III, chap. 3

In 2014, I finished my master's project at Mines ParisTech (France), in collaboration with Areva Mines (now Orano), about the environmental impacts of acid in-situ leaching of an uranium "roll-front" reservoir, predicted by reactive transport modeling. In this context, clays form the impermeable horizontal barriers around uranium ore deposit, which are necessary to avoid loosing dissolved uranium by gravity after injection of acid sulphate (H_2SO_4). Pyrite plays the role of reducing barrier, which forces soluble uranium from regional fluids to precipitate and accumulate, thus forming the deposit. Finally, smectite, thanks to its large cation exchange capacity, is a sink for protons (H^+) released from H_2SO_4, and buffers the pH (acidity) of the aquifers. During the exploration phase, geophysics is omnipresent and electrical resistivity is used in particular to find the clay layers, as well as to follow the acid plume.

In my PhD, I hired the same fascinating actors - smectite, pyrite and electrical resistivity, within a different scenario - harnessing geothermal heat rather than mining uranium. Indeed, I like to work at the interface between mineralogy and geophysics and I think that finding energy resources other than oil and gas is important. Yet, consuming energy in a sustainable way is fundamental for all that to make sense. My PhD dissertation will not address this question, although I have much to say about it, but I hope that my research, if ever useful to anyone, will not put Mother Earth into more troubles.

This PhD work is at the intersection of three different fields of Earth Sciences: petrophysics, geophysics and mineralogy. Although petrophysics is the dominant field, geophysics has an important place. Moreover, close collaboration with mineralogists has been the ground for focusing my petrophysical and geophysical research on two minerals: smectite and pyrite, which appear to be a key to understand present-day hydrothermal circulations. Working with volcanologists and geothermal explorers has made me keep some distance from complicated petrophysical models. Their "naive" (yet always relevant) questions have also forced me to clarify my own understanding of what I was doing and why I was doing it, at every step. Overall, I believe that this multi-disciplinary approach has helped me remain (somewhat) flexible and open-minded.

ABSTRACT

The electrical signature of volcanoes is affected by several characteristics of rocks: volume and salinity of pore fluid, abundance of conductive minerals, rock temperature and presence of molten crust (magma). Electromagnetic soundings are widely used to image the underground structure of volcanoes and look for high-temperature geothermal resources. However, the relative contribution of the above-mentioned elements to the measured resistivity is often an unsolved question when interpreting resistivity inversions. This thesis aims at improving the interpretation of electrical resistivity structures at active volcanoes, in order to develop innovative tools for the assessment of high-enthalpy geothermal resources. Focus is on conductive minerals, which can either be solid ionic conductors (clay minerals, in particular smectite) or electronic semi-conductors (pyrite and iron-oxides). Also investigated are the effects of porosity, salinity, temperature and melting. Iron-oxides are mostly formed during the primary crystallization of magma, while smectite and pyrite are formed upon hydrothermal alteration of volcanic rocks, thereby witnessing hydrothermal convections. Krafla volcano, Iceland, is used as a laboratory area, where extensive literature, borehole data, core samples, surface soundings and infrastructures are available. The contribution of smectite to the electrical conductivity of volcanic samples saturated with pore water at different salinity is first investigated in the laboratory (room temperature) by electrical impedance spectroscopy, also called complex resistivity. Non-linear variations of the conductivity at 1 kHz with salinity are observed and interfoliar conduction is suggested as an important mechanism by which smectite conducts electrical current. The influence of pyrite and iron-oxides on the charge-storage (capacitive) properties of the rock is then analyzed, using the frequency-dependent phase-angle of the impedance. Maximum phase-angle (MPA) higher than 20 mrad can be attributed to pyrite if the rock is conductive and to iron-oxides if the rock is resistive. Moreover, the MPA increases by about 22 mrad for each additional volumetric per cent of pyrite or iron-oxide. These laboratory frequency-domain findings are partly upscaled to interpret field time-domain complex resistivity tomography at Krafla: smectite, pyrite and iron-oxides can be identified down to about 200 m with the measurements carried out. The in-situ temperature, higher than in laboratory conditions, appears to significantly increase the conductivity associated to smectite. In general, time-domain complex resistivity measurements are recommended as a complementary method to electromagnetic soundings for geothermal exploration.

ÚTDRÁTTUR

Rafeiginleikar bergs, bæði eðlisviðnám og fasvik, á eldfjallasvæðum eru m.a. háðir póruhluta (holrýmd) bergs, styrk uppleystra jóna í póruvökvanum (seltu), magni rafleiðandi steinda í berginu, hita þess og hvort það er bráðið eða storkið. Rafsegulmælingar eru notaðar til þess að skoða innri gerð eldfjalla og kanna háhitasvæði með því að búa til viðnámslíkön af þeim. Túlkun þeirra er oft flókin og vandasamt er að greina á milli fyrrnefndra þátta sem hafa áhrif á eðlisviðnám og fasa. Þessari ritgerð er ætlað að auka skilning á eðlisviðnámi jarðlaga í virkum eldstöðvum í því skyni að þróa þá tækni sem notuð er til þess að meta stærð og eiginleika háhitasvæða. Ritgerðin fjallar einkum um rafleiðandi steindir, sem eru annað hvort málmleiðarar (leirsteindir, einkum smektít) eða hálfleiðarar (pýrít og járnoxíð). Einnig eru rannsökuð áhrif póruhluta, styrks jóna í póruvökva, hita og bráðnunar bergs. Járnoxíð eru að mestu frumsteindir, þ.e.a.s. þau kristallast þegar bergkvikan kólnar. Smektít og pýrít myndast hins vegar sem útfellingar eða við ummyndun og bera vitni um hringrás jarðhitavökva. Notuð eru gögn frá eldstöðvakerfi Kröflu en þar eru til miklar heimildir eins og borholugögn, borkjarnar og yfirborðsmælingar og góð aðstaða til rannsókna. Áhrif smektíts í bergi á eðlisviðnám bergsýna voru mæld við stofuhita í tilraunastofu. Pórur þeirra voru mettaðar vökva með breytilegum styrk jóna og áhrifin könnuð með litrófsmælingu á eðlisviðnámi og fasa (tvinntöluviðnám). Niðurstöður sýna ólínulegar breytingar í viðnámi við 1 kHz tíðni sem fall af seltu vökvans. Sú tilgáta er sett fram að leiðni milli atómlaga í kristöllum, *interfoliar conduction*, eigi mikilvægan þátt í rafleiðni smektíts. Áhrif pýríts- og járnoxíðsteinda á rafrýmd bergs var könnuð með því að skoða hvernig fasahorn tvinntöluviðnáms er háð tíðni. Ef hámark fasahornsins (MPA) er stærra en 20 mrad stafar það af tilvist pýríts ef bergið er velleiðandi en járnoxíða ef bergið er torleiðandi. Þá eykst MPA um 22 mrad við hverja prósentu-aukningu í rúmmáli pýrits- eða járnoxíðsteinda. Þessar niðurstöður úr tilraunastofumælingum á tíðniháðu tvinntöluviðnámi voru nýttar til þess að túlka yfirborðsmælingar á tvinntöluviðnámi á Kröflusvæðinu. Tvinntöluviðnámslíkan frá Kröflusvæðinu sýnir að greina má tilvist smektíts, pýríts og járnoxíðs niður á um 200 m dýpi í mælingunum sem gerðar voru. Hiti jarðlaga, sem er hærri en í tilraunastofumælingum, virðist hækka verulega leiðni bergs sem inniheldur smektít. Lagt er til að mælingar á tvinntöluviðnámi verði notaðar til viðbótar við hefðbundnar rafleiðnimælingar við jarðhitarannsóknir vegna þeirra viðbótarupplýsinga sem fást með slíkum mælingum.

"Talent wins games, but teamwork and intelligence wins championships."

— Michael Jordan

ACKNOWLEDGEMENTS

I sincerely thank Lee Slater and Jean-François Girard for accepting to be opponents to my PhD and providing detailed feedbacks on my thesis, as well as Sophie Violette and Philippe Cosenza for accepting to be external examiners at my defense.

The PhD project has benefited from existing collaborations between French and Icelandic researchers around volcanological and geothermal research. In March 2015, I met Ólafur Flóvenz and Gylfi Páll Hersir at ÍSOR to discuss the current challenges of geothermal exploration by resistivity soundings and the fact that I was interested in doing something about it. Following their advice, I contacted Benoit Gibert and Philippe Pezard, at University of Montpellier, who let me jump into their fruitful collaboration with ÍSOR. In parallel, Pierre Briole at ENS and Freysteinn Sigmundsson at University of Iceland, who had also been working together on the remote-sensing of volcano deformation, gave me academic support for building the PhD project I had in mind. I am very grateful to the six of you for being a wonderful and harmonious supervising group behind my PhD.

Freysteinn, thanks for your constant enthusiasm despite the gap between our respective research focuses - much smaller gap now ! Thanks for always taking the time to read my drafts and improving them greatly. Thank you also for pushing my limits and helping me out of complicated situations, in a smooth manner you only have the secret. I hope I have learned from your extraordinary scientific, human and diplomatic skills, which I very much admire. Benoit, I believe the PhD project has been much more interesting thanks to your motivation, efficiency and practical skills. Thanks for always encouraging me explore new ideas and for making these ideas become real, despite the apparent - only apparent - overload of projects. Ólafur and Gylfi, thanks for accepting to meet me in the first place and trusting me. Your joint awareness of industry needs and genuine interest for scientific questions was a dream-cocktail for an industry-oriented PhD project. Thanks also Gylfi for your devotion solving all sorts of issues and for the good biking tips. Gylfi, Freysteinn and Ólafur: thank you so much for the joint effort towards the Icelandic translation of the abstract, which I am very fond of. Pierre, thanks for your constant support, which has been the cement of the project from the beginning. Philippe, thanks for your wise advices - even though I have not always listened - and enthusiasm about my way of working.

The PSL-ITI program has made this project possible. Thanks to François Leuqueux and Jérôme Lesieur, for believing in student-built PhD projects and to Dominique Bruel and Benoit Mosser, for being so positive and encouraging despite the ingenuousness of my ideas.

My working philosophy is deeply influenced by Alain Rivière, my physics teacher in high-school, whom I thank here for teaching me to acknowledge firmly what I don't understand and ask questions until I get it, without being ashamed.

I have spent half of my PhD time in Iceland, which is now a second home. Many thanks to my co-workers at ÍSOR, in **Reykjavík** and **Akureyri**. Thanks to Siggi Sveinn and Helga Margrét for the nice working sessions and discussions related (or not) to alteration minerals. Thanks to Kristján S., Þráinn, Ester, Christina, Knútur, Bjarni G., Sigvaldi, Hrafnhildur, Imba, Vigís, Sigurjón and Albert for all the help and to Árni for giving me the motivation to bike during my first winter. Thanks to Unnur, Veiga and Dísa for always making my life þægilegra og skemmtilegra and for the two most memorable hikes of my life. Thanks to all the others for the good working atmosphere and everything you have taught me patiently, including Icelandic. Thanks also to friends I met before the PhD, at University of Iceland and ÍSOR: Matylda, Jan, Vaiva, Stéphanie, Sophie, Susan, Jóhann and Víkingur, as well as outside research: Milja, Christina, Jóhann Pétur and Jack. Þúsund þakkir for making my life in Reykjavík so sweet and for the numerous unforgettable adventures. Finally, I am so much thankful to Þorsteinn for this special experience of Icelandic countryside, engraved in my memory. It has been the best place on Earth to finish my PhD, as well as to awaken my sensitivity to space and time, from the fractal geometry of frost to the fascinating glow of the moon and the multiplicity of perspectives over Kerling mountain.

I am very grateful to the Laboratoire de Géologie (UMR 8538) at ENS in **Paris**, and in particular to Christophe Vigny and Nicolas Chamot-Rooke, for supporting my work in many ways. Thanks also to Hélène Lyon-Caen and Laure Meynadier for taking so great care of PhD students and to Angélique Manchon for helping me patiently prepare proper travel orders. Thanks to my mates from the rue Lhomond, Aurélien, Claire, Samson, Damian, Paoline and the others, for re-integrating me in the flow whenever I would be back at ENS. I thank Damien very much for transforming long afternoons in the basement into exciting sessions with his amazing microscope-skills and steady good mood. I also had the pleasure to meet Jérôme Fortin, Sophie Violette, Yves Guéguen and Bruce Velde at ENS, whom I thank for the good discussions. I have also enjoyed the regular (or less regular) lunches au Fournil with my old friends from the Boulevard Saint-Michel who happened to also do a PhD: Alice, Romain, Paul-Hervé, Charles, Thomas and Lénaïc. Thank you for sharing passion and disillusions about life in research and educating me with

your respective research fields. Thanks also to Bernard and Amy for all the nice discussions (and meals) on the right bank and to all my friends from Paris, whose warm presence prevented me from getting too emotional with this research. I also thank my parents, Myriam and Tony, who remain my most precious accomplices in the best and worst moments.

I have been warmly hosted six times at Géosciences **Montpellier** by the petrophysics group (and the weather). Thanks in particular to Nicolas, Fleurice, Franck and Jacinthe for being so welcoming and helpful (special mention to the goûter corner in the -1 floor, it made a big difference). Thanks to Bernard Fraisse and Annelise Faivre from University of Montpellier for their help with XRD measurements and preparation of basaltic melts. Audrey and Julie, thank you for making my last missions more sparkling and brighter. Jean and Joëlle, as well as Marion, thanks for the stable friendly presence in the South.

After six months of PhD, I got stuck with clay minerals and X-Ray diffraction and contacted clay mineralogists at the IC2MP laboratory (**Poitiers**). I visited them four times since then. Although the weather is not competitive with Montpellier, the passion, high-level of expertise and willingness to teach, which reign there, have very much impressed me. I am thankful to Philippe Cosenza, Alain Meunier, Daniel Beaufort, Eric Ferrage, Emmanuel Tertre and Patricia Patrier for patiently answering my numerous ill-posed questions. As close associated to the Poitiers group, I also thank very much Bruno Lanson and Nathanaël Findling at the University Joseph Fourier (**Grenoble**) for their help with fitting of my weird XRD patterns and Gilles Berger at University Paul Sabatier (Toulouse) for his detailed responses to my overwhelming batches of questions.

Around the same time, I realized my work overlapped with the current research of the Geophysics of Volcanoes team at ISTerre **Chambéry**. I have visited them four times and had the pleasure to meet in particular Svetlana Byrdina and Jean Vandemeulebrouck. Svetlana, thank you for being devoted to the field measurements, processing and interpretation until the end, it meant a lot to me. Jean, as well as Tullio, your positiveness and sense of humor have transformed unpleasing situations (e.g. carrying batteries and "bobines" in the rain and stressful atmosphere) into nostalgic memories. Thanks for the good vibe. Thanks also to Damien, Marine and Margaux for the nice companionship in **Krafla**. The interaction with Pradip Maurya, from Aarhus University, has been very precious for field data inversion; thanks for helping me so patiently. Thanks also to Alex Furman and Pauline Kessouri, from the Technion University, for all the explanations and good advices since our paths crossed. I finally thank my friends of the last months, Patrick Jane, Alice Nevers and Steve McGarett, for cooling down my brain after long working days.

A PhD grant from the PSL-ITI research program funded this project. This work also received funding from European Community's 7^{th} framework program (project IMAGE, grant agreement No. 608553) and European Commission's H2020 program (project GEMex, grant agreement No. 727550). The Jules Verne fund (Hubert Curien Program) funded travel expenses in 2016-2017 and 2018-2019. The power company Landsvirkjun provided a large volume of core samples, as well as accommodation at Krafla - I thank in particular Ási, Siggi and Anette for supporting my multiple requests.

Grund, Iceland, January, 29^{th} 2019

CONTENTS

LIST OF FIGURES

LIST OF TABLES

1 INTRODUCTION

1.1 OBJECTIVES

This thesis aims at improving the understanding of the underground electrical resistivity structure at active volcanoes, imaged by electrical and electromagnetic soundings. One long-term objective is the development of innovative tools for the assessment of high-enthalpy geothermal resources.

A link between the electrical structure of volcanoes and the presence of different stages of hydrothermal alteration (including in particular clay minerals) has been demonstrated many times and is a valuable tool for finding geothermal reservoirs (Árnason et al., 2000). However, the present understanding of electrical properties of altered volcanic rocks does not allow identifying which particular physico-chemical properties of the rock are behind an electrical signature measured by geophysical soundings. Moreover, alteration minerals can have different origins, which geophysical soundings cannot discriminate: burial diagenesis, old active hydrothermal system now "extincted", present economical geothermal reservoir. It is common that boreholes are drilled into crustal structures, which in the end drastically differ from what was expected based on geophysical interpretations. In order to provide solid bases for future exploration of high-enthalpy geothermal reservoirs, I investigated three different threads:

1. understanding the different physical processes which make volcanic rocks conductive or resistive
2. finding complementary investigation techniques, which could narrow down the interpretation of a given electrical structure
3. understanding better the link between hydrothermal circulations and alteration minerals

These threads of research, which have been driven by new questions raised step by step rather than by a well-defined plan, fall in three different fields of Earth Sciences: petrophysics, geophysics and mineralogy. I have become convinced that they need to be addressed together in order to make sure that solving the long-term objective is still over the horizon. For example, it's not until I interacted back and forth with several clay specialists, that I realized the presence of smectite at deep levels was more likely to originate from an active hydrothermal fluid than the presence of chlorite (Beaufort et al., 1995; Patrier et al., 1996). Moreover, a thorough understanding of the

crystal structure of smectite was necessary to investigate the different possible electrical conduction pathways of smectite. The original motive for looking into induced polarization (IP), as a complementary electrical property, was to distinguish the electrical signature of smectite and that of saline fluid. In the end, I found that the only things one could hope to distinguish with IP in these volcanic rocks, both in the laboratory and in the field, were the electrical signatures of pyrite and iron-oxides. Nevertheless, since pyrite carries relevant information about circulation of H_2S, which can originate either from magmatic gases or from reinjection after geothermal exploitation, IP is an interesting input to the overall problem.

1.2 OVERVIEW OF THE METHODOLOGY

This section summarizes the methods the PhD work, by chronological order of focus throughout the PhD's progress. The successive focuses and collaborations were not planned from the beginning but came out progressively as the most logical and exciting developments of my work. However, one aspect of the PhD project had been determined at the beginning and never changed: the studied area (Krafla volcano). Laboratory measurements on core samples from Krafla and field experiments at Krafla have been carried out and compared. In the laboratory, a large variety of petrophysical and mineralogical properties have been measured and analyzed together. In the field, geo-electrical data have been recorded, processed and inverted. Since this work is the result of several distinct collaborations, the following section describes not only the methods but also the people and institutions who have played a key role in the use of each method. All concepts mentioned are defined more thoroughly in the Background chapter.

1.2.1 *Material*

About 150 core samples (20 cm long and 4 cm diameter) in total have been retrieved from four boreholes at Krafla, KH1, KH3, KH5 and KH6, which were drilled in 1991, 2003 and 2006 (Gudmundsson, 1991; Jónsson et al., 2003; Gautason et al., 2007). I sampled the cores from Landsvirkjun collection in three steps, under the supervision of Ásgrímur Guðmundsson, Anette Mortensen and Steinn Águstsson: first at Iceland GeoSurvey (ÍSOR) storing facility in Akureyri in November 2015, with help from Bjarni Gautason and Sigurður Sveinn Jónsson, then at Landsvirkjun storing facility in Krafla in June 2016 and August 2018, with help from Karl Emil Sveinsson and Stefán Stefánsson. I chose the cores to be as homogeneous as possible, so that petrophysical measurements would be representative of a given type of rock. From these cores, I prepared 68 cylindrical plugs (2-3 cm long and 2.5 cm diameter) at Géosciences Montpellier with Benoit Gib-

ert in January 2016 and 20 additional plugs of similar size at ÍSOR with Sigurður Sveinn Jónsson in July 2016. Three additional plugs were prepared by Benoit Gibert in September 2018. In order to obtain cylinders, the extremities of the 91 plugs were sawed and polished by Benoit at Géosciences Montpellier. The remaining parts were kept for thin sections and powders.

Polished thin sections were prepared from one lateral face of each plug by Christophe Nevado and Doriane Delmas at Géosciences Montpellier and by Khaled Oubellouch and Damien Deldicque at Ecole Normale Supérieure (ENS, Paris). For some samples, two thin sections were prepared, where the second one was taken from the host core sample. I milled the remaining parts of the lateral faces at ÍSOR and Géosciences Montpellier, to obtain powders for X-Ray Diffraction and Cation Exchange Capacity measurements.

The host rock of the cores varies from basaltic glass of hyaloclastite type, to crystalline basalt of dolerite type. The dominant primary minerals from magmatic crystallization are plagioclases, pyroxenes and iron-titanium-oxides (e.g. titano-magnetite). The alteration level varies from fully altered glassy samples, where clay minerals dominate, often accompanied by zeolites, quartz and calcite, to almost fresh crystalline samples, with an abundance of unaltered plagioclase phenocrysts. For electrical measurements, the plugs were saturated with water containing six distinct NaCl concentrations, resulting in fluid conductivities ranging from 0.02 to 11 S/m.

1.2.2 *Cation Exchange Capacity (CEC)*

In the period August-December 2015, before the official beginning of the PhD, I was hired at ÍSOR to measure the CEC of drill-cuttings from borehole KJ-18 at Krafla. The protocol I used for CEC measurements was originally developed for high-CEC rocks (Meier and Kahr, 1999), so that the proportion of reactants suggested by the original protocol was not always optimal for our altered volcanic samples, some of them having a low CEC. Therefore, I analyzed the different sources of uncertainty in the CEC measurements and presented a modified protocol in a technical report (Lévy et al., 2016). I used this new protocol to carry out more than 400 CEC measurements during the PhD, on powder samples from the plugs, at ÍSOR. The CEC measurements were further used to determine the smectite weight fraction in each sample, as explained in details in Chapter 6.

1.2.3 *General petrophysics*

All the measurements presented here were carried out at Géosciences Montpellier in January 2016 and January 2017, with help from Benoit Gibert, Nicolas Marino, Didier Loggia and Franck Nono. After drying

the plugs in an oven at 60°C, I measured their dry weight and length. I determined the solid volume of each plug, using the so-called "Helium porosimetry" method, relying on isothermal decompression of helium in two well-known volumes, and calculated the total volume from length and diameter measurements. From there, I determined dry bulk porosity and density, as well as density of the solid matrix. Then, I saturated the plugs with low-salinity degassed water (fluid conductivity of about 100 µS/cm), after evacuating air-filled pores in a vacuum chamber. I determined the wet porosity and density by the triple weighting method, where the sample weight is measured in dry, saturated and immersed conditions (e.g. Pezard, 1990). I measured elastic velocities at 500 kHz both on dry and wet samples, using a digital oscilloscope, a pulse generator and coupled piezoelectric transducers. A coupling gel was used for P-waves and honey for S-waves. Elastic velocities measurements were finally not used in the PhD project but the data are available (see section 1.2.7 on data availability).

1.2.4 *Electrical impedance spectroscopy*

I measured electrical impedance on plugs over a large spectrum of frequencies (from 1-10 mHz to 1 MHz), using a Solartron 1260 impedancemeter at Géosciences Montpellier. More than half of the impedance measurements were carried out by Benoit Gibert, due to the spatial complexity of the PhD project and the extended periods of time between saturations of the samples at different salinities. Two different set-ups were used and compared: a 2-electrode set-up, where the sample is sandwiched between two metallic electrodes acting as current and voltage electrodes, and a 4-electrode set-up, where voltage and current electrodes are separated, which limits polarization at the measuring electrodes and allows more accurate measurements at frequency lower than 1 kHz. The sample holder for the 4-electrode measurements was built by Nicolas Marino and Benoit Gibert, following the design of Vinegar and Waxman (1984); it is shown in Paper 1.

In Paper 1, the dependence of the in-phase conductivity at 1 kHz upon salinity, CEC and porosity is analyzed for the 88 samples available in 2016, with several existing models. A phenomenological model is also fitted to the data. In Paper 2, the frequency-dependence of electrical impedance is analyzed for a subset of 30 samples, which contain significant volumes of pyrite or iron-oxides. The impedance spectra are fitted with a Cole-Cole model (Cole and Cole, 1941; Pelton et al., 1978), using the LEVMW software (Macdonald, 2000), but in the end, the fits are not used because the natural heterogeneity in these samples makes the interpretation of fitted parameters ambiguous. Fitting results are nevertheless presented in Supporting Information of Paper 2 and further analyzed in Chapter 7.

Electrical impedance of rhyolitic and basaltic glass from Krafla up to melting conditions (80-120 MPa confining pressure and 400-1260°C) was also measured by Benoit Gibert at Géosciences Montpellier in 2017, using the same impedance-meter as above but a more sophisticated set-up involving a Paterson Press (see protocol presented by Nono et al. (2018)). Before these measurements, I melted the basaltic sample at 1400°C with Annelise Faivre at the Charles Coulomb laboratory in University of Montpellier, to obtain glassy, bubble-free samples after air-quenching. Results from these experiments are presented in Chapter 7. This side-project was a follow-up of experiments carried out at Nýsköpunarmiðstöð Íslands (Innovation Center of Iceland) in collaboration with ÍSOR, in which I have been involved. The goal was to measure the conductivity of melted lava from the 2014-2015 eruption at Holuhraun in Northeastern Iceland.

1.2.5 *Mineralogy*

In February 2016, Benoit Gibert acquired a first run of X-Ray diffraction (XRD) scans, on the 68 roughly grained powders available at that time, at the Charles Gerhardt Institute in University of Montpellier, using a Philips X'Pert Pro Multi-Purpose Diffractometer. In March 2016, the 68 XRD scans were analyzed by Sigurður Sveinn Jónsson at ÍSOR to determine a qualitative mineral content in each sample. In January, March and May 2017, I acquired a second run of XRD scans at the Charles Gerhardt institute, with the help of Bernard Fraisse, on the 88 powders. For this second run, I had milled the powders to a smaller grain size and loaded them onto the sample holder with particular care to create a flat surface and avoid preferred orientation. The angular range investigated was also increased and the step-angle decreased, so that the scans could be analyzed quantitatively. I acquired this second run following a one-week course at University of Poitiers in January 2017, by Bruno Lanson and Eric Ferrage, about XRD quantitative analysis. Between January and May 2017, I quantified the mineral content of the 88 samples, using the software BGMN and the Profex graphical interface (Taut et al., 1998; Doebelin and Kleeberg, 2015), based on the Rietveld-refinements method. I was very much helped by Bruno Lanson and Nathanaël Findling at the University Joseph Fourier (Grenoble, France) for this quantification. XRD scans of fine fractions (which isolate clay minerals) were also recorded for part of the samples, first at ÍSOR by Sigurður Sveinn Jónsson and then at at the University Joseph Fourier by Nathanaël Findling.

I carried out petrographic observations on thin sections, first at ÍSOR using a binocular microscope, under the supervision of Helga Margrét Helgadóttir in March-August 2016, and then at ENS using a Scanning Electron Microscope (SEM) ZEISS ZIGMA (15 kV, 1-9

nA, 9 mm working distance), with Damien Deldicque in 2017-2018. I estimated the volume content of metallic particles (sulphides and iron-oxides) by analyzing the SEM photographs, using the ImageJ software (Abramoff et al., 2004).

I performed chemical analyses of minerals on polished thin sections at Géosciences Montpellier, using a CAMECA SX100 electron microprobe (22 keV, 10 nA), under the supervision of Jacinthe Caillaud in March and May 2017 (clay minerals) and Fleurice Parat in November 2017 and June 2018 (sulphides and iron-oxides).

1.2.6 *Geo-electrical field measurements*

Together with Jean Vandemeuleurbouck at ISTerre-Chambéry and Freysteinn Sigmundsson at University of Iceland, I organized field geoelectrical measurements at Krafla in August-September 2017, in order to be able to compare laboratory results to field data. Electrical Resistivity Tomography (ERT) and Time-Domain Induced Polarization (TDIP) measurements were performed along thirteen 1.24 km-long profiles, at three different sites around the eastern Krafla caldera. An ABEM Terrameter LS instrument was used to inject a square-wave current in the ground, using 50 cm-long steel electrodes. Measurements were recorded using different current-on times, in the range 0.4-4 s and current-off times, in the range 1-8 s. The acquisition protocol was designed by Svetlana Byrdina and André Revil (ISTerre-Chambéry). The cables, connectors and electrodes were borrowed from University of Clermont-Ferrand (France). In addition to the above-mentioned participants, the field work has benefited from the help of Damien Deldicque and Marine Roger at ENS, Daniel Juncu, Vincent Drouin and Sveinbjörn Steinþorsson at University of Iceland, Tullio Ricci at INGV (Italy) and Knútur Árnason at ÍSOR. The power company *Landsvirkjun* and University of Montpellier importantly contributed to the financial aspects, thanks to the support, in particular, of Sigurður Markússon and Benoit Gibert, respectively.

I wrote a proposal with Jean Vandemeulebrouck to obtain funding and permissions from INSU-CNRS and ISTerre. I coordinated logistics matters for the field campaign: housing and food at Krafla, with Edda Harðardóttir from *Landsvirkjun* and Steindór and Anna from *Steindór and Anna ehf*, batteries gathered and tested by Stefán Auðunn Stefánsson at ÍSOR and other material needed for the experiments (in particular bentonite made available by Pétur from *Jarðboranir* and 50 kg of salt bought at a retail shop by my friend Johann Pétur, who saved me this day!). My personal car and another car from University of Iceland were made available for transportation of people and equipment from Reykjavik to Krafla and on-site movements. Jean Vandemeulebrouck and Freysteinn Sigmundsson coordinated the transportation of equipment from Clermont-Ferrand and

Chambéry to Krafla (and back), as well as custom issues, helped by Svetlana Byrdina (ISTerre-Chambéry), Anthony Finizola (University of La Réunion, French oversea territories), Renault Trinquier (University of Montpellier), Sveinbjörn Steinþórsson, Vincent Drouin and Anna Kristín Árnadóttir (University of Iceland).

Three videos for outreach about my PhD, geothermal exploration and the field experiments were directed by Margaux Dzuilka from the Institut Pratique de Journalisme (IPJ) at Paris-Dauphine, with financial and technical support from Julie Iem, Caroline Hodak, Jérôme Lesieur and Milica Damjanovic at Paris Sciences et Lettres (PSL) and Pierre Briole at ENS. A link to the videos and newsletter article is given in A.

For the inversions of ERT/TDIP data, I used the 2D inversion code *AarhusInv* developed by Fiandaca et al. (2013) and Auken et al. (2014). This code incorporates the possibility of taking into account the waveform of the transmitted current, as well as of retrieving the spectral content of the IP signal from time-domain data sets by modeling the full voltage decay. Pradip Maurya from the Hydrogeophysics group at Aarhus University (Denmark) post-processed the full waveform datasets to obtain the longest decay curves possible, while removing noise. I filtered the processed data with the software *Aarhus Workbench*, thanks to a free temporary license granted by the company Aarhus GeoSoftware, to remove outliers in DC resistivity and TDIP decay curves and prepare a clean dataset for inversion. I inverted all the datasets (combining recordings using different on-times together) and plotted the results thanks to a Matlab routine, developed at Aarhus University. Collaboration with Pradip Maurya, as well as Svetlana Byrdina, Jean Vandemeuleubrouck and Knútur Árnason, have been essential to the processing, inversion and interpretation of the field data. Results are presented in Chapter 5.

1.2.7 *Data availability*

The Spectral Induced Polarization (SIP) and petrophysical data related to this PhD work are available on-demand and on the collaborative platform sip-archiv. A Matlab code for automatic fitting of the salinity variations of electrical conductivity using different models is available on demand. The field data related to this PhD work are available on-demand.

1.3 ORGANIZATION OF THE THESIS

Chapter 2 gives the reader background information to understand the main results of the PhD and their implications. Since the results address the electrical properties of hydrothermally altered rocks, both in laboratory and in the field, with a long-term application to geother-

mal exploration and a particular focus on the Krafla volcano, it is organized as follows:

1. Presentation of geothermal fields in the world and the place of geothermal energy in the low-carbon energy landscape.
2. Description of the structure of active continental hydrothermal systems and resulting hydrothermal alteration and its use in the mapping of geothermal reservoirs.
3. Introduction to the crystallo-chemical properties responsible for cation exchange capacity in clay minerals and zeolites.
4. Review of models describing the frequency-dependent electrical behavior of saturated rocks, including both conduction and polarization, with a focus on the influence of porosity, salinity, clay minerals and metallic minerals.
5. Presentation of geo-electrical methods used in the field for the geophysical investigation of the Earth, with a focus on Electrical Resistivity Tomography (ERT) and Time-Domain Induced Polarization (TDIP).
6. Outline of the geology at the Krafla volcano, in the context of the geology of Iceland, and geothermal exploration at Krafla.

The main results are presented as follows:

- Paper 1, published at Geophysical Journal International
- Paper 2, under review at Journal of Geophysical Research - Solid Earth
- Paper 3, under review at Geophysical Journal International
- Paper 4, manuscript in progress, intended for submission to Geothermics

A two-page summary is presented in Chapter 3 to Chapter 6 for Papers 1 to 4, respectively and the full versions are available in Appendix B. Chapter 7 includes additional unpublished results, obtained as part of the PhD but not intended for publication elsewhere. Chapter 8 describes on-going projects, which are not considered as part of the PhD but were launched as further developments of the PhD work. Chapter 9 is a two-page overall conclusion, combining all results in Chapter 3 to Chapter 7. Finally, A lists the contributions to conferences and public outreach.

2

BACKGROUND

2.1 GEOTHERMAL RESERVOIRS AND ENERGY

2.1.1 *Geothermal reservoirs in the world*

Geothermal fields are geological structures that enable the heat stored in the Earth's crust to be dissipated (Meunier, 2005). Geothermal reservoirs can be classified into high- or low-enthalpy, depending on whether the fluid enthalpy is greater than 800 kJ/kg (Axelsson, 2008). Alternatively, they can be classified into high-, medium- or low-temperature, if the temperature is $\geqslant$ 200°C, in the range 100-200°C or $\leqslant$ 200°C at 1 km depth, respectively. The overall distribution of high-temperature geothermal reservoirs in the world is dictated by the presence of hot spots and plate boundaries, responsible for volcanic and/or tectonic activity (Figure 1 and Figure 2). In these systems, temperatures may reach up to 350°C at exploitable depths ($<$ 2.5 km) (Henley and Ellis, 1983). From these reservoirs, both hot water and steam can be extracted. While hot water (up to 80-90°C) can be directly transferred to district heating networks through pipelines (e.g. in Reykjavík, Iceland and in Paris Basin, France), steam is separated and used for electricity production by triggering a rotational movement of turbines, which is then turned into a magnetic and electrical fields (similarly to the effect of wind on windmills).

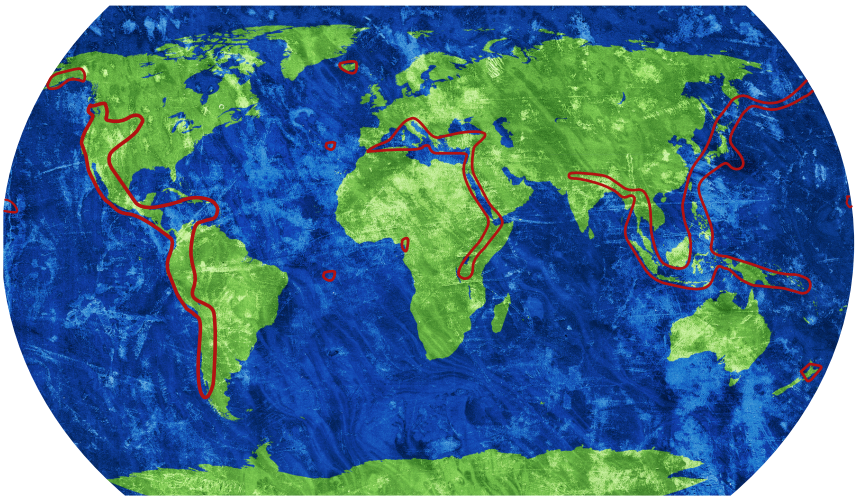

Figure 1: Schematic view of worldwide zones where very high enthalpy could exist at drillable depths. Re-drawn based on information from Elders et al. (2014).

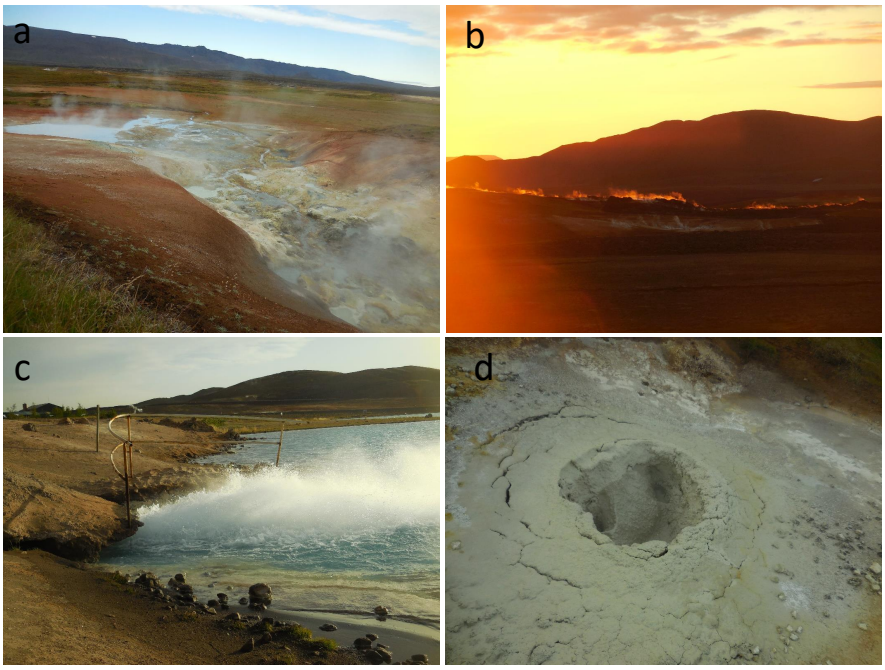

Figure 2: Surface manifestations of geothermal activity at the active plate boundary in Iceland: (a) Surface acidic alteration (native sulphur, gypsum) and mud pots at Þeistareykir; (b) Steam outflow along fissure eruptions triggered by the rifting episode at Krafla in 1975-1984 (viewed from the Víti crater); (c) steam outflow in the waste water basin at the Bjarnarflag power plant; (d) zoom on surface acidic clay alteration at Þeistareykir. All pictures were taken in Northeast Iceland in September 2015.

Low-temperature geothermal reservoirs refer to to any kind of heat in the ground, which can be harnessed. These reservoirs are more evenly distributed in the world. They are found, for example, in major sedimentary basins, as e.g. the Paris basin in France (Vernier et al., 2015), where permeable sedimentary layers at depth greater than 1 km coincides with temperature gradients higher than 30°C/km. Heat stored in the near surface during summers is another possible source of low-temperature geothermal energy, which can be found all over the globe and used with heat pump technology.

All geothermal systems exploited today are related to convection of hot water and are thus hydrothermal systems (Axelsson, 2008). Dry geothermal systems, with no or little natural water convection, might be exploited in the future by creating new or enhancing existing permeability by various stimulation methods. Such systems are called "Enhanced Geothermal Systems" (EGS) and the first operative EGS pilot plant is in Soultz-sous-Forêt, France (Vernier et al., 2015). Depending on the type of reservoir available, different types of geothermal power plants can be built. Geothermal plants are classified as binary, back pressure, single/double flash, dry steam or triple flash,

with an average installed capacity per unit ranging from 6 to 90 MW from binary to triple flash (Bertani, 2005).

2.1.2 *Geothermal in the low-carbon energy mix*

The first electricity production from a geothermal power plant took place in Larderello (Italy) in 1904. In 2015, the total installed geothermal capacity in the world was 12.7 GW for electricity production (Bertani, 2016). The expected geothermal installed capacity for electricity in 2050 is 70 GW for conventional hydrothermal resources and 140 GW in total, including EGS and other dry steam resources (Bertani, 2016). The global share of geothermal energy is predicted to rise up to 3.9% for heat and 3.5% for electricity production by 2050, allowing avoiding 800 megatons of CO_2 per year (IEA (International Energy Agency), 2011). One of the main challenges is to accelerate resource assessment.

The top five countries for installed geothermal capacity are the USA, Philippines, Indonesia, Mexico and New Zealand, with Italy, Iceland and Japan being next (Figure 3). Kenya and Turkey have undergone among the largest increases over the last years, both in installed capacity and energy produced, thus entering the top ten countries (Bertani, 2016).

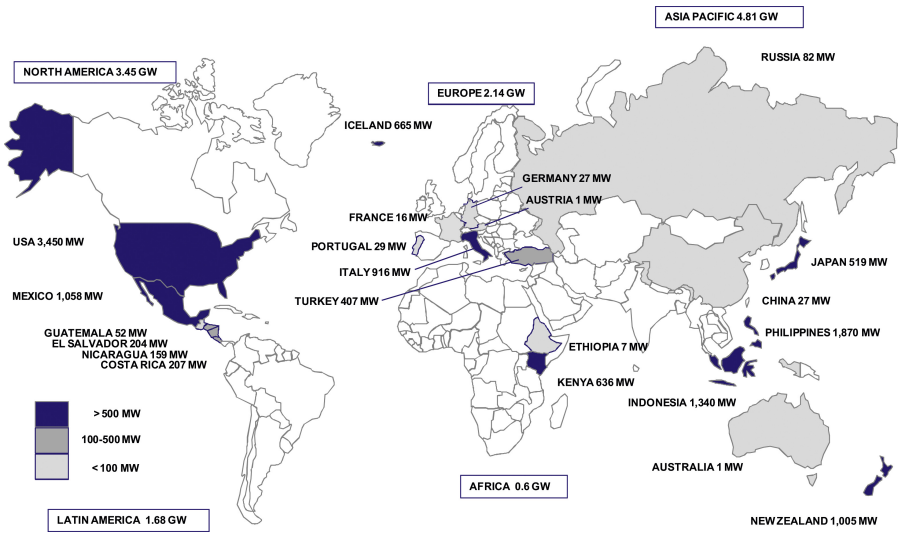

Figure 3: Worldwide geothermal installed capacity, for electricity production and space heating combined, in 2015. Reproduced from Bertani (2016), with permission from Elsevier.

In the USA, California has the greatest power production (2.7 GW installed and 13023 GWh produced annually), while Hawaii had the greatest share of geothermal energy in total electricity production (25% corresponding to 236 GWh produced annually) - at least until the Puna geothermal power plant was damaged following the Kilauea eruption in 2018 (Bertani, 2016). In Iceland, about 90% of space

heating and 25% of electricity are produced by geothermal energy (Figure 4). Eight geothermal power plants produce a total energy of about 5000 GWh annually (Figure 5).

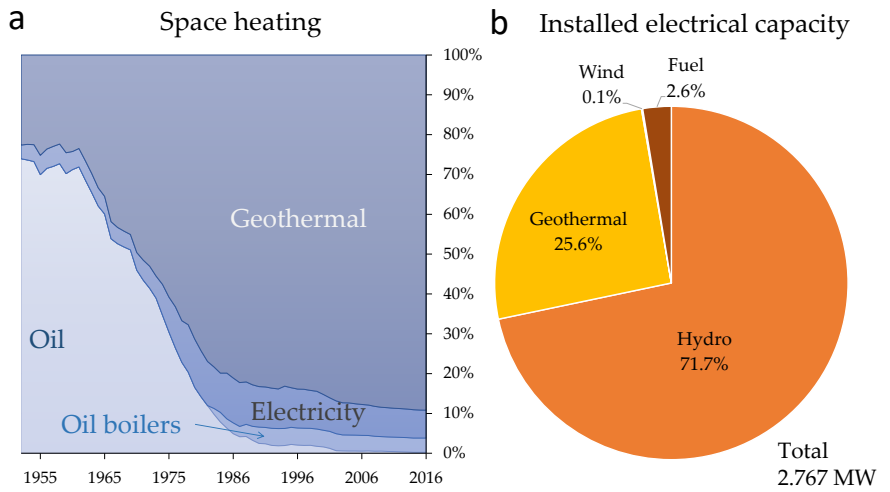

Figure 4: Energy sources in Iceland. (a) shows variations with time of energy sources for space heating and (b) shows distribution of energy sources for electricity production in 2017. Data from Orkustofnun repository (files: OS-2018-T010-01 and 0S-2018-T006-01).

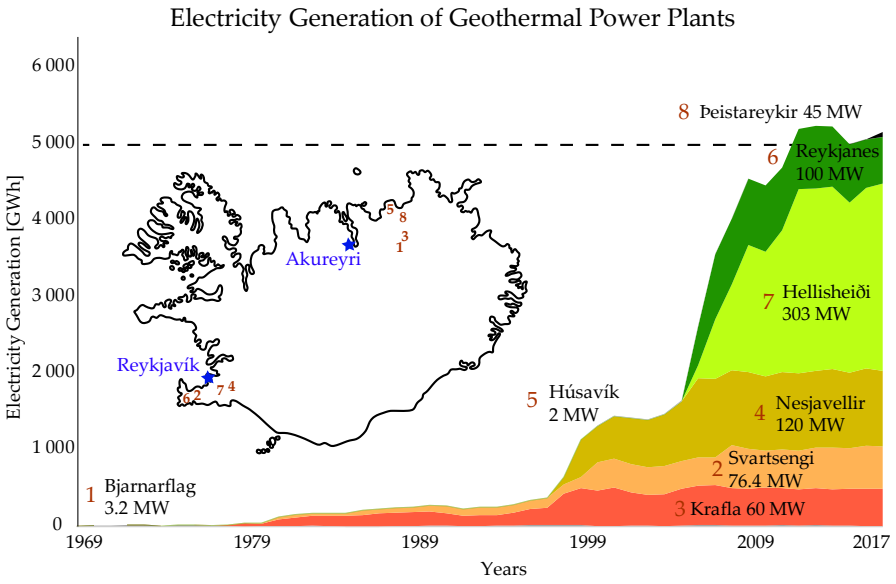

Figure 5: Electricity production from geothermal power plants in Iceland. Data from Orkustofnun repository (file: 0S-2018-T005-01).

The cost per kWh of electricity produced from high-enthalpy hydrothermal reservoirs is generally less than that from other renewable resources, apart from old generation nuclear plants, according to two different data sets from the International Energy Agency (IEA)

Table 1: Levelized Cost of Electricity[1] from renewable sources in 2017. EGS = Enhanced Geothermal Systems; PV = Photovoltaic; USD = US Dollar

Energy source	Category	USD/MWh[2]	USD/MWh[3]
Geothermal	High-enthalpy	60-100[4]	42
Geothermal	Binary	117	
Geothermal	EGS	97-270[5]	
Solar	PV	90-300[6]	50
Solar	thermal	100	130
Wind	On-shore	50-230	48
Wind	Off-shore	146-261	117
Nuclear		75-100[7]	93

[1] The Levelized Cost of Electricity (LCOE) is a normalized price of electricity, calculated so that if electricity was sold at that tariff, the power company would precisely break even, after payment of investors and debts - including discount and interest rates (OECD/IEA, 2015).

[2] Based on IEA data from Projected Costs of Generating Electricity (EGC) database, considering a discount rate of 10%. OECD/IEA 2015, www.iea.org/statistics. License: www.iea.org/t&c; as modified by Léa Lévy.

[3] Based on US Energy Information Administration (EIA) data from the *Annual Energy Outlook 2018*, available on www.eia.gov/, considering a discount rate of 7%.

[4] Range predicted to decline to 50-90 by 2050

[5] Estimation if operating in 2030

[6] Range predicted to decline to 40-160 by 2050

[7] LCOE for currently operated designs. New designs (Gen III) are expected to have higher LCOEs due to higher safety standards (IEA (International Energy Agency), 2015)

and the U.S. Energy Information Administration (EIA), respectively (see Table 1). Intermittence of geothermal power is not a concern, as opposed to solar panels or windmills. Moreover, geothermal heating (whether from low- or high-enthalpy reservoirs) is more energetically efficient than electrical heating since no energy conversion is needed. Therefore, geothermal energy is an important part of the long-term plans of reducing carbon dioxide emissions and closing nuclear power plants. However, geothermal resources are only renewable to some extent because the energy stored by heat conduction is renewed relatively slowly, on the order of hundreds of years, as compared to the extraction time-scale (Stefansson, 2000). Moreover, EGS resources are not yet competitive on the electricity market (Table 1).

2.2 STRUCTURE AND DYNAMICS OF HYDROTHERMAL SYSTEMS

Hydrothermal systems have been known since Antiquity for their hot springs and potential ore deposits (Meunier, 2005). The study of exhumed fossil systems has revealed that these geothermal fields form the upper part of a greater system whose deep roots often relate to porphyry copper deposits (Henley and Ellis, 1983), often also associated to shallower epithermal ore deposits (Hedenquist et al., 1998). Hydrothermal systems affecting deep sea-floor basalts, and arising from the floor surface in the form of "black smokers", have been discovered during the later half of the 20^{th} century but are better known today thanks to oceanic research programs (Alt, 1999). Iceland is the site of numerous on-land hydrothermal systems, on which we will focus here.

High-enthalpy continental geothermal fields are typically the near-surface expression of a hydrothermal activity related to the emplacement of magmatic intrusions. Two heat transfer processes take place simultaneously in different parts of hydrothermal systems: convection and conduction. Emplacement of magmatic intrusions enables the slow formation of thermal aureoles by conduction. The seismic activity opens faults, thus forming high-permeability networks that allow transfer of hot fluids by convection (Meunier, 2005). Heat convection cells are formed when the down-flowing dense cold water comes into contact with hot rock, heats up and move upward, due to the density difference between hot and the cold fluid (Figure 6). The chemical and mineralogical interactions accompanying these circulations cause the sealing of the networks through deposits of secondary minerals. The permeability of the networks may be reduced and heat conduction processes can start to dominate the heat transfers and mineral alteration (Bril et al., 1996), unless faults are re-opened at the same place. Over time, the "convective thermal plume" moves with the most efficient permeability network.

Hydrothermal alteration refers to interaction between hot aqueous fluids and solid rocks (Meunier, 2005). Stable isotopes studies indicate that meteoric water is the predominant source of cold water in the majority of hydrothermal systems, although seawater sometimes predominates in some regions, such as Reykjanes in southwest Iceland (Henley and Ellis, 1983).

2.2.1 *Mapping geothermal resources*

Surface mapping of volcano-tectonic features (fissures, faults, craters, ground tilting), as well as hydrothermal features (fumaroles, hot springs, surface alteration), if visible, allows a first assessment of directional trends and local concentrations of geothermal resources (Flóvenz et al., 2012). In very active geothermal areas (such as Krafla and Ná-

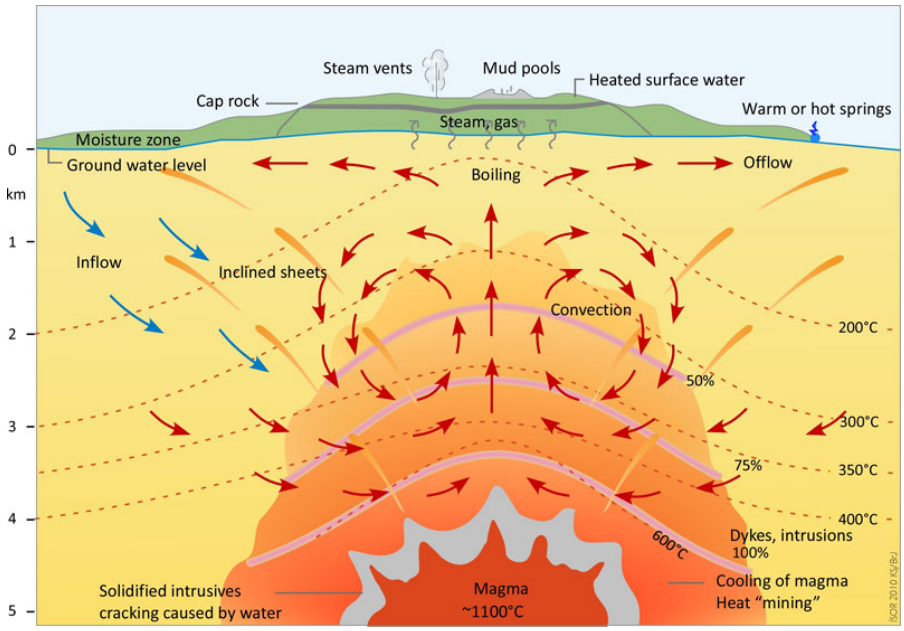

Figure 6: Simplified representation of hydrothermal systems in Iceland, drawn by Kristján Sæmundsson in Ketilsson et al. (2010). The percentages indicate the fraction of intrusive material (dykes, sheets and minor intrusions) in the rock matrix.

mafjall in Northeast Iceland), surface alteration can be observed over large areas, near fumaroles. Boiling in the subsurface causes the transfer of acidic gases (CO_2 and H_2S) to the steam fraction, which then penetrates the surface (see e.g. Figure 2). Surface alteration results in particular from the oxidation of hydrogen sulfur (H_2S) escaping from the fumaroles into acid sulfate (H_2SO_4), upon reaction with oxygen at the surface (Markússon and Stefánsson, 2011; Carson, 2015). H_2SO_4 is a strong acid, which easily leaches the rock surface. Different types of "acidic" alteration minerals can be observed at the surface: kaolinite, gypsum, jarosite, goethite. Sulphide minerals, such as pyrite, require reductive conditions (low oxygen pressure) to be thermodynamically stable and are thus never observed at the surface.

In the absence of clear surface manifestations, mapping subsurface lithology and alteration, usually based on drill-cuttings from exploration boreholes, is used to delineate hot and permeable zones (Gudmundsson, 2005). In Iceland, an abundance of pyrite has been correlated to the presence of aquifers (Gudmundsson, 1993; Gudmundsson et al., 2010). Moreover, the distribution of alteration minerals observed from drill-cuttings analysis is used to evaluate the rock temperature at the time where alteration minerals formed, according to a list of index minerals presented in Table 2 (Franzson, 1998). This list is a simplification, relevant for Icelandic rocks, of a more general classification including five series of minerals, where each series corresponds to the following major cations: Na^+, Ca^{2+}, $Ca^{2+} + Mg^{2+}$,

Table 2: Index minerals used in geothermal exploration and their temperature range, according to Franzson (1998).

Minerals	$Temp_{min}$ (°C)	$Temp_{max}$ (°C)
zeolites	40	120
laumontite	120	180
quartz	180	>300
wairakite	200	
smectite		<200
smectite-chlorite	200	230
chlorite	230	>300
calcite	50-100	280-300
prehnite	240	>300
epidote	230-250	>300
wollastonite	260	>300
actinolite	280	>300

K^+ and H^+ (Meunier, 2005; Utada, 1980). Indeed, in Iceland, most of alteration minerals fall in the Ca^{2+} (stillbite-heulandite-laumontite-wairakite) and the $Ca^{2+} + Mg^{2+}$ (smectite-chlorite-epidote-actinolite) series of minerals (Walker, 1960; Walker, 1974; Kristmannsdóttir and Tómasson, 1978; Kristmannsdottir, 1979). In New-Zealand, dominated by a different type of volcanism (more andesitic), alteration minerals rather fall in the K^+ series (smectite-illite-K-felspar) (Steiner, 1968).

In diagenetic smectite-chlorite series, smectite is indeed found in the range of temperature predicted by thermodynamics while chlorite dominates at higher temperatures (Bourdelle et al., 2013; Beaufort et al., 2015). At low temperature, typically below 150-180°C, smectite is thermodynamically stable and forms a clay cap, often observed in geothermal systems (Kristmannsdottir, 1975). Above 150-180°C, smectites of saponite-type (Mg-rich) and of montmorillonite-type (Al-rich) are progressively transformed into corrensite and then chlorite and into mixed-layer illite/smectite and then illite, respectively, if enough time is given so that a thermodynamic equilibrium can be reached (Beaufort et al., 2015). Therefore, the boundary between smectite-rich and chlorite-rich layers is often used as a geothermometer (e.g. Kristmannsdottir, 1979).

Chemical kinetics rates indicate the speed of chemical reactions, provided that thermodynamics conditions are favorable (e.g. chemical elements available, temperature, pressure, oxidation-reduction conditions). Kinetics rates are typically faster at higher temperatures and can be so slow at low temperature that a crystal can be stable outside its thermodynamics stability range. Because of slow kinetics rates of chlorite dissolution (high energy barrier), the retrograde transfor-

mation of chlorite into smectite upon cooling is unlikely to occur in volcanic environments although it has been observed locally in laboratory experiments using chlorite gels (Vidal et al., 2012). Oxidizing conditions can on the other hand alter chlorite crystals and transform them into vermiculite by oxidation of Fe(II) into Fe(III) (Beaufort et al., 2015).

Moreover, the crystallization of smectite, which is considered to be a temporary step in the kinetic formation of chlorite (Beaufort et al., 2015), is amongst the first mineral to appear in hydrothermal systems, even at temperatures up to 300°C, due to its fast kinetic rate (Beaufort et al., 1995; Patrier et al., 1996). Therefore, the use of clay minerals as geothermometers in volcanic environments is limited by the fact that "high-temperature" minerals can be stable at low temperatures after their crystallization and "low-temperature" minerals can also be stable for short times at high temperatures. However, this is not the only limit of using alteration minerals for mapping geothermal resources.

2.2.2 *Different origins of clay minerals in volcanic rocks*

Although secondary minerals deposited upon circulation of hydrothermal fluids can indicate active or former hydrothermal convection cells, they can also originate from other processes, which do not involve hydrothermal convection cells (e.g. Schenato et al., 2003). We review here the four main sources of alteration minerals, and in particular clay minerals, in volcanic rocks: (i) precipitation from over-saturated hot fluids by hydrothermal convection in fracture networks ("útfellingar" in Icelandic), (ii) local alteration of volcanic glass and minerals upon hydration ("ummyndun" in Icelandic), (iii) "auto-alteration" of volcanic glass and minerals (Meunier et al., 2012; Meunier et al., 2010; Anderson, 1975) and (iv) crystallization from evolved volatile-rich magmatic fluid in closed vesicles "vesicle segregation" (Schenato et al., 2003; Merle et al., 2005).

First, clay minerals precipitate from over-saturated fluids in permeable fracture networks, usually leading to their clogging at some point (Bril et al., 1996). This specific occurrence of clay minerals is probably the most relevant for geothermal exploration, since it definitely indicates leaching and intense hydrothermal activity. However, in such conditions, the occurrence of clay minerals does not respect thermodynamics predictions, since smectite has been observed at temperatures higher than 300°C, e.g. in Chipilapa (El Salvador) and Milos (Greece) (Beaufort et al., 1995; Patrier et al., 1996). Clay minerals formed from over-saturated hydrothermal fluids can be chemically equilibrated with the local mineralogy or not. For example, Al-rich and di-octahedral clay minerals (montmorillonite, illite, kaolinite) are abundantly found in fractures of basaltic rocks, although these minerals are not chemically equilibrated with basalts. But Mg/Fe-

rich tri-octahedral clay minerals (saponite, corrensite, chlorite), which are in chemical equilibrium with basalts, can also precipitate in fractures (Meunier et al., 2008). Other secondary minerals, such as zeolites and quartz, are common alteration products from hydrothermal convection (e.g. Vergara et al., 1993) and tend to form big isolated chunks, as shown for sample L4 in Figure 7. Calcite tends to fill all the free spaces, inside fractures but also the voids remaining after clay minerals, such as chlorite, crystallize, as shown for sample L93 in Figure 7. Dissolution of titano-maghemite leads to the formation of iron-sulphides and rutile and leaves ghost textures (Oliva-Urcia et al., 2011), as shown for sample L9 in Figure 7. Pyrite precipitation is observed as disseminated or connected patterns, with a wide range of crystal size (Figure 8). Upon predominance of heat conduction processes after clogging of the permeable networks, smectite and zeolites can be replaced by chlorite and epidote, respectively.

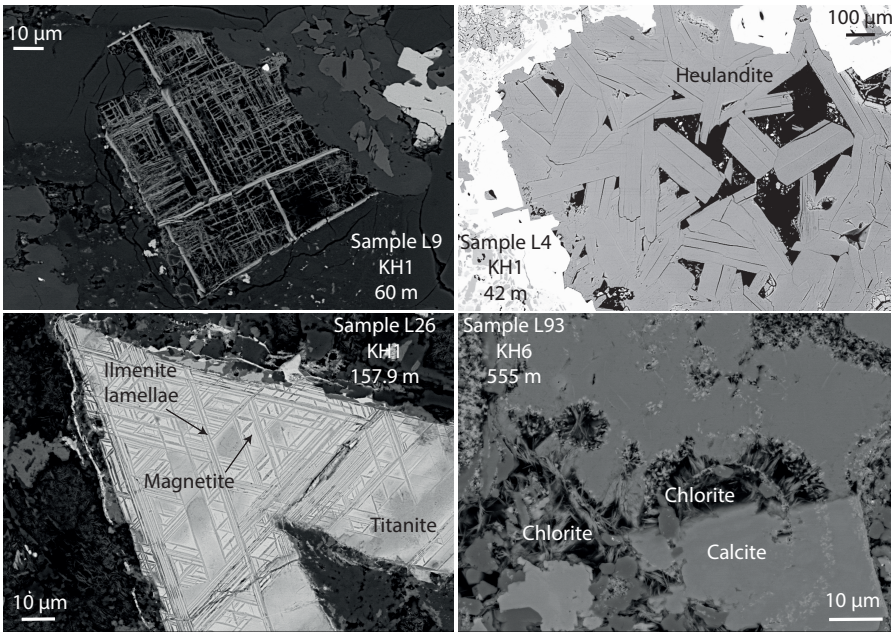

Figure 7: SEM photographs of four thin sections from samples: L9, L4, L26 from borehole KH1 and L93 from hole KH6. Sample L9 shows ghost texture left by dissolution of iron-oxides. Sample L4 shows a big vesicle filled with large heulandite (zeolite) crystals. Sample L26 shows a former titano-magnetite transformed into magnetite with exsolution strips of ilmenite; the assemblage being further replaced by titanite. Sample L93 shows calcite and chlorite. The depth of each sample in the corresponding borehole is indicated under the name of the sample and borehole.

Second, clay minerals are the main products of volcanic glass alteration "palagonitization", which mostly consists in hydration, as part of the local alteration process ("ummyndun" in Icelandic). Palagonitization can occur by reaction with a liquid aqueous phase if the temperature is above 40-70°C (Peacock and Fuller, 1928; Singer and

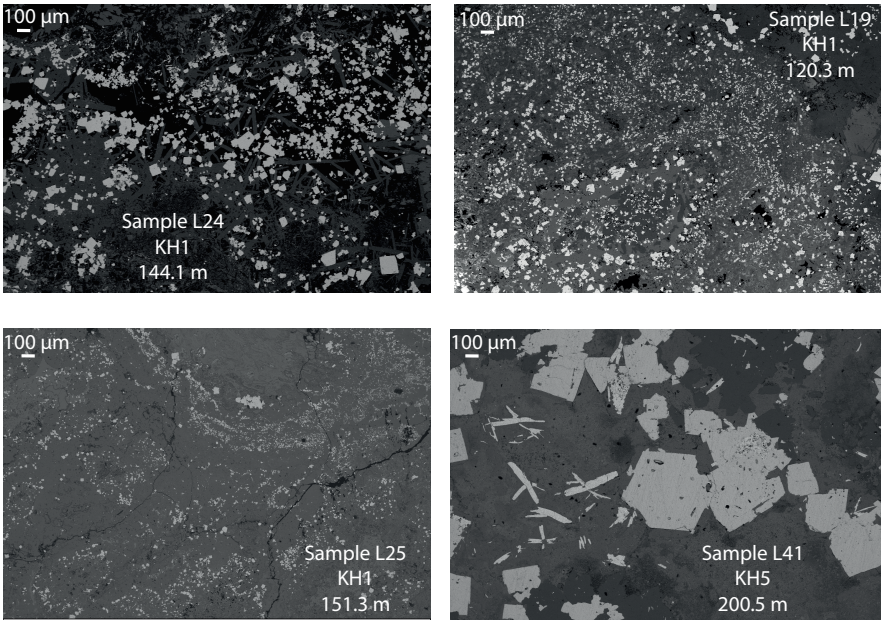

Figure 8: SEM photographs of four thin sections from samples showing abundant sulphide (mostly pyrite) precipitation, as a result of hydrothermal circulations: L24, L19 and L25 from borehole KH1 and L41 from hole KH5. The bright color highlights the sulphides. The scale is the same on all the photographs but the sulphide grain sizes are different. The depth of each sample in the corresponding borehole is indicated under the name of the sample and borehole.

Banin, 1990). Liquid water usually has a supergene origin – rainwater or glacier melting. Volcanic glass erupted under a glacier (hyaloclastite) and at the surface (top and base of lava piles) can be in contact with supergene water for a long time after the magma has crystallized. Depending on the rock temperature, the hydration of volcanic glass and minerals by supergene water will cause different alteration minerals ("ummyndun") (Beaufort et al., 1992). These minerals will be in chemical equilibrium with the glass, e.g. in the series saponite-corrensite-chlorite for clay minerals in basaltic glass (Meunier et al., 2008; Berger and Velde, 1992).

Third, "late-magmatic" clay minerals can be the result of an "auto-alteration" process, by interaction between volatiles from the magma (endogeneous) and solid basaltic glass. According to recent experimental and modeling work related to the origin of clay minerals on Mars, conditions for auto-alteration of volcanic glass include the presence of dense steam or supercritical fluid, supersaturated in H_2O and CO_2 (Cannon et al., 2017; Meunier et al., 2012; Schaefer, 2017; Berger et al., 2014). Since lava flows and hyaloclastites are erupted on the surface or under cold water close to the surface, it is unlikely that the conditions required for "auto-alteration" of volcanic glass into "late-magmatic clays" are satisfied in the context of Icelandic volcan-

ism. Nevertheless, auto-alteration of primary iron-oxides minerals is common. For example, at about 600°C under oxidizing conditions, titano-magnetite ($Fe_{3-x}Ti_xO_4$) crystallized from the lava is replaced by magnetite (Fe_3O_4), accompanied by oxy-exsolution lamellae of ilmenite ($FeTiO_3$) (Haggerty, 1991; Hoisé, 2011), as shown for sample L26 in Figure 7 (one of the samples investigated in this thesis). Lower-temperature oxidation (250-350°C) will then produce titano-maghemite ($Fe_{3-x}Ti_xO_3$), as well as titanite ($CaTi(SiO_5)$) in the vicinity of the former iron-titanium-oxide mineral.

Fourth, clay minerals can also be found as partial or total in-filling of closed vesicles (Sanders, 1986; Merle et al., 2005). An infiltration of hydrothermal liquid, by very narrow drains, in apparently closed vesicles is a first possible explanation for the formation of clay minerals in vesicles. Another likely explanation is the chemical reaction between an evolved volatile-rich supercritical fluid – trapped in cooling basalt and shaping a future vesicle, and basaltic glass surrounding the vesicle (Berger et al., 2018). This process is also called "vesicle segregation". Indeed, the supercritical fluid would concentrate incompatible elements at the end of basalt crystallization and thus lack in particular Mg, Fe to form clay minerals such as corrensite and chlorite by direct recrystallization. But the H_2O and CO_2 pressure would be sufficient to alter the surrounding basaltic glass by similar processes to those mentioned above. Additionally, minerals of rhyolitic composition (e.g. K-feldspar) can form in closed vesicles by direct recrystallization from the evolved supercritical fluid, enriched in H_2O, CO_2, Si, Al and K. Evidences of such vesicles filled with clay minerals are believed to be the first source of clays in early planets (Meunier et al., 2012; Schaefer, 2017).

While "útfellingar", and to some extent "ummyndun", are clear signs of past or present hydrothermal activity, auto-alteration and vesicle segregation can indicate past or present supercritical fluids or steam. The different origins of alteration minerals is not the focus of the thesis but are addressed in Chapter 3 and Chapter 4, where, in particular, high connectivity of smectite (and associated conductivity) is assumed to indicate an hydrothermal origin.

2.3 CLAYS, ZEOLITES AND CATION EXCHANGE CAPACITY

In soil science or petroleum engineering, clays are referred to as the small-grain-size end-member of the sands-clays scale, where sands, sandstones, limestones, shaly sands and clays have a decreasing grain size, from 2 mm to $\leqslant 2\mu m$. In mineralogy, clays are minerals belonging to the phyllosilicate family, also named sheet-silicates. In this thesis I always refer to clays as the latter definition.

2.3.1 *Crystalline structure of phyllosilicates and zeolites*

The building bricks of phyllosilicates are:

- tetrahedrons SiO_4 with Si^{4+} atoms in the centers and oxygen atoms in the four corners
- octahedrons $Al_2(OH)_2$ or $Mg_3(OH)_2$ with Al^{3+} or Mg^{2+} in the centers, and oxygen atoms or hydroxyl groups (OH) in the eight corners

The tetrahedrons can share oxygens to form hexagonal rings, and the repetition of this pattern forms a flat tetrahedral sheet T (Figure 9 (a) and (b)). Similarly, octahedrons share oxygens and form an octahedral sheet O. An $Al_2(OH)_2$ octahedral layer is called „di-octahedral“, as only two of three octahedrons contain Al, the third one being empty, while a $Mg_3(OH)_2$ octahedral layer is called „tri-octahedral“, as the three octahedrons contain Mg. The T and O sheets are stacked on top of each other, to form basic building blocks: T-O-T or T-O. A rich variety of mineral structures is created from these blocks (Lyklema, 2001). During the genesis of T-O-T phyllosilicates (e.g smectite, illite), substitution of multivalent cations by cations of lower valency often takes place, due to the limited availability of some species: Si^{4+} by Al^{3+} or Fe^{3+} in tetrahedral layers and Al^{3+} by Fe^{2+}, Mg^{2+}, Cr^{2+}, or other "heavy" bivalent cations in di-octahedral layers. As a consequence, a negative volume charge, called "permanent charge" develops on the sheets. In T-O phyllosilicates (e.g. kaolinite, serpentine), no such substitution occurs; the reason for that is unclear (Meunier, 2013).

The permanent charge of T-O-T phyllosilicates varies from 0 to 2 per Si_4O_{10} (half unit cell). This charge can be compensated in the inter-sheet “interfoliar” space by hydrophilic (Na, Ca) or less hydrophilic cations (K) or by a brucitic layer (polymer of $Mg(OH)_6$) in the case of chlorite (Ferrage et al., 2005). Below 0.7 charges per Si_4O_{10} (smectite), weak Coulombic bondings allow the penetration of water with any cations, which causes the structure to expand and allows cation exchanges (Figure 9 (d)). Around 0.7 charges per Si_4O_{10} (vermiculite) and beyond (illite, micas), cation exchange properties depend on the cation: hydrophilic cations will be accompanied by wa-

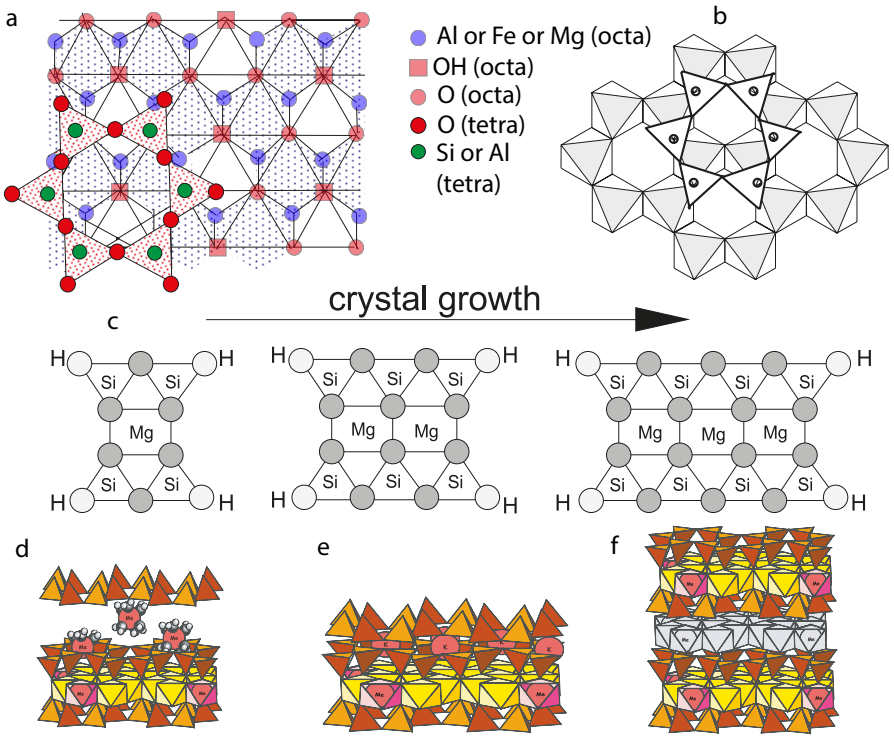

Figure 9: Crystal structure of clay minerals. (a) Two-dimensional view of the horizontal superposition of octahedral and tetrahedral sheets in clay minerals, simplified from Meunier (2005). (b) same view as (a) showing only the geometry, reproduced from Meunier (2005) with permission from Alain Meunier. The circles indicate Si atoms at the center of the tetrahedrons and the shaded triangles indicate the faces of octahedrons in the horizontal plane; (c) horizontal growth of clay crystals, respectively, reprinted from Meunier (2005). The gray circles represent oxygen atoms; (d), (e), (f) three-dimensional sketches of smectite, illite and chlorite, reproduced from Ferrage (2016), with permission from Eric Ferrage. The orange and yellow colors indicate tetrahedrons and octahedrons, respectively. The red spheres sandwiched between two tetrahedral layers in d-e indicate interlayer cations, surrounded or not by water molecules (small white spheres). The pink octahedrons indicate that the theoretical atom has been substituted by an atom of lower valence (e.g. Al^{3+} by Mg^{2+}).

ter and allow cation exchanges, while less hydrophilic cations will be more attracted by the crystal than by water, seal the structure and prevent cation exchanges. Most minerals having more than 0.7 charges per Si_4O_{10} are K-saturated (muscovite, illite) and therefore non-expandable (Figure 9 (e)). The brucitic layer in chlorite (1 charge per Si_4O_{10}) prevents any water intake or cation movements in the interlayer space (Figure 9 (f)).

Zeolites are only composed of SiO_4 tetrahedrons, piled onto each other to form three-dimensional channels. Substitution of Si^{4+} by Al^{3+} or other cations of lower valence creates a negative charge in

the channels. The most common cation compensating the structural charge is Ca^{2+}, but K^{+}, Na^{+} and, to some extent, Sr^{2+} are also common. They are located inside the channels shaped by the aluminum-silicate framework (Pabalan and Bertetti, 2001). Zeolites can be divided into two groups:

- "rigid" zeolites (e.g. laumontite, mesolite, analcime, natrolite and scolecite), whose chemical formula is well-defined. Extra-framework cations (other than Al and Si) cannot be replaced but the water content can vary.
- "flexible" zeolites (e.g. heulandite, chabazite and clinoptinolite), which exhibit a wide and continuous range of extra-framework cation composition, as they can be exchanged (Fridriksson et al., 2004).

Wairakite is a framework silicate, often classified as a zeolite because its appearance and chemical composition are similar to that of analcime. However, as opposed to zeolite minerals, wairakite is always dehydrated (Ames, 1966).

2.3.2 *Cation Exchange Capacity (CEC)*

The Cation Exchange Capacity (CEC) of minerals, traditionally expressed in “milli equivalent”, that is mmol of electrons per 100 grams of rock (1 meq/100g = 964.85 Coulomb/kg), is the sum of the “variable CEC” and the “permanent CEC”. The variable CEC occurs on crystal surfaces and "variable" refers to a pH-dependency. Indeed, imperfectly interrupted chemical bonds at the end of crystal growth result in a negative external surface charge on most minerals. Therefore, most minerals in contact with water adsorb and desorb spontaneously cations along their "external" surface (Figure 9 (c)). The variable CEC increases with the pH because a decrease of H^{+} concentration in water causes a release of H^{+} cations occupying external exchange sites. The permanent CEC occurs inside the crystal lattice: interlayer or "interfoliar" spaces for swelling clays or channels for flexible zeolites, also called "internal" surfaces. The permanent CEC is pH-independent (Lyklema, 2001). The total CEC of smectite, which includes 70 to 97% of permanent CEC and the rest of variable CEC (Vogt and Köster, 1978; Lagaly, 1981), is much higher than the total CEC of non-swelling clays (Table 3), where only the variable CEC contributes by definition (Figure 10). While soil scientists and chemists tend to focus on permanent CEC, physicists are interested in both types of CEC, as they participate in electrical current conduction and polarization. In flexible zeolites, the total CEC can be very high (see Table 3) but the permanent CEC is limited to a certain size of cations, as the channels cannot expand (Meier and Kahr, 1999).

Table 3: CEC range for clay minerals and zeolites. Smectite and vermiculite are swelling phyllosilicates and heulandite is a flexible zeolites. Other minerals in the table do not have a permanent CEC. The ranges given include the maximum measured CEC, when appropriate molecules are used to maximize the exchange.

Mineral	CEC in meq/100g	Reference
Smectite	80-120	Bouchet et al. (2000)
Vermiculite	100-150	Bouchet et al. (2000)
Chlorite	5-15	Bouchet et al. (2000)
Illite	25-40	Bouchet et al. (2000)
Kaolinite	5-15	Bouchet et al. (2000)
Heulandite	300	Fridriksson et al. (2004)
Laumontite	0.5-9	Dyer et al. (1991)
Wairakite	0	Ames (1966)

A linear correlation between the CEC and the smectite fraction was found by Hower and Mowatt (1966) in a series of smectite-illite samples, emphasizing that cation exchanges mostly take place in smectite. Based on this result, we show in Paper 4 that the CEC of volcanic rocks, measured by a molecule which does not fit in the channels of flexible zeolites, provides with a reliable quantification of the smectite weight fraction, which is otherwise complicate to obtain. However, obtaining CEC values with such a molecule, which are comparable for different types of rock (including different levels of alteration) is not trivial. This will be addressed in Paper 4.

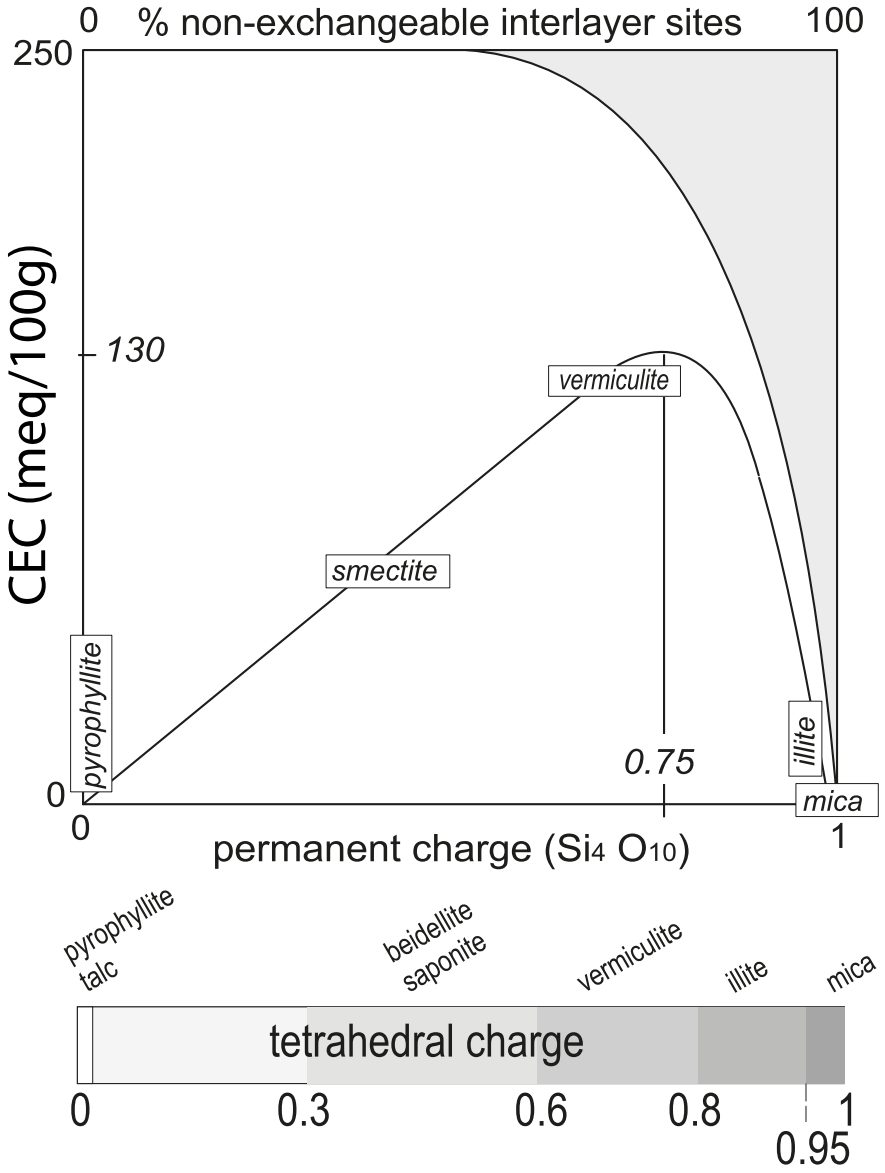

Figure 10: Schematic representation of the Cation Exchange Capacity (CEC) as a function of the structural tetrahedral permanent charge. Modified from Meunier (2005) and Bouchet et al. (2000), with permission from Alain Meunier.

2.4 COMPLEX ELECTRICAL CONDUCTIVITY OF SATURATED ROCKS

For a sinusoidal voltage $U(t) = U_0 \cos(\omega t + \theta_U)$ and current $I(t) = I_0 \cos(\omega t + \theta_I)$, the electrical impedance Z is given by $U(t) = ZI(t)$, where ω is the angular frequency in rad/s and θ_I and θ_U in rad are the phase angles of the sinusoidal current and voltage, respectively. Due to the alternating character of the voltage and current, it is convenient to write Z as a complex number (Equation 1) (e.g. Barsoukov and Macdonald, 2018; Agarwal and Lang, 2005; Sumner, 2012).

$$Z(\omega) = \frac{U_0 e^{i(\omega t + \theta_U)}}{I_0 e^{i(\omega t + \theta_I)}} = |Z(\omega)| e^{i\theta(\omega)} = Z'(\omega) + iZ''(\omega) \tag{1}$$

where Z, U and I are the impedance in Ω, voltage in V, and current in A, respectively. Z' and Z'' are the real and imaginary parts of the impedance, which is a complex number. t is the time in s, (U_0, θ_U) and (I_0, θ_I) are the amplitudes and phases of the sinusoidal voltage and current, respectively. $\theta(\omega) = \theta_I - \theta_U$ in rad is the frequency-dependent delay "phase angle" between the voltage and current. Most of the time, the phase angle of the complex conductivity is negative, corresponding to a phase delay of the voltage relative to the current.

The electrical conductivity σ is an intrinsic rock characteristic, independent of the geometry of a sample. For samples in the forms of plugs, as used in this thesis work, it is related to Z by Equation 2.

$$\sigma(\omega) = |\sigma(\omega)| e^{i\theta(\omega)} = \sigma' + i\sigma'' = \frac{Z'(\omega)}{|Z(\omega)|^2} \frac{L}{A} + \frac{Z''(\omega)}{|Z(\omega)|^2} \frac{L}{A} \tag{2}$$

where $|\sigma|$ and θ are respectively the frequency-dependent modulus and phase angle of the complex conductivity (Figure 11), σ' and σ'' are the in-phase (real) and quadrature (imaginary) parts of the complex conductivity and L and A are the length and cross-sectional area of a plug.

2.4.1 *In-phase electrical conductivity*

At a given temperature, the in-phase conductivity mainly depends on the pore volume, spatial distribution and salinity of pore water, as well as the clay content (Waxman and Smits, 1968; Revil et al., 1998). The in-phase conductivity of a volume of rock σ_{bulk} can be written as the sum of two parallel conductivities (Waxman and Smits, 1968): free ions in pore water σ_w and ions exchanged with minerals from the solid matrix σ_s (Equation 3). The latter contribution, often called "surface" or "interface" conductivity, is attributed in particular to an Electrical Doubler Layer (EDL) around solid grains that carry a natural negative charge (see model in Figure 12 (b)).

$$\sigma_{bulk} = x\sigma_w + y\sigma_s = \frac{\sigma_w + \sigma_s}{F} \tag{3}$$

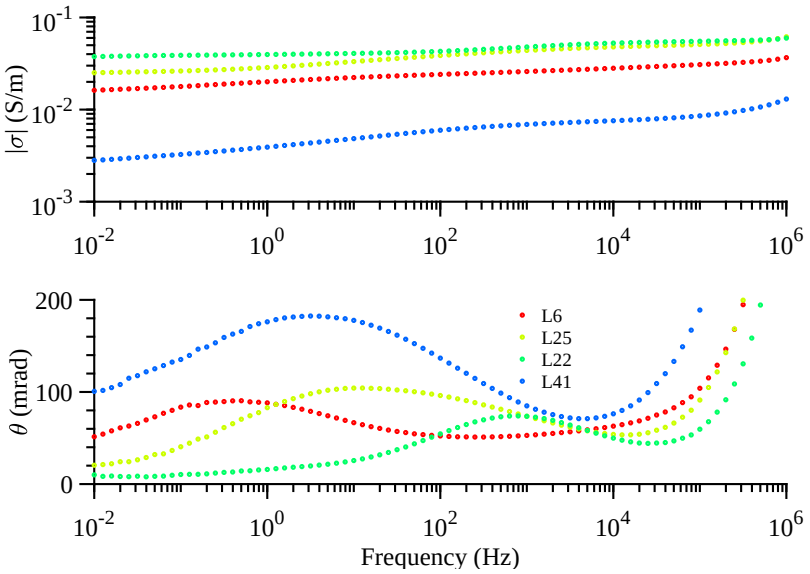

Figure 11: Frequency-dependence of the complex conductivity modulus and phase angle for four samples from this study, saturated with a pore water conductivity of 0.1 S/m. The phase angle is negative.

where σ_{bulk}, σ_w, and σ_s are in S/m, x and y are geometrical factor associated to ions in pore water and ions associated with clays. Assuming that the electrical current transported by exchange ions associated with clays travels along the same tortuous path as current associated to ions in pore water, the formation factor F (dimensionless) is defined by $x = y = \frac{1}{F}$.

According to Waxman and Smits (1968), the surface conductivity σ_s is defined by Equation 4.

$$\sigma_s = BQ_sSg \tag{4}$$

where B is the maximum equivalent ionic conductance of exchange ions (also called mobility of exchange ions), in As^2/kg, Q_s is the number of equivalents of exchange cations per unit of surface area, in meq/cm^2, S is the specific surface area of the clay, in cm^2 per gram of clay, and g is the weight of clay per unit of rock pore volume, in gram of clay per cm^3.

The most commonly used version of Waxman & Smits 1968 equations is given by Equation 5 (e.g. Pezard, 1990; Revil et al., 2017a).

$$\sigma_{bulk} = \frac{\sigma_w + BQ_v}{F} \tag{5}$$

where $Q_v = Q_sSg$ is the ratio between charge available and volume of fluid available in the rock in $C.kg^3$ or sometimes in meq/ml). By writing the ratio between volume of solid and volume of pore fluid as a function of the porosity (Equation 6), the parameter Q_v can also be

written as a function of the porosity, CEC and solid density (Equation 7), which are parameters more easily measured in the laboratory (e.g. Pezard, 1990; Revil et al., 2017a).

$$\frac{V_g}{V_{pore}} = \frac{1-\phi}{\phi} \tag{6}$$

where V_g and V_{pore} are the volumes of the solid "grain" and of pores in the rocks in L, respectively and ϕ is the volume fraction occupied by pore water (the porosity, dimensionless).

$$Q_v = \frac{m_g}{V_g} CEC \frac{1-\phi}{\phi} = \rho_g CEC \frac{1-\phi}{\phi} \tag{7}$$

where m_g and ρ_g are the weight in kg and density in kg/m^3 of the solid "grain", respectively, and CEC is the charge available per unit mass of solid in C/kg (the cation exchange capacity).

However, a deviation from this linear model was observed by Waxman and Smits (1968) for fluid conductivities lower than 5 S/m, especially for rocks with high Q_v, and explained by an exponentially-increasing mobility of clays exchange ions with fluid conductivity (Equation 8).

$$B(\sigma_w) = \beta(1-\alpha)e^{-\frac{\sigma_w}{\gamma}} \tag{8}$$

where β is the maximum mobility of exchanged cations (As^2/kg) when $\sigma_w \gg \gamma$. α (dimensionless) is determined by the mobility of exchange cations in theoretical deionized water. γ (S/m) is determined by the rate of increase of mobility from $\beta(1-\alpha)$ to β. Measurements of Na^+ self-diffusion coefficients (Richman and Thomas, 1956) confirm that the mobility of exchange ions increases with the fluid conductivity.

Different models than that of Waxman and Smits (1968) have also been developed to explain the non-linear dependence of the bulk conductivity upon the fluid conductivity (Revil and Glover, 1998; Wyllie and Southwick, 1954; McKelvey Jr et al., 1955).

Based on the model from Equations 5 and 8, with α, β and γ being constant, Vinegar and Waxman (1984) developed a complex conductivity model, where the quadrature conductivity, sensitive to delayed conduction phenomena, accounts for accumulation (polarization) and relaxation of electrical charges at the interface between clay and pore water. The complex conductivity model by Vinegar and Waxman (1984) was not validated for Q_v higher than 1 meq/ml. They suggested that beyond this value, clay particles may be sufficiently connected to create a clay-conduction pathway, preventing any polarization to occur. Henry (1997) also pointed out that the assumption

that all exchangeable cations participate equally to surface conduction may be wrong in the case of smectite, where most exchangeable cations are interlayer cations.

Solid ionic conduction has been studied at various temperatures ($\leqslant$ 100°C) in immersed conditions on single-crystal vermiculite (Whittingham, 1987; Maraqah et al., 1991; Maraqah et al., 1990) as well as on vermiculite nano-sheets (Sun et al., 2018; Shao et al., 2015), emphasizing that the ionic conductivity of ion-exchanged vermiculite highly depends on the ion filling the sheets. The highest conductivity (at all temperatures) is found for sodium ($3 \cdot 10^{-2}$ S/m) and the lowest for zinc ($8 \cdot 10^{-5}$ S/m) while the contribution of protons to the overall conductivity of single-crystal vermiculite is considered negligible (Maraqah et al., 1990; Maraqah et al., 1991). Measurements of ionic conductivity for ion-exchanged montmorillonite (a low-charge smectite), as those by Salles et al. (2008) and Slade et al. (1987), result in similar conductivity values than for single-crystal vermiculite, especially at room temperature (Maraqah et al., 1990). Since the crystallinity of montmorillonite is much lower than that of vermiculite, montmorillonite has a much larger surface exposed and its conductivity is likely to be dominated by surface rather than interfoliar cation exchanges. As a consequence, Maraqah et al. (1990) suggest that the mobility of cations (and in particular Na-ion) is about the same in the EDL and in interlayer spaces. In these studies, the observed temperature dependence of interfoliar conductivity is very high (several orders of magnitude of conductivity increase for less than 100°C increase).

Since interfoliar spaces are part of the solid matrix (and not of the solid/electrolyte interface) and may be responsible for a non-negligible electrical current, we use in this thesis the term "solid conduction" rather than "surface conduction" or "interface conduction". This idea is developed further in Paper 1, presented in Chapter 3.

2.4.2 *Electrical polarization*

Rock polarization is particularly sensitive to the presence of disseminated metallic particles, such as sulphides and iron-oxides (Pelton et al., 1978; Gurin et al., 2015; Revil et al., 2015b; Gurin et al., 2018; Wait, 1958; Wong, 1979) but also, to a lesser extent, the pore throat diameter in the case of sandstones, the presence of clay minerals and the electrolyte conductivity (Weller and Slater, 2012; Lesmes and Frye, 2001; Binley et al., 2005; Slater and Sandberg, 2000; Kruschwitz et al., 2010; Weller et al., 2013; Leroy et al., 2017; Klein and Sill, 1982; Revil and Skold, 2011; Vinegar and Waxman, 1984).

The strongest polarization effects are associated to disseminated metallic particles. Because of their semi-conducting properties, an external electric field will cause electrons to redistribute rapidly within

the metallic particle to cancel out the external field (e.g. Pridmore and Shuey, 1976; Shuey, 2012). Since the metallic particles are not connected to each other, a charge is created at the surface of each particle and attracts ions from the fluid (e.g. Bücker et al., 2018; Placencia-Gómez and Slater, 2016; Misra et al., 2016; Revil et al., 2015b). However, induced polarization mechanisms in the presence of semi-conducting (metallic) particles are still not fully understood (Abdulsamad et al., 2017). Several models have been developed to describe the sequence of mechanisms by which ions may accumulate at the interface between pore fluid and metallic particles (Figure 12 (a)) and at the interface between pore fluid and negatively charged particles (e.g. clay minerals) upon reorganization of charges in the EDL (Figure 12 (b)). The largest induced polarization effects associated with clay minerals in sedimentary rocks are considered to occur when clay contents are in the range 3-10%, due to possible connectivity of clay particles beyond that range, which would prevent polarization (e.g. Vinegar and Waxman, 1984; Telford et al., 1990; Parkhomenko, 2013).

Phase-angles associated to rocks rarely exceed 200 mrad ($\approx 10°$) and thus a simple relationship exists between σ'' and θ (Equation 9).

$$\sigma'' = |\sigma| \sin\theta \approx |\sigma|\theta \tag{9}$$

When measured in the laboratory, the phase-angle usually rapidly increases at frequency higher than 10 kHz (Figure 11). This corresponds to high-frequency (HF) polarization phenomena. It includes dielectric absorption by reorientation of water molecules, accumulation of ions at all interfaces between two different phases (e.g. liquid/-solid or $\mathtt{liquid}_1/\mathtt{liquid}_2$), also known as the Maxwell-Wagner polarization (Chelidze et al., 1999) and impedance of the measuring device (Macdonald, 2000; Lesmes and Frye, 2001; Volkmann and Klitzsch, 2015; Abdulsamad et al., 2016). Because of these significant HF polarization phenomena not related to the rock itself, phase-angle peaks due to polarization in the rock can only be observed at low frequency (typically $f \leqslant 10^4$ Hz). Polarization effects described here refer to low-frequency effects, unless the term HF polarization is used.

The complex frequency-dependent response (impedance spectrum) of a material can often be fitted with equivalent electrical circuit models, using regression algorithms such as the non-linear least-square Levenberg-Marquardt algorithm, implemented for instance in the LEVMW software (Macdonald, 2000). While a simple resistor has a response independent of frequency, a circuit "R-C" composed of a resistor in parallel with a capacitance (Figure 13) has a response, which tends to that of a simple resistor at low frequency and of an ideal capacitance at high frequency (Huebner and Dillenburg, 1995). The impedance response of a "R-C" circuit, calculated by Equation 10, corresponds in

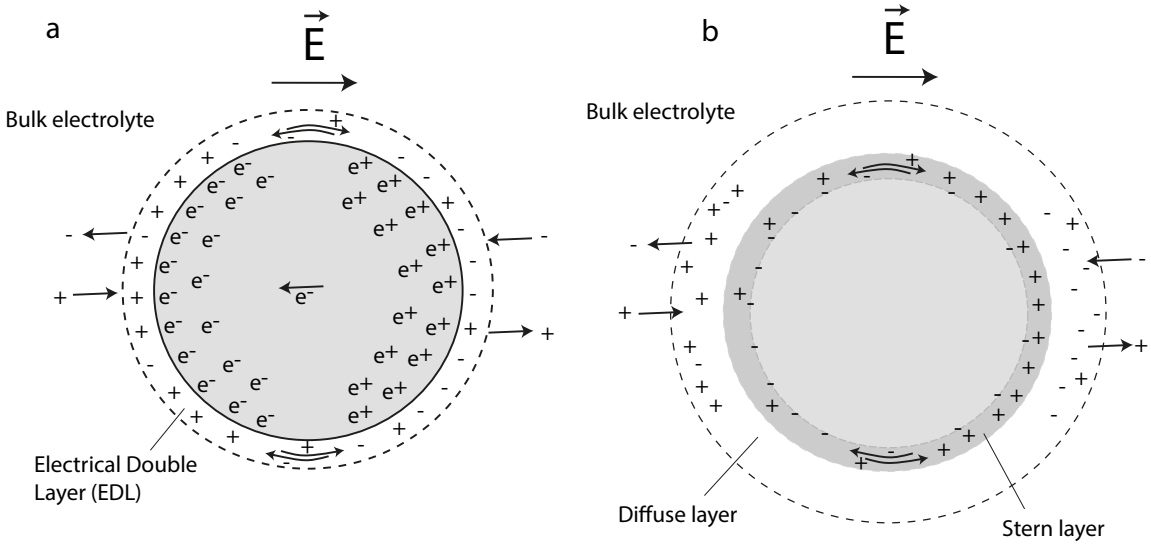

Figure 12: Simplified representation of the charge redistribution around a spherical particle immersed in an electrolyte, under the influence of an external electrical field. (a) Case of a metallic particle (e.g. sulphide or iron-oxides), based on models described by Placencia-Gómez and Slater (2016) and Bücker et al. (2018). Symbols e^-, e^+, $-$ and $+$ correspond to electrons, holes, anions and cations, respectively. Holes, defined as an absence of electrons, behave like positrons (positively charged particles) (see e.g. discussion in Ashcroft and Mermin, 1976). The gray area corresponds to the particle itself, from which electrons cannot move out. Curved and straight arrows indicate tangential flux of ions in the Electrical Double Layer (EDL) and normal flux of ions between the electrolyte and the EDL, respectively. (b) Case of a negatively charged particle (e.g. clay particle or silica grain), based on models described by Chelidze and Gueguen (1999) and Revil and Florsch (2010). Symbols $-$ and $+$ correspond to anions and cations, respectively. The lighter gray area corresponds to the particle itself, whose surface is negatively charged. The darker gray area corresponds to the Stern layer, where cations compensate the surface negative charge and mostly move along a tangential flux (curved arrows). Straight arrows indicate normal flux of ions between the diffuse layer and the electrolyte. Tangential flux in the diffuse layer, as well as normal flux between diffuse and Stern layers can also occur. The EDL consists of the Stern and diffuse layers.

the complex plane to an arc centered on the real axis (red curve in Figure 14).

$$Z_{RC} = \frac{R}{1 + i\omega RC} \tag{10}$$

where ω is the angular frequency in rad/s and R and C are the resistance in Ω and capacitance in F of the circuit, respectively.

Impedance arcs of earth materials usually deviate from the semi-circular shape of an ideal R-C circuit and are better described by a "R-CPE" circuit (Figure 13), where CPE stands for "constant-phase element" and is a non-ideal capacitance (Huebner and Dillenburg, 1995). Three R-CPE circuits in series can represent for example grain interiors, grain boundaries and electrode effects in high-temperature (dry) polycrystalline electrolytes (Gaillard, 2004; Huebner and Dillenburg, 1995). The impedance response of the R-CPE circuit, calculated by Equation 10, is presented by the yellow curves in Figure 14. The complex plane representation in Figure 14 shows in particular that the impedance arc is centered below the real axis.

$$Z_{RCPE} = \frac{R}{1 + RC(i\omega)^{\Phi}} \tag{11}$$

where ϕ is a dimensionless exponent accounting for the so-called distribution of relaxation times (non-ideal behavior).

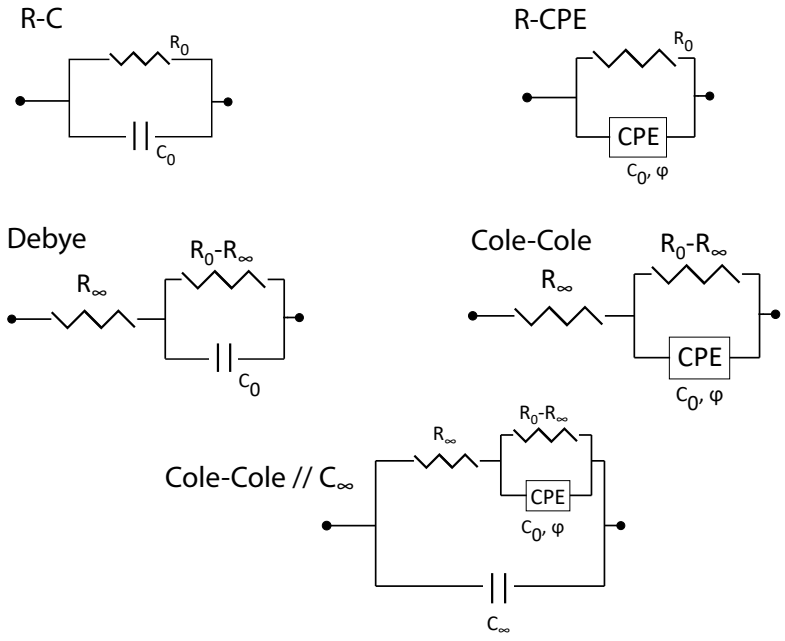

Figure 13: Five equivalent electrical circuit models R = resistance, C = capacitance, CPE = constant phase element = imperfect capacitance.

The low-frequency polarization of water-saturated rocks is often characterized by a slightly more complex model, the Cole-Cole model (Pelton et al., 1978; Hallof and Klein, 1983). This model, originally developed for describing dielectric polarization in polymers (Cole and Cole, 1941), has been adapted to fit resistivity or conductivity spectra rather than dielectric permittivity spectra (Macnae, 2015; Tarasov and Titov, 2013; Florsch et al., 2012). A resistance is added in series to the R-CPE circuit (Figure 13). The impedance response of the Cole-Cole

circuit, calculated by Equation 12, is presented by the blue curves in Figure 14.

$$Z_{CC} = R_\infty + \frac{R_0 - R_\infty}{1 + (j\omega\tau)^\phi} \tag{12}$$

where R_0 and R_∞ are the low- and high-frequency asymptotes of the resistance in Ω, respectively, ϕ is the so-called Cole-Cole exponent (dimensionless) and τ, usually called "relaxation time" is given by $\tau = C(R_0 - R_\infty)^\phi$ in s. In practice, the Cole-Cole impedance is often written as in Equation 13 (e.g. Pelton et al., 1978; Kruschwitz et al., 2010; Pelton et al., 1983).

$$Z_{CC} = R_0(1 - m(1 - \frac{1}{1 + (j\omega\tau)^\phi})) \tag{13}$$

In the case $\phi = 1$, the Cole-Cole model reduces to the so-called Debye relaxation model (Pelton et al., 1983), whose impedance response is presented by the green curves in Figure 14. The complex modulus spectra of the Debye and Cole-Cole models (Figure 14) show that these circuits are not fully chargeable, as opposed to the R-C and R-CPE circuits. Indeed, the chargeability m, defined by $m = \frac{R_0 - R_\infty}{R_0}$, is always inferior to 1 for the Cole-Cole and Debye models, provided that $R_\infty \neq 0$. In other words, the circuits do not reduce to a (non-ideal) capacitance at high frequency, as opposed to R-C and R-CPE circuits, where $m = 1$. Recent studies show that the Cole-Cole model is equivalent to the superposition of several Debye models and suggest to use the so-called "Debye decomposition" method to allow more flexibility in the description of impedance spectra of earth materials (Weigand and Kemna, 2016b; Weigand and Kemna, 2016a; Gurin et al., 2013; Nordsiek and Weller, 2008).

Most of the HF polarization is attributed to parasitic capacitances associated with the instrumentation and is observed to increase with the resistance of the rock-sample and in particular with the resistance of the fluid saturating the rock sample (Huisman et al., 2016; Placencia-Gómez and Slater, 2014; Abdulsamad et al., 2016). If the rock polarization targeted by experiments occurs at frequencies lower than 100-1000 Hz, the HF part of the impedance spectra can be neglected and only the frequencies lower than 100-1000 Hz are included in the modeling (e.g Leroy et al., 2017). However, polarization can occur at frequencies higher than 1000 Hz in natural samples (e.g. Placencia-Gómez and Slater, 2014; Kruschwitz et al., 2010). In these cases, it is important to include the HF polarization in the model. This can be done e.g. by adding a capacitance in parallel to the Cole-Cole equivalent circuit, resulting in the model "Cole-Cole // C_∞", whose equivalent circuit is presented in Figure 13 (Abdulsamad et al., 2016; Kruschwitz et al., 2010). This can also be done by correcting the impedance spectra by the instrumentation response, if the latter can be predicted (Placencia-Gómez and Slater, 2014; Huisman et al.,

2016). The impedance response of the "Cole-Cole // C_∞" model, calculated by Equation 14, overlaps with the Cole-Cole impedance response, up to a certain frequency where HF polarization dominates (around $f = 10^4$ Hz in Figure 14).

$$\frac{1}{Z_{CC//C_\infty}} = jC_\infty\omega + \frac{1}{Z_{CC}} \tag{14}$$

where C_∞, in F, is gathers all HF polarization effects.

Quantitative relationships between chargeability and volume fraction of metallic particles have been established, based on the assumption that electronic conduction associated to metallic particles does not contribute to the in-phase electrical conduction (e.g. Wong, 1979; Misra et al., 2016; Revil et al., 2015b; Gurin et al., 2018; Wait, 1958). This means that no oxidation-reduction occur at the interface metal/electrolyte, otherwise the electrical current could be transferred from ions to electrons. It also means that metallic particles are not in contact with each other, otherwise electrons could travel over a long distance throughout a connected pathway. The original models by Wong (1979) and Wait (1958) also assume that metallic particles are spherical and that the background material is not polarizable - which means that the conductivity of the material in which the metallic particles are embedded is independent of frequency. Deviations to the three above-mentioned assumptions have been investigated and included in more recent models. First, modified versions of Wait's and Wong's models are suggested, assuming metallic particles are spheroids rather than spheres (e.g. Wait, 1987; Wong and Strangway, 1981). Depending on the orientation of spheroids with respect to the electrical field, the effect of elongation is different: models predict that a transverse elongation decreases the chargeability while an axial elongation increases chargeability. A dimensionless polarizability α can be calculated with Equations 15 and 16, and is used to take into account the effects of elongation on chargeability and relaxation time (e.g. Wait, 1987).

$$\alpha = -1 + L^{-1} \tag{15}$$

where L is the depolarization factor, which accounts for the orientation of the particle relative to the polarizing field. This factor can be calculated for a spheroid of semi-major axis b and semi-minor axis a according to Equation 16, based on the expression given in Gurin et al. (2018) and Misra et al. (2016).

$$\begin{aligned} L_{axial} &= \frac{ab^2}{2}\int_0^\infty \frac{ds}{(s+b^2)^2\sqrt{s+a^2}} \\ L_{transverse} &= \frac{ab^2}{2}\int_0^\infty \frac{ds}{(s+b^2)(s+a^2)\sqrt{s+a^2}} \end{aligned} \tag{16}$$

where L_{axial} and $L_{transverse}$ are the depolarization factors for a spheroid oriented along the electrical field and transversally to the electrical field, respectively. In case of spherical particles, $\alpha_{transverse} = \alpha_{axial} = 2$. For an elongation ratio of $\frac{a}{b} = 0.5$, $\alpha_{transverse} = 1$ and $\alpha_{axial} = 3$. For higher elongation ratios (particles closer to spherical particles), $\alpha_{transverse}$ and α_{axial} are closer to 2.

Second, a background chargeability can be included in Wong's model (1979), to account for polarizability of the medium without metallic particles. No explicit expression of M_b is given in Wong's model (1979) but several studies have attempted to estimate M_b, either by measuring the chargeability of synthetic samples with no metal content but different clay fractions (Revil et al., 2017d) or the chargeability of natural samples with $\leqslant 0.3\%$ metal volume fraction (Gurin et al., 2018). The resulting values of M_b are in the range 0.03-0.08.

Finally, an imperfect polarization of the fluid/metal interface, caused by a current flow through this interface involving oxidation-reduction charge transfer reactions, was also considered by Wong (1979) and investigated more thoroughly in recent models (Placencia-Gómez and Slater, 2014).

In this study, the spectral induced polarization (SIP) response of volcanic rocks is mainly related to the volume of metallic particles (Paper 2). Clay minerals (predominantly smectite) do not seem to cause a detectable SIP response. Since the final objective is to provide interpretations for parameters obtained in the field (see Paper 3), the simplest parameter representing the magnitude of low-frequency polarization is preferred: the maximum phase angle θ_{max} (MPA). The MPA is usually proportional to the chargeability (Wong, 1979; Revil et al., 2015a). Nevertheless, fitting results using the fourth circuit described in Figure 13, corresponding to Equation 14, are presented in the Supporting Information of Paper 2 and analyzed in Chapter Chapter 7.

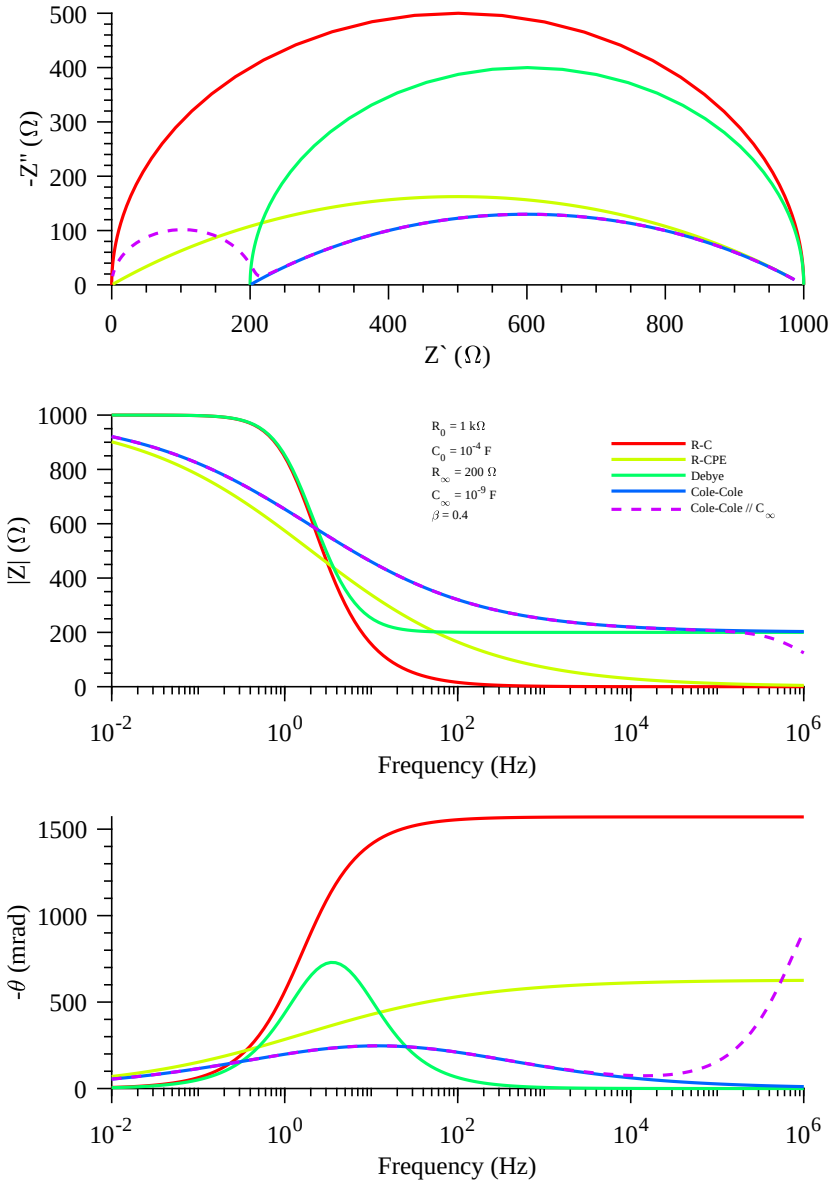

Figure 14: Impedance response of the five equivalent electrical circuit models presented in Figure 13, using parameter values indicated at the center of panel (b). (a) Complex plane representation (imaginary versus real impedance); (b) impedance modulus versus frequency and (c) impedance phase angle versus frequency. The impedance functions corresponding to the five models R-C, R-CPE, Debye, Cole-Cole and Cole-Cole // C_∞ are given in Equations 10, 11, 12 (including the case $\phi = 1$ for the Debye model) and 14. The plain blue curve overlaps with the broken magenta curve at frequencies up to 10^4 Hz.

2.5 GEO-ELECTRICAL INVESTIGATIONS OF THE EARTH

Geological and geochemical mapping of geothermal resources is limited to direct observations on the surface or in boreholes. The objective of geophysical surface exploration is to map, in a non-destructive way and from the surface, the distribution of physical properties of the rocks at depth (Flóvenz et al., 2012). Oil, gas and mining industries have been the driving force for the development of geophysical exploration, and in particular of electrical and electromagnetic methods.

2.5.1 *Electrical resistivity*

Electrical resistivity of saturated rocks is particularly sensitive to the pore volume, fluid salinity and rock temperature, as well as to the presence of clay minerals, as explained in Section 2.4. In geothermal exploration projects, the resistivity structure of geothermal areas and volcanoes is often interpreted in terms of clay minerals distribution, assuming that other parameters influencing the resistivity are more or less uniform. The temperature distribution is then interpreted based on the clay distribution, ignoring its direct effect on the resistivity, which is assumed to be much less important than the effect of different clay minerals (Figure 15).

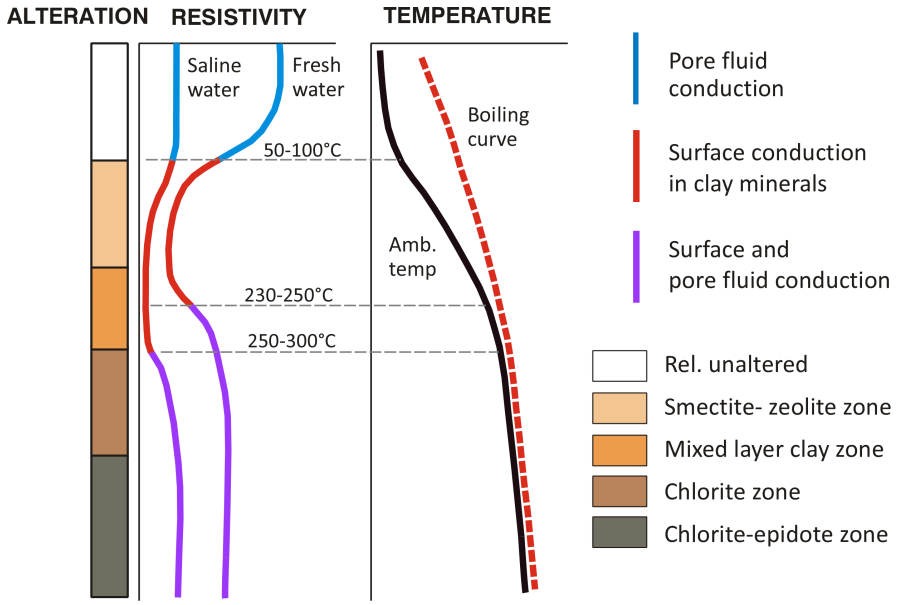

Figure 15: Typical model of the resistivity structure in altered volcanic rocks, used to interpret the resistivity pattern in terms of fluid temperatures. Reproduced from Flóvenz et al. (2012), with permission from Elsevier.

Magnetotelluric (MT) and Transient Electro-Magnetic (TEM) soundings measure the Earth's response to time-varying magnetic fields, al-

ternating and decaying, respectively. Natural oscillations in the Earth's magnetic field induce an alternating "telluric" current in the ground and the resulting electrical field can be measured at the surface (MT method). Switching off an artificial electrical current flowing in a loop at the surface, causes inductive coupling in the ground, which depends on the resistivity structure and is measured by the decay rate of the magnetic field (TEM method). MT and TEM soundings are commonly performed at the same location to correct for the so-called static-shift in the MT measurements (Flóvenz et al., 2012).

In the following, I focus on Electrical Resistivity Tomography (ERT), used for field measurements during the PhD. ERT consists of injecting a Direct Current (DC) along a profile, through grounded electrodes (A and B) and measuring the resulting voltage at two other electrodes (M and N). The quadruple A-B-M-N is selected at each step of the acquisition protocol from the electrodes available on the profile. For each quadruple, the apparent resistivity ρ_a, calculated by Equation 17, is more or less an average of the true resistivity of the Earth, detected by the measurement down to the penetration depth (Flóvenz et al., 2012).

$$\rho_a = k\frac{V_M - V_N}{I_{AB}} \tag{17}$$

where I_{AB} is the current injected between electrodes AB, V_M and V_N the potentials measured at electrodes M and N, respectively, and k the so-called geometrical factor, defined in Equation 18 (e.g. Bertin and Loeb, 1976).

$$k = \frac{2\pi}{\frac{1}{AM} - \frac{1}{AN} - \frac{1}{BM} + \frac{1}{BN}} \tag{18}$$

The rate of decrease of the signal-to-noise ratio (SNR) with depth depends on the geometrical factor, which changes for different types of electrode configuration (e.g. Bertin and Loeb, 1976). Two main types of electrode configurations (also named arrays) are the dipole-dipole array, where AB and MN dipoles do not overlap, and nested arrays, where MN dipole is between A and B (Figure 16). Nested arrays can have MN dipole at the center of the array (Wenner and Schlumberger arrays) or not (multi-gradient array). In the Wenner array, the three inter-electrode distances are always equal and a new quadruple involves a translation of all the electrodes together. In the Schlumberger array, the current electrodes are progressively separated further away from the center, while the potential electrodes remain at the same position, until the observed voltage becomes too small to measure (Loke, 2004). The multi-gradient array allows simultaneous recording of the voltage at different MN dipoles, for a given current AB dipole, provided that a multichannel data-acquisition system is available (Dahlin and Zhou, 2006).

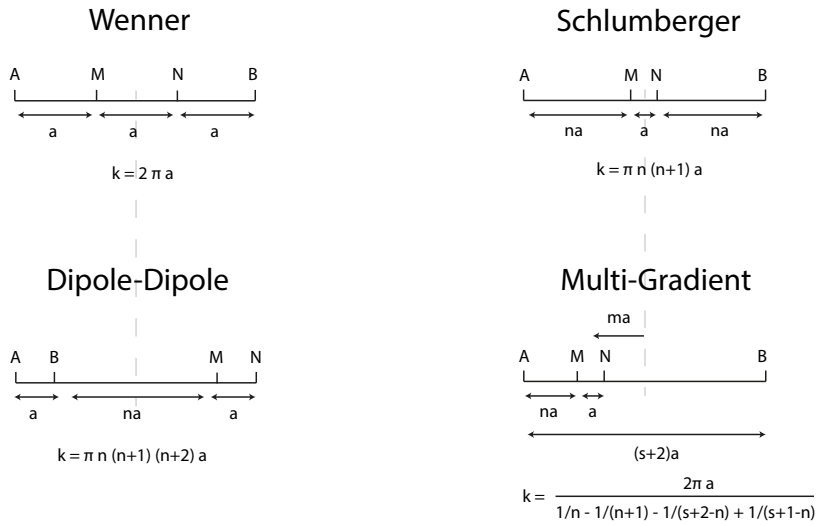

Figure 16: Four different electrode arrays commonly used in ERT measurements: (a) Wenner, (b) Schlumberger, (c) Dipole-Dipole and (d) Multi-Gradient. A and B represent current electrodes, while M and N represent potential electrodes. k is the geometrical factor (see Equation 18). The broken gray lines indicate the center of arrays and coincide with the AB and MN midpoints for the Wenner and Schlumberger arrays, but only with the AB midpoint for the Multi-Gradient array. The parameters a and n are usually referred to as the dipole length and the dipole separation factor, respectively (Loke, 2004). In the multi-gradient array, the parameter n is re-defined by Dahlin and Zhou (2006) as the smallest relative spacing between current and potential electrodes. In addition, the parameters m and s are defined as the mid-point factor (distance between the center of AB and the center of MN) and the separation factor (Dahlin and Zhou, 2006). The parameter m is positive or negative, depending on the position of the MN midpoint compared to the AB midpoint. Figure drawn after information from Loke (2004) for (a)-(c) and from Dahlin and Zhou (2006) for (d).

A convenient means to display results of ERT measurements at a profile is the two-dimensional "pseudo-sections" plot, which can be obtained, for example, by placing each apparent resistivity measurement at a horizontal mid-point and a pseudo-depth (Loke and Barker, 1996). The pseudo-depth offers the possibility to merge the pseudo-sections of different types of arrays in a unified manner (Edwards, 1977). It is defined as the median "effective" depth of investigation of the array and is calculated based on the Frechet derivatives for a homogeneous half space (Loke, 2004; Edwards, 1977; Menke, 2012). It can be understood as the depth at which one half of the signal originates from above and the other half from below (Okpoli, 2013). It practically depends on the relative positions of both the current and potential electrodes and not only on the depth of current pen-

etration, which is determined by the current electrodes separation (Okpoli, 2013). The particular mid-point and pseudo-depth definitions for the multi-gradient array can be found in Dahlin and Zhou (2006). Similarly, the apparent resistivity obtained from EM sounding can be represented by a one-dimensional (vertical) pseudo-curve. For TEM, the pseudo-depth corresponds to the square root of time after current was turned off (expressed in μs). For MT, it is, as a rule of thumb, proportional to the square root of the ratio between the resistivity of the homogeneous half space and the frequency of the natural recorded electromagnetic field (Hersir and Björnsson, 1991).

In order to obtain a realistic image of the resistivity structure, the ρ_a pseudo-sections (or curves) are inverted. A model of distribution of true resistivity structures is initially guessed and the resulting apparent resistivity pseudo-section is predicted, based on "forward" equations, defined by the theory. The initial model can, for example, consists of an uniform resistivity structure, whose value is the average of all the apparent resistivities measured. In this case, the forward apparent resistivity will also be uniform. A dimensionless misfit χ between the predicted and measured apparent resistivity pseudo-section is calculated, for example using Equation 19 in the case of AarhusInv software for inversion of ERT data, and a new model is calculated until the misfit reaches a minimum.

$$\chi = \sqrt{\frac{1}{N}\sum_{i=1}^{N}\frac{(d_{obs,i} - d_{fwd,i})^2}{\sigma_{d_i}^2}} \tag{19}$$

where d_{obs}, d_{fwd}, σ_d and N are the logarithm of the observed data, logarithm of the forward predictions, standard deviation of the observed data and number of data points, respectively.

A large variety of optimization methods exist to generate new models with better misfits. Iterative methods evaluate derivatives of the misfit function to define a search direction. Examples of approaches include Newton's and gradient-descent methods, where the Hessian matrix and Gradient vector are evaluated, respectively (Menke, 2012). Since geophysical inversion problems are usually under-determined (more unknown than data), *a-priori* constraints are necessary to obtain a convergence to a minimum misfit (e.g. boundary conditions, layered earth, smooth lateral variations). When a minimum misfit is reached, it means that the optimization method cannot find a better inversion model, given the data, initial guess-model and *a-priori* constraints. Yet, it does not mean that the resulting inversion model is a picture of the true resistivity structure. First, because the minimum misfit may be too high, for example if the noise in the measured data is too important. Second, because many different inversion models can have the same misfit. In other words, different resistivity structures can result in more or less the same apparent resistivity measured data. Measurements redundancy (e.g. parallel ERT profiles) and use of different op-

timization methods, initial guess-models and *a-priori* constraints are ways to reduce the uncertainty on whether a model is close to the reality or not.

TEM soundings at a specific point are more adapted to investigate resistivity changes with depth down to 1 km, while ERT soundings along a profile offer better resolutions for near-surface lateral resistivity changes, typically down to 300 m (Flóvenz et al., 2012; Hersir and Björnsson, 1991). The penetration depth of the TEM method, which is induction-based, is larger than the potential-based DC method (Hersir and Björnsson, 1991) in conductive environments such as geothermal areas, because the SNR of DC methods depends on the voltage created in the ground (Gazoty et al., 2013), and this voltage is smaller when the electrical current can flow through conductive bodies (Ohm, 1827).

2.5.2 *Induced Polarization*

Induced Polarization (IP) is another electrical process, which is sensitive to the charge storage capabilities of the rock (Marshall and Madden, 1959; Slater and Lesmes, 2002b; Kemna et al., 2012). IP methods are used in particular for mineral exploration (Pelton et al., 1983; Pelton et al., 1978), for monitoring landfills, mine tailings and pollution (Leroux et al., 2007; Vanhala, 1997; Placencia-Gómez et al., 2015; Flores Orozco et al., 2015), as well as for predicting subsurface permeability ranges (Maurya et al., 2018b). IP can be measured in the field with the same instrument and electrode configuration as ERT (e.g. Ward, 1988; Binley and Kemna, 2005; Oldenburg and Li, 1994) and can also be extracted from TEM measurements on the ground if the Earth is moderately conductive (Flis et al., 1989), as well as from airborne TEM data in a larger range of conditions (Kang and Oldenburg, 2016; Couto et al., 2018; Kaminski and Viezzoli, 2017). A workflow combining grounded TEM and ERT measurements has also recently been suggested to optimize the recovery of both resistivity and chargeability of the ground (Kang and Oldenburg, 2018). The spectral IP signal can be obtained from both frequency-domain (FDIP) and time-domain measurements (TDIP) in the field (Maurya et al., 2018a). While the former is more time-consuming and can only cover small areas, and thus shallower investigation depths, the latter contains noise from more sources (Olsson et al., 2016; Gazoty et al., 2013). FDIP measurements are similar to laboratory impedance spectroscopy presented in Section 2.4. TDIP measurements are further described here.

A current square-wave is injected in the ground, with an on-time T_{on} and an off-time T_{off}. The simple case of a 50% duty cycle ($T_{on} = T_{off}$) is represented in Figure 17. In this simplified representation, the

voltage follows a stretched-exponential decay with time (Equation 20).

$$U = U_0 e^{(\frac{-t}{\tau})^{\phi}} \tag{20}$$

where U_0 is the primary voltage, in V, τ is the relaxation time in s and ϕ is a dimensionless exponent. The primary voltage corresponds to the maximum voltage at the time the current is turned off.

Equation 20 is commonly used to describe polarization phenomena in time-domain. In the case $\phi = 0.5$, the Laplace transform of the time-derivative of the ratio $\frac{U}{U_0}$ is equivalent in frequency-domain to the ratio $\frac{Z_{CC} - R_\infty}{R_0 - R_\infty}$, where Z_{CC} follows the Cole-Cole impedance function presented in Equation 13 (Kohlrausch, 1854; Williams and Watts, 1970). In real field measurements, the term "IP discharge curve" is used to describe the voltage response, which can be far from the ideal (and even decay-like) response presented in Figure 17.

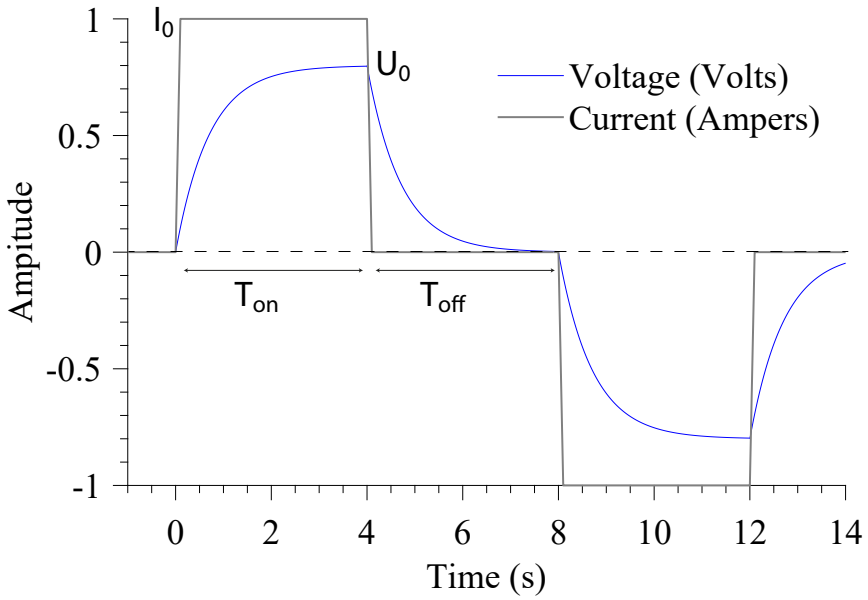

Figure 17: Square wave current injected and stretched exponential voltage decay response for $T_{on} = T_{off} = 4$ s. In reality the first milliseconds of the voltage decay are much steeper than the stretched exponential curve shown here, due, in particular to electromagnetic inductive effects (Bertin and Loeb, 1976).

The polarity of the current is reversed in order to remove background potentials caused by unavoidable polarization at the measuring electrodes (e.g. Olsson, 2016). The repeated observed voltage pattern (pulse train) is stacked to reduce the influence of noise but stacking also modifies significantly the IP response (Fiandaca et al., 2012). Although most TDIP measurements are recorded during the off-time, recording during the on-time can increase the SNR by a factor two, while reducing the acquisition time (Olsson et al., 2015b). The apparent chargeability m_0 (unit mV/V) at a time t is the ratio between the

voltage measured at this time and the primary voltage (e.g. Bertin and Loeb, 1976). The integral apparent chargeability <M> in $msec$, in a given time-window, is the area enclosed by the discharge curve and its zero asymptote during this time-window, divided by the primary voltage (e.g. Bertin and Loeb, 1976). Smaller integral apparent chargeabilities are observed when smaller injection times are used, due to the finite length of the current pulse and in particular the fact that the voltage at the end of T_{on} is not yet maximum (Olsson et al., 2015a). Therefore, the exact waveform of the transmitted current needs to be taken into account in the inversion, including in particular T_{on} and the number of pulses (Bertin and Loeb, 1976).

Capacitive and inductive coupling are common sources of noise in TDIP. Capacitive coupling can be reduced by using two distinct cables for current injection and potential measurement (Dahlin and Leroux, 2012). Inductive coupling is particularly important in nested arrays and increases with the distance between electrodes as well as the conductivity of the ground, but mostly takes place in the early times after current turn-off (Ingeman-Nielsen and Baumgartner, 2006; Dahlin and Leroux, 2012).

2.6 KRAFLA VOLCANO AND ASSOCIATED GEOTHERMAL AREA

2.6.1 *Geology of Iceland*

Iceland is the result of complex interplay between a mid-oceanic ridge and an area of excessive mantle upwelling (hotspot) (Sigmundsson et al., 2018; Morgan, 1971; Björnsson, 1985). The topographic relief caused by the hotspot extends from Greenland to Scotland and is also called the Greenland-Iceland-Faroe ridge complex (Hjartarson et al., 2017). The most recent onset of seafloor spreading in the North Atlantic is considered to have taken place during the late Paleocene-early Eocene, about 55 million years ago (Larsen, 1978; Larsen and Saunders, 1998). Volcanism related to activity of the Icelandic hotspot would have started when a deep seated mantle plume reached the lower crust below central Greenland and generated the North Atlantic Igneous Province, now found on both sides of the Atlantic, about 60 million years ago (Vink, 1984; Hjartarson et al., 2017; Sigmundsson, 2006). The oldest exposed age-dated rocks, found in the northwestern part of the country (the West fjords region), are 15-16 million years old according to potassium-argon dating techniques (e.g. Moorbath et al., 1968; Sigmundsson et al., 2018). The most recent rocks are found at the plate boundary, which traverses Iceland as a series of seismic and volcanic rift zones (Figure 18). Based on paleobotanological observations, Iceland became an isolated island approximately 6 million years ago (Denk et al., 2011; Hjartarson et al., 2017). The marginal parts of the Greenland-Scotland transverse ridge were gradually submerged during the Miocene-Pliocene (Nilsen, 1978; Denk et al., 2011). Volcanism associated to melt generation at the hotspot, taking place on 10-100 km-long fissure swarms, maintains Iceland above sea level, despite a plate spreading rate of about 18-19 mm/yr (Ito et al., 1999; Einarsson, 1991; DeMets et al., 1990; Sigmundsson et al., 2018).

Volcanic rocks in Iceland belong to three main rock series: tholeiitic, transitional-alkaline and alkaline. Tholeiitic volcanic deposits are most abundant within rift zones, while transitional and alkaline rocks occupy off-rift zones of active volcanic areas (e.g. Sigmarsson et al., 2008; Sigmarsson and Steinthórsson, 2007). Rift zones are the on-land expression of the Mid-Atlantic Ridge (Sigmundsson, 2006). Tholeiitic basalts in Iceland are enriched in incompatible elements, compared to "abyssal" basalts from the Mid-Atlantic Ridge to the south and north of Iceland (Engel et al., 1965; Gast, 1968; Schilling and Noe-Nygaard, 1974; Ito et al., 2003). The alkaline and transitional rocks in Iceland are again enriched in incompatible trace elements, compared to tholeiitic rocks from the Icelandic rift zones (Sigmarsson et al., 2008). Radiogenic isotope systematics suggest that at least three distinct mantle components are involved in the generation of basaltic rocks in Iceland

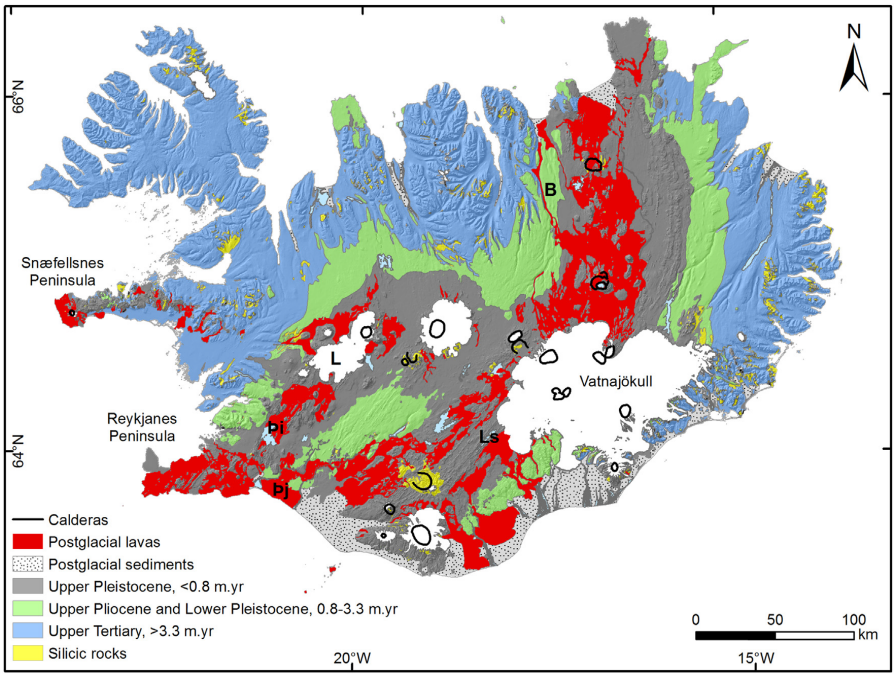

Figure 18: Geological map of Iceland, showing extrusive rocks, from basaltic to intermediate compositions, with color coding according to periods. Silic rocks of all age shown in yellow. Shaded topography in the background. Ice caps shown in white. Selected glaciers L = Langjökull and Vatnajökull; Selected placenames: Þi = Þingvellir and Ls = Lake Langisjór; Selected lava flows: Þj = Þjórsárhraun and B = Bárðalshraun. Reproduced from Sigmundsson et al. (2018), with permission from Elsevier.

(Bailey and Noe-Nygaard, 1976; Maclennan, 2008). Furthermore, silicic rocks occur as intrusives, extrusive flows, as well as various types of tuffs and welded flows (e.g. ignimbrites and air-fall tuffs), and are apparently more common in Iceland than in the oceanic crust and many oceanic islands (Jónasson, 2007). These formations are characteristic products of central volcanoes. Remelting of crust and extinct volcanic centers has been suggested as a cause for the presence of silicic rocks (Sigmundsson, 2006). Based on observations mostly carried out in eastern Iceland, the volume of the Icelandic volcanic pile composed of acidic to intermediate rocks is estimated to about 10% (Walker, 1966; Sæmundsson, 1979).

Thanks to the coexistence of hotspot and rifting activities, among the world highest background temperature gradients are observed in the Icelandic crust, with up to 150°C/km (Flóvenz and Saemundsson, 1993). The highest values are found along the spreading axis and the gradient decreases with distance from the axis. High annual precipitations, along with young tectonic fractures, allow the existence of numerous active hydrothermal systems (Figure 19). Near-surface temperature gradients above geothermal systems are usually much higher (up to 500°C/km) than in the deeper parts of the geothermal

systems, where convection along fractures allows mixing with cold water (Flóvenz and Saemundsson, 1993). High-temperature geothermal fields, found within volcanic zones, are connected to hot intrusions, while low-temperature geothermal fields, away from the volcanic zones, mine heat from underlying crust. One high-temperature geothermal field is located at the Krafla volcano, in the Northern Volcanic Zone of Iceland.

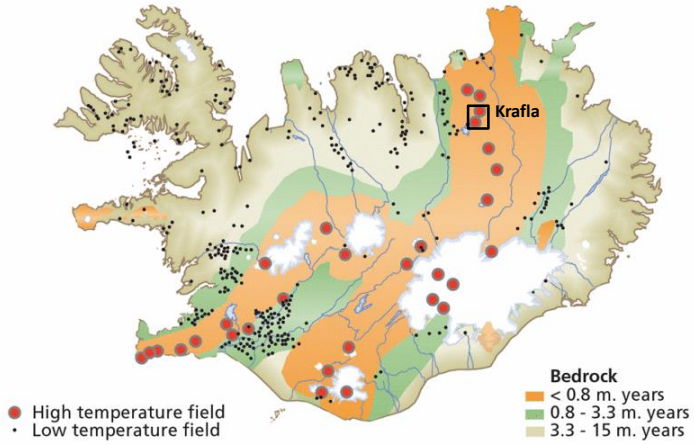

Figure 19: Simplified geological map of Iceland, showing the low- and high-temperature geothermal areas. Reproduced with permission from ÍSOR. The Krafla area in the Northeast is pointed out.

2.6.2 *Geology of the Krafla central volcano*

The Krafla volcano is a system composed of a 15-km diameter central volcano and a 100 km long (and 4 to 19 km-wide) NNE-SSW trending fissure swarm running through it (Saemundsson, 1978; Ármannsson et al., 1987; Hjartardóttir et al., 2012). The oldest exposed rocks at the Krafla central volcano date back to nearly 300,000 years (Sæmundsson, 2015). Volcanic activity due to rifting episodes at Krafla has been inferred 6 times in the last 3000 years, with an average interval of about 500 years and the latest eruptive episode happening between years 1975 and 1984 (Björnsson, 1985; Sæmundsson, 2015). Prior to that, in the period 3000-5000 years, only one eruption is known (Sæmundsson and Sigmundsson, 2013). The main Krafla geothermal area covers about 15 km^2 and is located in the eastern part of the Krafla caldera, which formed about 100.000 years ago during the early part of the last interglacial period (Sæmundsson, 1983; Sæmundsson and Sigmundsson, 2013). An estimated total spreading of about 2 km has taken place since the formation of the caldera; This has caused the elongated caldera shape in the east-west direction (Sæmundsson, 1991; Hjartardóttir et al., 2012). Caldera rims, shown in Figure 20 and

Figure 21, have been defined by mapping a reddish welded ash flow of dacitic composition, called Halarauður. Indeed, the formation of this ash flow is related to the first collapse of the caldera, based on the fact that about 90 fissure eruptions of similar age and composition occurred all around the caldera (Jónasson, 1994; Sæmundsson, 1991; Sæmundsson, 2015). About 24.000 years ago, a rhyolitic fissure eruption beneath thin ice inside the caldera formed Hrafntinnuhryggur (Figure 20), a 2.5-km-long NNE-SSW trending ridge of obisidan (Sæmundsson et al., 2000; Tuffen and Castro, 2009). Only minor acidic or intermediate eruptions have occurred since the end of the last glacial period, but high-silica rhyolite melts have been accidentally drilled into at 2-3 km depth in boreholes in the Suðurhliðar and Leirbotnar fields, indicating the presence of a rhyolitic magma body at shallow depth (Mortensen et al., 2010; Elders et al., 2011). A popular explanation for the origin of rhyolites at Krafla is the melting of hydrothermally altered basalt, on the peripheries of an active basaltic magma chamber or intrusive domain (Jónasson, 1994; Zierenberg et al., 2013).

The lithology at Krafla is divided between extrusive igneous rocks (subglacial "hyaloclastite" formations and interglacial or postglacial lavas), dominant from the surface down to a depth of 1200-1300 m, and basaltic intrusions, dominant below 1300 m (Ármannsson et al., 1987). Felsic intrusions also occur at variable depths (Thorsteinsdóttir, 2017). The extrusive part would be about 4 km thick (based on volcanic production and spreading rate) but intrusions increase in geothermal areas to well over 70% at 2.5 km depth (Sæmundsson, 2015).

Strong attenuation of S-waves at 3-7 km depth in two areas within the Krafla caldera, as opposed to a general absence of attenuation in the northeastern rift zone at these depths, has been interpreted as the expression of a localized magma chamber under the Krafla central volcano (Einarsson, 1978; Sæmundsson, 2015). At the main geothermal area, the lower limit of the seismogenic zone, the so-called brittle-ductile boundary where rocks stops breaking under strain and thus earthquakes stop has been estimated at about 2 km depth (Schuler et al., 2015).

2.6.3 *Geothermal exploration at Krafla*

The main production area at Krafla is aligned in a WNW-ESE direction, along an elongated intrusive complex (Thorsteinsdóttir, 2017). The direction of this complex, oblique to the main trend of the fissure swarm is attributed to shearing stress (Saemundsson, 1974). Two magnetic lows, trending WNW-ESE and NNE-SSW are running through the production area (Karlsdóttir et al., 1978). The magnetization loss is attributed to the demagnetisation of magnetic minerals from the basalt (titanomagnetite and ilmenite) upon low-temperature oxida-

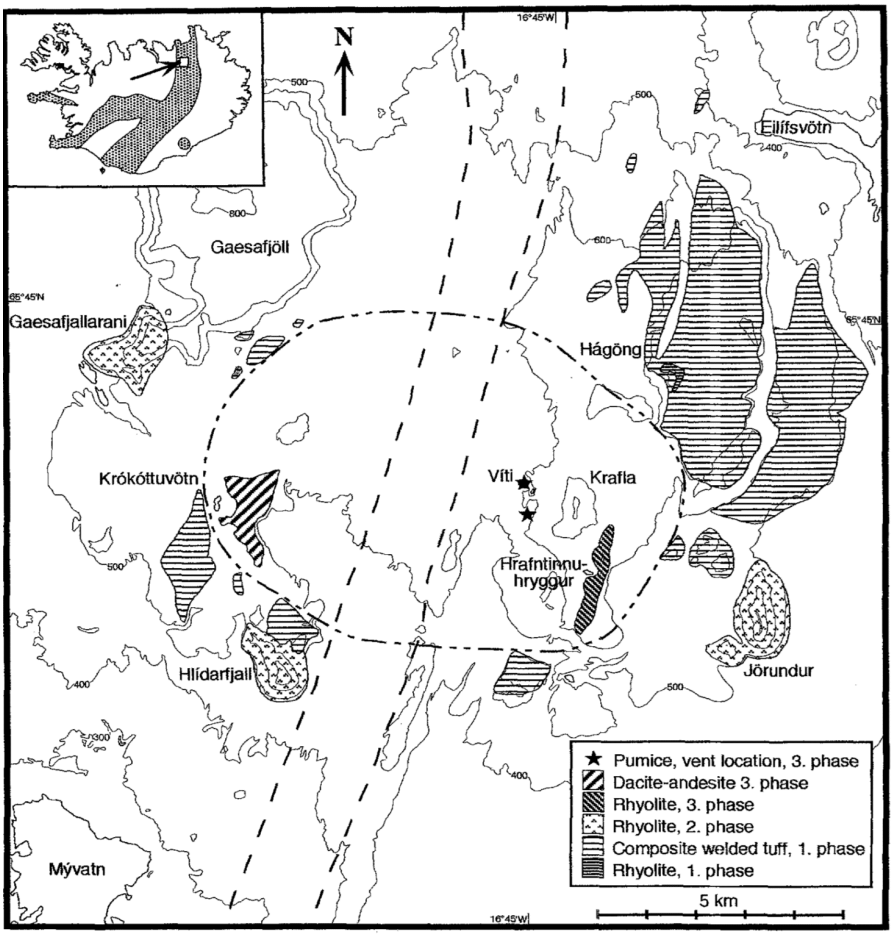

Figure 20: Simplified geological map of Krafla, showing the active fissure swarm and the caldera rims (broken lines), as well as the occurrences of silicic exposed rocks (see legend). The inset map shows the neovolcanic zones of Iceland and the location of the Krafla cenral volcano. Figure reproduced from Figure 1 in Jónasson (1994) (which was modified after Sæmundsson (1991)), with permission from Springer.

tion and higher temperature alteration (Oliva-Urcia et al., 2011). MT data reveal a conductor in the uppermost few hundred meters and a deep lying conductor at a depth of 8-12 km, which domes up to 2-3 km depth beneath the main geothermal field. 3D inversion shows an ESE-WNW trending high-resistivity structure bordered by low resistivity on each side down to 4 km, probably related to a dike complex (Árnason et al., 2007; Rosenkjaer et al., 2015; Árnason and Magnússon, 2001).

A total of 47 boreholes have been drilled at the Krafla volcano, for exploration and production of geothermal electricity. The longest borehole was directionally drilled over a distance of 2900 m. Twenty production holes are currently in use for a total installed power capacity of 62 MW (Thorsteinsdóttir, 2017). This corresponds to an annual

Table 4: Relevant information about the five drillholes (four cored) at the Krafla volcano, used in the present work.

Borehole	KH1[1]	KH3[2]	KH5[3]	KH6[4]	KS1 - not cored[5]
Depth (m)	200	400	550	750	2500
Max Temp (°C)	180	40	150	220	350

[1] Located at Sandabotnaskarð. See Gudmundsson (1991).
[2] Located at Hágong. See Jónsson et al. (2003).
[3] Located at Arnarhóll. See Gautason et al. (2007).
[4] Located at Leirhjnúkur. See Gautason et al. (2007).
[5] Located at Sandabotnaskarð. See Gudmundsson et al. (2007).

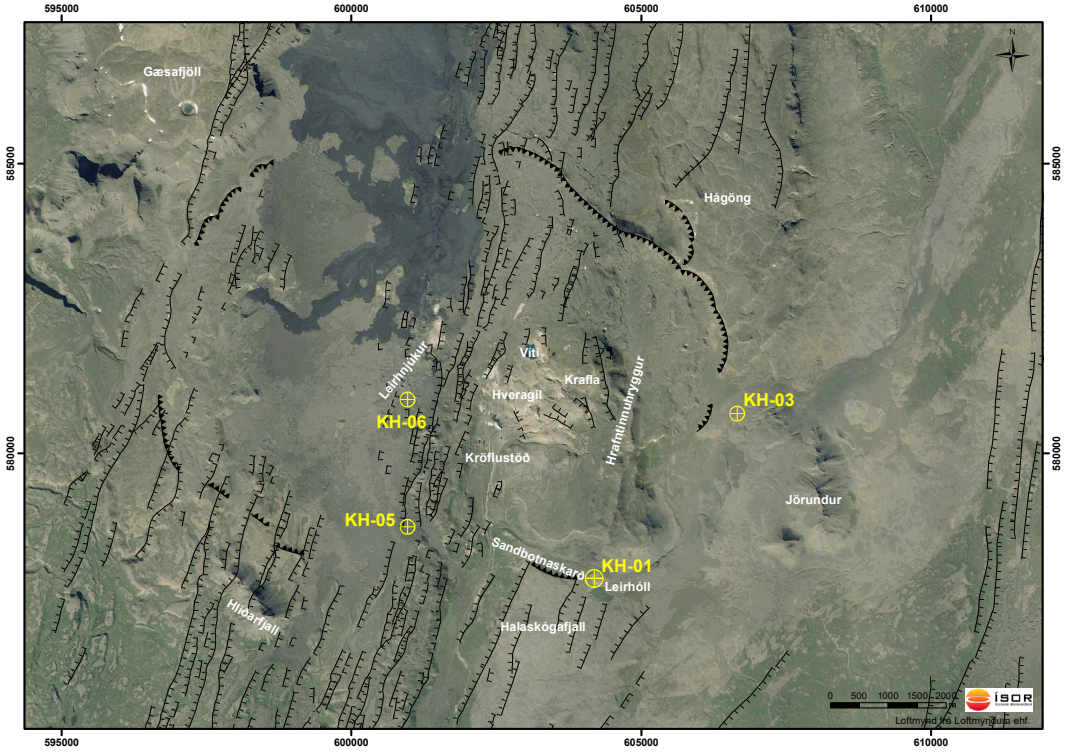

Figure 21: Aerial map of the Krafla central volcano, with known caldera rims and faults represented as black lines (Saemundsson et al., 2012) and cored boreholes used in this study as yellow circles with crosses. The geothermal power plant operated by Landsvirkjun is located at the center of the figure, marked by the white name Kröflustöð.

power output of about 0.5 TWh. Four shallow exploration boreholes have been cored and are used in the present work (see details in Table 4, Figure 21 and Figure 22).

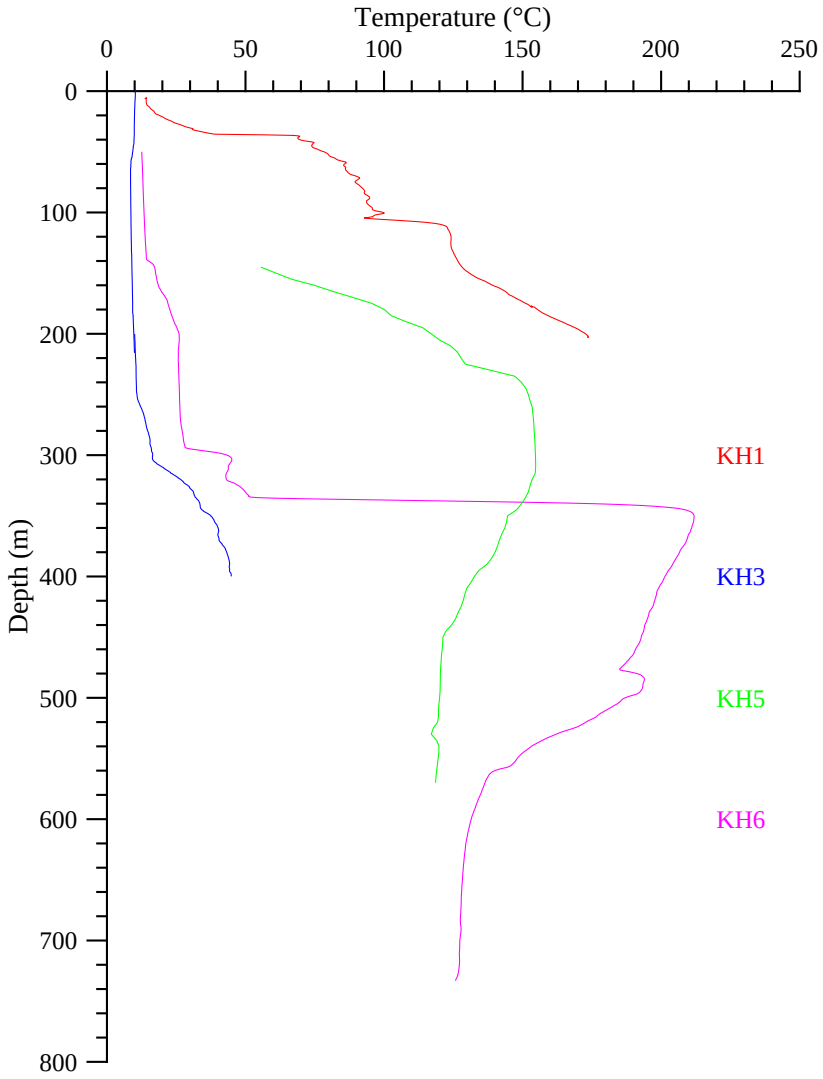

Figure 22: Temperature profiles in the four cored boreholes, from temperature logs run at the time of coring, based on data from Jónsson et al. (2003), Gautason et al. (2007), and Gudmundsson (1991).

3

THE ROLE OF SMECTITES IN THE ELECTRICAL CONDUCTIVITY OF ACTIVE HYDROTHERMAL SYSTEMS: ELECTRICAL PROPERTIES OF CORE SAMPLES FROM KRAFLA VOLCANO, ICELAND - PAPER 1

This chapter presents an article published at Geophysical Journal International on August, 18th, 2018. The full manuscript can be found in Appendix B.1.

3.1 SUMMARY

In this article, we study the dependence of the bulk in-phase electrical conductivity of altered volcanic rocks upon salinity, porosity and smectite content. We present an extensive data set of petrophysical and mineralogical properties of 88 core samples from Krafla volcano, Iceland: porosity, density, CEC, mineral content and three runs of electrical conductivity at 1 kHz, measured both with 4-electrode and 2-electrode set-ups and with conductivity of the pore-saturating fluid increased, decreased and re-increased in the range 0.02-11.1 S/m. We analyze the loss of linearity in the bulk conductivity versus fluid conductivity relationship, upon an increased smectite content, with three different models: (i) a model introduced by Waxman and Smits (1968) involving exponential decrease of the exchange ions mobility with increased salinity, (ii) a simple power function with no physical grounds, which is also suggested by Weller and Slater (2012) to fit the salinity-dependence of quadrature conductivity and (iii) a model similar to that presented by Wyllie and Southwick (1954) and McKelvey Jr et al. (1955) with three resistors elements in parallel, where the last element in our case consists of smectite interlayer spaces in series with pore water.

3.2 MAIN RESULTS

- CEC measurements can be used to calculate smectite content, with a method further described in Paper 4 (Chapter 6).
- The non-linear dependence of the bulk conductivity upon the fluid conductivity becomes important when the volume ratio between smectite sheets and fluid is higher than 25 per cent.
- The bulk conductivity of low-salinity hydrothermal systems can be approximated by a function of porosity and smectite content.

However, small variations of salinity may affect significantly the conductivity in smectite-rich rocks, due to the non-linearity of the salinity-dependence.

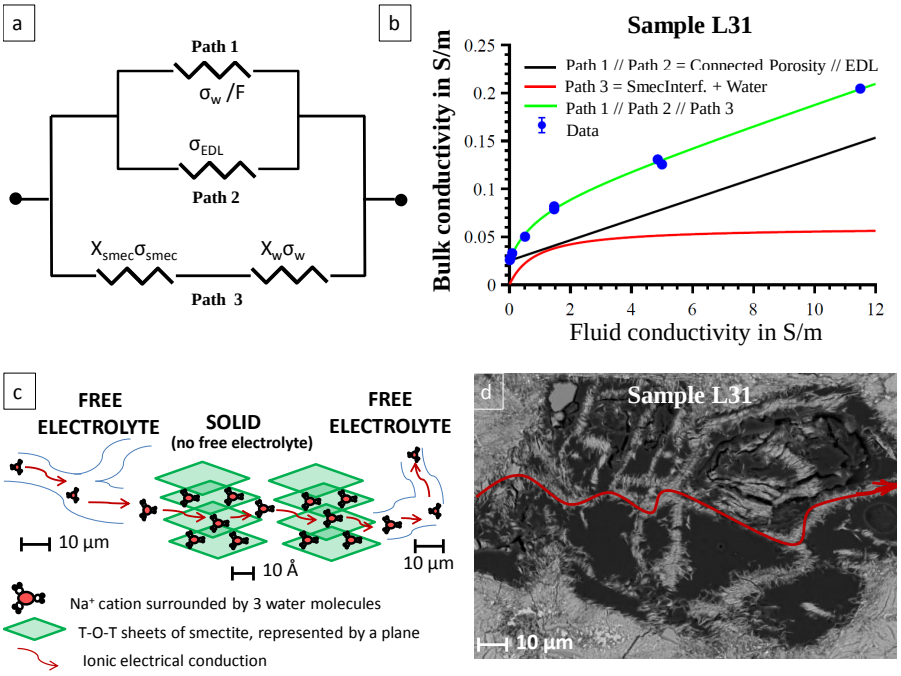

Figure 23: Conceptual model for electrical conduction in smectite-rich rock, involving a conduction pathway through connected interfoliar spaces. (a) Electrical equivalent circuit with three branches in parallel, similar to that proposed by McKelvey Jr et al. (1955); (b) Fit of the bulk conductivity dependence upon fluid conductivity, using the Equivalent Circuit model for sample L31: the linear (fluid in the connected porosity, in parallel to EDL) and non-linear (smectite interfoliar spaces, in series with water outside the connected porosity) components are shown as black and red plain lines, respectively; (c) Sketch of ionic conduction through interfoliar spaces of smectite (d) SEM photograph showing smectite in the former permeable network of sample L31. The red line shows smectite crystals connected over 100 µm.

4

TRACKING MAGMATIC HYDROGEN SULPHUR CIRCULATIONS USING ELECTRICAL IMPEDANCE : COMPLEX ELECTRICAL PROPERTIES OF CORE SAMPLES AT THE KRAFLA VOLCANO, ICELAND - PAPER 2

This chapter presents an article published at Journal of Geophysical Research - Solid Earth on February, 15^{th} 2019. The full manuscript can be found in Appendix B.2.

4.1 SUMMARY

In this paper, we study the possibility to track pyrite mineralization, a witness of magmatic H_2S circulations in volcanic rocks, by means of complex electrical conductivity. We use of subset of 30 samples from Krafla volcano, which contain various volumes of pyrite, iron-oxides and smectite. We focus on the influence of pyrite and iron-oxides on the low-frequency parts of the phase-angle spectra ($f \leqslant 10^4$ Hz) and use the maximum phase angle (MPA) to describe the main polarization peak. We present a method to discriminate pyrite from iron-oxides, using the MPA and the bulk real conductivity. We also investigate the influence of smectite abundance and pore fluid conductivity on the MPA.

4.2 MAIN RESULTS

- Pyrite, iron-oxides, smectite and pore fluid conductivity influence the electrical impedance phase angle of volcanic rocks.
- Volcanic rocks with MPA $\geqslant$ 30 mrad contain pyrite if the real conductivity is $\geqslant 3 \cdot 10^{-2}$ S/m or on the right side of the division line in Figure 24 (a).
- We explain this clear discrimination by the fact that pyrite is mainly found in hydrothermally altered rocks, which are often more porous and contain smectite, whereas iron-oxides are rather found in crystalline dense unaltered rocks.
- A broad linear correlation exists between the MPA and the volume fraction of metallic particles (pyrite or iron-oxides), with an increase of 22 mrad by volume per cent of metallic particles.
- Deviations to the correlation can be explained by (i) the uncertainty on metallic particles quantification in natural volcanic

rocks (Figure 24 (b)) and (ii) the counter effect of smectite on the MPA. Indeed, smectite abundance seems to decrease the overall polarization, which may be due to the existence of continuous conduction pathways, as suggested by e.g. Vinegar and Waxman (1984) and Telford et al. (1990).

- For samples with small volumes of smectite, the MPAdecreases with increasing salinity but for samples with large volumes of smectite, the MPA reaches a maximum at intermediate salinity.

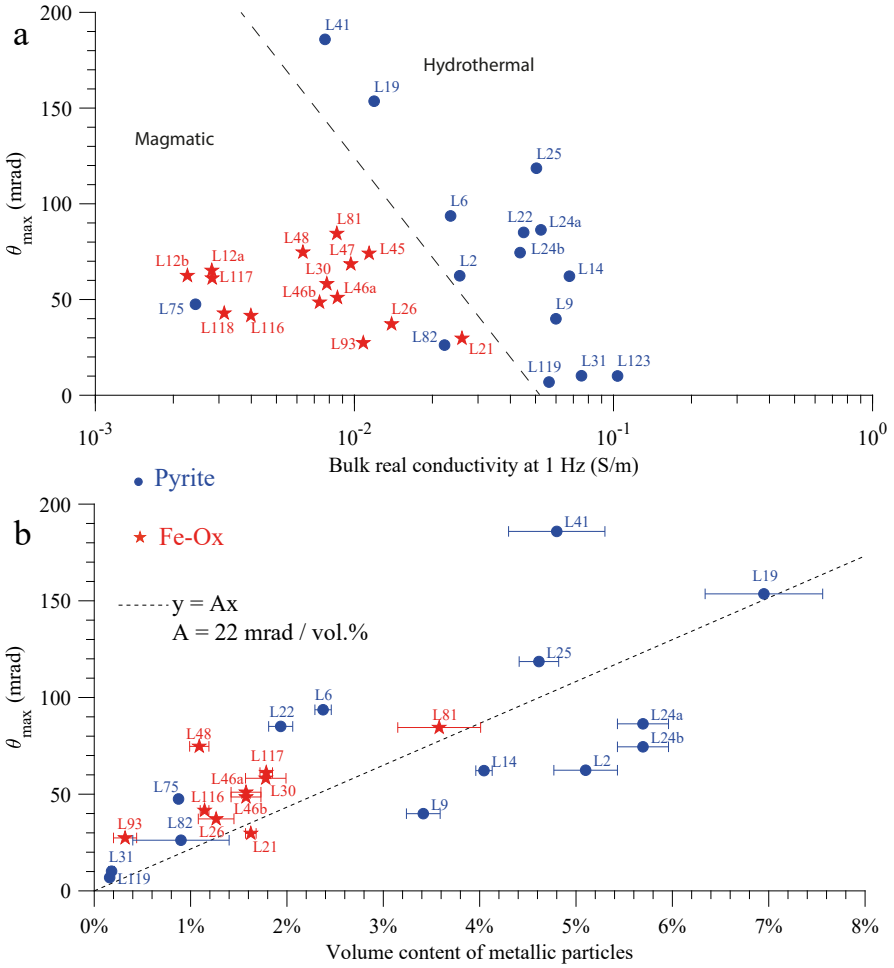

Figure 24: Discrimination and quantification of metallic particles. (a) Maximum Phase Angle (θ_{max}) versus bulk real conductivity at 1 Hz, with a division line between pyrite-rich "hydrothermal" samples and iron-oxides-rich "magmatic" samples; (b) MPA versus volume fraction of metallic particles; with a least-square regression line. Blue circles and red stars correspond to pyrite-rich and iron-oxide-rich samples, respectively. Measurements correspond to a pore fluid conductivity of 0.13 S/m.

5

ELECTRICAL RESISTIVITY TOMOGRAPHY AND TIME-DOMAIN INDUCED POLARIZATION FIELD INVESTIGATIONS OF GEOTHERMAL AREAS AT KRAFLA, ICELAND: COMPARISON TO BOREHOLE AND LABORATORY FREQUENCY-DOMAIN ELECTRICAL OBSERVATIONS - PAPER 3

This chapter presents a manuscript submitted to Geophysical Journal International in October, 23rd 2018, and sent back to the journal after moderate revision in April 2019. The full manuscript can be found in Appendix B.3.

5.1 SUMMARY

In 2017, we carried out Electrical Resistivity Tomography (ERT) and Time-Domain Induced Polarization (TDIP) measurements, along 13 profiles at three sites around the eastern caldera rim of the Krafla volcano. The sites, outside the main exploited geothermal area, are located around three boreholes: KH1 and KH3, described in Papers 1 and 2 and KS1, described in Gudmundsson et al. (2007). We present two-dimensional inversions of complex resistivity, down to 200 m. We invert for the maximum phase angle, relaxation time and resistivity and interpret inversions in terms of mineralogy. We compare in-situ electrical logs and laboratory frequency-domain electrical measurements on core samples to the inversions in order to evaluate, at the field scale, the effect of temperature on resistivity and MPA.

5.2 MAIN RESULTS

- Bodies of high maximum phase angle (MPA) are identified at KH1 and KS1 and interpreted as pyrite-rich and iron-oxides-rich, respectively (Figure 25 for KH1), based on the discrimination method suggested in Paper 2. Interpretations are confirmed by estimated mineral abundances in the boreholes.
- Spectral analyses of the IP decays indicate longer relaxation times at the pyrite-rich site (KH1) than the iron-oxide site (KS1). This is in line with laboratory observations (see Paper 2 in Appendix). It can be explained by the larger size and higher degree of connectivity of pyrite crystals formed upon hydrothermal alteration, compared to disseminated iron-oxides formed upon magma crystallization, already noted by (Pelton et al., 1978).

- Comparison between inversions, borehole logs and laboratory measurements at KH1 indicate that an increase of the electrical conductivity of 6% per °C is needed to explain the discrepancy between in-situ and laboratory measurements (at 25°C).
- Low-resistivity body identified at KH1 (Figure 25) is interpreted as an up-flow zone, resulting from the N-S trending rifting axis and the southern caldera rim.
- Low resistivity, due in particular to the abundance of smectite, creates noise in the IP data up to a point that IP data could not be inverted at one site (KH3).
- Upscaling laboratory quantifications from Paper 2 is complicated due to the limited frequency-range investigated by TDIP.

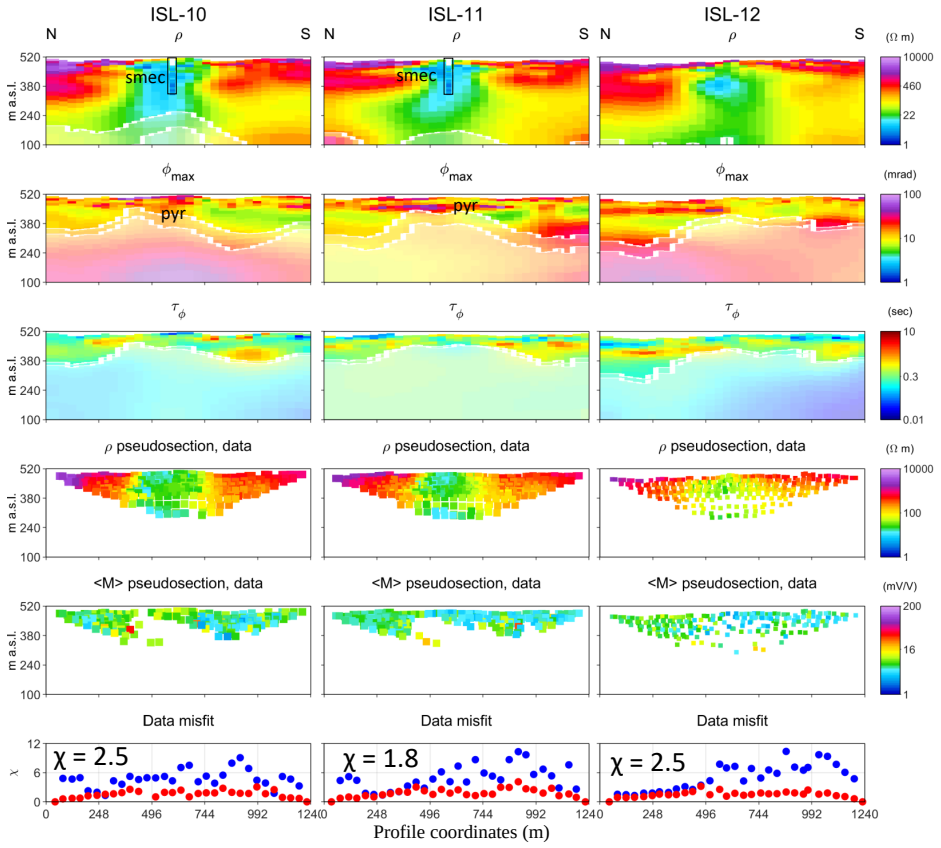

Figure 25: Two-dimensional inversion of ERT/TDIP data of profiles ISL-10, ISL-11 and ISL-12, parallel and spaced 100 m apart at KH1. Six figures are shown for each profile, from top to bottom: resistivity, MPA and relaxation time inversion models, apparent resistivity and integral apparent chargeability pseudo-sections and final misfit calculated by Equation 19 (resistivity=blue; IP=red). The white lines in top three panels correspond to depths of investigation, calculated in conservative and standard manners.

.

6

SMECTITE QUANTIFICATION IN HYDROTHERMALLY ALTERED VOLCANIC ROCKS - PAPER 4

This chapter presents a manuscript submitted to Geothermics on March, 7^{th} 2019. The full manuscript can be found in Appendix B.4.

6.1 SUMMARY

The paper describes a method developed at ÍSOR in 2015-2016, to carry out accurate and fast Cation Exchange Capacity (CEC) measurements on altered volcanic rocks, using back-titration of an organic complex "Cu-trien". It also develops a method for mineral quantification by Rietveld-refinements, used to quantify the smectite weight content independently from CEC measurements. These methods were only briefly presented in Paper 1. The originality of the approach presented here lies in the quantification of the CEC measurement uncertainty, coming from two sources: the detection limit of the spectrophotometer used for the titration in oversaturated conditions and the partial exchange reaction in undersaturated conditions. These sources of uncertainty were already mentioned e.g. by Orsini and Remy (1976), but these authors did not investigate the theoretical grounds behind the optimal ratio of reactants.

6.2 MAIN RESULTS

- Using simplified thermodynamic equations to represent the cation exchanges between rock and Cu-trien reactant, we explain why the apparent measured CEC can be reduced to half of the total CEC if more than 30% of the Cu-trien initially present is consumed, in particular if the thermodynamic constant K of the exchange reaction is inferior to 50 (Figure 26 (a) and (b)).
- By quantifying thoroughly the uncertainty of the laboratory measurement itself, we show that this uncertainty rapidly increase from 10% up to 300% of the CEC value, when less than 20% of the Cu-trien initially present is consumed (Figure 26 (b)).
- We show that CEC and smectite weight content are proportional in altered volcanic rocks, and that the CEC measured with an optimal ratio of reactants gives an absolute quantification of the smectite weight fraction, regardless of the abundance of other alteration minerals in the rocks (Figure 26 (c)).

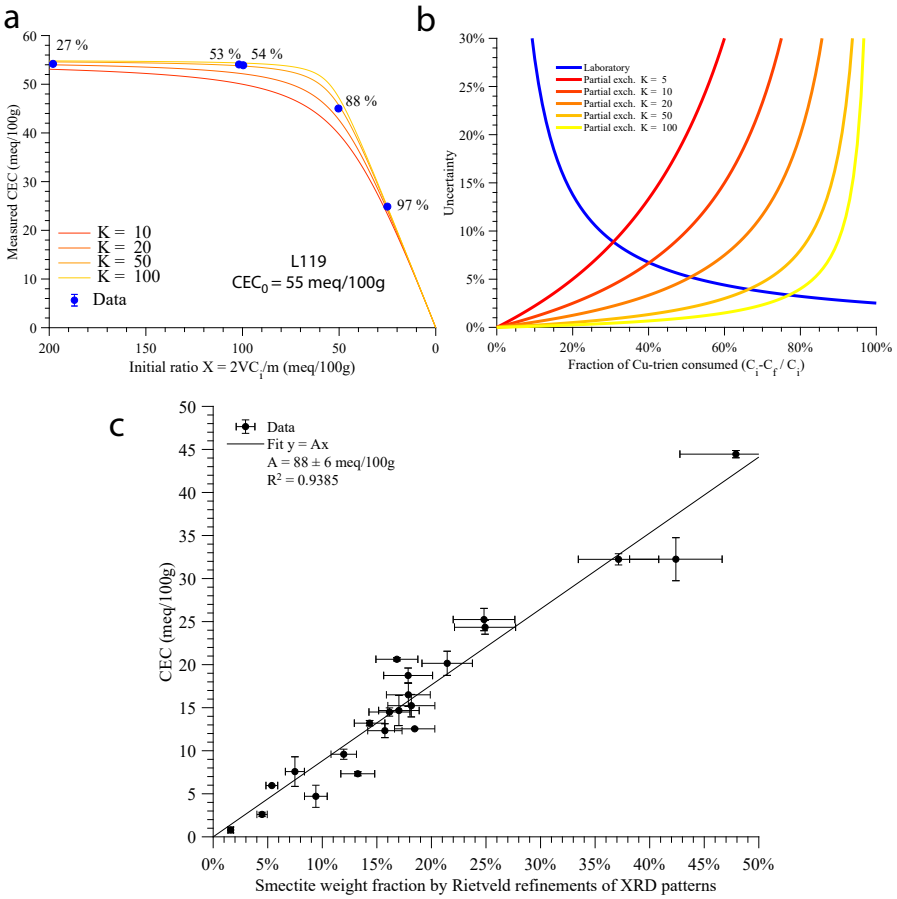

Figure 26: Optimization of CEC measurements for smectite quantification. (a) Decreasing measured CEC with decreasing initial ratio of reactants (increasing initial rock mass). The percentages indicate the fraction of Cu-trien consumed at the end of the reaction and evidence that limited exchange occurs above 80% of Cu-trien consumption for sample L119. (b) Predicted uncertainty from two different sources: detection limit of the spectrophotometer (blue line) and limited exchange with Cu-trien (red to yellow lines), calculated for different values of K, based on equations presented in the Paper. The total uncertainty can be minimized by working with fractions of Cu-trien consumed between 30% and 80%. (c) CEC measured with optimized protocol and fine grain size, versus weight fraction of smectite sheets, quantified by Rietveld refinements of XRD patterns, for samples where smectite is the only clay mineral.

7 ADDITIONAL RESULTS

7.1 ELECTRICAL CONDUCTIVITY OF VOLCANIC GLASS AND MELTS

Low-resistivity bodies are sometimes observed in MT inversion models and interpreted as bodies of molten material (magma). In order to investigate whether clay minerals and melts have distinct electrical signatures, electrical conductivity measurements of rhyolitic and basaltic glasses from Krafla were carried out at in-situ conditions, up to melting conditions (80-120 MPa, 400-1260°C). Basaltic and rhyolitic lavas were sampled in Krafla in 2017 by Helgi Arnar Alfreðsson. The basaltic lava was melted at 1400°C prior to the experiments to remove gas bubbles. Chemical compositions of the glasses were carried out by Scanning Electron Microscope (SEM) at Gésociences Montpellier and presented in Table 5, together with chemical analyses from the literature.

Table 5: Chemical analyses of rhyolitic and basaltic glasses. % Oxides are in wt.%.

% Oxides	Obsidian[1]	Obsidian[2]	Quenched rhyolite[3]	Basalt[4]	Basalt[5]
SiO_2	75.35	75.23	74.99	57.46	50.75
Al_2O_3	12.17	12.00	11.79	11.58	15.76
Na_2O	4.07	4.15	3.72	1.90	1.76
K_2O	2.86	2.75	2.99	0.31	0.28
CaO	1.71	1.66	1.32	9.11	11.35
MgO	0.12	0.10	0.19	4.63	6.99
FeO	3.43	3.28	2.7	13.06	12.24
MnO	0.00	0.11	0.07	0.00	0.22
TiO_2	0.24	0.23	0.32	1.87	1.80

[1] Obsidian from Hrafntinnuhryggur used in our experiments
[2] Obsidian from Hrafntinnuhryggur (Tuffen and Castro, 2009)
[3] Glass from borehole IDDP1 in Krafla (Zierenberg et al., 2013)
[4] Basalt from the Krafla Fires used in our experiments
[5] Basalt scoria from the Krafla Fires (Jónasson, 1994)

The results of electrical conduction measurements, using a similar approach to that of Nono et al. (2018), are presented in Figure 27 and Table 6.

The obsidian displays a linear increase of the logarithm of conductivity as a function of reciprocal temperature from 400 to 1100°C,

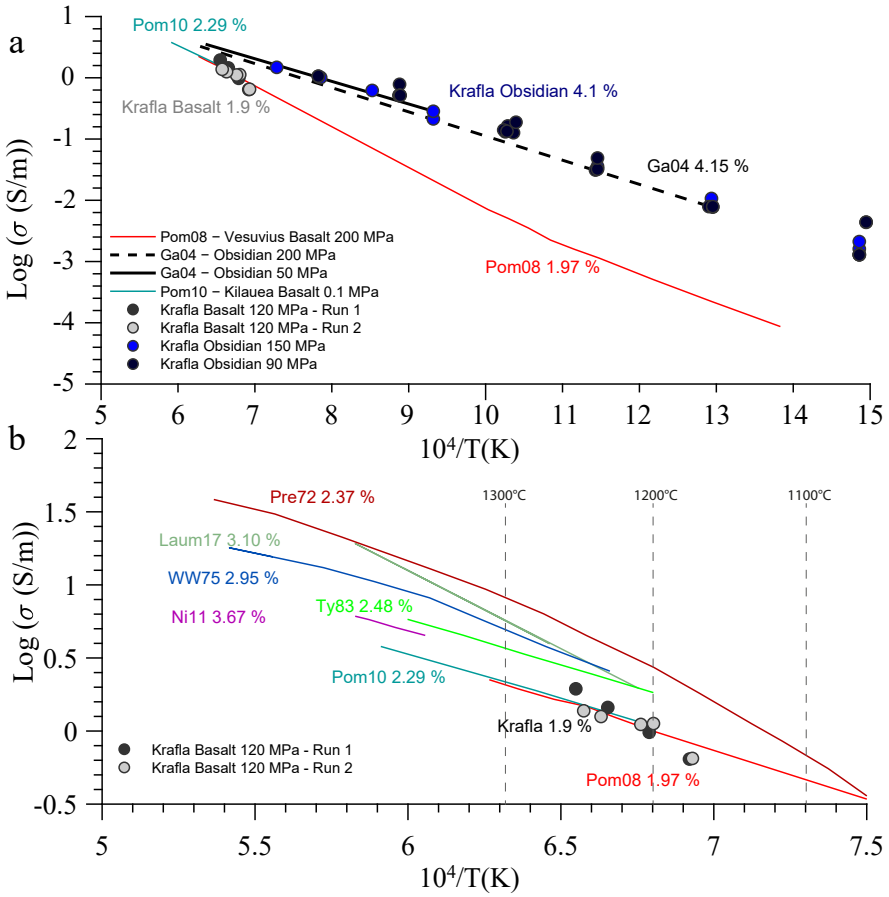

Figure 27: Electrical conductivity of obsidian and basalt glasses: (a) from 400 to 1500°C; (b) from 1050 to 1500°C. Krafla = this study; Pom08=Pommier et al. (2008); Pom10=Pommier et al. (2010); Ga04=Gaillard (2004); Ni11=Ni et al. (2011); WW75=Waff and Weill (1975); Pre72=Presnall et al. (1972); Laum17=Laumonier et al. (2017); Ty83=Tyburczy and Waff (1983).

indicating an Arrhenian behaviour (Equation 21) with a single conduction mechanism in the glass and melt regions.

$$\sigma = Ae^{\frac{-E_a}{k_B T}} \tag{21}$$

where σ is the temperature-dependent conductivity in S/m, k_B is the Boltzmann constant ($1.38 \cdot 10^{-23}$ J/K), T the temperature in K, A a constant in S/m, and E_a the activation energy in kJ/mol.

The activation energy resulting from our measurements on the obsidian glass is 75 kJ/mol, compatible with a conduction due to sodium mobility. The electrical conductivity at 900-1000°C (estimated in-situ temperature for rhyolitic melt) is 1 ± 0.2 S/m, which is similar to values obtained by Gaillard (2004) on a dry obsidian having the same Na content (Figure 27 (a)).

The conductivity of the basaltic glass increases from 0.6 to 2 S/m, with temperature from 1170 to 1250°C, and also follows an Arrhe-

Table 6: Electrical conductivity measurements of rhyolitic and basaltic glasses up to melting conditions. σ is calculated from the resistance R and the sample dimensions (diameter d and initial length l).

Sample/Conditions	T(°C)	10^4/T(K)	R (Ω) at 1 kHz	σ (S/m)
Basalt	1172	6.92	$3.63 \cdot 10^2$	$6.43 \cdot 10^{-1}$
130 MPa	1200	6.79	$2.38 \cdot 10^2$	$9.81 \cdot 10^{-1}$
d=6mm; l=6.6mm	1230	6.65	$1.61 \cdot 10^2$	1.45
Run 1 (May 2017)	1254	6.55	$1.20 \cdot 10^2$	1.95
Basalt	1170	6.93	$3.81 \cdot 10^2$	$6.50 \cdot 10^{-1}$
130 MPa	1197	6.80	$2.20 \cdot 10^2$	1.13
d=6mm; l=7mm	1206	6.76	$2.23 \cdot 10^2$	1.11
Run 2 (Aug. 2017)	1235	6.63	$1.97 \cdot 10^2$	1.26
	1248	6.57	$1.80 \cdot 10^2$	1.38
Obsidian	499	12.95	$1.02 \cdot 10^4$	$7.73 \cdot 10^{-3}$
90 MPa	600	11.45	$2.46 \cdot 10^3$	$3.22 \cdot 10^{-2}$
d=9.5mm; l=5.6 mm	702	10.26	$6.02 \cdot 10^2$	$1.31 \cdot 10^{-1}$
Run 1 (March 2017)	699	10.29	$5.50 \cdot 10^2$	$1.44 \cdot 10^{-1}$
	692	10.36	$6.23 \cdot 10^2$	$1.27 \cdot 10^{-1}$
	689	10.40	$4.20 \cdot 10^2$	$1.88 \cdot 10^{-1}$
	396	14.95	$1.81 \cdot 10^4$	$4.36 \cdot 10^{-3}$
	396	14.95	$1.79 \cdot 10^4$	$4.40 \cdot 10^{-3}$
	600	11.45	$1.61 \cdot 10^3$	$4.90 \cdot 10^{-2}$
	704	10.24	$5.63 \cdot 10^2$	$1.40 \cdot 10^{-1}$
	854	8.87	$1.53 \cdot 10^2$	$5.16 \cdot 10^{-1}$
	1005	7.82	$7.50 \cdot 10^1$	1.05
Obsidian	400	14.86	$5.53 \cdot 10^4$	$1.61 \cdot 10^{-3}$
150 MPa	500	12.94	$8.30 \cdot 10^3$	$1.07 \cdot 10^{-2}$
d=9.5mm; l=6.3 mm	600	11.45	$2.66 \cdot 10^3$	$3.34 \cdot 10^{-2}$
Run 2 (May 2017)	700	10.28	$6.60 \cdot 10^2$	$1.35 \cdot 10^{-1}$
	800	9.32	$4.17 \cdot 10^2$	$2.13 \cdot 10^{-1}$
	400	14.86	$4.20 \cdot 10^4$	$2.12 \cdot 10^{-3}$
	400	14.86	$6.90 \cdot 10^4$	$1.29 \cdot 10^{-3}$
	600	11.45	$2.47 \cdot 10^3$	$3.59 \cdot 10^{-2}$
	800	9.32	$3.13 \cdot 10^2$	$2.84 \cdot 10^{-1}$
	900	8.53	$1.43 \cdot 10^2$	$6.22 \cdot 10^{-1}$
	1000	7.86	$8.80 \cdot 10^1$	1.01
	1100	7.28	$6.00 \cdot 10^1$	1.48

nian behaviour. Results are consistent with measurements by Pommier et al. (2010) and Pommier et al. (2008) on basalts at the Kilauea volcano (Hawaii) and the Vesuvius (Italy), respectively, which have similar sodium content (Figure 27 (a)). The distinct conductivity from other basalts with different sodium composition (Figure 27 (b)) confirms that sodium is the main charge carrier in glass and melt (Pommier et al., 2010). The range 700-1100°C was not investigated for the basaltic glass, since crystals (plagioclases, pyroxenes) could form at these temperatures and interfere with the melt during the conductivity measurements.

7.2 ANALYSIS OF THE RELAXATION TIME IN NATURAL VOLCANIC ROCKS

The relaxation time τ of the main low-frequency polarization peak, observed on the phase-angle spectra, is obtained by fitting the impedance spectra with the "Cole-Cole // C_∞" model, which consists in a Cole-Cole equivalent circuit in parallel with a capacitance. The corresponding impedance function is presented in Equation 14. Our results first indicate that τ is systematically lower than 10^{-3} seconds for samples with iron-oxides but spans the whole range of relaxation times for samples with pyrite (see Table in Supporting Information of Paper 2). Empirical observations by previous studies show that τ decreases with increased fluid conductivity (Gurin et al., 2015; Placencia-Gómez and Slater, 2016) or clay content (Revil et al., 2017d). The expression of the relaxation time suggested by Wait (1987), based on assumptions presented in Chapter 2, predicts a decrease with an increased bulk conductivity (Equation 22).

$$\tau = \left(\frac{1}{A\alpha\sigma_0}\frac{b^2}{a}\right)^{1/\phi} \tag{22}$$

where σ_0 is the total real conductivity of the matrix, α the depolarizability coefficient, b and a the semi-major and -minor axes of the elongated metallic particles, respectively, ϕ the Cole-Cole exponent and A a dimensionless coefficient.

Wait's model 1987 is relatively consistent with our experimental observations (Figure 28), assuming spheroidal ratios b^2/a between 10 and 250 µm. Samples L41, L02 and L25, which are very altered and have the largest and most connected pyrite grains, follow the same trend, corresponding approximately to the bottom black line in Figure 28 and thus the longest relaxation times of the analyzed data set. Samples L45-L46a-L46b-L47-L48, which are rather unaltered, contain iron-oxides and have the smallest spheroidal ratios (narrowly distributed in the range 10-30 µm), follow the same trend, above the upper black line in Figure 28, and correspond to the shortest relaxation times of the data set. Therefore, the predictions of Wait's model

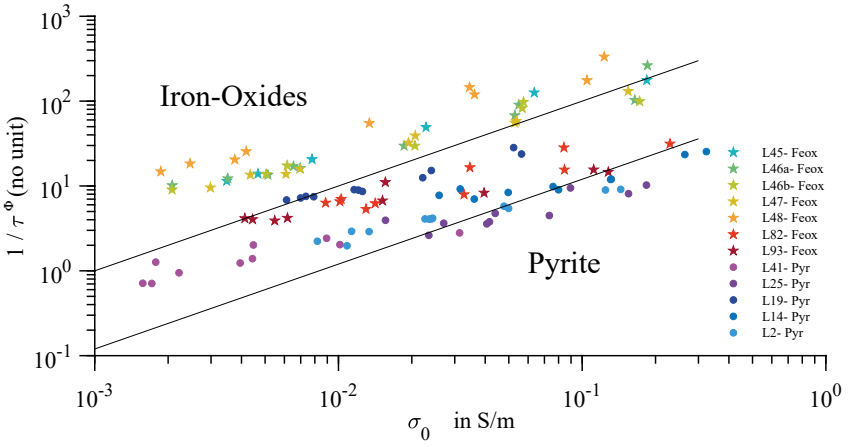

Figure 28: Relationship between the relaxation time τ, the Cole-Cole exponent Φ and the bulk conductivity σ_0, calculated after fitting impedance spectra measured at distinct pore water conductivities. Pore water conductivity increases from left to right. The black lines correspond to Equation 22 with $\alpha = 3$, $A = 0.01$ (adjusted to fit the data) and $b^2/a = 30$ µm (upper line) or $b^2/a = 250$ µm (bottom line).

are qualitatively correct. However, the broad and complex distribution of grain sizes in natural volcanic samples containing pyrite does not allow a quantitative comparison of the metallic grain size and the relaxation time.

7.3 EVOLUTION OF IMPEDANCE SPECTRA WITH TIME

Measurements performed one year apart yield similar impedance spectra for most samples (see L48 and L19 in Figure 29). However, two samples (L25 and L41) show a decrease of the maximum phase angle, broadening of the polarization peak and decrease in the real part of the impedance with time (Figure 29). These changes are consistent with experimental and modeling results by Placencia-Gómez and Slater (2014) where artificial pyrite-sand mixtures become oxidized, due in particular to the diffusion of atmospheric oxygen into the samples during successive saturation processes. If an oxidation-reduction reaction occurs at the interface electrolyte/pyrite, a charge transfer from aqueous ions into metallic electrons may occur and decrease the impedance of the sample. Moreover, the quantity of metallic particles may have been reduced from one saturation to another, due to changes of pore fluid chemistry and flushing. This would have caused a decrease of the maximum phase angle. The abundance of connected sulphides, as well as the different chemistry associated to sulphides in L25 (pyrite associated with exsolutions of gold and palladium) and L41 (abundance of troilite, the Fe-rich end-member of

the pyrite-pyrrhotite solid solution) compared to other samples, may be involved in the different behavior of these two samples.

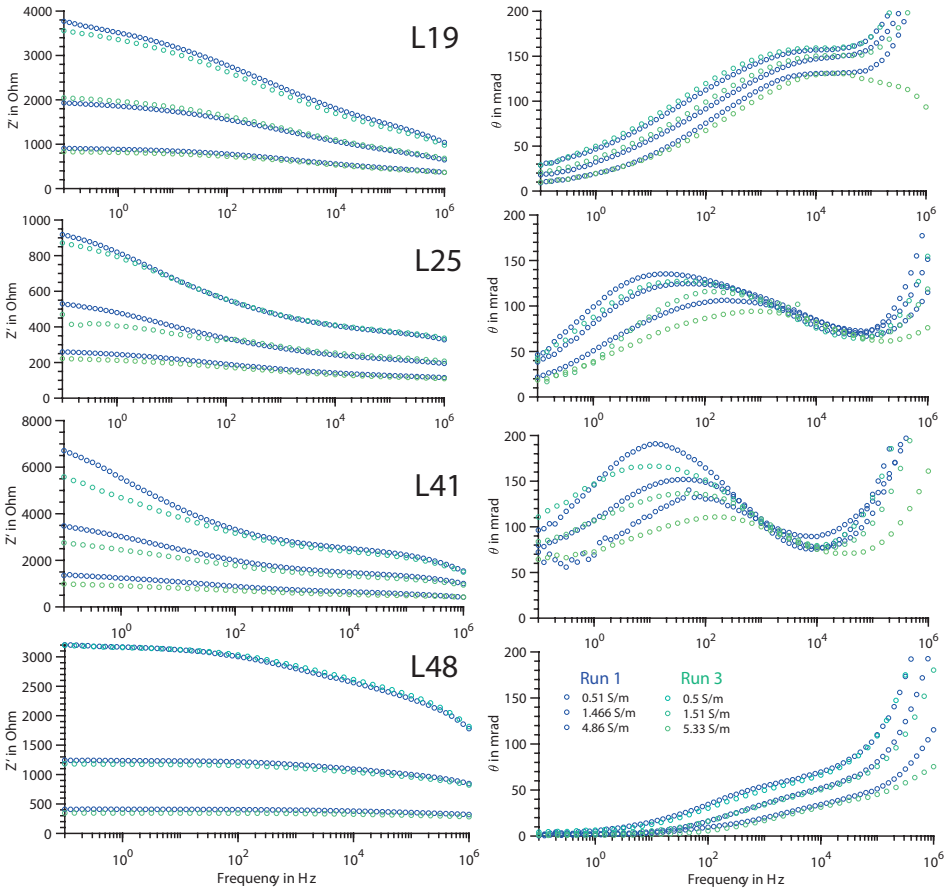

Figure 29: Real part of the impedance Z′ (left panels) and phase-angle θ (right panels) for four samples at three pore water conductivities. For each spectrum, two sets of measurements are shown: Run 1 in late 2016 and Run 3 in late 2017. In-between, the fluid conductivity of the saturating fluid was increased, decreased and re-increased, from 0.02 to 11 S/m. Increasing fluid conductivity corresponds to lower values for Z′ and θ at all frequencies.

8

PERSPECTIVES

This chapter presents four on-going projects, launched in relation to my PhD work but not mature enough to be part of the PhD thesis.

In order to investigate further the processes of interfoliar conduction related to swelling-clays, and their relative importance compared to surface conduction, experiments on simple and well-characterized material are valuable. A synthetic single-crystal Na-vermiculite was made available by Fabien Hubert and Philippe Cosenza from the IC2MP laboratory at Poitiers. Vermiculite is a clay mineral, whose structural charge is very close to that of saponite, the most common smectite in basaltic environments (Figure 10). Electrical conductivity measurements were carried out on this single crystal by Sabine Devautour-Vinot at the Charles Gerhardt Institute from University of Montpellier, at 25°C in controlled humidity conditions (95%, 40% and 0%). Different hydration conditions correspond to different numbers of water layers surrounding the Na-ion in the interlayer spaces (2, 1 and 0, respectively). First results indicate that the absence of water layers around Na-ion in the interfoliar spaces prevents ionic conduction but allow important dielectric polarization by re-orientation of the Na-ion, trapped between the T-O-T sheets. Hydration to 1 water layer results in a release of Na-ions from their site and strong increase of interfoliar conduction. Hydration to 2 water layers causes an additional increase of two orders of magnitude in interfoliar conduction, resulting in an average interfoliar conductivity of 9×10^{-4} S/m. Next steps include conductivity measurements of vapor-saturated compacted powders of natural saponite and saponite-rich core samples from Krafla, to investigate if saponite can be conductive through its interfoliar spaces without liquid water (as e.g. in a steam cap).

Measurable polarization phenomena associated to clay minerals have been observed in numerous studies (Weller et al., 2013; Revil et al., 2017b; Slater and Lesmes, 2002a; Joseph et al., 2015; Revil et al., 2017c). These studies suggest that the quadrature conductivity obtained by frequency-domain conductivity measurements can allow discriminating between the effect of clays and of saline fluid on the bulk in phase conductivity. We tested this hypothesis on a subset of our volcanic samples, which contain negligible volumes of metallic particles. We observe similar phase-angle spectra for all samples, despite a wide range of in-phase conductivity, CEC and clay content (CEC from 0 to 55 meq/100g, smectite from 0 to 50 wt.% and chlorite from 0 to 20 wt.%). Moreover, the variations of the phase-angle with salinity are less important than the variations of the in-phase conduc-

tivity with salinity. Therefore, the variations of quadrature conductivity with salinity and smectite content seem to be controlled by the variations of the in-phase conductivity. These results tend to indicate that quadrature conductivity does not bring more information than in-phase conductivity for this type of samples.

Clay mineralogy and volcanology are the farthest disciplines involved in my PhD but I have been working towards their reconciliation. The project "AGERG", a collaboration between ENS (me), University of Montpellier (Benoit Gibert, Jacinthe Caillaud), University of Poitiers (Patricia Patrier, Daniel Beaufort) and University Joseph Fourier in Grenoble (Bruno Lanson), was funded in 2018 by INSU-CNRS to investigate in greater details the origin of clay minerals in borehole KH6 and relations to lithology and fractures. A student from Géosciences Montpellier, David Escobedo, did his master project within that collaboration. His work illustrated in particular that corrensite and chlorite found in closed vesicles probably had a late-magmatic origin, given the unaltered minerals around and the complete filling of the vesicles by clays, zeolites and alkaline feldspar. His work also evidenced that aluminium-rich and di-octahedral clay minerals (montmorillonite, illite, kaolinite) were associated with very altered and fractured rocks. With Gylfi Páll Hersir, I organized a workshop in August 2018 to discuss the first results, as well as the general use of resistivity to identify alteration minerals and constrain geothermal exploration. Mineralogists and geophysicists from ÍSOR, University of Iceland, Landsvirkjun, Reykjavik Energy, Poitiers and Montpellier were involved. I also presented a poster at the GEORG conference in November 2018, on behalf of David. New samples were taken at Krafla in August 2018 and the collaboration established is to be continued beyond the AGERG project or my PhD. Since less conduction and more polarization may be expected in presence of unconnected smectite, compared to connected smectite, a discrimination between "hydrothermal" and "magmatic/supercritical" clay minerals may be possible by studying the influence of smectite connectivity on the electrical signature of volcanic rocks.

Swelling-clays also affect the elastic and failure mechanical properties of volcanic rocks. With Aurélien Nicolas, Jérôme Fortin and Li Zhi at ENS and Olivier Sissman at Institut Français du Pétrole, we artificially altered fresh natural andesite at different temperatures and studied the changes in the mechanical behavior. Results indicate that the very small amount of smectite formed, mainly in microcracks, increased the bulk elastic wave velocities and decreased elastic compaction and peak stress at failure during tri-axial loading. My contribution in this project was to quantify the alteration level and in particular the smectite content in the fresh and altered samples. Throughout the preparation of a manuscript with this working group, I learned a lot about rock mechanics.

9 GENERAL CONCLUSIONS

The objective of this PhD was to improve the understanding of the electrical resistivity structure around active volcanoes.

The first thread of research was to better understand which physical processes are responsible for low resistivity of volcanic rocks. The first (chronological) achievement was to show that the weight fraction of smectite sheets in altered volcanic rocks controls the cation exchange capacity (CEC). An experimental protocol was optimized for accurate CEC measurements and smectite quantification (Paper 4). The second achievement was to develop a physical model involving electrical conduction along connected interfoliar spaces of smectite, a process described in the literature (Maraqah et al., 1990) but not included in Electrical Double Layers models. This model fits the observed non-linear increase of in-phase conductivity with salinity (Paper 1) and its mathematical formulation is similar to that of models from the literature, based on different hypotheses (e.g. McKelvey Jr et al., 1955; Revil and Glover, 1997). In-situ borehole logs and Electrical Resistivity Tomography (ERT) illustrate that the electrical conductivity of smectite-rich volcanic rocks can increase by up to 6% per °C, with an in-situ conductivity of up to 0.5 S/m at 180°C and 200 m depth (Paper 3). This value is close to the conductivity of volcanic glass at melting conditions, as shown by our measurements on rhyolitic and basaltic glasses from Krafla, which are consistent with previous studies (Pommier et al., 2010; Gaillard, 2004).

The second thread of research was to find complementary investigation techniques. Based on previous studies, Induced Polarization (IP) was a good candidate to discriminate between the contributions of smectite and fluid to the total conductivity. However, in these volcanic rocks, the magnitude of polarization is controlled by the presence of pyrite and iron-oxides, while no polarization seems to be associated to smectite. This is consistent with the process of interfoliar conduction emphasized in Paper 1 for swelling clay minerals, such as smectite: since ions can cross the interface fluid/smectite, they do not accumulate and polarization is by-passed. Paper 2 presents a method to evaluate the volume of metallic particles and discriminate pyrite from iron-oxides in natural volcanic rocks, based on the maximum phase angle at low frequency (MPA) and the in-phase resistivity at 1 Hz. We observe that samples with low resistivity and high MPA always contain pyrite, while most samples with high resistivity and high MPA contain iron-oxides; samples with MPA lower than 20 mrad contain negligible volume of metallic particles. We also ob-

serve that the MPA increases of about 22 mrad per vol.% of metallic particles, but decreases with fluid conductivity smectite abundance. Spectral inversion of field Time-Domain Induced Polarization (TDIP) data has allowed identifying bodies of high MPA, associated with a low-resistivity anomaly at one site, which were attributed to the presence of pyrite (Paper 3). Layers of high MPA, associated with overall high resistivity, were identified at another site and attributed to the presence of iron-oxides. Both attributions were confirmed by mineral analyses on borehole samples. A limit for upscaling the laboratory quantifications is the shorter frequency-range investigated by TDIP, compared to laboratory frequency-domain IP. The best IP signal in the field is obtained in resistive zones, which can correspond e.g. to fresh unaltered basalt or to altered basalt with chlorite instead of smectite. Low-resistivity bodies, related to smectite abundance, are associated to bad quality IP signal, which confirms that smectite is an obstacle to polarization and cannot be detected by IP measurements in these environments. Finally, a low-resistivity anomaly identified from ERT profiles, and attributed to a localized up-flow zone, illustrates the importance of improving the resolution of resistivity models in the first hundreds of meters. Indeed, this anomaly had not been detected in previous electromagnetic soundings. Therefore ERT sounding are complementary to classical electromagnetic soundings for geothermal exploration.

The third thread of research was to investigate further the link between clay minerals and hydrothermal circulations. Observations on samples from borehole KH6, in the context of the on-going fruitful collaboration with the laboratory IC2MP at Poitiers, have confirmed that clay minerals can be witnesses of hydrothermal convection but also of volatile-rich evolved supercritical fluids. Studying the connectivity of clay minerals from different origins, and the effect of connectivity on electrical conductivity, may be a next step to have clay mineralogists and geophysicists converge towards an integrated approach for geothermal exploration.

To summarize, my work emphasized that smectite abundance is the main parameter controlling the bulk electrical conductivity of volcanic rocks, while pyrite and iron-oxides abundances control the magnitude of polarization. I suggested that interfoliar conduction, thanks to high connectivity of smectite in fractures, is a key process to explain both the increase of conduction and decrease of polarization, associated to an increased abundance of smectite in volcanic rocks. Moreover, I observed that pyrite-rich volcanic rocks are more conductive than iron-oxides-rich volcanic rocks, because the former often correspond to altered rocks associated with smectite. This allows detecting separately pyrite and iron-oxides at the field scale. Finally, I opened new doors to interpret the inferred presence of smectite in terms of hydrothermal history.

A

COMMUNICATION ABOUT THE RESEARCH

ORAL PRESENTATIONS AT INTERNATIONAL CONFERENCES

- Lévy, L., Byrdina S., Gibert, B., Vandemeulebrouck J., Sigmundsson, F., Deldicque D., Árnason, K., Maurya, P.K., Hersir, G.P., Flóvenz, Ó.G. and Briole, P. Constraining geothermal exploration in volcanic environments with complex electrical measurements - Krafla, Iceland. **AGU (American Geophysical Union): 10-14 December 2018, Washington D.C., USA**. Program and abstracts available on AGU Fall Meeting website.

- Lévy, L., Gibert, B., Sigmundsson, F., Byrdina S., Vandemeulebrouck J., Flóvenz, Ó.G., Hersir, G.P., Maurya, P.K. and Briole, P. Tracking secondary mineralization in volcanic environments by means of complex electrical resistivity. 26^{th} **Hubbert Quorum USGS meeting: 9 December 2018, Reston VA, USA**.

- Lévy, L., Gibert, B., Sigmundsson, Byrdina S., Vandemeulebrouck J., Deldicque, D., Hersir, G.P., Flóvenz, Ó.G. and Briole, P. Tracking hydrogen sulphur circulations by means of complex electrical resistivity: field and laboratory investigations at the Krafla volcano, Iceland. **GEORG Geothermal Workshop: 14-15 November 2018, Reykjavík, Iceland**. Program and abstracts available on GEORG website.

- Lévy, L. Influence of smectite and pyrite on electrical properties of hydrothermal systems. **Workshop on interpreting electrical soundings in terms of hydrothermal activity - Advances and Challenges:** 27^{th} **August 2018, ÍSOR, Reykjavík, Iceland**. Program available on ISOR website.

- Lévy, L., Gibert, B., Sigmundsson, F., Hersir, G.P., Flóvenz, Ó.G., Briole, P., Pezard, P. Electrical conduction: a quantitative measure of the smectite and chlorite content? Study based on cores from Krafla. **GEORG Geothermal Workshop: 27-28 November 2016, Reykjavík, Iceland**. Presentation available on Slideshare.

POSTERS AT INTERNATIONAL CONFERENCES

- Escobedo, D., Patrier, P., Gibert, B., Lévy, L., Beaufort, D., Lanson, B. and Caillaud, J. Clay minerals distribution and petrophysical properties. Borehole KH6, Krafla, Iceland. **GEORG Geothermal Workshop: 14-15 November 2018, Reykjavík, Iceland**.

- Lévy, L., Byrdina S., Vandemeulebrouck J., Maurya, P.K., Sigmundsson, Árnason, K., Gibert, B., F., Hersir, G.P., Flóvenz, Ó.G. and Briole, P. Tracking secondary mineralization in hydrothermal systems with electrical impedance: 2D inversions of ERT and TDIP data - Krafla, Iceland. 5^{th} **Workshop on Induced Polarization: 2-5 October 2018, Newark NJ, USA.**

- Lévy, L., Gibert, B., Sigmundsson, F., Deldicque, D., Parat, F., Hersir, G.P., Flóvenz, Ó.G. and Briole, P. Tracking secondary mineralization in hydrothermal systems with electrical impedance: laboratory observations - Krafla, Iceland. 5^{th} **Workshop on Induced Polarization: 2-5 October 2018, Newark NJ, USA.**

- Lévy, L., Gibert, B., Sigmundsson, F., Hersir, G.P., Flóvenz, Ó.G., Briole, P. and Pezard, P. Quantitative impact of hydrothermal alteration on electrical resistivity from a joint analysis of laboratory and borehole data - Krafla, Iceland. **EGU (European Geosciences Union) Spring Meeting: 18-22 April 2016, Vienna, Austria.**

COMMUNICATION WITHIN THE IMAGE PROJECT

- Lévy, L., Gibert, B., Flóvenz, Ó.G. and Hersir, G.P. Role of smectite in the resistivity signal. **Highlight in IMAGE Final Book, Deliverable D2.05, November 2017**. Available on IMAGE.

- Lévy, L., Gibert, B., Sigmundsson, F., Hersir, G.P., Flóvenz, Ó.G., Briole, P. and Pezard, P. The role of smectites in the electrical conductivity of active hydrothermal systems - Krafla, Iceland. **Poster at the final IMAGE meeting: 4-6 October 2017, Akureyri, Iceland.**

- Gibert, B., Lévy, L., Sigmundsson, F., Hersir, G.P. and Flóvenz, Ó.G. Electrical conductivity of basaltic and rhyolitic melts from Krafla central volcano, Iceland. **Poster at the final IMAGE meeting: 4-6 October 2017, Akureyri, Iceland.**

- Lévy, L., Hersir, G.P. and Flóvenz, Ó.G. Quantitative Impact of Hydrothermal Alteration on Electrical Resistivity. **Technical report in IMAGE Task 3.3, September 2016.**

OUTREACH

- Three videos made with Margaux Dzuilka during the field campaign at Krafla in August 2017, available on Youtube ENS. Newsletter available on PSL website.

- Participation to "Ma these en 180 secondes" in March 2018: 3-min presentation of the PhD in front of a jury and non-scientific public (about 150 persons). Video available on MT180 (in French).

B

FULL VERSION OF FOUR PAPERS

Geophysical Journal International

Geophys. J. Int. (2018) **215,** 1558–1582
Advance Access publication 2018 August 18
GJI Rock and mineral physics, rheology

doi: 10.1093/gji/ggy342

The role of smectites in the electrical conductivity of active hydrothermal systems: electrical properties of core samples from Krafla volcano, Iceland

L. Lévy,[1,2,3] B. Gibert,[4] F. Sigmundsson,[2] Ó.G. Flóvenz,[3] G.P. Hersir,[3] P. Briole[1] and P.A. Pezard[4]

[1]*Laboratoire de Géologie, Ecole Normale Supérieure - PSL Research University, CNRS, UMR* 8538, *Paris, France. E-mail: lea.levy@ens.fr*
[2]*Nordic Volcanological Center, Institute of Earth Sciences, University of Iceland,* 101 *Reykjavík, Iceland*
[3]*ÍSOR-Iceland GeoSurvey, Grensásvegur* 9, 108 *Reykjavík, Iceland*
[4]*Géosciences Montpellier, Université de Montpellier, Montpellier, France*

Accepted 2018 August 16. Received 2018 July 20; in original form 2017 November 21

SUMMARY

The underground circulation of hot water, of interest for geothermal energy production, is often indirectly inferred from the presence of minerals formed by hydrothermal alteration at different temperatures. Clay minerals, such as smectite and chlorite, can be mapped from the surface using electrical soundings and give information about the structure of the geothermal system. Here, we investigate the specific role of smectite in the electrical response of igneous basaltic rocks and evaluate what physical processes make smectite a better electrical conductor than surrounding minerals. Laboratory measurements of cation exchange capacity (CEC), mineralogy, porosity and electrical conductivity are presented for 88 core samples from four boreholes at the Krafla volcano, Northeast Iceland. CEC is found to be a reliable measure of the smectite weight fraction in these volcanic samples, through a comparison with an independent quantification of the smectite content using Rietveld refinements of X-ray diffraction patterns. The bulk electrical conductivity, measured at fluid conductivities in the range 0.02–11.7 S m^{-1}, increases non-linearly with the fluid conductivity for samples with high smectite content. This non-linear variation is fitted with a function and a model for a conduction process through connected interlayer spaces within smectite. The process differs from electrical double layer conduction, which involves only cations on the crystal edges of smectite, not in the interlayer spaces. The laboratory results can help refine interpretations of electrical soundings in the context of geothermal exploration.

Key words: Electrical properties; Hydrothermal systems.

1 INTRODUCTION

Electrical resistivity soundings are used in exploration geophysics because resistivity of rocks is sensitive to the presence of natural elements relevant for industrial and research purpose: clay minerals, sulphides and metal oxides, molten magma and water of varying quantity, salinity and temperature. Discriminating the influence of these different components is challenging because of the heterogeneity of the conductive media and the wide range of conductivities of each of its component. We address here the particular contribution of expandable minerals (subcategory of clay minerals, e.g. smectite) to the electrical signature of the investigated area. Expandable minerals are abundant in volcanic geothermal systems (Meunier 2005), in subduction zones (Hyndman *et al.* 1997) and in some major faults (Chester *et al.* 2013). In volcanic systems, expandable minerals precipitate readily in permeable horizons during the circulation of hydrothermal fluids (Beaufort *et al.* 1995; Patrier *et al.* 1996). They are therefore amongst the first alteration minerals to precipitate from hydrothermal activity. At low temperature (80 °C–180 °C), these expandable minerals are thermodynamically stable and form a clay cap observed in geothermal systems, that can be mapped by electrical soundings (e.g. Árnason *et al.* 2000; Flóvenz *et al.* 2012). Above 180 °C, the expandable minerals are progressively replaced by chlorite and other 'high-temperature' minerals (Kristmannsdóttir 1975), if a thermodynamic equilibrium can be reached. The alteration mapping of an equilibrated geothermal system (Walker 1960; Kristmannsdóttir 1979; Alt *et al.* 1986) can be carried out by electrical soundings (Flóvenz *et al.* 1985; Hersir & Björnsson 1991; Árnason *et al.* 2010), based on the lower electrical conductivity of chlorite (non-expandable) compared to smectite (expandable) and the intermediate conductivity of mixed-layer clays (Flóvenz *et al.* 2005). One of the

current challenges in geothermal exploration is to distinguish between active and inactive sections of a geothermal system. Mapping the presence of smectite outside the clay cap would be a step forward to meet that challenge as smectite can indicate recent circulations of hydrothermal fluids (Beaufort *et al.* 1995). However, this requires more understanding of the physical processes responsible for the unique conductive behaviour of smectite, related to its high cation exchange capacity (CEC), as shown by e.g. Flóvenz *et al.* (2005) and Revil *et al.* (2017a).

Electrical conductivity of rocks containing clay minerals has been extensively studied from a theoretical and experimental point of view. The pioneering study of Archie (1942) showed that electrical resistivity of sandstones depends on salinity of the pore fluid as well as on the quantity of pore fluid transporting electrical charges (usually lower than the total porosity). Electrical measurements on basaltic samples from Iceland were used by Flóvenz *et al.* (1985) to show that the temperature dependence of resistivity was different from what one would expect if only pore fluid was contributing, emphasizing the importance of clay contribution to the measured conductivity. The clay contribution was introduced by Hill & Milburn (1956) with a constant shaliness parameter. Following this idea, Rink & Schopper (1974) wrote the bulk conductivity as a linear function of the fluid conductivity with two constant parameters independent of the salinity: the 'formation factor' F accounting for the topology of the pore space and the 'surface conductivity' C_s—also called 'interface conductivity' by Flóvenz *et al.* (1985). In these studies, C_s represents a contribution from the clays to conduction, which is much lower than the contribution of the pore fluid. Limits of the linear function had however been shown by Waxman & Smits (1968), based on a large set of measurements on shaly sands and the use of linear-scale representation. Moreover, the possibility of electrical conduction along a pathway of connected clays in the rock matrix (not only along the interface clay–water) was mentioned by Vinegar & Waxman (1984), based on the absence of charge accumulation beyond a certain clay content. However, such a model was not formulated, partly because sedimentary samples with high content of expandable clay minerals are not easily manipulated in the laboratory (Waxman & Thomas 1974). Since altered igneous samples can have a high content of expandable clay minerals and yet be manipulated in the laboratory, the study of such samples can reveal the conduction processes for high smectite content. Our work is a step in that direction, following the work carried out by Flóvenz *et al.* (2005) and Kristinsdóttir *et al.* (2010) with Icelandic basaltic samples at different alteration stages.

Three types of properties have been measured in the laboratory on 88 Icelandic igneous basaltic core samples: chemistry (CEC), mineralogy (XRD) and petrophysical properties including porosity, grain density and electrical impedance measurements at six distinct pore water conductivities. We focus on the in-phase conductivity of these core samples, which is relevant when studying the role of smectite and other expandable minerals. The samples are from the well-studied Krafla high-temperature geothermal field, where cores are available in four boreholes, down to 700 m (Fig. 1). This field, where a geothermal powerplant is operated, is located within the caldera of the Krafla central volcano (Sigmundsson 2006) in northeast Iceland. The texture of our samples varies between fully glassy basalt (tuff, hyaloclastite) to highly crystalline basalt (intrusions). The smectite content varies up to 50 wt. per cent, which is more than twice as the maximum values found in previous studies [15 per cent in Waxman & Smits (1968), 25 per cent in Flóvenz *et al.* (2005) and Revil *et al.* (2017a)].

2 ELECTRICAL CONDUCTIVITY OF HYDROTHERMALLY ALTERED ROCKS

2.1 Cation exchanges in clay minerals

Smectite and chlorite are two major alteration minerals in basalts, both belonging to the phyllosilicate (sheet silicates) family. Their cation-exchange properties are, however, different. All minerals in the phyllosilicates family carry a permanent charge in the sheets, varying from 0 to 2 per Si_4O_{10} (half unit cell). Drawings of several sheet silicates are shown in Fig. 2. This charge can be compensated in the intersheet 'interfoliar' space by hydrophilic cations (Na, Ca) or hydrophobic cations (K) or by a brucitic layer (polymer of $Mg(OH)_6$) in the case of chlorite (Ferrage *et al.* 2005). Below 0.7 charges per Si_4O_{10} (smectite), weak Coulombic bondings allow the penetration of water with any cations, which in turn causes the structure to expand and allows cation exchanges. Around 0.7 charges per Si_4O_{10} (vermiculite) and beyond (illite, micas), cation exchange properties depend on the cation: hydrophilic cations will be accompanied by water and allow cation exchanges, while hydrophobic cations will be more attracted by the crystal than by water, seal the structure and prevent cation exchanges, as illustrated in Fig. 2. Most minerals having more than 0.7 charges per Si_4O_{10} are K-saturated (muscovite and illite) and therefore non-expandable. The brucitic layer in chlorite (1 charge per Si_4O_{10}) prevents any water intake or cation exchanges in the interlayer space.

Cation exchanges are key phenomena to understand the deviations from Archie's theory. The CEC of minerals is the sum of the so-called 'permanent CEC' (e.g. cation exchanges in the interlayer spaces for phyllosilicates; in the channels for zeolites) and the 'variable CEC' (cation exchanges on crystal edges). The variable CEC increases with the pH because a decrease of H^+ concentration in water causes a release of H^+ cations occupying external exchange sites. The permanent CEC is pH-independent (Lyklema 2001).

The total CEC of smectite, which includes 70–97 per cent of permanent CEC and the rest of variable CEC (Vogt & Köster 1978; Lagaly 1981), is much higher than the total CEC of non-expandable phyllosilicates (see Table 1), where only the variable CEC contributes by definition. A linear correlation between the CEC and the smectite fraction was found by Hower & Mowatt (1966) in a series of smectite–illite samples, emphasizing that cation exchanges mostly take place in smectite.

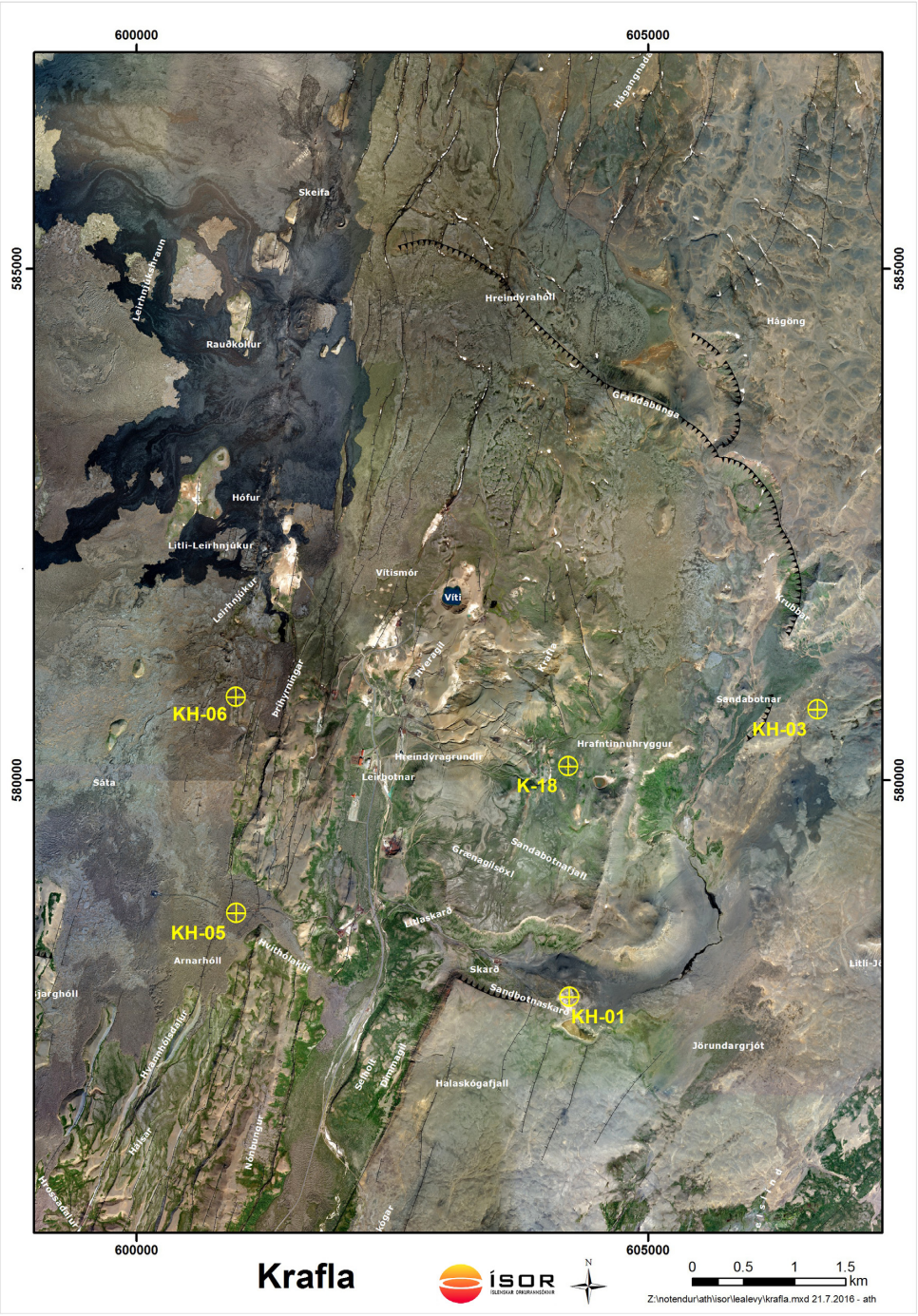

Figure 1. Aerial map of the Krafla high-temperature geothermal field. The caldera rim is marked with a black line. The four cored boreholes used in this study are marked in yellow: KH-01, KH-03, KH-05 and KH-06. A fifth borehole, K-18 is also shown for reference, as it has been used extensively for geophysical logging purposes. However, no core is available from it.

2.2 Bulk conductivity of water-saturated rocks

For a sinusoidal voltage $U(t) = U_0 \cos(\omega t + \varphi_1)$ and current $I(t) = I_0 \cos(\omega t + \varphi_2)$, the electrical impedance Z is given by $U(t) = ZI(t)$. Due to the alternating character of the voltage and current, Z is a complex number and can be written in two different ways: (1) amplitude $|Z|$ and phase θ; (2) in-phase impedance Z' and quadrature impedance Z'' (eq. 1).

$$Z = Z' + \mathrm{i}Z'' = |Z| \cos\theta + \mathrm{i}|Z| \sin\theta = |Z| e^{\mathrm{i}\theta} \quad (1)$$

The electrical conductivity is an intrinsic parameter independent of the geometry of the sample. The conductivity σ is calculated from the impedance Z, using the distance between electrodes, L, and the cross-sectional area of the cylinder, S (see the electrical cell in Fig. A1).

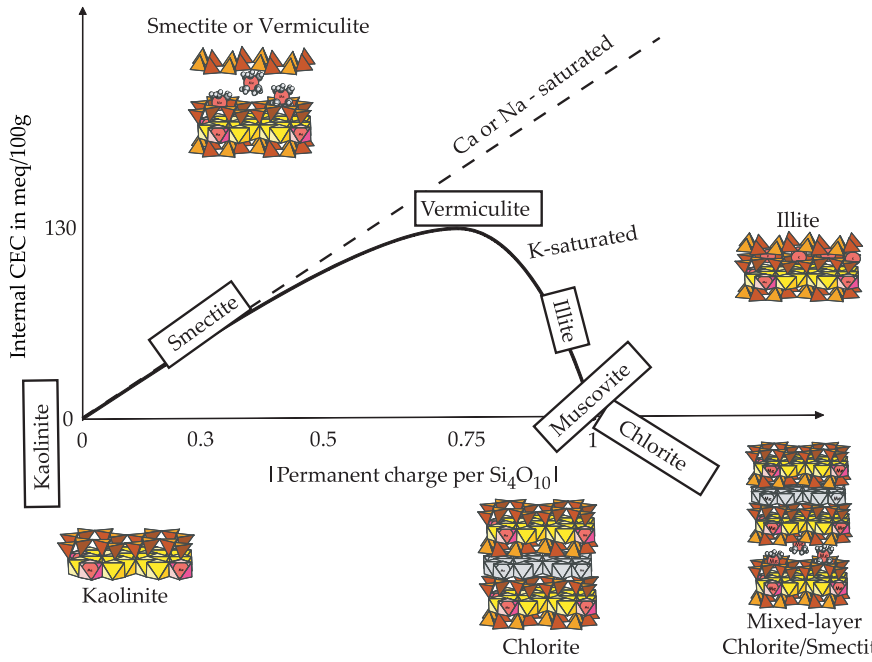

Figure 2. Schematic representation of the internal (permanent) cation exchange capacity (CEC) as a function of the structural permanent charge. Adapted from Bouchet *et al.* (2000) and Ferrage (2016).

Table 1. Examples of CEC values found in the literature (1 meq/100 g = 964.85 C kg^{-1}).

	CEC meq/100g	References
Smectite	80–120	Bouchet *et al.* (2000)
Vermiculite	100–150	Bouchet *et al.* (2000)
Chlorite	5–15	Bouchet *et al.* (2000)
Illite	25–40	Bouchet *et al.* (2000)
Kaolinite	5–15	Bouchet *et al.* (2000)
Heulandite	300	Fridriksson *et al.* (2004)
Laumontite	0.5–9	Dyer (1991)
Wairakite	0	Ames (1966)

It results in the in-phase conductivity σ' and the quadrature conductivity σ'' (eq. 2).

$$\sigma = \frac{L}{S}\frac{1}{Z} = \frac{L}{S}\left(\frac{Z'}{|Z|^2} - \mathrm{i}\frac{Z''}{|Z|^2}\right) = \sigma' + \mathrm{i}\sigma'' \tag{2}$$

We review here existing models for relating the bulk in-phase conductivity to the fluid conductivity in porous media containing clays. Assuming that the electrical current transported by counter ions associated with clays travels along the same tortuous path as current associated to ions in pore water, Waxman & Smits (1968) write the in-phase conductivity of a volume of rock (σ_{bulk}) as the sum of two parallel conductivities: free ions in pore water (σ_{w}) and ions exchanged with minerals from the solid matrix (σ_{s}).

$$\sigma_{\mathrm{bulk}} = \frac{1}{F\phi}\left(\phi\sigma_{\mathrm{w}} + (1-\phi)\sigma_{\mathrm{s}}\right) = \frac{\sigma_{\mathrm{w}}}{F} + \frac{(1-\phi)\sigma_{\mathrm{s}}}{F\phi}, \tag{3}$$

where ϕ is the volume fraction occupied by water (the porosity), $1-\phi$ the volume fraction occupied by the solid matrix and F the formation factor. The product $F\phi$ is called the 'tortuosity'. An expression of σ_{s} is given in eq. (4), considering that all exchangeable ions in the solid contribute similarly to the solid conductivity:

$$\sigma_{\mathrm{s}} = B\frac{m_{\mathrm{g}}\mathrm{CEC}}{V_{\mathrm{g}}} = B\rho_{\mathrm{g}}\mathrm{CEC}, \tag{4}$$

where B is the mobility of exchangeable ions, V_{g}, m_{g} and ρ_{g} the volume, mass and density of the solid 'grain' and CEC the charge available per unit mass of solid. By relating the CEC to the ratio Q_{v} between charge available and volume of fluid available in the rock sample (eq. 5), the Waxman & Smits formulation is obtained (eq. 6).

$$Q_{\mathrm{v}} = \rho_{\mathrm{g}}\frac{(1-\phi)}{\phi}\mathrm{CEC} \tag{5}$$

$$\sigma_{\text{bulk}} = \frac{1}{F}\,(\sigma_{\text{w}} + BQ_{\text{v}}) \tag{6}$$

This linear equation is extensively used to describe the in-phase electrical behaviour of saturated rocks (e.g. Pezard , Revil *et al.* 2017a). A deviation from this linear model was observed by Waxman & Smits (1968) for fluid conductivities lower than 5 S m^{-1}, especially for samples with high Q_{v}. It was explained by an exponentially increasing mobility of exchange ions, associated with clays, with fluid conductivity:

$$B\,(\sigma_{\text{w}}) = \beta\left(1 - \alpha e^{-\frac{\sigma_{\text{w}}}{\gamma}}\right), \tag{7}$$

where β is the maximum mobility of exchanged cations when $\sigma_{\text{w}} >> \gamma$, α is determined by the mobility of exchange cations in theoretical deionized water and γ is determined by the rate of increase of mobility from $\beta(1-\alpha)$ to β. Measurements of Na^{+} self-diffusion coefficients (Richman & Thomas 1956) confirm that the mobility of exchange ions increases with the fluid conductivity. Based on the model from eqs (6) and (7), with α, β and γ being constant, Vinegar & Waxman (1984) developed a complex conductivity model, where the quadrature conductivity, sensitive to 'delayed' conduction phenomena, accounts for accumulation (polarization) and relaxation of electrical charges at the interface between clay and pore water. The complex conductivity model by Vinegar & Waxman (1984) was not validated for Q_{v} higher than 1 meq mL^{-1} (ratio charge to volume of fluid). They suggested that beyond this value, clay particles may be sufficiently connected to create a clay-conduction pathway, preventing any polarization to occur.

Finally, a model where the dominant conduction path shifts from the pore space to the mineral–water interface (the so-called electrical double layer 'EDL'), as salinity decreases, was suggested by Revil *et al.* (1998). In this model, the shift is responsible for the non-linear variations. This model was validated on the data set from Waxman & Smits (1968), where the smectite content reaches 15 wt. per cent but was not tested on samples with higher smectite content.

3 METHODS AND MATERIALS

Eighty-eight samples were collected from a variety of lithologies, alteration facies and depths ranging from 12 to 700 m, from four cored boreholes in the Krafla high-temperature area. The cores are cylinders with an average diameter of 4 cm. The host rock of the cores is composed of successive layers of hyaloclastite, pillow breccias, vesicular lava, basaltic intrusion and more sporadically rhyolitic intrusions (Guðmundsson 1991; Jónsson *et al.* 2003; Gautason *et al.* 2007). The alteration level varies from fully/very altered samples (mainly tuff and hyaloclastite) to almost fresh samples (silicic extrusives and basaltic dykes). Electrical and porosity measurements were made on cylindrical plugs, with average length of 30 mm and average diameter of 25 mm, taken from the core samples. The surrounding material of the cores were milled into powders (grain size <40 μm) for CEC determination and XRD mineral quantification.

As the main objective of this study is to compare mineralogical and petrophysical properties of the rock, the representativeness of powder samples is important. Although core samples are taken from homogeneous geological layers, variability of the mineral content can be expected throughout different sections of the cylindrical plugs.

3.1 Mineral quantification

A quantitative phase analysis of the X-ray diffraction (XRD) patterns was carried by the Rietveld refinement method using the BGMN software (Taut *et al.* 1998). The powders were front-loaded onto the sample holder, using a razor blade to smoothen the surface, in order to avoid preferred orientations (see Bish & Reynolds (1989)).

3.2 Cation exchange capacity

A protocol originally designed to measure the CEC on pure clay samples (Meier & Kahr 1999) using Copper-triethyletetramine(II) 'Cu-trien' was chosen to measure the CEC in this study. Kaufhold & Dohrmann (2003) suggested that the CEC of bentonites, measured by Cu-trien, is a measure of the smectite content in these bentonites. In samples containing zeolites, the CEC measurement may include a contribution from zeolites, but Meier & Kahr (1999) showed that the CEC of pure clinoptinolite is reduced from 160 meq/100 g, when measured with the classical ammonia method, to 5 meq/100 g, when measured by Cu-trien. Indeed the Cu-trien molecule is too big to fit in the channels of zeolites, as opposed to the ammonia molecule. The Cu-trien method is therefore adapted to measure the smectite content in altered volcanic samples. However, the low smectite content in our samples, compared to the two previously mentioned studies, required an adaptation of the protocol to obtain reliable CEC values. The adapted protocol developed by Lévy *et al.* (2016) was used for CEC measurements on the set of powders. The reacting solutions have a pH between 6.5 and 8.5 without using any pH buffer. This range is consistent with *in situ* pH values in most of Krafla area (Gudmundsson & Arnórsson 2002). However, little pH dependency is expected here, due to the dominant contribution of the pH-independent permanent CEC of smectite.

3.3 Porosity and density

The porosity and density were determined on saturated core samples using the 'Triple Weighting' method: the plug mass was first measured on dry samples (dried at 60 °C in an oven for 48 hr), then measured on saturated samples, and finally measured in immersed conditions. The plugs were saturated with low-salinity (about 100 μS cm^{-1}), degassed water after evacuating air-filled pores in a vacuum chamber.

3.4 Electrical conductivity

3.4.1 Experimental device

Electrical impedance was acquired over a large spectrum of frequencies (from 0.001–0.1 Hz to 1 MHz) using a Solartron 1260 impedance meter. Two different experimental set-ups were used to measure the electrical conductivity: two-electrode set-up, where the sample is sandwiched between two metallic electrodes acting as current and voltage electrodes and a four-electrode set-up [following Vinegar & Waxman (1984)], where the voltage and current electrodes are separated. In the four-electrode set-up, Nickel electrodes are used to inject the current and non-polarizable Ag/AgCl electrodes are used for voltage measurement. The contact between current electrodes and the sample is ensured by a fluid layer situated in-between (5 mm thick at each side). The fluid layer, which contains the same fluid as the sample, is responsible for an additional resistance, in series with the sample impedance. This additional resistance has been quantified as a function of fluid conductivity using several tubular samples of different lengths, similarly to the approach of Waxman & Smits (1968). Although the four-electrode set-up improves the quality of the conductivity spectra, especially below 10 kHz, where effects of electrode polarization are removed, the values at 1 kHz for both set-ups are comparable [Figs 3(a) and (b)]. Indeed, from eq. (1), it can be seen that the real part of the impedance Z' is close to its modulus when θ is low. The relative difference between Z' and $|Z|$ is less than 2 per cent when θ is less than 200 mrad, which is the maximum reached by the phase angle at 1 kHz on our samples. Therefore, we can assume that the in-phase conductivity at 1 kHz is negligibly affected by the phase and thus by polarization effects. In the following, we focus on the relationship between electrical conduction and smectite content and use only the in-phase conductivity data at 1 kHz.

3.4.2 Experimental procedure

Each core was saturated after evacuating air-filled pores in a vacuum chamber with electrolytes of different salinities, using aqueous NaCl solutions at different concentrations. After changing the salinity of the pore fluid, all the samples were kept together in the same fluid for at least one month in order to achieve rock/fluid equilibrium. Glover (2016) showed that the actual fluid conductivity in a sample can be up to 30 per cent higher than the conductivity of the soaking fluid for fluid conductivities between 0.01 and 0.1 S m^{-1}, up to 15 per cent higher for fluid conductivities between 0.1 and 1 S m^{-1}, and up to 5 per cent lower for fluid conductivities higher than 1 S m^{-1}, due to dissolution/precipitation reactions or incomplete saturation/homogenization. We use these percentages to calculate an uncertainty on the conductivity of the fluid saturating the sample.

Two groups of samples were investigated. For Group 1, three series of measurements were performed in order to test the reproducibility of the measurements and possible hysteresis, following Waxman & Smits (1968): (i) Run 1: fluid conductivity increasing from 0.02 to 11.5 S m^{-1}, (ii) Run 2: fluid conductivity decreasing from 0.5 to 0.02 S m^{-1} and (iii) Run 3: fluid conductivity increasing from 0.02 to 5.33 S m^{-1}. For Group 2, one series of measurement was performed between 0.05 and 11.1 S m^{-1}. The fluid conductivity in the Krafla geothermal system is about 0.07 S m^{-1} (Flóvenz *et al.* 2005), but covering a large range of fluid conductivities is necessary to analyse the relative influence of pore fluid and minerals on the bulk conductivity. For both groups, the data set from Run 1 is the richest and is therefore used in the rest of the study for both groups of samples (details in Table 2).

4 RESULTS

The measurements of CEC, porosity and mineralogy distribution are given in Table B1.

4.1. The relation between CEC and the smectite content

In Fig. 4, we compare the CEC using Cu-trien and the smectite content from XRD quantitative analysis using the Rietveld structure models. Due to the complexity of Rietveld refinements when several types of clays are involved (Bruno Lanson, private communication, 2017), the XRD quantification of smectite content was only made for samples without chlorite. Additional measurements allowed us to verify the absence of contribution to the CEC from other mineral phases. The contribution of heulandites in our CEC measurements was assessed by a Cu-trien back titration of the exact same heulandites samples as used by Fridriksson *et al.* (2004). The CEC measured for natural heulandite and Na-saturated heulandite are, respectively, 0.5 ± 0.2 and 1.5 ± 0.2 meq/100 g, that is 0.1–0.3 per cent of the total CEC measured by Fridriksson *et al.* (2004). Given that other families of zeolites (e.g. laumontite) do not have the ability to exchange cations in their channels at all (Dyer 1991), we conclude that the contribution of zeolites in our samples is negligible. The negligible contribution of high-temperature alteration minerals, including chlorite, to the CEC is shown in Table 3. We consider that the contribution of interstratified smectite/chlorite

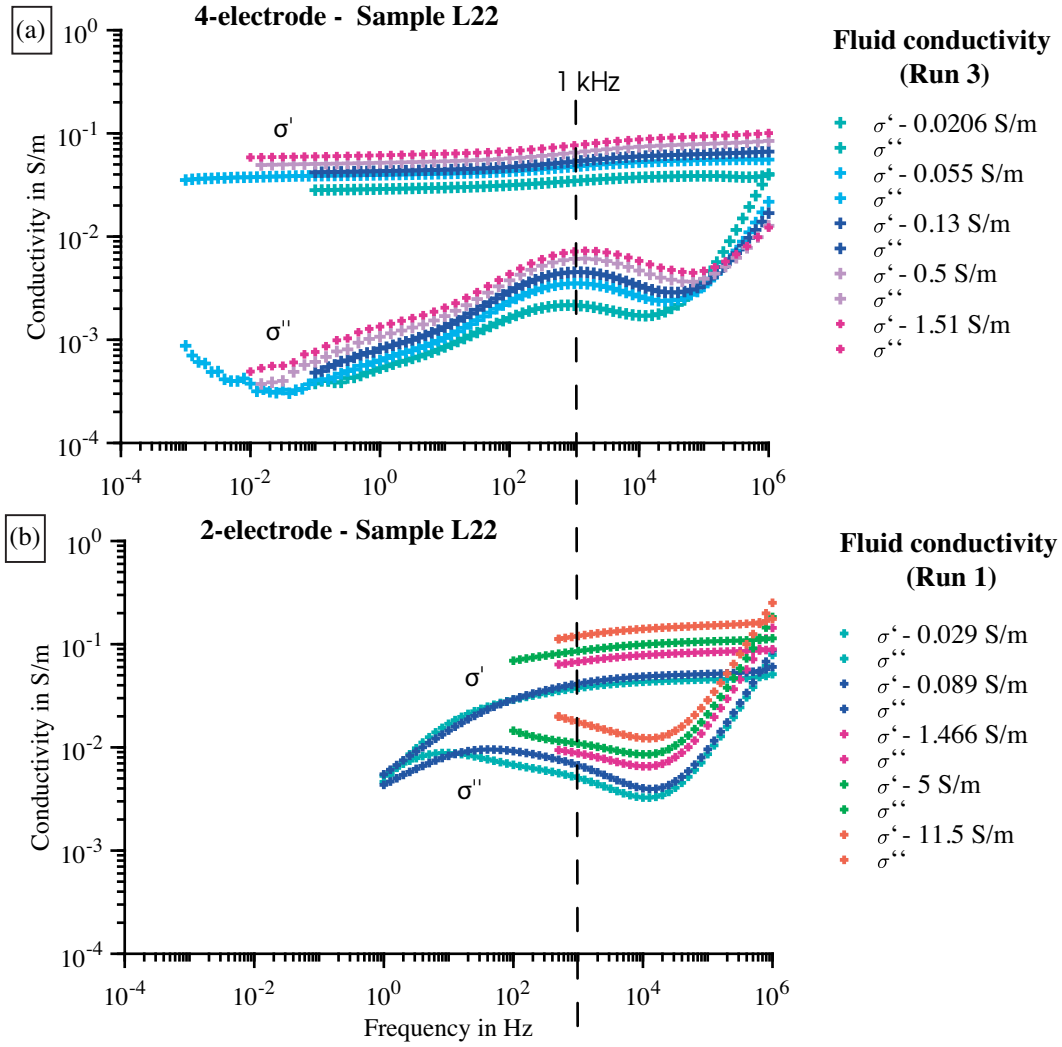

Figure 3. In-phase (σ') and quadrature (σ'') conductivity spectra of sample L22 for different fluid conductivities. (a) Four-electrode measurements and (b) two-electrode measurements. The data quality is much improved with the four-electrode set-up but the in-phase conductivities at 1 kHz measured by two and four electrodes are comparable at a given fluid conductivity. Only few measurements were available in Run 1 for the four-electrode set-up, therefore the measurements from Run 3 are shown here.

Table 2. Fluid conductivity in Run 1 for Group 1 (Samples L02–L103) and Group 2 (Samples L104–L123).

Group1 Run1		Group2 Run1	
2elec	4elec	2elec	4elec
S m^{-1}	S m^{-1}	S m^{-1}	S m^{-1}
0.02		0.05	0.05
0.0895		0.1	0.1
	0.51	0.5	0.5
1.466	1.466	1.5	1.5
5	5	4.96	4.96
11.5		11.1	11.1

minerals (e.g. corrensite) to the CEC is directly correlated to their smectite fraction, based on the results of Hower & Mowatt (1966) with smectite/illite mixed-layers series and the fact that the CEC of pure chlorite is lower than the CEC of illite. We finally assume that the CEC of other minerals present in the samples, and not mentioned in this section, is close to 0.

The linear fit shown in Fig. 4 has a slope $CEC_0 = 91$ meq/100 g and a regression coefficient $R^2 = 0.9457$. We consider that CEC_0 is the CEC of pure smectite in our samples, which is consistent with the range 80–120 meq/100 g presented in Table 1. In what follows, we use the following equation to calculate the smectite weight content in all samples:

$$\frac{CEC}{CEC_0} = \frac{m_{smectite}}{m_g}, \tag{8}$$

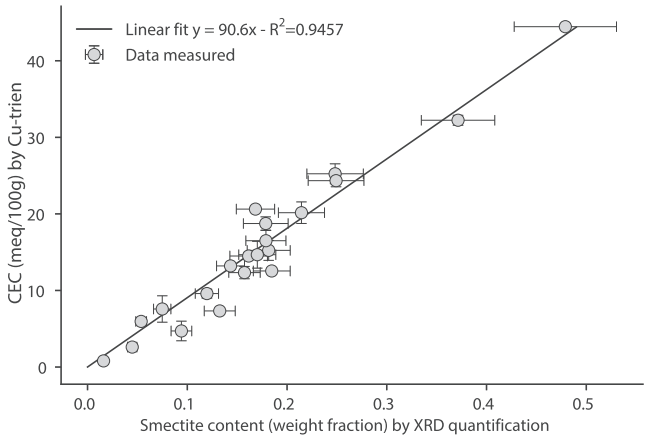

Figure 4. Correlation between CEC, measured using Cu-trien, and smectite content determined by XRD for samples with smectite as the only clay mineral. Here, the unit meq/100 g is used for comparison with reference values listed in Table 1. The SI unit is however C kg^{-1} with 1 meq/100 g = 964.85 C kg^{-1}.

Table 3. CEC, measured by Cu-trien, of samples with high-temperature alteration.

Sample	CEC in meq/100g
L49	0.2 ± 0.2
L50	0.25 ± 0.25
L47	0.35 ± 0.05
L48	0.35 ± 0.35
L46a	0.45 ± 0.35
L67a	0.45 ± 0.4

Notes: Chlorite is the only clay mineral in these samples (see also Table B1). Based on XRD mineral quantification of the chlorite phase, we calculate that the CEC of pure chlorite in the samples is lower than 6 ± 4 meq/100 g.

where m_{smectite} and m_g are the mass of smectite and the total mass of solid (the 'grain' mass) in the sample, respectively.

4.2 Analysis of electrical measurements

Electrical conductivity spectra were obtained for each sample saturated with six distinct saline solutions, with both the two-electrode and four-electrode set-ups, as shown in Fig. 3. Only real conductivity values at 1 kHz are used here and available as Supporting Information.

Reliable electrical measurements are inferred for 76 of the total 88 samples. Twelve samples show unreliable electrical measurements: L12a, L30, L35, L76, L81, L85, L104, L106, L108, L111, L112 and L117 (see four examples in Fig. A2). Their porosity ranges from 1 to 10 per cent (Table B1) and unreliable results are attributed to incomplete saturation of pores or lack of fluid/rock equilibrium (Glover 2016).

From Runs 1 to 3, the bulk conductivity increases up to 50 per cent at a given fluid conductivity for samples with high smectite content (Fig. 5). Non-repeatable measurements were also observed by Waxman & Smits (1968) until seven different saturations at high fluid conductivity were made. These authors suggested a very slow rehydration of montmorillonite after complete dehydration (following the encasing in epoxy resin) as a possible explanation. We suggest that the increased conductivity after repeated flushing with NaCl may also be due to a progressive replacement of exchange cations associated to smectite: Na^+ replaces Ca^{2+} naturally present. Since Na^+ is more mobile than Ca^{2+}, the electrical conductivity associated with smectite would increase after this replacement. However, specific measurements are needed to confirm this hypothesis.

Non-linear variations of the bulk conductivity with the fluid conductivity are observed for samples with high smectite content and are preserved from Runs 1 to 3 [Figs 5(c) and (d)], indicating that they are not due to a transient behaviour in Run 1. These non-linear variations were also observed by Waxman & Smits (1968) even after successive saturations allowing to reach a steady state. In what follows, data from Run 1 only are used.

A new model accounting for the observed non-linear behaviour and valid for our whole sample set, containing 0 to 50 wt per cent smectite, is needed. Reciprocally, our data set is useful to test existing and new models. First, the linear version of Waxman & Smits (1968) model is used to analyse the measurements of in-phase conductivity. This model (eq. 6 with B independent of the fluid conductivity), suggested by Rink & Schopper (1974), was used by Flóvenz *et al.* (1985), Pezard (1990), Flóvenz *et al.* (2005) as well as Revil *et al.* (2017a). The two constant parameters $a_0 = 1/F$ and $c_0 = BQ_v/F$ are retrieved by least-squares fitting of eq. (9) ('Linear'):

$$\sigma_{\text{bulk}} = a_0\, \sigma_w + c_0, \tag{9}$$

We observe in Fig. 6 that eq. (9) fits well samples with low smectite content, but important deviations are observed for samples with high smectite content. About 30 per cent of the samples have high smectite content and are not correctly fitted with eq. (9).

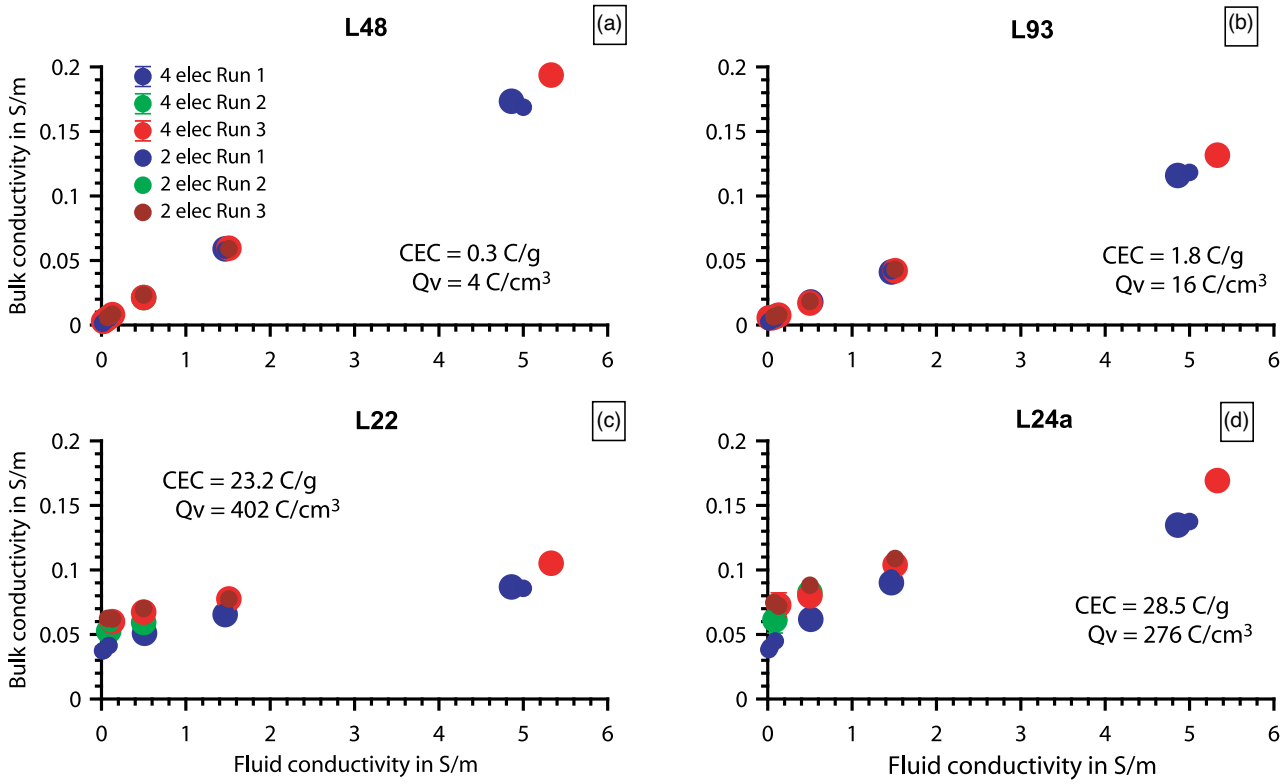

Figure 5. Results from electrical measurements at 1 kHz for four samples with increasing CEC. Panels (a), (b), (c) and (d) show results for samples L48, L93, L22 and L24a, respectively. For samples with high CEC (high smectite content), the bulk conductivity increases from one run to the following.

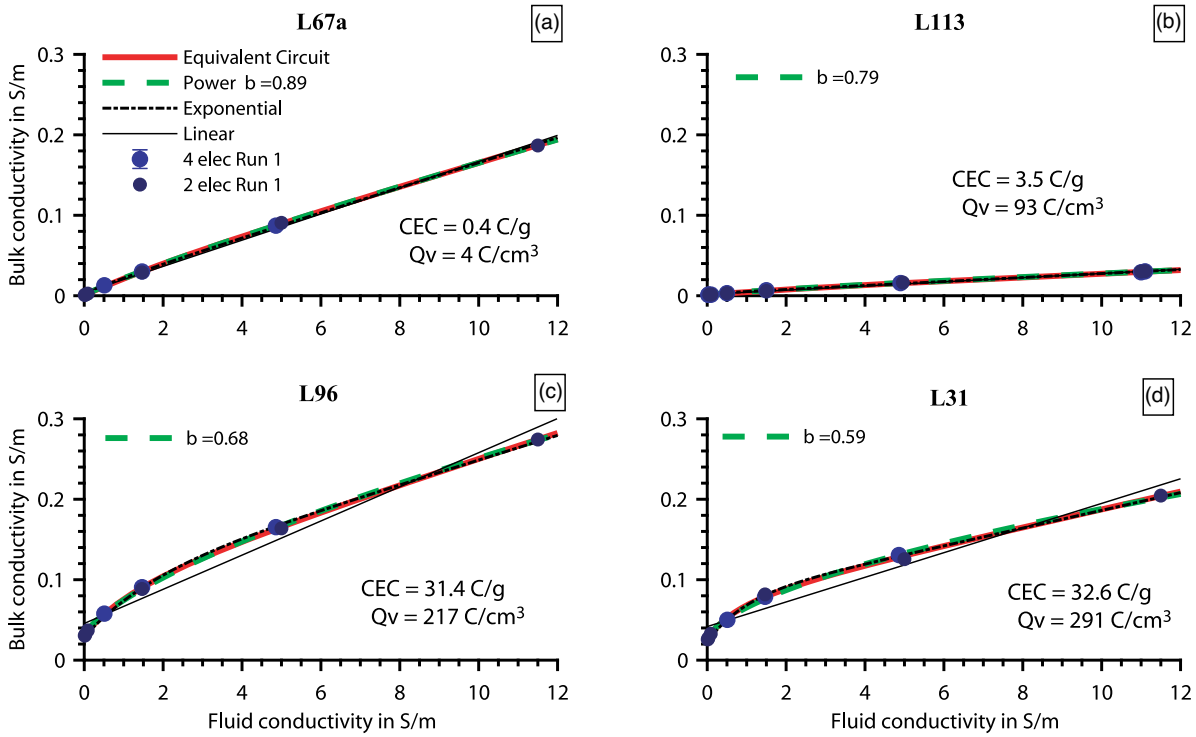

Figure 6. Observed bulk conductivity at 1 kHz versus fluid conductivity for four samples with increasing Q_v. Panels (a), (b), (c) and (d) show results for samples L67a, L113, L96 and L22, respectively. Three non-linear functions are used to fit the data, in addition to the classical linear function: Power, Exponential and Equivalent Circuit. The Power and Equivalent circuit models are overlapping for the four samples. Data shown in the figure and used for the fit are from Run 1 only (both two-electrode and four-electrode). The *in situ* fluid conductivity in Krafla is below 0.1 S m^{-1}, in the steepest part of the curves.

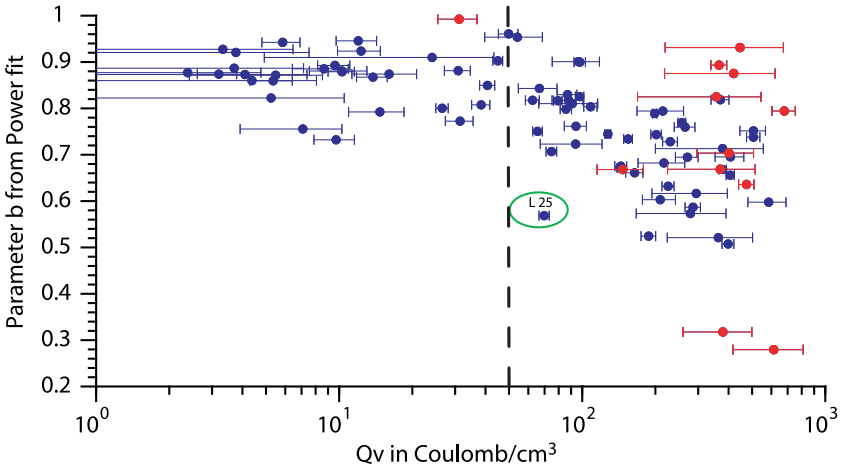

Figure 7. Comparison of the parameter b derived from the fit Power ($\sigma_{bulk} = a\sigma_w{}^b + c$) with Q_v. The dotted line marks the threshold value of Q_v where b starts to decrease significantly from 1 (non-linear behaviour). The red data points correspond to the 12 samples with unreliable electrical data.

Next, the full version of Waxman & Smits (1968) model is used (eq. 10):

$$\sigma_{bulk} = a_1\, \sigma_w + c_1 \left(1 - 0.7e^{-\frac{\sigma_w}{\gamma}}\right), \tag{10}$$

by combining eqs (6) and (7), with $a_1 = 1/F$, $c_1 = \beta Q_v$ and using α fixed to the average value 0.7. This equation ('Exponential') provides improved fit to the data (Fig. 6). However, the γ parameter does not show any dependence to the smectite content.

Finally, eq. (11) ('Power') is developed by adding an exponent to eq. (9) :

$$\sigma_{bulk} = a\sigma_w{}^b + c \tag{11}$$

This is the closest non-linear function to the linear model. The physical meaning of a and c is similar to that of a_0 and c_0. Eq. (11) allows an improved fit to the data (Fig. 6) and the b parameter depends on the smectite content: it is close to 1 for samples with low Q_v and down to 0.4 for samples with high Q_v (Fig. 7).

The fitting parameters for Linear, Exponential and Power fits are listed in Table C1. The parameters a, a_0 and a_1 follow an exponential relationship with the porosity. Similarly to the so-called 'formation factor' F, the inverse of these parameters can be approximated by the original Archie's law $F = \phi^{-m}$ (Archie 1942) or by its modified form $F = A\phi^{-m}$ (Winsauer *et al.* 1952). A discussion of these two empirical functions is given in Glover (2016). Both functions do approximate the relationship between $1/a$ and ϕ (Fig. C1). Parameters c, c_0 and c_1 increase linearly with Q_v/F, similarly to the 'EDL conduction' (more details in Fig. C2).

We also validated eq. (11) using electrical measurements on shaly sands by Waxman & Smits (1968), on altered igneous rock from Iceland by Flóvenz *et al.* (2005) and on igneous rock from Hawaii with low alteration stage by Revil *et al.* (2017a). For a given porosity, the shaly sandstones have a lower formation factor than igneous rocks [Fig. 8(a)] and for a given value of Q_v/F, the shaly sandstones have a higher conductivity 'associated to clay' than igneous rocks [Fig. 8(c)]. These two differences between shaly sandstones and igneous rocks are possibly due to a better connectivity of both pore water and clays in permeable sandstones. Given the large scattering observed, the parameter c cannot be accurately predicted with the parameter Q_v/F. The four data sets show the same dependence of b upon Q_v [Fig. 8(b)]; this confirms the role of smectite in the non-linear behaviours.

In the next section, we analyse further the dependence of the b parameter on the smectite content and build a phenomenological model which can explain the non-linear variations of bulk conductivity with fluid conductivity, as well as the dependence of this non-linearity upon the smectite content.

4.3 From a new fitting function to a phenomenological model

Fig. 7 highlights a general dependence of the b parameter on Q_v. Parameter b is close to 0.8–0.9 for $Q_v < 50$ C cm^{-3} and significantly decreases for $Q_v > 50$ C cm^{-3}. We calculate the corresponding volumetric ratio between smectite sheets and pore fluid in the rock by combining eqs (5) and (8) into eq. (12):

$$\begin{aligned} Q_v &= \frac{(1-\phi)}{\phi} \mathrm{CEC}_0\, \rho_g \frac{m_{smectite}}{m_{solid}} = \frac{(1-\phi)}{\phi} \mathrm{CEC}_0\, \rho_{smec} \frac{V_{smectite}}{V_{solid}} \\ &= \mathrm{CEC}_0\, \rho_{smec} \frac{V_{smectite}}{V_{fluid}}, \end{aligned} \tag{12}$$

where ρ_{smec} is the average density of smectite minerals and $\mathrm{CEC}_0\ \rho_{smec} = 202$ C cm^{-3}. This leads to a smectite/fluid ratio of $\frac{V_{smectite}}{V_{fluid}} = \frac{Q_v}{\mathrm{CEC}_0 \rho_{smec}} = 50/202 = 25$ per cent. We interpret this ratio as a threshold beyond which a conduction path across the solid becomes important

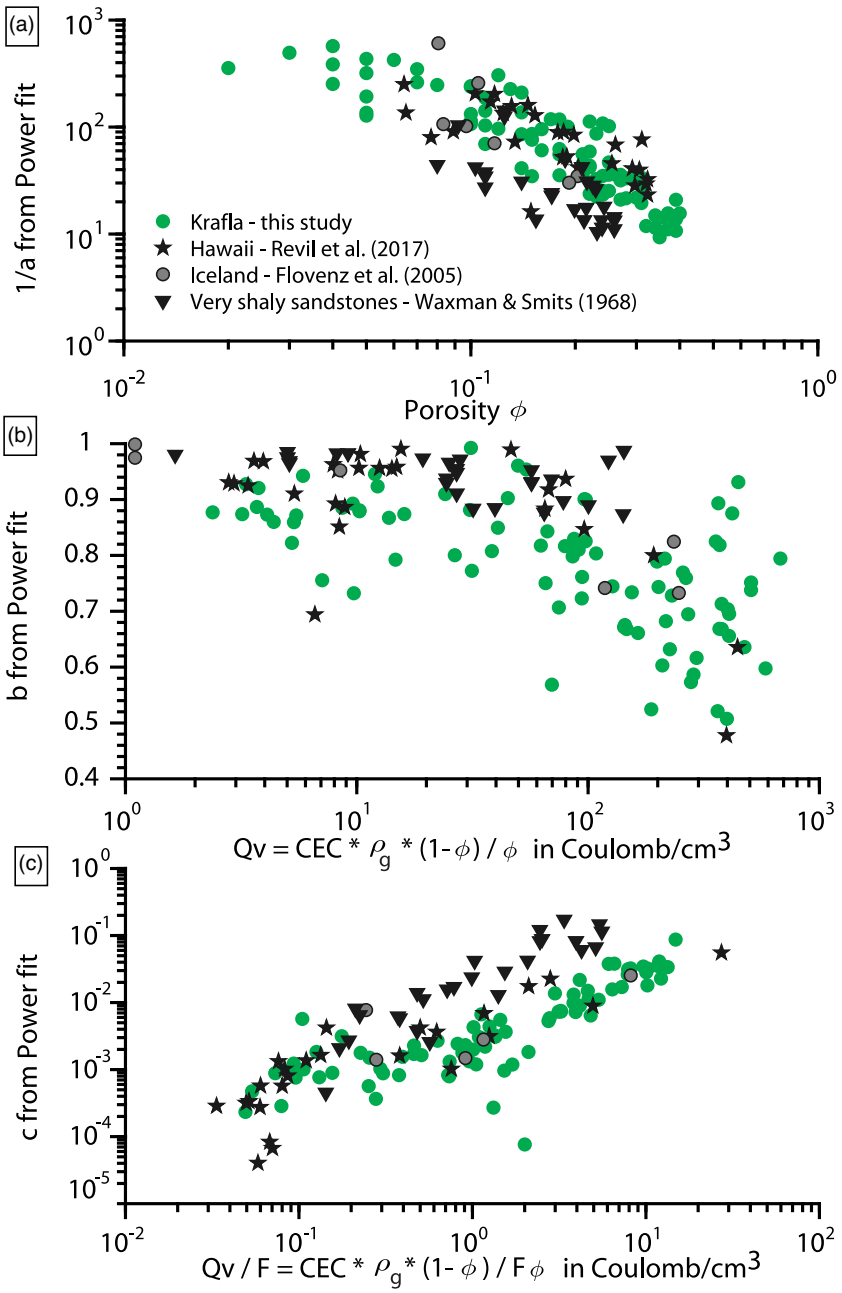

Figure 8. Comparison of the results with three other studies. The three parameters derived from the Power fit are displayed respectively in (a), (b) and (c).

compared to the conduction path across the fluid. This path only exists when a certain critical amount of smectite is present. The amount needed is a percolation threshold, similarly to the minimum porosity needed for water to percolate throughout an heterogeneous media (Gueguen & Dienes 1989). This concept extends the idea developed by Douglas (1981) and Flóvenz *et al.* (1985) that continuity of smectite exists and can permit the volume conduction of smectite sheets. According to Vinegar & Waxman (1984), eq. (5) is validated by their complex electrical measurements only for reservoir sands where the ratio between electrical charges and pore fluid Q_v remains lower than 1 meq mL^{-1} = 96 C cm^{-3}. This threshold value is close to the value determined from Fig. 7. These authors suggest that for Q_v higher than 1 meq mL^{-1}, the clay-free zones become so short that no polarization occurs and a continuous clay conduction path is shaped.

Based on these observations, we present an 'Equivalent Circuit' function, corresponding to a new phenomenological model. Using an equivalent circuit representation of electrical conduction [Fig. 9(a)], the above-mentioned conduction path corresponds to an additional branch across the solid (pathway no. 3), added in parallel to the classical circuit (see e.g. Vinegar & Waxman 1984) composed of electrolytic conduction (pathway no. 1) in parallel to EDL conduction (pathway no. 2). The bulk conductivity corresponding to the three pathways in parallel is then given by:

$$\sigma_{\text{bulk}} = \frac{\sigma_w}{F} + \sigma_{\text{EDL-interface}} + \sigma_{\text{intra-solid}} \quad (13)$$

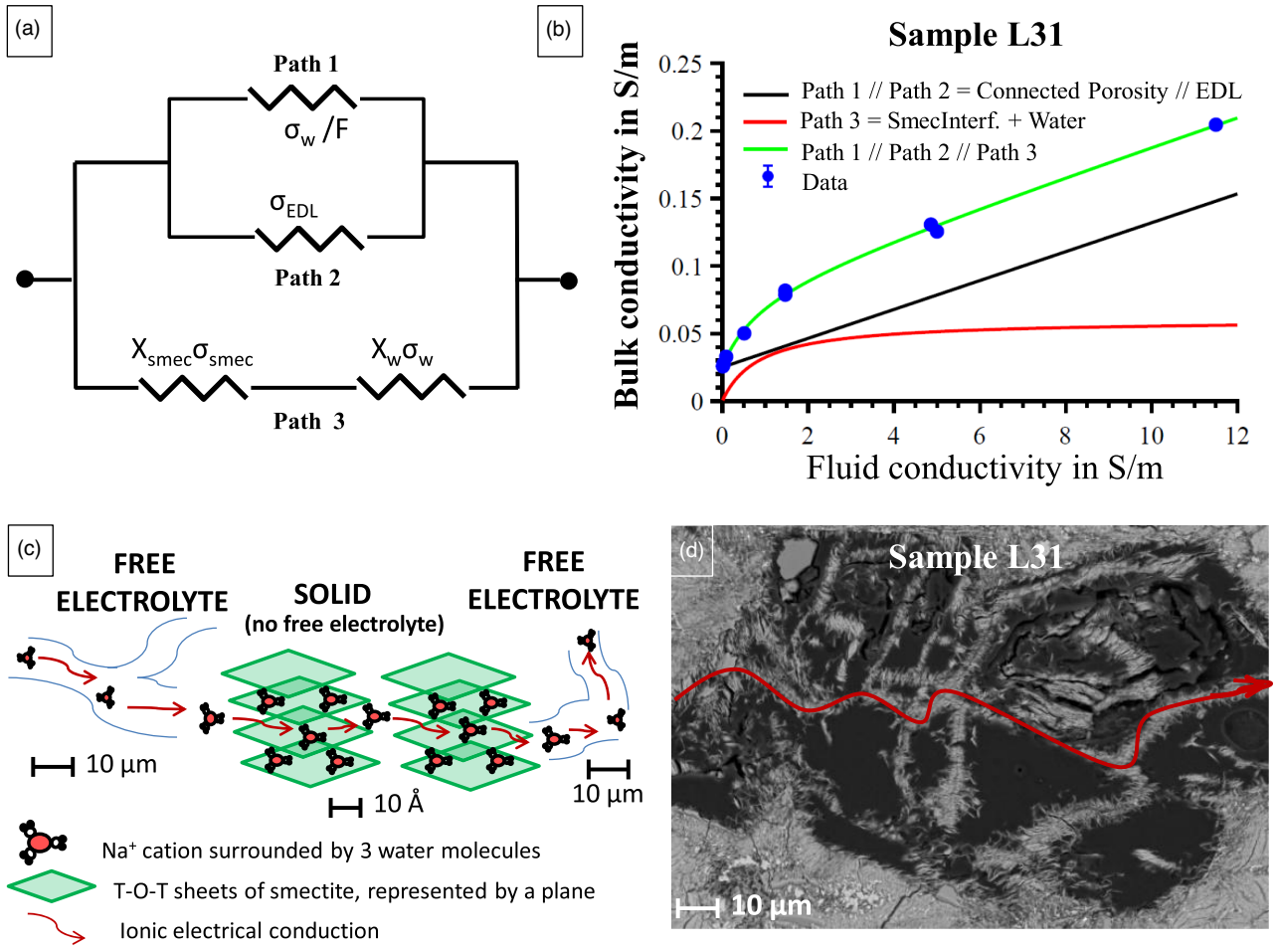

Figure 9. Conceptual model for electrical conduction in smectite-rich rock, involving an additional conduction pathway. (a) Equivalent circuit including the new conduction path as a parallel branch to the classical circuit; (b) fitted bulk conductivity, using the Equivalent Circuit model for sample L31, with best-fitting parameters: $F = 94$, $\sigma_{EDL} = 0.025$ S m^{-1}, $X_w = 7$ per cent and $\sigma_{smec} = 0.18$ S m^{-1} (the volumetric content of smectite sheets $X_{smec} = 34$ per cent is used, based on CEC and porosity measurements). The decomposition of the fitted conductivity into its linear component (fluid in the connected porosity, in parallel to EDL—black linear curve) and its non-linear component (smectite interfoliar spaces, in series with water outside the connected porosity—red non-linear curve) is also given; (c) schematic view of ionic conduction through interfoliar spaces of smectite and (d) SEM image of 'connected smectite' in the sample L31. The red line shows continuous smectite over 100 µm.

The conduction path across the solid need not to be continuous throughout the whole sample: provided that charge carriers are ions, this conduction path can be bridged by electrolytic conduction. The intra-solid conductivity, represented by solid and electrolyte in series, increases non-linearly with the electrolytic conductivity:

$$\sigma_{\text{intra-solid}} = \frac{1}{\frac{1}{X_w \sigma_w} + \frac{1}{X_{sol}\sigma_{sol}}} \tag{14}$$

Here, X_{sol} is the fraction of solid contributing to intra-solid conduction, σ_{sol} is the intrisic conduction of the solid and X_w is the fraction of electrolyte bridging solid conduction. The quantity of water accounted in X_w is part of pathway no. 3 but not part of pathway no. 1. Indeed the cations conducting electricity in the connected porosity are already occupied by pathway no. 1 and cannot conduct electricity in the pathway no. 3. We name the parameter $F' = 1/X_w$ the formation factor of the intra-solid pathway, by analogy with the formation factor of the connected porosity (pathway no. 1).

Fig. 9(b) shows that eq. (15), which is a reformulation of eqs (13) and (14) represents well the behaviour observed in sample L31 (containing 32 wt per cent of smectite).

$$\sigma_{bulk} = a_2\,\sigma_w + b_2 + \frac{c_2\sigma_w}{1 + \frac{c_2}{d_2}\sigma_w} \tag{15}$$

Here, $a_2 = 1/F$, $b_2 = \sigma_{EDL}$, $c_2 = X_w = 1/F'$ and $d_2 = X_{sol}\sigma_{sol}$.

The bulk-fluid conductivity variations of the 76 samples with reliable electrical data were correctly fitted using eq. (15), named 'Equivalent circuit' (Fig. 6). The four fitting parameters can be found in Table C1 for the whole sample set. While a_2 follows an exponential relationship to porosity, clear correlations between b_2, c_2 and d_2 and other parameters, such as CEC, porosity and Q_v are missing.

Despite this ambiguity about new parameters, we interpret the additional conduction as occurring through connected interfoliar spaces of smectite. Indeed this intra-solid conduction must respect three characteristics: (1) the charges transferred are ions to ensure that saline water can bridge the gaps, (2) high smectite content is required because the non-linear feature depends on the smectite content of the solid phase (Fig. 7) and (3) the free electrolyte path is interrupted when the solid is encountered because two distinct conductors are in series in the model. This additional path involves ions transfer without electrolyte. It therefore differs from EDL conduction. Moreover, the increasing mobility of exchange ions with salinity introduced by Waxman & Smits (1968) in the Exponential function does not describe a dependence of the non-linear effect to the smectite content.

Cations transfer through connected interfoliar spaces of smectite particles matches the three characteristics mentioned above, as illustrated in Fig. 9(c). An example of smectite connectivity over a long distance is shown in Fig. 9(d). We therefore name the intra-solid conduction 'interfoliar conduction' in what follows. Considering now that the solid fraction contributing to solid conduction is comprised of smectite interfoliar spaces, we have $X_{\mathrm{sol}} = X_{\mathrm{smec}}$, the volume fraction of smectite in the bulk rock which is connected to either smectite or water. The same smectite particle can contribute in parallel to EDL conduction (pathway no. 2, external edges involved) and to intra-smectite conduction (pathway no. 3, interfoliar spaces involved). Pathway no. 3 includes however more smectite particles than pathway no. 2: smectite in sealed fractures, altered glass or in replacement of plagioclases can only be part of pathway no. 3. If all smectite particles are connected, $X_{\mathrm{smec}} = \frac{V_{\mathrm{smectite}}}{V_{\mathrm{tot}}} = \frac{\mathrm{CEC}\rho_{\mathrm{g}}(1-\phi)}{\mathrm{CEC}_0\rho_{\mathrm{smec}}}$. Finally, $\sigma_{\mathrm{sol}} = \sigma_{\mathrm{smec}}$ is the intrisic conductivity of smectite interfoliar spaces.

Given the shape of eq. (15), interfoliar conduction is more important than fluid conduction when $\sigma_{\mathrm{w}} < |X_{\mathrm{smec}}(F' - F)\sigma_{\mathrm{smec}}|$, if $F' < F$ (which is the case for most samples containing smectite). The values taken by this threshold vary between 0.1 and 10 S m^{-1} and increase with the smectite content. Therefore, for typical fluids found in geothermal systems, interfoliar conduction dominates in rocks presenting sufficient smectite connectivity ($F' < F$).

This phenomenological model is a step forward to understand conduction processes in rocks where both the pore fluid and smectite sheets contribute to the total conduction along different pathways.

5 DISCUSSION

5.1 Process of electrical conduction in smectite

Previous studies (Waxman & Smits 1968; Flóvenz *et al.* 2005; Revil *et al.* 2017a) emphasized that the CEC (or the Q_{v}) is a key parameter controlling the electrical conductivity of shaly sands and altered volcanic rocks, which is confirmed here. We showed that the CEC in altered volcanic rocks is mainly caused by cation exchanges associated with smectite. We explained that the CEC of smectite includes more than 70 per cent of interfoliar sites. A conduction process associated to mobile cations within interfoliar spaces was therefore considered to explain the high conductivity of smectite-rich samples, and a phenomenological model presented. This model suggests that a third pathway exists for ionic conduction, in addition to pore fluid and EDL conductions: intra-solid conduction through connected interfoliar spaces of smectite in the solid matrix. This model explains the non-linear behaviour found in smectite-rich samples and allows a better representation of experimental data than models having only pore fluid and EDL conductions. Interfoliar conduction does not involve a free electrolyte, but mobile cations hydrated by 2–3 water shells. Therefore, interfoliar conduction cannot be included in EDL models, which require a free electrolyte and only account for cations on external faces of phyllosilicates [see Lyklema (2001) and Leroy & Revil (2009)].

Given the small crystal size of phyllosilicates such as smectite and illite, the external specific surface area (SSA) of these minerals is higher than in better-crystallized minerals. According to EDL models, the high CEC, and therefore the high conductivity of clay-rich materials, is explained solely by the high external SSA of clays (see e.g. Leroy & Revil 2009; Revil *et al.* 2017b). However, since a large part of the CEC of smectite is located in the interlayer spaces (internal SSA), not on its external surface (Lagaly 1981), the CEC and external SSA of smectite are not proportional [see e.g. Diamond & Kinter (1958), Henn *et al.* (2001), Paz-Ferreiro *et al.* (2013)]. Accordingly, in the particular case of smectite-rich materials, high CEC and high electrical conductivity cannot be explained solely by a high external SSA. The interfoliar spaces (internal SSA) significantly contribute to cations transfer, which is taken into account in the phenomenological model presented here.

A behaviour of similar nature occurs for Li-ion transport in batteries, with smectite sheets being an analog to cobalt-oxide sheets (Howard *et al.* 2010). In both cases, the removal of positive charge from the interlayer space is compensated; in our case by the constant supply of cations from surrounding smectite sheets and in the case of Li-ion batteries by the loss of electrons during cobalt oxidation.

5.2 Electrical conduction in other alteration minerals

We have assumed in this study that there were only two types of contributors to conductivity: the pore fluid and smectite sheets. However, altered igneous rocks contain other minerals, which are susceptible to conduct the electrical current. We briefly discuss here the possible contributions of zeolites and pyrite.

This study does not show a clear contribution of zeolites to electrical conductivity, which is consistent with other studies, e.g. with electrical logs in hole 504B of the Ocean Drilling Project (Pezard 1990) and with laboratory results of Revil *et al.* (2002). Zeolites such as heulandite have a high CEC, as opposed to wairakite and laumontite (Table 1), although it is not accounted for in the CEC measured by

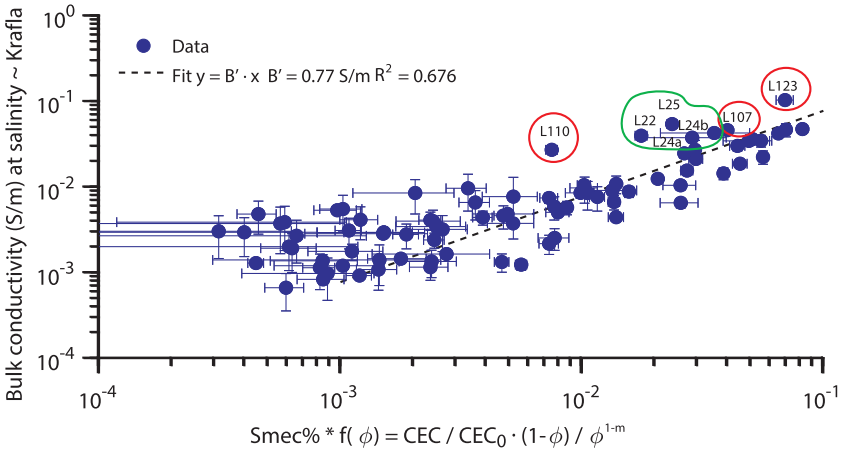

Figure 10. Simplified analysis using minimum number of parameters: conductivity at low fluid conductivity (average of two measurements between 0.03 and 0.1 S m^{-1}), CEC and porosity. Two groups of outliers are indicated: samples circled in green contain a significant amount of pyrite (9–14 wt. per cent), which may affect the electrical conductivity, while samples circled in red contain little to no sulphide or iron oxide but may contain very connected smectite particles.

Cu-trien, as explained in Section 4.1. As a consequence, heulandite-type zeolites may have high intrinsic conductivity. However, heulandite tends to form large crystals and precipitate in bulk rather than in a continuous fashion, as opposed to smectite. This may explain why a contribution of heulandite to electrical conduction is not clearly seen, but electrical measurements on pure heulandite are necessary to advance further this question.

Sample L25 deviates from the trend of Fig. 7. This can be explained by the presence of veined pyrite, which could be sufficiently connected to provide another conduction path [see e.g. Thommerel *et al.* (2002)]. It is also common to observe electrical polarization associated to the presence of pyrite (Wong 1979). Polarization is observed in samples containing a significant amount of pyrite (see Fig. 3 for sample L22) but the effect on the in-phase conductivity at 1 kHz is limited to less than 2 per cent of the total value (see Section 3.5.1.).

5.3 Upscaling laboratory results to geophysical interpretation

In this section, we address several obstacles, which need to be overcome before laboratory results can be exploited for geophysical applications, and in particular for geothermal exploration. First, we investigate to what extent the expression of bulk electrical conductivity can be simplified in order to calculate porosity and smectite content from field electrical measurements. Then, we show the limits of interpreting the mineralogy in terms of reservoir temperature. Finally, we compare the electrical resistivity values obtained in laboratory to resistivity values obtained by borehole logging in two of the boreholes.

Since electrical measurements in the field are made at the *in situ* fluid conductivity, it is impossible to use directly the functions presented in Sections 4.2 and 4.3. For fluid conductivities lower than 0.1 S m^{-1} (typical of the Krafla geothermal system), the term σ_{EDL} in eq. (13) may represent the largest part of the bulk conductivity (see e.g. Fig. 9b). Based on the semi-quantitative relationship between the parameter c and Q_v/F suggested by Waxman & Smits (1968) and shown in Fig. C2, eq. (16) presents a simplified function of smectite content and porosity describing the bulk conductivity, under the assumption that $\sigma_{\mathrm{EDL}} \gg \frac{\sigma_w}{F}$ and $\sigma_{\mathrm{EDL}} \gg \sigma_{\mathrm{intra-solid}}$.

$$\sigma_{\text{bulk for } \sigma_w = 0.03-0.1 \text{ Sm}^{-1}} \approx \sigma_{\mathrm{EDL}} \approx B' \cdot \frac{\mathrm{CEC}}{\mathrm{CEC}_0} \cdot \frac{1-\phi}{F\phi} \approx B' \cdot \mathrm{Smec\%} \cdot \frac{1-\phi}{\phi^{1-m}}, \tag{16}$$

We have three constants: $\mathrm{CEC}_0 = 91 \pm 8$ meq/100g $= 88 \pm 8$ C · g^{-1} is the average CEC of pure smectite (Fig. 4); $m = 2.3$ is the exponent of Archie's approximation $F = \phi^{-m}$ (Fig. C1) and $B' = (7.7 \pm 0.7) \cdot 10^{-1}$ S · m^{-1} is a proportionality constant (Fig. 10).

Eq. (16) can predict, to some extent, the electrical conductivity measured in Krafla (Fig. 10). Although eq. (16) cannot separate the effects of porosity and smectite content based on a single conductivity measurement, it can provide relevant information about porosity and formation factor in drill holes where electrical logs are measured and drill cuttings available for CEC measurements. Moreover, a general consistency between the quantity of alteration (using XRD quantification of the mineralogy) and porosity is observed for all samples (Fig. 11), indicating that porosity and smectite content (one of the first alteration products) are not independent parameters. A possible explanation for this consistency is the lithological control on both the porosity and alteration quantity: while hyaloclastite are very porous and glassy (thus easily altered), intrusions have very low porosity and higher crystallinity (thus harder to alter).

However, two groups of outliers are evident in Fig. 10, showing the limits of this simplified function. The samples circled in green contain 9–14wt. per cent pyrite, which is ignored in eq. (16). Electronic conduction throughout pyrite grains could be included in the term $\sigma_{\mathrm{intra-solid}}$ if a contact between electronic and ionic conductions can be ensured at the pyrite/water interface. The samples circled in red contain little to no sulphide or iron oxide. The higher conductivity observed in these samples, compared to the general trend, can be explained by

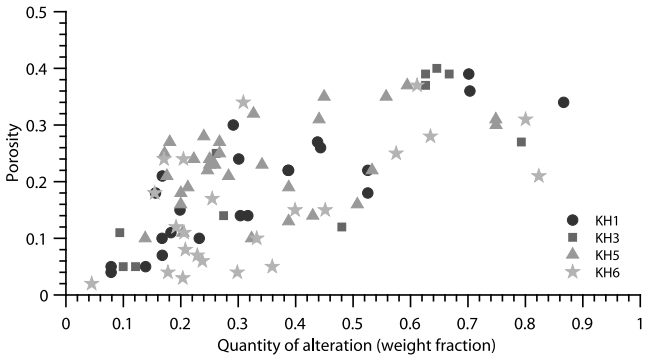

Figure 11. Comparison between quantity of alteration and porosity for all samples. The following minerals, quantified by Rietveld refinements of XRD patterns, were accounted for in the alteration: smectite, zeolites, chlorite, wairakite, epidote, amphibole, prehnite, pyrite, titanite and Fe–Ti oxides.

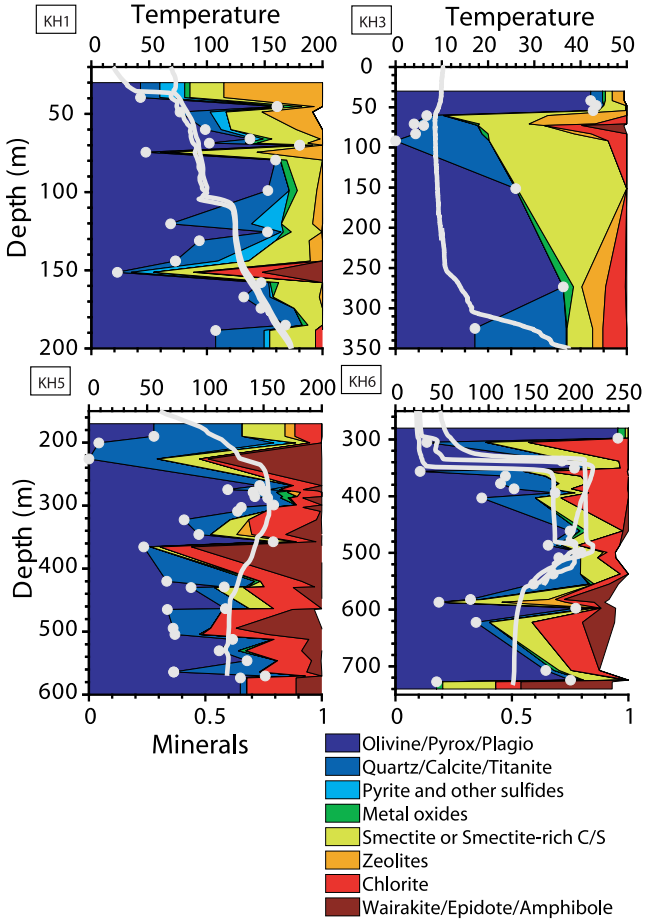

Figure 12. Comparison between mineralogy (quantified by Rietveld refinements of XRD analyses on powders) and temperature (borehole logging, white thick line) in (a) KH1, (b) KH3, (c) KH5 and (d) KH6. The filled white circles only give the depth of each analysed sample.

more connectivity of smectite particles, which is also a parameter ignored in eq. (16). A high connectivity indicates that smectite particles are rather distributed in a fracture network [see Fig. 9(d)] than isolated in voids, which is valuable information for geothermal exploration. Next steps to gain a better understanding of these effects would be to measure independently the connectivity of smectite particles and to study the conduction processes associated to the presence of veined pyrite. Finally, in the range 0.03–0.1 S m^{-1} used here, the term $\sigma_{\text{intra}-\text{solid}}$ increases rapidly with fluid conductivity for samples with high smectite content (eq. 15). In these conditions, electrical conductivity may also be sensitive to slight variations of fluid composition.

The boundary between smectite and chlorite is often used as a geotherm (see e.g. Kristmannsdóttir 1979) because thermodynamics predicts two distinct stability domains for chlorite and smectite, controlled by the temperature and at a smaller scale, the fluid/mineral chemistry (Vidal *et al.* 2012). In diagenetic smectite–chlorite series, discrete smectite is indeed found in the range of temperature predicted by thermodynamics, i.e. 80–180 °C, while chlorite dominates at higher temperatures (Beaufort *et al.* 2015). However, in active volcanic systems

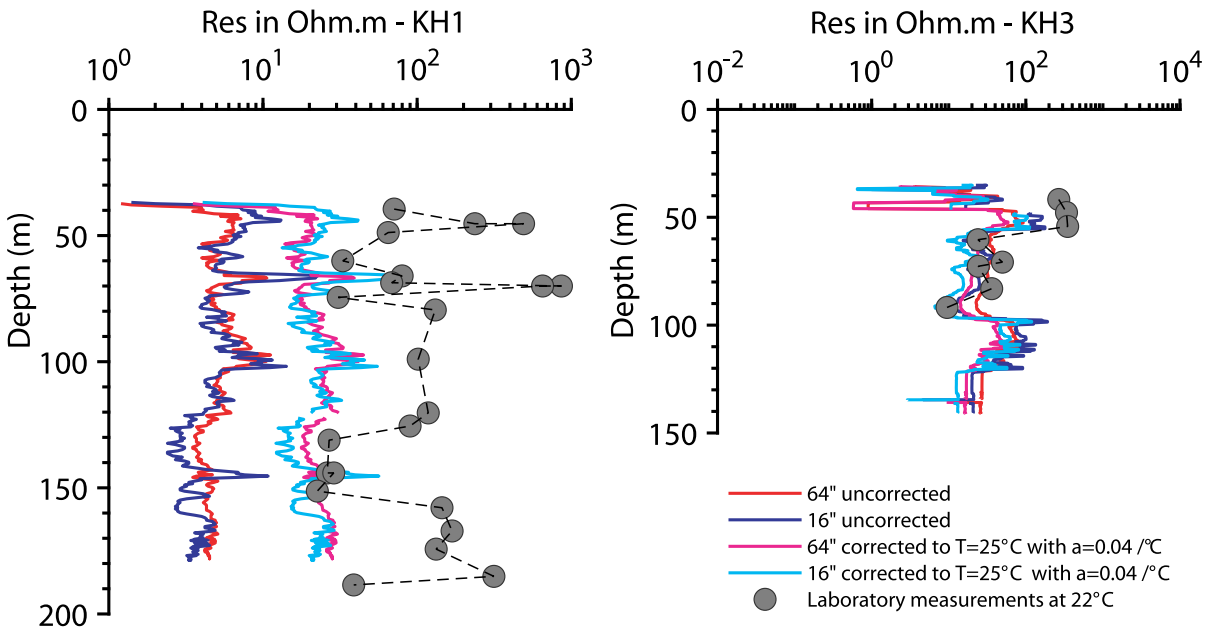

Figure 13. Comparison of resistivity data obtained in the lab with resistivity logs at two boreholes (KH1 and KH3). The raw data from the 16/64 logging tool are in dark blue and red, while the corrected data, accounting approximately for the effect of temperature difference are in light blue and pink. The grey circles are laboratory measurements, and the black hatched lines are only guiding the eye: the resistivity is probably not so straight between samples.

such as Chipilapa (El Salvador) and Milos (Greece), smectite is observed at temperature higher than 300 °C by Beaufort *et al.* (1995), while in Icelandic volcanic systems, discrete chlorite only appears above 270 °C (Schiffman & Fridleifsson 1991). These studies therefore indicate that care must be taken when inferring absolute temperature values.

Our set of samples confirms some discrepancy between theoretical equilibrium temperature based on mineral assemblages and actual temperature measured *in situ*. The temperature profiles of the four boreholes are presented in Fig. 12. The temperature in KH3 is low: mainly 10 °C and increasing to 40 °C at the bottom, while the temperature in KH6 is high: 220 °C at 500 m depth. The temperatures in KH1 and KH5 are intermediate. The distribution of minerals in these boreholes (as quantified by XRD on each sample), also shown in Fig. 12, is different from what would be expected if the system was at an equilibrium. In KH6, smectite is found at temperatures up to 220 °C. In KH5, 'high-temperature' alteration minerals (epidote, actinolite, wairakite) are found in horizons where the temperature does not exceed 150 °C. In KH3, large amounts of chlorite are found in horizons where the temperature does not exceed 10 °C: chlorite was most likely formed at an earlier stage, when the temperature was superior to 200 °C. In KH1, wairakite and chlorite are found in large amount in sample L25, whereas the two neighboring samples with similar temperature (L24—7m above and L26—6m below) do not contain any of these minerals. The distribution of minerals can, therefore, not be directly interpreted in terms of the present temperature of the system.

Resistivity values from borehole logs (using a 16/64 tool: measurements made with 16 and 64 inches spacing between electrodes) and from laboratory experiments on cores are compared on Fig. 13 for boreholes KH1 and KH3. The laboratory measurements were performed at 22 °C and the fluid conductivity used for the comparison is in the range 0.03–0.07 S m^{-1}. No borehole logs were available in KH5 and KH6.

A correction is made to account for the effects of the temperature in the borehole measurements, using the temperature presented in Fig. 12 and eq. (17).

$$\frac{\sigma\,(T)}{\sigma\,(T_0)} = 1 + \alpha_{T_0}\,(T - T_0)\,, \tag{17}$$

where T and T_0 are the actual and reference temperature, respectively, and α_{T_0} is the correction coefficient, which varies with the reference temperature T_0 and the type of medium conducting the electrical current. The two coefficients $\alpha_{T_0,\mathrm{fluid}} = 0.023\ ^\circ\mathrm{C}^{-1}$ and $\alpha_{T_0,\mathrm{clay}} = 0.04\ ^\circ\mathrm{C}^{-1}$, used by Kulenkampff *et al.* (2005), based on calculations by Revil *et al.* (1998) for $T_0 = 25$ °C, are tested here. The largest corrections, using $\alpha_{T_0,\mathrm{clay}}$, are presented in Fig. 13.

Corrections in KH3 are small and laboratory data are consistent with borehole data. In KH1 the correction of the borehole data has an important effect. Although the correction is overestimated in Fig. 13, the corrected resistivity logs do not reach the higher resistivity values found in laboratory data. Most of the relative variations are well preserved (at 50, 70 and 140 m), despite a slight depth shift. The relative variations of the laboratory resistivity are larger (higher peaks and lower lows) than those of the borehole logs. This can be explained by the averaging inherent to the logging tool, while core measurements are made more locally. The difference of an order of magnitude between the baselines of laboratory and borehole resistivity, especially at deeper levels, needs to be investigated. A systematic bias in the measurement by the 16/64 tool, for example due to conductive lead in the tool, may be a cause for this shift.

5.4 How can these results be useful for geothermal exploration?

Although alteration minerals should not be used directly as a temperature index, the presence of smectite (outside the shallow 'clay cap', where smectite is thermodynamically stable), especially connected smectite, gives valuable information about the status of the system such as boiling, recent fault opening or chemical disequilibrium. Indeed Beaufort *et al.* (1995) show a strong correlation between the presence of smectite and horizons with highly active hydrothermal circulations. This correlation was also confirmed by Patrier *et al.* (1996). In borehole KH6 at Krafla, a strong temperature gradient is observed at 350 m. An intense circulation of hydrothermal fluids at this depth is likely and could have caused the formation of connected smectite in a fracture network. This would explain the high conductivity in sample L110 (depth: 356 m), the most striking outlier in Fig. 10. Detecting the presence of connected smectite with electrical soundings is, therefore, interesting for understanding the dynamics of hydrothermal systems.

5 CONCLUSIONS

We show that:

(1) CEC measurements using Cu-trien provide a reliable measure of the weight fraction of smectite sheets in altered volcanic samples containing up to 15 different minerals, including zeolites, chlorite and corrensite. Our results extend the result of Kaufhold & Dohrmann (2003), who suggested that CEC using Cu-trien is proportional to smectite content in bentonites.

(2) Samples containing a high amount of smectite sheets show an important deviation from a linear relationship between bulk conductivity and pore fluid conductivity. A power function with three free parameters is suggested here. It approaches a linear relationship when the amount of smectite is low. A new parameter b, used as an exponent to the fluid conductivity, is close to 1 for samples where the ratio between smectite sheets and volume of fluid is less than 25 per cent and decreases for samples with higher ratio.

(3) This non-linear behaviour is interpreted to originate from a conduction pathway in addition to pathways involving pore fluid and crystal edges (EDL). A conceptual model is suggested: cations cross the solid lattice through connected interfoliar spaces of smectite sheets. A new model, corresponding to the sum of the three pathways in parallel, fits the whole dataset.

(4) The bulk conductivity at low fluid conductivity can be semi-quantitatively approximated by a function of porosity and smectite quantity, in the absence of highly connected smectite and/or pyrite. However, small variations in fluid conductivity can significantly affect the bulk conductivity if a large amount of smectite is present.

This study provides improved understanding of electrical conduction in smectite-rich rocks: electrical conduction through interfoliar spaces of smectite sheets is a physical process that can explain our observations. Further measurements can provide more details on this process, and its importance and relevance amongst other conduction processes.

ACKNOWLEDGEMENTS

LL warmly thanks Sigurður Sveinn Jónsson, Helga Margrét Helgadóttir and Bjarni Gautason for their help with identifying primary and alteration minerals and Þráinn Friðriksson for his help in understanding the thermodynamics of cation exchanges and his explanations about zeolites. Christophe Nevado, Doriane Delmas and Khaled Oubellouch are thanked for the preparation of thin sections. LL is very thankful to Bruno Lanson and Nathanaël Findling, whose help with XRD quantification of mineralogy has been invaluable. LL also thanks Alain Meunier, Eric Ferrage Emmanuel Tertre, Daniel Beaufort, Patricia Patrier and Philippe Cosenza for sharing their eclectic knowledge about cation exchanges and expandable minerals. André Revil is thanked for his explanations about the current theory of electrical conduction in rocks, as well as for suggesting the use of a four-electrode set-up for electrical measurements. Thanks also to Yves Guéguen, Jérôme Fortin and Aurélien Nicolas for their explanations about non-linear phenomena in rock physics. Nicolas Marino is thanked for his assistance in electrical conductivity measurements and Christina Guenther and Ester Inga Ingólfsdóttir for their valuable help with CEC measurements. Thanks to Nataliya Denchik and Knútur Árnason for their help in interpreting borehole resistivity logs. Finally, the authors are grateful to Landsvirkjun, and especially Ásgrímur Guðmundsson, for providing the data and cores for this work. This research was supported by the IMAGE FP7 EC project (Integrated Methods for Advanced Geothermal Exploration, grant agreement no. 608553) and by a PhD grant from Paris Sciences et Lettres. The two anonymous reviewers are sincerely thanked for their constructive comments and interesting ideas.

REFERENCES

Alt, J.C., Honnorez, J., Laverne, C. & Emmermann, R., 1986. Hydrothermal alteration of a 1 km section through the upper oceanic crust, Deep Sea Drilling Project Hole 504B: mineralogy, chemistry and evolution of seawater-basalt interactions, *J. geophys. Res.,* **91,** 10309–10335.

Ames, L.L., 1966. Cation exchange properties of wairakite and analcime, *Am. Mineral.,* **51,** 39–42.

Archie, G.E., 1942. The electrical resistivity log as an aid in determining some reservoir characteristics, *Trans. AIME,* **146,** 54–62.

Árnason, K., Eysteinsson, H. & Hersir, G.P., 2010. Joint 1D inversion of TEM and MT data and 3D inversion of MT data in the Hengill area, SW Iceland, *Geothermics,* **39,** 13–34.

Árnason, K., Karlsdóttir, R., Eysteinsson, H., Flóvenz, Ó.G. & Gudlaugsson, S.T., 2000. The resistivity structure of high-temperature geothermal systems in Iceland, in *World Geothermal Congress,* pp. 923–928, Kyushu-Tohoku, Japan.

Beaufort, D., Papapanagiotou, P., Patrier, P., Fujimoto, K. & Kasai, K., 1995. High-temperature smectites in active geothermal systems, *Proceedings*

8th Water-Rock Interaction Symposium, Vladivostok, in *Water-Rock Interaction,* edsKharaka &Chudaev. Balkema, Rotterdam, pp. 493–496.

Beaufort, D., Rigault, C., Billon, S., Billault, V., Inoue, A., Inoue, S. & Patrier, P., 2015. Chlorite and chloritization processes through mixed-layer mineral series in low-temperature geological systems—a review, *Clay Miner.,* **50,** 497–523.

Bish, D.L. & Reynolds, R.C., 1989. Sample preparation for X-ray diffraction, *Rev. Mineral. Geochem.,* **20,** 73–99.

Bouchet, A., Meunier, A. & Sardini, P., 2000. *Minéraux Argileux: Structure Cristalline, Identification Par Diffraction de Rayons X,* edn, Vol. **23,** Editions Elf Exploration.

Chester, F.M. *et al.*, 2013. Structure and composition of the Plate-Boundary slip zone for the 2011 Tohoku-Oki Earthquake, *Science,* **342,** 1208.

Diamond, S. & Kinter, E.B., 1958. Surface areas of clay minerals as derived from measurements of glycerol retention, *Clays Clay Miner.,* **5,** 334–347.

Douglas, G.R., 1981. The development of bonded discontinuities in basalt, and their significance to freeface weathering, *Jökull,* **31,** 1–9.

Dyer, A.S., 1991. The natural zeolite, laumontite, as a potential material for the treatment of aqueous nuclear waste, *J. Radioanal. Nucl. Chem., Lett.,* **154,** 265–276.

Ferrage, E., 2016. Investigation of the interlayer organization of water and ions in smectite from the combined use of diffraction experiments and molecular simulations. A review of methodology, applications, and perspectives, *Clays Clay Miner.,* **64,** 348–373.

Ferrage, E., Lanson, B., Sakharov, B.A. & Drits, V.A., 2005. Investigation of smectite hydration properties by modeling experimental X-ray diffraction patterns: Part I. Montmorillonite hydration properties, *Am. Mineral.,* **90,** 1358–1374.

Flóvenz, Ó.G., Georgsson, L.S. & Árnason, K., 1985. Resistivity structure of the upper crust in Iceland, *J. geophys. Res.,* **90,** 10136–10150.

Flóvenz, Ó.G., Hersir, G.P., Sæmundsson, K., Ármannsson, H. & Friðriksson, T., 2012. Geothermal energy exploration techniques, ed. Sayigh, A., **7,** 51–95, Oxford: Elsevier.

Flóvenz, Ó.G., Spangenberg, E., Kulenkampf, J., Arnason, K., Karlsdottir, R. & Huenges, E., 2005. The role of electrical interface conduction in geothermal exploration, in *Proceedings of the 2005 World Geothermal Congress,* Ankara, Turkey, Paper 0742, 9.

Fridriksson, T., Neuhoff, P.S., Vinani, B.E. & Bird, D.K., 2004. Experimental determination of thermodynamic properties of ion-exchange in heulandite: binary ion-exchange experiments at 55 and 85°c involving Ca2+, Sr2+, Na+ and K+, *Am. J. Sci.,* **304,** 287–332.

Gautason, B., Egilson, T., Anett, B. & Danielsen, P.E., 2007. *Krafla: Borun Tveggja Kjarnahola, KH5 og KH6, Veturinn 2006–2007,* ÍSOR, Reykjavik, Iceland.

Glover, P.W.J., 2016. Archie's law – a reappraisal, *Solid Earth,* **7,** 1157–1169.

Guðmundsson, Á., 1991. *Borun Kjarnaholu í Sandabotnaskarði,* Orkustofnun, Reykjavik, Iceland.

Gudmundsson, B.T. & Arnórsson, S., 2002. Geochemical monitoring of the Krafla and Námafjall geothermal areas, N-Iceland, *Geothermics,* **31**(2), 195–243.

Gueguen, Y. & Dienes, J., 1989. Transport properties of rocks from statistics and percolation, *Math. Geol.,* **21,** 1–13.

Henn, F., Durand, C., Cerepi, A., Brosse, E. & Giuntini, J.C., 2001. Are pore lining chlorites a cause of low resistivity in sandstones? *Soc. Core Anal.,* **34,** 1–12.

Hersir, G.P. & Björnsson, A., 1991. *Geophysical Exploration for Geothermal Resources: Principles and Application,* Orkustofnun, Reykjavik, Iceland.

Hill, H.J. & Milburn, J.D., 1956. Effect of clay and water salinity on electrochemical behavior of reservoir rocks, *Soc. Petrol. Eng,* **207,** 65–72.

Howard, W.G., Schmidt, C.L. & Scott, E.R., 2010. *Lithium-Ion Battery Google Patents,* U.S. Patent number 7,662,509, 16. Feb. 2010.

Hower, J. & Mowatt, T.C., 1966. The mineralogy of illites and mixed-layer illite/montmorillonites, *Am. Mineral.,* **51,** 825–854.

Hyndman, R.D., Yamano, M. & Oleskevich, D.A., 1997. The seismogenic zone of subduction thrust faults, *Island Arc,* **6,** 244–260.

Jónsson, S.S., Guðmundsson, A. & Thordarson, S., 2003. *Krafla: Borun Kjarnaholu KH3 Milli Jörundar og Háganga,* ÍSOR, Reykjavik, Iceland.

Kaufhold, S. & Dohrmann, R., 2003. Beyond the methylene blue method: determination of the smectite content using the cutriene method, *Z. Angew. Geol.,* **49,** 13–17.

Kristinsdóttir, L.H., Flóvenz, Ó.G., Árnason, K., Bruhn, D., Milsch, H., Spangenberg, E. & Kulenkampff, J., 2010. Electrical conductivity and P-wave velocity in rock samples from high-temperature Icelandic geothermal fields, *Geothermics,* **39,** 94–105.

Kristmannsdóttir, H., 1975. Clay minerals formed by hydrothermal alteration of basaltic rocks in Icelandic geothermal fields, *GFF,* **97,** 289–292.

Kristmannsdóttir, H., 1979. Alteration of Basaltic Rocks by Hydrothermal-Activity at 100–300° C, *Dev. Sedimentol.,* **27,** 359–367.

Kulenkampff, J., Spangenberg, E., Flóvenz, Ó.G., Raab, S. & Huenges, E., 2005. Petrophysical parameters of rocks saturated with liquid water at high temperature geothermal reservoir conditions, in *World Geothermal Congress,* pp. 24–29, Antalya, Turkey.

Lagaly, G., 1981. Characterization of clays by organic compounds, *Clay Miner.,* **16,** 1, 1–21.

Leroy, P. & Revil, A., 2009. A mechanistic model for the spectral induced polarization of clay minerals, *J. geophys. Res.,* **114**.

Lévy, L., Flóvenz, Ó.G. & Hersir, G.P., 2016. Quantitative Impact of Hydrothermal Alteration on Electrical Resistivity, Based on Cores from Krafla, in *IMAGE Task 3.3 - Physical properties of rock at reservoir conditions,* Iceland GeoSurvey (ISOR).

Lyklema, J., 2001. *Fundamentals of Interface and Colloid Science. Volume II Solid-Liquid Interfaces,* Academic Press.

Meier, L. & Kahr, G., 1999. Determination of the cation exchange capacity (CEC) of clay minerals using the complexes of Copper(II) ion with Triethylenetetramine and Tetraethylenepentamine, *Clays Clay Miner.,* **47,** 386–388.

Meunier, A., 2005. *Clays,* Springer.

Patrier, P., Papapanagiotou, P., Beaufort, D., Traineau, H., Bril, H. & Rojas, J., 1996. Role of permeability versus temperature in the distribution of the fine (< 0.2 μm) clay fraction in the Chipilapa geothermal system (El Salvador, Central America), *J. Volc. Geotherm. Res.,* **72,** 101–120.

Paz-Ferreiro, J., da Luz, L.R.Q.P., Lado, M. & Vázquez, E.V., 2013. Specific surface area and multifractal parameters of associated nitrogen adsorption and desorption isotherms in soils from Santa Catarina, Brazil, *Vadose Zone J.,* **12**.

Pezard, P.A., 1990. Electrical properties of mid-ocean ridge basalt and implications for the structure of the upper oceanic crust in Hole 504B, *J. geophys. Res.,* **95,** 9237–9264.

Revil, A., Cathles, L.M., Losh, S. & Nunn, J.A., 1998. Electrical conductivity in shaly sands with geophysical applications, *J. geophys. Res.,* **103,** 23925–23936.

Revil, A., Hermitte, D., Spangenberg, E. & Cochemé, J.J., 2002. Electrical properties of zeolitized volcaniclastic material, *J. geophys. Res.,* **107**.

Revil, A., Le Breton, M., Niu, Q., Wallin, E., Haskins, E. & Thomas, D.M., 2017a. Induced polarization of volcanic rocks—1. Surface versus quadrature conductivity, *Geophys. J. Int.,* **208,** 826–844.

Revil, A., Murugesu, M., Prasad, M. & Le Breton, M., 2017b. Alteration of volcanic rocks: a new non-intrusive indicator based on induced polarization measurements, *J. Volc. Geotherm. Res.,* **341,** 351–362.

Richman, D. & Thomas, H.C., 1956. Self-diffusion of sodium in a cation exchange resin, *J. Phys. Chem.,* **60,** 237–239.

Rink, M. & Schopper, J.R., 1974. Interface conductivity and its implications to electric logging, in *SPWLA 15th Annual Logging Symposium,* ,Analysts, S. o. P. a. W.-L, Society of Petrophysicists and Well-Log Analysts,

Schiffman, P. & Fridleifsson, G.O., 1991. The smectite-chlorite transition in drillhole N 1–15, Nesjavellir geothermal field, Iceland: XRD, BSE and electron microprobe investigations, *J. Metamorph. Geol.,* **9,** 679–696.

Sigmundsson, F., 2006. *Iceland Geodynamics: Crustal Deformation and Divergent Plate Tectonics,* Springer Science & Business Media.

Taut, T., Kleeberg, R. & Bergmann, J., 1998. Seifert Software: the new Seifert Rietveld program BGMN and its application to quantitative phase analysis, *Mater. Struct.,* **5,** 57–66.

Thommerel, E., Valmalette, J.C., Musso, J., Villain, S., Gavarri, J.R. & Spada, D., 2002. Relations between microstructure, electrical percolation

and corrosion in metal—insulator composites, *Mater. Sci. Eng. A,* **328,** 67–79.
Vidal, O., Baldeyrou, A., Beaufort, D., Fritz, B., Geoffroy, N. & Lanson, B., 2012. Experimental study of the stability and phase relations of clays at high temperature in a thermal gradient, *Clays Clay Miner.,* **60,** 200–225.
Vinegar, H.J. & Waxman, M.H., 1984. Induced polarization of shaly sands, *Geophysics,* **49,** 1267–1287.
Vogt, K. & Köster, H.M., 1978. Zur mineralogie, kristallchemie und geochemie einiger montmorillonite aus bentoniten, *Clay Miner.,* **13,** 25–43.
Walker, G.P.L., 1960. Zeolite zones and dike distribution in relation to the structure of the basalts of eastern Iceland, *J. Geol.,* **68,** 515–528.
Waxman, M.H. & Smits, L.J.M., 1968. Electrical conductivities in oil-bearing shaly sands, *Soc. Pet. Eng. J.,* **8,** 107–122.
Waxman, M.H. & Thomas, E.C., 1974. Electrical conductivities in Shaly Sands-I. The relation between hydrocarbon saturation and resistivity index; II. The temperature coefficient of electrical conductivity, *J. Petrol. Tech.,* **26,** 213–225.
Winsauer, W.O., Shearin, H.M., Jr, Masson, P.H. & Williams, M., 1952. Resistivity of brine-saturated sands in relation to pore geometry, *AAPG Bull.,* **36,** 253–277.
Wong, J., 1979. An electrochemical model of the induced-polarization phenomenon in disseminated sulfide ores, *Geophysics,* **44,** 1245–1265.

SUPPORTING INFORMATION

Supporting information are available at *GJI* online.
SupplementaryTable_2elec.pdf
SupplementaryTable_4elec.pdf
Please note: Oxford University Press are not responsible for the content or functionality of any supporting materials supplied by the authors. Any queries (other than missing material) should be directed to the corresponding author for the paper.

APPENDIX A: ELECTRICAL IMPEDANCE MEASUREMENTS

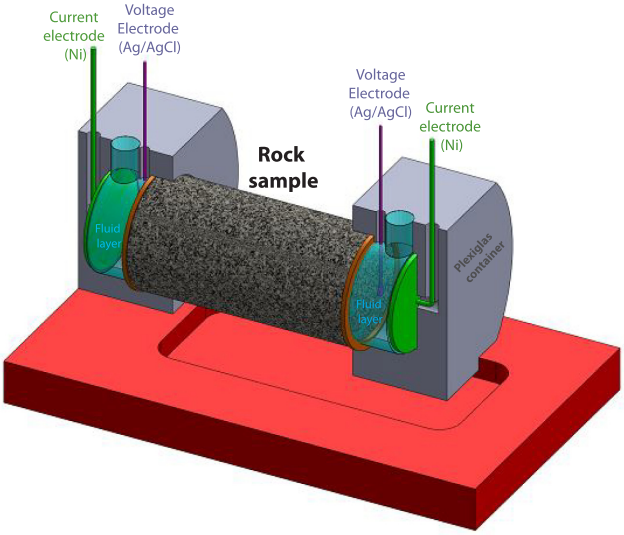

Figure A1. Schematic view of the four-electrode measurement cell. The spaces between current and voltage electrodes are filled with water at the same fluid conductivity as the fluid saturating the sample. This water layer ensures the contact between the injected current and the sample.

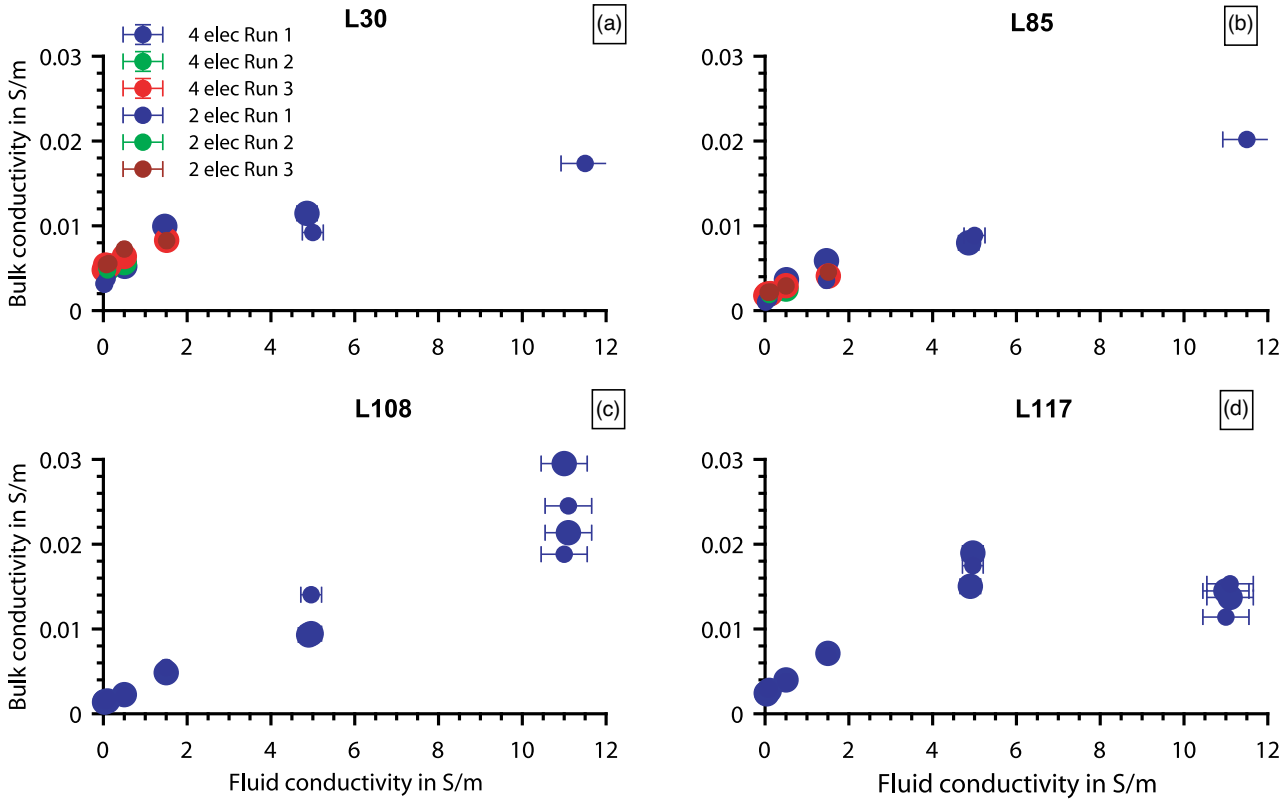

Figure A2. Four samples with unreliable electrical data (L30, L85, L108 and L117). Fitting the variations with fluid conductivity is not possible. The same applies for eight other samples: L12a, L35, L76, L81, L104, L106, L111 and L112.

APPENDIX B: PETROPHYSICS AND MINERALOGY DATA

Table B1. Key parameters for samples: CEC, along with its uncertainty (Unc CEC), porosity, Q_v and mineralogy distribution. Poro = porosity; Plg = plagioclases; Ol = olivine; Pyx = pyroxènes; Smec = Smectite (also includes corrensite or smectite-rich mixed-layer clay in samples where chlorite is present); Chl = chlorite (can include chlorite-rich mixed-layer clay); Zeol = zeolites (includes: heulandites, laumontite and other zeolites); Wai = wairakite; Amp = amphiboles; ep = epidote; Pre = prehnite; Pyr = pyrite (includes other sulphides); Fe-ox = iron oxides (includes titano-magnetite, ilmenite and hematite); Tit = titanite; Qtz = quartz; Clc = calcite.

ID	CEC	Unc CEC	Poro	Grain density	Qv	Plg & Ol & Pyx	Smec or MLC	Chl	Zeol	Wai	Amp & Ep & Pre	Pyr	Fe-ox	Tit	Qtz & Clc
Unit	C g^{-1}	C g^{-1}	per cent	g cm^{-3}	C cm^{-3}	per cent	per cent	per cent	per cent	per cent	per cent	per cent	per cent	per cent	per cent
L02	13.75	0.71	36.0	2.7	65.6	21.3	14.7	0.0	42.6	0.0	0.0	10.7	2.3	0.0	8.4
L05a	7.33	1.56	21.5	2.7	72.6	80.4	5.4	0.0	3.6	0.0	0.0	0.0	7.8	0.0	2.9
L05b	7.33	1.56	6.5	2.7	285.1	80.4	5.4	0.0	3.6	0.0	0.0	0.0	7.8	0.0	2.9
L06	30.88	11.58	26.4	2.6	225.5	38.4	15.5	0.0	21.9	0.0	0.0	6.9	0.0	0.0	13.1
L09	36.42	12.07	27.5	2.8	264.8	49.3	28.3	0.0	11.3	0.0	0.0	4.3	0.0	0.0	6.9
L10	23.16	0.96	30.2	2.9	153.6	68.6	20.9	0.0	1.0	0.0	0.0	3.5	3.8	0.0	2.2
L11	21.95	0.76	22.1	2.9	225.0	51.0	21.8	0.0	6.3	0.0	0.0	0.4	4.8	5.4	10.2
L12a	5.07	2.31	3.9	3.0	376.0	90.1	4.2	0.0	0.0	0.0	0.0	0.0	2.8	0.8	2.0
L12b	5.07	2.31	4.7	3.1	317.6	90.1	4.2	0.0	0.0	0.0	0.0	0.0	2.8	0.8	2.0
L14	34.25	3.78	39.5	2.7	140.5	23.6	37.5	0.0	28.3	0.0	0.0	4.4	0.0	0.0	6.3
L15	17.17	1.54	10.5	2.9	428.7	79.7	15.5	0.0	0.0	0.0	0.0	0.1	2.7	0.0	2.0
L16	19.88	1.25	9.8	2.8	518.2	76.4	8.4	0.0	2.5	0.0	0.0	0.0	3.5	2.4	6.9
L19	20.65	6.19	21.6	2.9	213.9	34.3	13.5	0.0	4.3	0.0	0.0	12.9	0.0	8.1	27.0
L21	25.09	6.17	14.9	2.9	411.6	76.2	13.3	0.0	0.0	0.0	0.0	0.9	3.5	2.2	3.8
L22	23.16	3.44	13.9	2.8	401.9	46.7	14.5	0.0	5.8	0.0	0.0	5.7	0.0	5.7	21.6
L24a	28.46	10.13	22.2	2.8	276.3	36.4	26.6	0.0	5.3	0.0	0.0	13.3	0.0	7.4	11.0
L24b	28.46	10.13	17.8	2.8	367.7	36.4	26.6	0.0	5.3	0.0	0.0	13.3	0.0	7.4	11.0
L25	12.78	0.24	34.4	2.8	68.4	11.3	17.2	27.5	2.3	25.9	0.0	9.7	0.0	4.0	2.0
L26	14.23	3.11	9.9	2.9	375.8	73.4	19.0	0.0	0.0	0.0	0.0	0.6	3.7	0.0	3.4
L28	33.77	4.82	13.6	2.8	605.8	65.9	20.0	0.0	1.4	0.0	0.0	1.3	0.0	7.7	3.7
L29	15.58	6.33	17.7	2.8	205.1	73.4	12.3	0.0	0.0	0.0	0.0	0.1	0.0	3.2	11.0
L30	11.34	0.24	5.0	2.8	616.3	84.0	6.3	0.0	0.0	0.0	0.0	0.0	2.5	5.1	2.2
L31	32.56	1.69	23.6	2.8	291.5	53.8	19.8	3.1	0.0	0.0	0.0	2.4	0.0	4.8	16.1
L116	9.02	1.14	11.3	2.9	209.0	84.4	3.0	0.0	5.2	0.0	0.0	0.0	1.3	0.0	5.1
L117	6.86	0.10	5.1	2.9	371.1	86.8	9.4	0.0	0.5	0.0	0.0	0.1	0.0	0.0	3.3
L118	6.88	0.49	4.9	2.9	387.9	85.4	11.6	0.0	0.6	0.0	0.0	0.0	0.0	0.0	2.4
L119	54.03	0.96	26.9	2.6	380.0	13.5	44.5	0.0	34.2	0.0	0.0	0.6	0.0	0.0	7.2
L120	14.53	0.58	39.0	2.8	62.4	8.0	21.5	13.7	28.6	0.0	0.0	0.4	2.6	0.0	25.3
L121	31.36	0.48	40.1	2.7	126.7	12.2	28.3	16.5	0.0	18.2	1.3	0.4	0.0	0.0	23.3
L122	24.90	1.24	38.7	2.8	109.8	8.6	37.2	15.4	7.4	0.0	0.0	0.0	2.7	0.0	28.8
L123	35.22	2.45	36.5	2.7	167.7	0.0	51.4	8.0	0.0	0.0	0.0	0.0	0.0	3.2	37.4
L35	20.99	0.24	12.1	2.6	398.7	52.0	47.4	0.0	0.0	0.0	0.0	0.0	0.6	0.0	0.0
L36	3.14	0.72	13.9	2.8	54.3	72.5	3.6	8.5	10.3	0.6	0.0	0.0	4.4	0.0	0.0
L37	5.45	0.14	24.8	2.8	45.5	34.3	11.1	10.3	4.5	0.0	0.0	0.4	0.0	0.0	39.5
L40	10.47	0.34	23.4	2.8	95.7	27.9	18.4	11.5	4.3	0.0	0.0	0.0	0.0	0.0	37.9
L41	4.10	0.24	11.3	2.8	91.0	4.3	6.1	4.9	0.0	0.0	0.0	9.4	0.0	0.0	75.2
L42	6.75	0.48	30.6	2.7	41.6	0.0	17.9	3.7	0.0	42.8	6.0	0.4	0.0	4.1	25.1
L43	0.63	0.14	18.3	3.0	8.5	73.3	0.0	12.2	0.0	0.0	0.0	0.7	0.0	7.2	6.7
L44	0.92	0.05	21.4	3.0	10.0	59.6	0.0	10.1	0.0	6.9	1.0	4.4	0.0	5.9	12.1
L45	0.68	0.10	27.1	2.9	5.3	75.0	0.0	11.6	0.0	1.8	0.0	0.3	0.0	4.4	6.9
L46a	0.43	0.34	24.4	3.0	4.0	70.5	0.0	9.1	5.6	0.0	0.0	0.0	4.7	5.7	4.5
L46b	0.43	0.34	23.4	3.0	4.3	70.5	0.0	9.1	5.6	0.0	0.0	0.0	4.7	5.7	4.5
L47	0.34	0.05	24.0	3.0	3.2	71.2	0.0	10.5	0.0	0.0	0.0	0.0	6.3	5.5	6.5
L48	0.34	0.34	20.5	3.0	3.9	76.8	0.0	5.5	0.9	8.1	0.0	0.0	3.2	0.0	5.7
L49	0.19	0.19	10.3	3.0	5.1	79.3	0.0	10.9	0.0	0.0	0.0	0.0	0.0	2.9	6.9
L50	0.24	0.24	23.2	3.0	2.4	65.4	0.0	11.9	0.0	8.1	0.0	0.0	1.9	4.0	8.7
L51	0.77	0.10	28.1	3.0	5.8	63.8	0.0	23.4	0.0	0.0	0.6	0.0	0.0	0.0	12.2
L52	5.11	0.29	14.4	2.8	84.3	40.9	7.9	29.1	0.0	2.1	0.0	0.2	0.0	3.7	15.9
L54	1.64	1.25	15.9	2.8	24.3	47.2	11.2	14.6	6.4	5.0	10.5	0.0	0.0	3.1	2.1
L55	2.12	0.19	16.0	2.8	30.8	79.1	9.1	8.5	0.0	0.4	2.0	0.0	0.0	0.0	0.8
L56	2.17	0.24	30.3	2.7	13.6	23.5	4.1	13.5	0.0	24.4	31.6	0.0	0.0	1.4	1.6
L57	1.16	0.48	32.0	2.9	7.1	33.4	0.0	17.6	0.0	0.0	8.7	0.0	2.4	3.9	33.9
L58	3.38	0.48	12.7	3.0	68.8	58.1	6.7	21.6	0.0	0.0	3.1	1.3	0.0	6.0	3.1
L59	3.81	0.24	21.9	2.8	38.5	43.9	12.5	21.3	0.0	0.0	12.2	0.0	0.0	7.3	2.8
L60	7.24	0.48	18.5	2.9	90.8	58.6	10.4	20.7	0.0	0.0	0.0	0.0	0.0	7.7	2.6
L61	2.75	0.63	34.7	2.9	14.9	33.7	0.0	29.9	0.0	0.0	9.3	0.0	0.0	5.7	18.2
L69	1.78	0.34	34.7	2.9	9.8	36.2	0.0	10.9	0.0	0.0	36.7	0.1	0.0	8.0	8.1
L71	5.35	0.24	37.1	2.9	26.4	36.9	0.0	28.2	1.2	0.0	23.2	0.0	0.0	6.9	3.7
L62	0.77	0.10	18.5	2.9	9.9	61.7	0.0	14.9	0.0	0.0	6.0	0.3	0.0	0.0	17.5
L73	1.54	0.39	31.0	3.0	10.3	55.9	0.0	23.9	0.0	0.0	8.6	0.0	3.2	8.3	0.0

Table B1. Continued

ID	CEC	Unc CEC	Poro	Grain density	Q_v	Plg & Ol & Pyx	Smec or MLC	Chl	Zeol	Wai	Amp & Ep & Pre	Pyr	Fe-ox	Tit	Qtz & Clc
L66	1.16	0.19	22.3	2.9	11.8	67.9	0.0	14.6	0.0	0.0	4.1	0.3	0.0	5.7	7.1
L67a	0.43	0.39	25.2	2.8	3.7	36.4	0.0	19.9	0.0	0.0	6.4	0.5	0.0	0.0	36.8
L67b	0.43	0.39	27.4	2.8	3.2	36.4	0.0	19.9	0.0	0.0	6.4	0.5	0.0	0.0	36.8
L75	0.63	0.34	24.7	2.9	5.6	62.4	0.0	7.1	0.0	0.0	16.2	0.7	2.0	6.1	5.5
L76	1.16	0.10	9.9	3.0	31.6	65.0	0.0	21.1	0.0	0.0	11.1	0.0	0.1	0.0	2.7
L106	1.00	0.22	1.9	3.0	157.1	95.5	1.3	0.0	0.0	0.0	0.0	0.0	3.2	0.0	0.0
L107	20.33	0.27	36.6	2.8	99.2	13.5	17.8	42.9	0.0	0.0	0.0	0.0	0.4	0.0	25.4
L108	9.95	0.91	5.9	2.9	452.8	71.5	19.7	3.9	0.0	0.2	0.0	0.0	0.0	0.0	4.8
L109	7.20	0.87	4.3	2.9	470.2	76.8	14.3	3.4	0.0	0.1	0.0	0.0	0.0	0.0	5.4
L110	9.12	0.51	15.4	2.8	140.3	10.6	9.9	34.4	0.0	0.5	0.0	0.3	0.0	0.0	44.3
L111	6.82	0.86	5.1	2.7	349.3	47.2	15.0	20.5	0.0	0.0	0.0	0.5	0.0	0.0	16.9
L112	6.14	0.65	4.2	2.8	400.8	45.1	12.1	17.5	0.0	0.1	0.0	0.1	0.0	0.0	25.1
L113	3.46	0.25	9.9	2.9	92.5	50.9	8.8	24.1	0.0	0.3	0.0	0.1	0.0	0.0	15.9
L114	2.54	0.38	7.3	2.9	91.6	68.6	5.9	17.0	0.0	0.0	0.0	0.0	0.0	0.0	8.6
L115	5.98	1.50	14.8	2.8	95.2	37.0	11.0	28.9	0.0	0.0	0.0	0.0	0.0	0.0	23.1
L81	20.26	0.96	8.0	2.9	676.7	75.0	15.7	0.0	0.0	0.0	2.3	0.1	2.7	0.0	4.2
L82	5.55	0.72	34.1	2.9	31.2	65.6	7.1	17.8	0.0	0.0	0.0	2.3	0.0	3.7	3.5
L85	3.86	0.29	2.8	2.9	386.2	79.6	9.6	3.6	1.6	0.0	0.0	0.0	0.0	5.6	0.0
L87	5.40	0.39	23.7	2.9	50.7	70.1	7.3	7.7	0.0	0.0	0.0	0.0	0.0	5.4	9.4
L91	8.10	0.19	11.1	2.9	185.6	67.7	17.2	3.4	0.0	0.0	0.0	0.0	0.0	0.0	11.7
L93	1.78	0.53	24.0	2.8	16.1	59.3	0.0	6.5	0.0	0.0	3.9	0.6	1.9	4.3	23.6
L96	31.36	6.27	27.9	2.7	217.9	32.2	28.1	3.8	3.0	12.7	6.6	1.1	0.0	8.3	4.3
L99	32.80	0.19	30.5	2.7	202.7	18.6	27.1	12.3	27.4	0.0	4.5	0.0	0.0	8.8	0.0
L100	0.96	0.19	18.5	2.8	11.9	77.4	2.4	0.0	0.0	1.2	5.0	0.7	1.1	5.0	6.7
L102	9.84	0.19	25.3	2.7	77.8	34.6	18.3	21.6	0.0	8.8	5.0	0.0	0.0	3.8	5.8
L103	5.93	0.14	17.0	3.0	85.9	64.6	5.2	12.0	0.0	0.0	0.0	0.0	2.2	6.0	3.5
L104	21.78	0.67	12.4	3.0	455.3	75.2	17.9	0.0	1.3	0.0	0.0	0.0	0.0	0.0	5.7
L105	24.85	0.33	21.1	2.7	255.3	17.7	22.8	10.8	0.0	31.2	7.9	0.0	2.7	7.0	0.0

APPENDIX C: FITTING PARAMETERS

Table C1. Parameters from four fits: Linear (Lin), Exponential (Exp), Power (Pow) and Equivalent Circuit (EC).

	Formation factor				EDL conduction				Other parameters			
Parameter	1/*a*0	1/*a*1	1/*a*	1/*a*2	*c*0	*c*1	*c*	*b*2	*b*	γ	*c*2	*d*2
Fit type	Lin	Exp	Pow	EC	Lin	Exp	Pow	EC	Pow	Exp	EC	EC
L2	26	30	14	33	3.7E-02	7.6E-02	1.5E-02	1.7E-02	0.8	1.1	6.6E-02	1.1E-01
L5a	114	136	56	165	9.6E-03	2.1E-02	3.2E-03	4.2E-03	0.7	1.4	1.5E-02	3.6E-02
L5b	466	503	262	548	3.2E-03	4.3E-03	2.0E-03	2.0E-03	0.8	0.1	5.1E-03	4.0E-03
L6	70	83	36	84	2.5E-02	4.3E-02	1.6E-02	1.5E-02	0.7	0.8	4.9E-02	3.2E-02
L9	72	81	34	86	4.2E-02	5.2E-02	3.1E-02	2.9E-02	0.7	0.1	1.0E-01	3.2E-02
L10	63	74	33	78	2.1E-02	4.0E-02	1.1E-02	1.1E-02	0.7	0.9	3.9E-02	3.9E-02
L11	146	167	59	207	2.0E-02	2.7E-02	1.3E-02	1.4E-02	0.6	0.1	2.3E-02	2.6E-02
L12a	838	1016	385	1009	2.3E-03	3.8E-03	1.3E-03	7.4E-04	0.7	0.5	1.8E-02	3.1E-03
L12b	491	636	193	719	3.2E-03	6.7E-03	9.7E-04	1.3E-03	0.6	1.2	6.3E-03	7.9E-03
L14	23	28	11	29	5.8E-02	1.2E-01	3.4E-02	2.8E-02	0.7	1.3	3.5E-01	1.1E-01
L15	216	239	104	270	1.1E-02	1.4E-02	7.2E-03	7.3E-03	0.7	0.1	1.4E-02	1.2E-02
L16	250	268	132	287	1.2E-02	1.4E-02	9.9E-03	9.3E-03	0.7	0.0	1.9E-02	7.4E-03
L19	117	156	44	198	1.6E-02	3.4E-02	6.4E-03	8.6E-03	0.6	1.3	2.3E-02	4.7E-02
L21	177	203	76	220	1.6E-02	2.2E-02	1.1E-02	1.0E-02	0.7	0.1	4.0E-02	1.5E-02
L22	143	162	41	215	4.6E-02	5.3E-02	3.4E-02	3.6E-02	0.5	0.0	5.0E-02	3.1E-02
L24a	69	81	24	100	5.4E-02	7.1E-02	3.5E-02	3.8E-02	0.6	0.1	7.1E-02	5.9E-02
L24b	118	141	35	167	4.6E-02	5.6E-02	3.2E-02	3.3E-02	0.5	0.1	7.7E-02	3.4E-02
L25	34	47	11	51	7.8E-02	1.5E-01	3.8E-02	4.5E-02	0.6	1.1	1.2E-01	1.3E-01
L26	177	190	114	196	9.5E-03	1.2E-02	7.3E-03	6.0E-03	0.8	0.1	3.1E-02	7.9E-03
L28	558	637	210	703	8.0E-03	9.5E-03	5.8E-03	5.4E-03	0.6	0.0	2.4E-02	5.4E-03
L29	116	134	62	138	1.3E-02	2.2E-02	7.5E-03	6.9E-03	0.7	0.7	3.0E-02	1.8E-02
L30	891	1407	128	1397	5.0E-03	8.2E-03	6.7E-07	2.8E-03	0.3	0.5	1.2E-02	5.9E-03
L31	65	91	23	94	4.2E-02	7.6E-02	2.3E-02	2.5E-02	0.6	1.0	7.0E-02	6.0E-02
L116	312	326	187	371	4.3E-03	5.5E-03	2.9E-03	3.0E-03	0.8	0.1	3.8E-03	7.4E-03
L117	966	6946	136	1999	4.7E-03	1.3E-02	1.5E-08	1.8E-03	0.3	2.1	1.0E-02	9.8E-03
L118	660	693	319	849	3.3E-03	4.0E-03	2.2E-03	2.4E-03	0.7	0.1	2.7E-03	4.9E-03
L119	75	79	32	106	5.4E-02	6.0E-02	4.1E-02	4.3E-02	0.7	0.0	3.0E-02	5.9E-02
L120	33	38	21	91	2.7E-02	6.2E-02	1.4E-02	1.8E-02	0.8	2.2	3.1E-02	5.8E-01
L121	30	38	16	41	5.8E-02	1.3E-01	3.2E-02	3.7E-02	0.7	2.3	4.5E-02	1.4E-01
L122	23	26	14	28	4.7E-02	1.0E-01	2.6E-02	2.9E-02	0.8	1.8	4.6E-02	1.3E-01
L123	27	29	11	39	1.3E-01	1.5E-01	8.7E-02	9.6E-02	0.7	0.1	8.1E-02	1.8E-01
L35	199	235	97	235	1.3E-02	1.8E-02	9.0E-03	6.7E-03	0.7	0.3	6.7E-02	1.2E-02
L36	153	158	137	157	2.1E-03	3.5E-03	1.6E-03	7.0E-04	1.0	0.3	2.4E-02	2.5E-03
L37	45	47	36	48	8.5E-03	1.6E-02	4.4E-03	3.2E-03	0.9	0.7	2.5E-02	1.8E-02
L40	111	116	87	116	8.4E-03	1.1E-02	6.7E-03	4.5E-03	0.9	0.1	5.0E-02	7.6E-03
L41	124	140	70	148	7.5E-03	1.5E-02	3.1E-03	3.0E-03	0.8	0.9	1.8E-02	1.7E-02
L42	41	43	28	45	1.3E-02	2.5E-02	5.5E-03	4.2E-03	0.8	0.8	3.9E-02	3.1E-02
L43	73	77	56	79	4.0E-03	8.8E-03	8.9E-04	5.1E-04	0.9	1.0	1.3E-02	1.4E-02
L44	61	64	45	66	5.7E-03	1.2E-02	1.8E-03	1.5E-03	0.9	1.1	1.5E-02	1.8E-02
L45	29	31	21	70	1.1E-02	2.7E-02	1.5E-03	4.4E-03	0.9	1.3	2.9E-02	6.7E-01
L46a	32	34	24	80	8.1E-03	2.0E-02	4.3E-09	2.1E-03	0.9	1.3	2.6E-02	7.2E-01
L46b	31	33	22	76	8.5E-03	2.3E-02	1.7E-10	1.5E-03	0.9	1.6	2.8E-02	6.0E-01
L47	34	36	25	39	9.2E-03	2.1E-02	1.8E-03	1.9E-03	0.9	1.1	2.1E-02	4.2E-02
L48	49	50	40	52	4.3E-03	9.6E-03	1.2E-03	1.2E-03	0.9	1.2	9.3E-03	1.6E-02
L49	164	176	107	198	2.5E-03	5.8E-03	2.3E-04	4.4E-04	0.8	1.1	6.0E-03	1.4E-02
L50	44	46	33	52	6.5E-03	1.5E-02	8.8E-04	1.8E-03	0.9	1.2	1.2E-02	5.2E-02
L51	38	39	33	39	5.9E-03	1.1E-02	3.1E-03	6.8E-04	0.9	0.5	4.6E-02	1.2E-02
L52	130	140	86	141	7.0E-03	1.1E-02	4.3E-03	2.7E-03	0.8	0.4	3.6E-02	9.7E-03
L54	119	124	96	126	2.0E-03	4.7E-03	5.7E-04	9.9E-04	0.9	1.4	3.6E-03	6.0E-03
L55	81	85	61	89	4.5E-03	9.8E-03	1.6E-03	1.6E-03	0.9	1.2	9.9E-03	1.4E-02
L56	30	32	22	80	1.2E-02	2.7E-02	2.7E-03	5.4E-03	0.9	1.4	2.9E-02	8.0E-01
L57	21	24	12	164	2.4E-02	6.7E-02	4.3E-09	3.8E-03	0.8	1.7	6.9E-02	1.0E + 00
L58	328	347	226	355	2.0E-03	3.3E-03	1.0E-03	9.4E-04	0.8	0.3	7.3E-03	3.0E-03
L59	67	74	42	86	8.5E-03	2.0E-02	2.3E-03	3.2E-03	0.8	1.4	1.4E-02	4.6E-02
L60	156	170	100	178	4.3E-03	8.2E-03	1.8E-03	1.7E-03	0.8	0.9	9.9E-03	1.0E-02
L61	17	19	10	85	2.4E-02	6.7E-02	1.0E-09	2.7E-03	0.8	1.6	7.5E-02	1.3E + 00
L69	18	20	9	517	3.2E-02	9.0E-02	2.1E-10	2.3E-03	0.7	1.7	9.6E-02	1.3E + 00
L71	25	28	16	83	1.8E-02	4.6E-02	1.2E-03	6.1E-03	0.8	1.6	4.4E-02	7.7E-01
L62	130	135	100	138	2.4E-03	4.5E-03	7.6E-04	2.7E-04	0.9	0.6	1.3E-02	5.7E-03
L73	45	47	34	53	6.1E-03	1.5E-02	8.8E-04	1.5E-03	0.9	1.4	1.2E-02	4.9E-02
L66	128	131	113	132	1.8E-03	3.0E-03	1.0E-03	2.4E-04	0.9	0.4	1.8E-02	3.2E-03
L67a	61	64	47	71	3.9E-03	1.0E-02	2.9E-04	8.5E-04	0.9	1.5	7.9E-03	3.4E-02
L67b	43	44	36	45	4.2E-03	9.1E-03	1.0E-03	4.1E-04	0.9	0.9	1.5E-02	1.5E-02
L75	139	146	102	151	2.3E-03	4.8E-03	4.7E-04	1.1E-04	0.9	0.7	9.8E-03	7.6E-03

Table C1. Continued

	Formation factor				EDL conduction				Other parameters			
Parameter	1/*a*0	1/*a*1	1/*a*	1/*a*2	*c*0	*c*1	*c*	*b*2	*b*	γ	*c*2	*d*2
L76	242	245	238	244	8.2E-04	1.2E-03	7.7E-04	3.9E-04	1.0	0.1	1.6E-02	6.0E-04
L106	540	542	356	1859	1.1E-04	1.7E-04	1.6E-09	1.4E-04	0.7	0.2	2.4E-03	1.1E-02
L107	23	28	15	83	5.8E-02	1.4E-01	3.8E-02	4.6E-02	0.8	3.3	4.5E-02	1.1E + 00
L108	501	501	424	515	1.4E-03	1.5E-03	1.2E-03	1.2E-03	0.9	0.1	9.5E-04	8.1E-04
L109	450	500	253	773	1.5E-03	3.7E-03	7.6E-05	4.4E-04	0.8	1.1	2.3E-03	1.5E-02
L110	81	133	35	114	3.4E-02	8.7E-02	2.2E-02	2.4E-02	0.7	3.6	2.5E-02	5.5E-02
L111	668	691	434	733	2.9E-03	3.4E-03	2.4E-03	2.5E-03	0.8	0.1	1.9E-03	1.9E-03
L112	780	785	571	842	1.1E-03	1.2E-03	7.9E-04	9.0E-04	0.9	0.0	7.2E-04	1.3E-03
L113	385	402	241	461	1.7E-03	2.7E-03	8.3E-04	1.1E-03	0.8	0.3	2.0E-03	6.0E-03
L114	445	448	347	480	7.5E-04	9.2E-04	3.7E-04	5.6E-04	0.9	0.1	6.9E-04	2.5E-03
L115	172	204	86	252	6.6E-03	1.5E-02	3.1E-03	3.9E-03	0.7	1.4	8.7E-03	2.7E-02
L81	401	440	247	458	6.4E-03	8.0E-03	5.3E-03	4.3E-03	0.8	0.1	2.0E-02	4.5E-03
L82	26	29	15	37	2.2E-02	5.2E-02	1.8E-03	5.3E-03	0.8	1.4	4.3E-02	1.7E-01
L85	638	665	495	658	1.6E-03	2.1E-03	1.3E-03	8.1E-04	0.9	0.1	1.8E-02	1.3E-03
L87	119	121	108	121	2.9E-03	4.3E-03	2.3E-03	8.4E-04	1.0	0.2	3.8E-02	3.4E-03
L91	458	588	142	657	3.8E-03	7.3E-03	2.7E-04	5.1E-04	0.5	0.7	1.9E-02	8.7E-03
L93	47	50	35	55	7.0E-03	1.6E-02	1.7E-03	2.2E-03	0.9	1.3	1.3E-02	4.2E-02
L96	47	66	22	65	4.6E-02	9.6E-02	2.8E-02	3.0E-02	0.7	1.7	4.9E-02	7.7E-02
L99	33	37	19	38	3.2E-02	6.0E-02	1.8E-02	1.7E-02	0.8	0.9	6.7E-02	5.6E-02
L100	141	147	118	148	6.7E-03	8.8E-03	5.7E-03	4.1E-03	0.9	0.1	3.3E-02	5.1E-03
L102	40	43	25	47	1.7E-02	3.5E-02	7.3E-03	7.7E-03	0.8	1.1	3.0E-02	5.2E-02
L103	193	213	118	234	3.1E-03	7.0E-03	8.3E-04	1.1E-03	0.8	1.4	6.0E-03	1.2E-02
L104	761	812	305	1336	4.9E-03	5.6E-03	3.7E-03	4.0E-03	0.6	0.0	2.3E-03	9.1E-03
L105	64	84	35	89	2.6E-02	6.5E-02	1.7E-02	1.9E-02	0.8	3.2	1.7E-02	7.3E-02

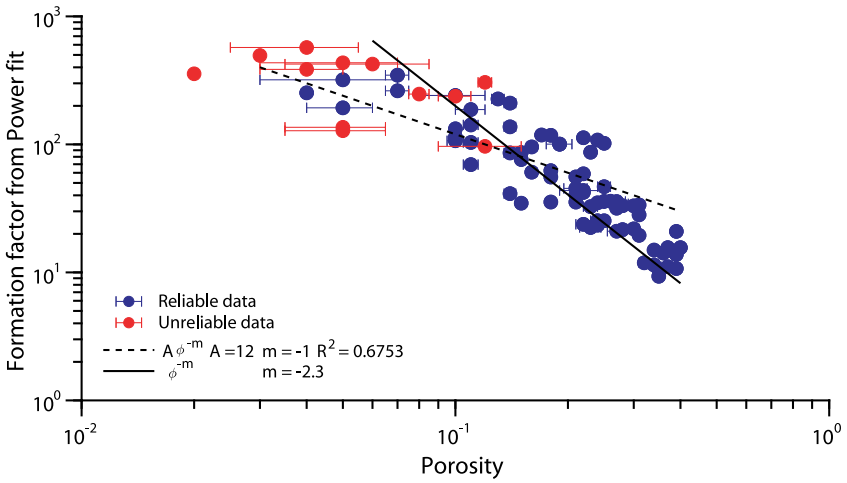

Figure C1. Formation factor (inverse of *a* from Power fit) versus porosity. Two empirical equations describe the formation factor as a function of the porosity: $F = \phi^{-m}$ (Archie 1942) and $F = A\phi^{-m}$ (Winsauer *et al.* 1952). Twelve samples with unreliable electrical data are marked in red. These samples have porosity lower than 10 per cent.

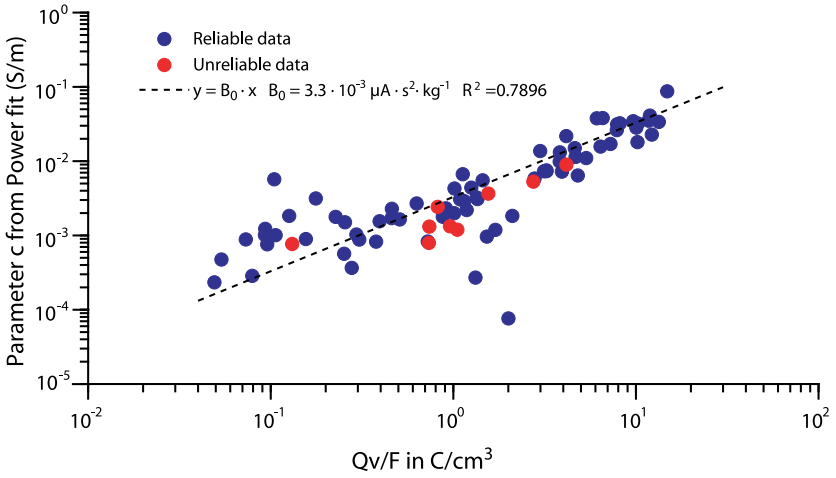

Figure C2. Parameter *c* from Power fit versus *Qv/F*. The samples with unreliable electrical data are marked in red. For clarity purposes, five of them are absent of the figure because their parameter c takes value between 10^{-10} and 10^{-5} S m^{-1} although their Q_v/F is within the range shown in the figure.

JGR Solid Earth

RESEARCH ARTICLE
10.1029/2018JB016814

Key Points:
- Pyrite, iron oxides, smectite, and pore fluid conductivity influence the electrical impedance phase angle of volcanic rocks
- Volcanic rocks with high maximum phase angle contain pyrite if the real conductivity is also high
- For a given pyrite content, the maximum phase angle decreases with increasing smectite content

Supporting Information:
- Supporting Information S1
- Table S1
- Table S2
- Data Set S1

Correspondence to:
L. Lévy,
lea.levy@ens.fr

Citation:
Lévy, L. E., Gibert, B., Sigmundsson, F., Deldicque, D., Parat, F., & Hersir, G. P. (2019). Tracking magmatic hydrogen sulfur circulations using electrical impedance: Complex electrical properties of core samples at the Krafla volcano, Iceland. *Journal of Geophysical Research: Solid Earth*, *124*. https://doi.org/10.1029/2018JB016814

Received 2 OCT 2018
Accepted 15 FEB 2019
Accepted article online 23 JUN 2018

Tracking Magmatic Hydrogen Sulfur Circulations Using Electrical Impedance: Complex Electrical Properties of Core Samples at the Krafla Volcano, Iceland

L. Lévy[1,2], B. Gibert[3], F. Sigmundsson[2], D. Deldicque[1], F. Parat[3], and G. P. Hersir[4]

[1]Laboratoire de Géologie, Ecole Normale Supérieure-PSL, CNRS, Paris, France, [2]Nordic Volcanological Center, Institute of Earth Sciences, University of Iceland, Reykjavík, Iceland, [3]CNRS, Géosciences Montpellier, Université de Montpellier, Montpellier, France, [4]ÍSOR-Iceland GeoSurvey, Reykjavík, Iceland

Abstract Interaction of H_2S escaping from magma and basaltic rocks leads to pyrite mineralization, witnessing active hydrothermal circulation. We study the possibility to track this process using geoelectrical methods. Complex conductivity spectra of 30 core samples from the Krafla volcano, Iceland, measured in the laboratory, indicate that pyrite can be discriminated from other minerals present in volcanic environments, such as iron oxides and clays. Joint evaluation of the maximum phase angle of electrical impedance and its real part at low frequency is required. The volume of metallic particles (pyrite or iron oxides) can be estimated from the maximum phase angle, but a decrease of the maximum phase angle with increased fluid conductivity or smectite volume is also observed and needs to be considered in the estimation. The laboratory observations can guide interpretation of field observations for estimation of pyrite volume in volcanic environments.

Plain Language Summary Hydrogen sulfur is a magmatic gas flowing under volcanoes. Its presence indicates ongoing geothermal activity, a clean and efficient source of energy. Upon exploitation of geothermal energy, this gas is extracted and needs to be reinjected in order to limit the environmental impacts. When hydrogen sulfur flows underground, a mineral forms by chemical transformation of the rock: pyrite. Therefore, pyrite indicates both where geothermal activity is and if hydrogen sulfur has been sequestrated upon reinjection. In order to track pyrite with geoelectrical methods, we study here the electrical signature of 30 natural samples from the Krafla volcano (Iceland): the capacity of the samples to both transfer and store electrical charges (conduction and polarization). Volcanic samples contain other minerals sensitive to electrical stimulation: iron oxides and smectite. Based on mineral quantification of pyrite, smectite, and iron oxides in the 30 samples, as well as on polarization and conduction measurements in a large range of frequency, we show that conduction at low frequency and maximum polarization are enough to discriminate pyrite from iron oxides. We also show that the volume of pyrite can be estimated from the maximum polarization but that an abundance of smectite tends to reduce this maximum, for a given pyrite volume.

1. Introduction

Hydrogen sulfur (H_2S), gas of magmatic origin, flows naturally toward the surface in volcanic areas but is also a by-product of geothermal energy exploitation, contributing to air pollution (Júlíusson et al., 2015). As basaltic rocks contain iron, pyrite (FeS_2) can easily form when H_2S-enriched fluids interact with a basaltic matrix in magmatic hydrothermal systems (Stefánsson et al., 2011). Libbey and Williams-Jones (2013) suggest that pyrite mineralization, as a witness of upflow zones, can help delineate the location of high-enthalpy geothermal reservoirs. The abundant presence of pyrite at deeper levels than the shallow discharge zone has also been observed to correlate to the presence of aquifers (Gudmundsson et al., 2010). Therefore, mapping pyrite distribution in a geothermal reservoir can constrain its current activity. Monitoring the evolution of pyrite mineralization with time may also help demonstrate the success of H_2S sequestration based on injection of waste water from geothermal power plants into basaltic rocks (Prikryl et al., 2018) and thus be valuable for the social acceptation of geothermal utilization.

Detecting underground massive metallic ore deposits and discriminating disseminated sulfides, veinlets sulfides and graphite is feasible by means of induced polarization (IP) field measurements (Börner et al., 2018;

Pelton et al., 1978; Placencia-Gómez, 2015). The reorganization of charges, at the interface between pore fluid and metallic particles (or negatively charged particles, such as clay minerals), creates local electrical "displacement" currents, which add up until a steady maximum voltage is reached. The time delay between maximum voltage and maximum current, also known as the phase angle for sinusoidal signals, is a measure of the polarization (Bücker et al., 2018; Chelidze & Gueguen, 1999; Olhoeft, 1985). Strong polarization effects are in particular associated to disseminated metallic particles (e.g., pyrite or magnetite) because of their semiconducting properties. Under an external electric field, electrons can rapidly redistribute within the metallic particle in response to the external field (e.g., Pridmore & Shuey, 1976; Shuey, 1975). This redistribution causes accumulation of ions at the interface between fluid and metallic particles. Several models have been developed to describe how ions reversibly accumulate at the interface between pore fluid and metallic particles, causing polarization. Such models use either analytical equations for simple geometries (e.g., Misra et al., 2016; Placencia-Gómez & Slater, 2016; Revil et al., 2015; Wait, 1987; Wong, 1979) or numerical finite-element solutions to equations describing the physics involved (e.g., Abdulsamad et al., 2017; Bücker et al., 2018). Some of these models successfully predict the low-frequency ($f \leq 10^4$ Hz) complex conductivity of synthetic samples containing disseminated metallic particles in an electrolyte (e.g., Abdulsamad et al., 2017; Revil et al., 2017; Wong, 1979). However, these models typically assume that metallic particles are not connected to each other, whereas the connectivity of metallic particles may cause conduction rather than polarization. Down-hole electrical logging and laboratory electrical measurements on core samples from drill holes 735B and 1105A, at the Southwest Indian Ridge, suggest that the presence of abundant (20–30%) and connected iron and titanium oxides in mid-ocean ridge gabbros can contribute to up to 80% of the measured electrical conductivity, by electronic conduction (Einaudi et al., 2005; Pezard et al., 1991).

Rock polarization is also sensitive, to a lesser extent, to the pore size, the presence of clay minerals, and the electrolyte conductivity, especially in the case of sandstones (Binley et al., 2005; Klein & Sill, 1982; Kruschwitz, 2007; Kruschwitz et al., 2010; Leroy et al., 2017; Lesmes & Frye, 2001; Revil & Skold, 2011; Slater & Sandberg, 2000; Weller & Slater, 2012; Weller et al., 2013). Similarly to connected metallic particles, connected clay minerals may also prevent polarization and cause conduction instead. Indeed, the largest IP effects associated with clay minerals in sedimentary rocks are considered to occur when clay contents are in the range 3–10%, while lesser effects are observed for higher percentages, interpreted as the onset of conduction throughout connected clay pathways (e.g., Parkhomenko, 1971; Telford et al., 1990; Vinegar & Waxman, 1984).

Magmatic hydrothermal systems differ from typical economical sulfide ore deposits in that sulfides are present in lower concentration. Moreover, the presence of iron oxides from magmatic crystallization, the high temperature of pore fluids, and the abundance of clay minerals, including the very conductive clay mineral smectite (Lévy et al., 2018), may complicate significantly the detection and quantification of sulfide mineralization. In order to provide geothermal industry with constraints for geophysical interpretations of field IP measurements, at exploration or H_2S sequestration stages, the information contained in the IP response of rocks in these environments requires a better understanding. Sulfides grain sizes in natural samples may also span a larger range than synthetic samples, which complicates the analysis of IP parameters. In order to bridge the gap between field studies and theoretical models tested on synthetic samples, we provide here an analysis of the complex electrical properties of natural samples from an active volcanic area. Our approach is to investigate if relationships between IP parameters and mineral parameters can be observed for a set of heterogeneous and very different natural volcanic rocks (wide range of iron oxides, sulfides and smectite volumes, and different mineral textures), representative of the variability found in natural volcanic environments like the Krafla volcano. Rather than using theoretical model to interpret our data, we here analyze the influence of mineralogy on two simple IP parameters, which can be retrieved both in the laboratory and in the field: the maximum phase angle (MPA) and the bulk real conductivity at 1 Hz.

2. Materials and Methods

2.1. Rock Samples

Eighty-eight core samples from four boreholes at the Krafla volcano, Iceland, were available for this study. The host rock varies from basaltic glass of hyaloclastite type to crystalline basalt of dolerite type (Gautason et al., 2007; Gudmundsson, 1991; Jónsson et al., 2003). The dominant primary minerals from magmatic crystallization are plagioclases, pyroxenes, and iron-titanium-oxides (titanomagnetite, rutile, and ilmenite).

The alteration level varies from fully altered glassy samples, where clay minerals dominate, often accompanied by zeolites, quartz, and calcite, to almost fresh crystalline samples, with an abundance of unaltered plagioclase phenocrysts.

Cylindrical plugs, with average length of 30 mm and average diameter of 25 mm, were prepared for electrical measurements and saturated under vacuum with water containing six distinct NaCl concentrations, resulting in fluid conductivities ranging from 0.02 to 11 S/m. Measurements at each fluid conductivity were carried out in average 30 days after changing the NaCl concentration. Indeed, monitoring of the bulk conductivity showed a steady value after 30 days (less than 5% relative change over 6 weeks for most samples). Therefore, we consider that the salinity inside the pore spaces is homogenized after 30 days (see Figure S2 in the supporting information). The saturating procedure and measurements of porosity, density and cation exchange capacity (CEC), as well as bulk real conductivity at all fluid conductivities, are presented for these 88 samples in Lévy et al. (2018).

Among these 88 samples, 30 samples with varying complex electrical properties were selected in this study for further analysis of the sulfides and iron-titanium-oxide minerals and comparison to the complex electrical signature. For each plug, thin sections were prepared either from one end of the plug (transverse section) or from the host core sample in the vicinity of the hole created by the plug (axial section).

2.2. Analysis of the Mineralogy

The chemistry of metallic particles was analyzed quantitatively by Electron Probe Micro-Analysis at Géosciences Montpellier and qualitatively by scanning electron microscope (SEM) at Ecole Normale Supérieure (Paris). As shown by the ternary diagram presented in Appendix B, most of the iron-titanium-oxide minerals analyzed belong to the titanomagnetite series, but a few oxides belong to the titanohematite series. Yet, these are located near the ilmenite-end rather than hematite-end. Indeed, no hematite was found in our samples. Considering a general structural formula Fe_xS_1 for sulfides, most sulfides analyzed in our samples have x in the range 0.63–0.67, corresponding to pyrite. However, sulfide with $x = 1.1$ occurs in more than half of the analyses in sample L41, corresponding to the composition of troilite, the Fe-rich end-member of the pyrite-pyrrhotite solid solution (Figure B1). For simplification, we will mostly refer to iron-titanium-oxide minerals and sulfide minerals by the terms titanomagnetite and pyrite, respectively. Our data set does not allow to distinguish the IP responses of titanomagnetite and ilmenite or those of pyrite and pyrrhotite.

The volume fraction of pyrite and titanomagnetite are estimated using SEM images of entire thin sections (width between 25 and 40 mm). These images are processed using the freeware ImageJ (Abramoff et al., 2004). The fraction of the surface covered by metallic particles is estimated by adjusting the brightness threshold to count only metallic particles. With the resolution chosen for the analysis of whole thin sections, pixels at the edges of metallic particles have a brightness between metallic and nonmetallic. This introduces an uncertainty, which was evaluated by processing figures with two different brightness thresholds. Volume fractions, derived by extrapolation from the inferred surface fractions and assuming homogeneous rock samples, are presented in Table 1. Two samples, L41 and L82, have a particularly heterogeneous two-dimensional distribution of metallic particles (Figure 1 for sample L41). Therefore, two distinct cross-sectional areas of the plugs were analyzed and reported in Table 1.

Indeed, local heterogeneity cannot be avoided although the plugs have been prepared from homogeneous layers of the boreholes. This limits the accuracy of this method, but the overall uncertainty on the volume fraction was estimated to 30% in the most extreme cases (L41 and L82). Other quantification methods, such as X-Ray computed tomography density statistics, are problematic given the variability and complexity of the background mineralogy (Clennell et al., 2010). The method chosen here was considered as the most reliable for quantifying the volume fraction of metallic particles in natural samples.

For smectite quantification, a large fraction of the original sample was crushed and mixed, so that the uncertainty stemming from possible three-dimensional heterogeneity of a core is mitigated. The smectite volume is calculated from the CEC and the dry density of each sample, following equation (1).

$$\mathrm{Smec}_{\mathrm{vol.\%}} = \frac{\mathrm{CEC}}{\mathrm{CEC}_0}\frac{\rho_{\mathrm{dry}}}{\rho_{\mathrm{smec}}} \tag{1}$$

where CEC and $\mathrm{CEC}_0 = 91$ meq/100 g are the CEC of the sample and of pure smectite, respectively, $\rho_{\mathrm{smec}} = 2.3\ \mathrm{g/cm^3}$ is the density of smectite, and ρ_{dry} is the density of the dry sample. The value for CEC_0 corresponds

Table 1
Relevant Mineralogy Information Obtained From SEM and EPMA Analyses, As Well As Petrophysical Measurements

ID	Rock type	Major	ν_{min}	ν_{max}	Smec	Min MPA	Max MPA	$\sigma_{1Hz,0.13S/m}$	Porosity
—	—	—	(vol.%)	(vol.%)	(vol.%)	(mrad)	(mrad)	(S/m)	(%)
L02	welded breccia	Pyr	4.8%	5.4%	12%	36	62	2.55E−2	36.0%
L06	bas. breccia	Pyr	2.3%	2.5%	30%	62	94	$2.35{\cdot}10^{-2}$	26.4%
L09	bas. breccia	Pyr	3.2%	3.6%	38%	36	44	5.99E−2	27.5%
L14	hyaloclastite	Pyr	4.0%	4.1%	28%	50	65	6.76E−2	39.5%
L19	dense lava	Pyr	6.3%	7.6%	25%	105	154	1.19E−2	21.6%
L22	ves. lava	Pyr	1.8%	2.1%	27%	64	93	4.50E−2	13.9%
L24a	hyaloclastite	Pyr, Pyrrh	5.4%	6.0%	31%	59	90	5.25E−2	22.2%
L24b	hyaloclastite	see L24a	see L24a	see L24a	see L24a	56	84	4.36E−2	17.8%
L25	bas. breccia	Pyr	4.4%	4.8%	12%	83	127	5.04E−2	34.4%
L31	hyaloclastite	Pyr	0.2%	0.2%	35%	9	16	7.52E−2	23.6%
L41	bas. breccia	Troil, Pyr	4.3%	5.3%	5%	111	186	7.70E−3	11.3%
L75	ves. lava	Pyr, Hayc	0.9%	0.9%	1%	15	61	2.44E−3	24.7%
L82	bas. breccia	Pyr	0.4%	1.4%	5%	13	26	2.23E−2	34.1%
L119	hyaloclastite	Pyr	0.2%	0.2%	51%	7	11	5.64E−2	26.9%
L123	hyaloclastite	Pyr, Rut	0.5%	0.5%	31%	9	18	1.04E−1	36.5%
L12a	dense lava	Ti-Mag	No analysis	No analysis	7%	51	74	2.82E−3	3.9%
L12b	dense lava	see L12b	No analysis	No analysis	7%	42	68	2.27E−3	4.7%
L21	dense lava	Mag	1.6%	1.7%	30%	20	30	2.60E−2	14.9%
L26	ves. lava	Mag, Ilm	1.1%	1.5%	18%	34	37	1.39E−2	9.9%
L30	dyke	Mag, Ilm	1.6%	2.0%	16%	23	59	7.82E−3	5.0%
L45	ves. lava	see L46a	No analysis	No analysis	1%	20	89	1.14E−2	27.1%
L46a	ves. lava	Mag, Ilm	1.4%	1.7%	0%	23	59	8.60E−3	24.4%
L46b	ves. lava	see L46a	see L46a	see L46a	see L46a	25	58	7.34E−3	23.4%
L47	ves. lava	Mag	No analysis	No analysis	0%	24	77	9.68E−3	24.0%
L48	ves. lava	Mag	1.0%	1.2%	0%	17	89	6.33E−3	20.5%
L81	dense lava	Mag	3.2%	4.0%	27%	40	84	8.55E−3	8.0%
L93	dyke	Mag	0.2%	0.4%	2%	4	28	1.08E−2	24.0%
L116	dense lava	Ti-Mag, Ilm	1.1%	1.2%	12%	29	44	3.99E−3	11.3%
L117	dense lava	Ti-Mag, Ilm	1.7%	1.9%	10%	21	66	2.83E−3	5.1%
L118	dense lava	see L117	No analysis	No analysis	10%	22	46	3.14E−3	4.9%

Note. The columns rock type and major indicate, for each sample, the type of rock and of dominant metallic minerals, respectively. Other minor metallic minerals are sometimes sporadically observed in the matrix. The columns ν_{min} and ν_{max} give the estimated volume fraction of metallic grains, using low- and high-brightness thresholds for the image analysis, respectively, except for samples L82 and L41 where the two values correspond to quantification on two different images. The smectite volume fraction is given in the next column. The estimated maximum phase angle (MPA) is shown in the next two columns. Since the MPA depends on the fluid conductivity, the two extreme values are given. The MPA are retrieved at frequencies below 1 kHz, except for samples L19 and L81 where they are retrieved at frequencies below 10 kHz. The last two columns give the in-phase conductivity at 1 Hz and 0.13 S/m and the porosity. For five samples (L24b, L12b, L45, L46b, and L118), the type of metallic mineral was not directly analyzed but inferred from the composition of neighboring samples coming from the same lithological layer and having very similar X-ray diffraction patterns. In addition, three of these samples (L24b, L12b, and L46b) come from the same original core but were prepared in an orthogonal direction as their analog (L24a, L12a, and L46a); therefore, the mineral quantification of their analog sample is assumed to be a relevant estimate. Pyr = pyrite = FeS_2; Pyrrh = pyrrhotite = $Fe_{0.8-1}S$; Troil = troilite = FeS; Hayc = haycockite = $Cu_4Fe_5S_8$; Rut = rutile = TiO_2; Mag = magnetite = $FeO{,}Fe_3O_4$; Ti-Mag = titanomagnetite = $Fe_{2-3}Ti_{0-1}O_4$; Ilm = ilmenite = $FeTiO_3$. Ves. lava = vesicular lava; bas. breccia = basaltic breccia. SEM = scanning electron microscope; EPMA = Electron Probe Micro-Analysis.

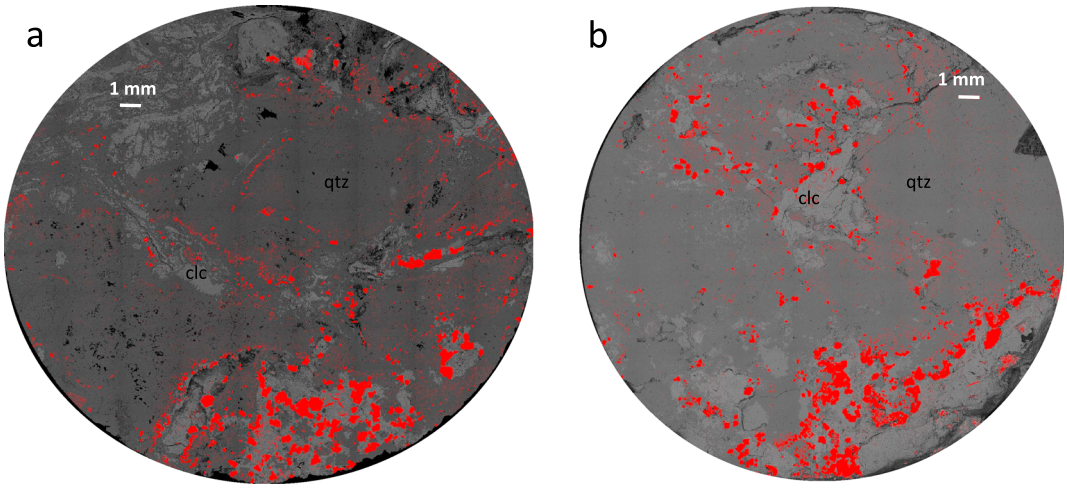

Figure 1. SEM pictures of sample L41: (a) polished thin section of one end of the cylindrical plug and (b) cross-sectional area in the middle of the cylindrical plug, which was transversally cut after all measurements were completed; the resulting half-plug was polished. These two different SEM images are used for quantification and allow to assess the extent of the three-dimensional heterogeneity. The sulfide minerals are emphasized in red, after image processing by the software ImageJ. The resulting surface fractions are 4.3% and 5.3%, respectively. SEM = scanning electron microscope.

to the average CEC of smectite in these samples, fitted to the linear trend $\mathrm{CEC} = f(\mathrm{Smec}_{\mathrm{wt.\%}})$ (Lévy et al., 2018).

2.3. Electrical Impedance

The electrical impedance was measured with a Solartron 1260 impedance-meter and a four-electrode setup, following Vinegar and Waxman (1984), where the voltage and current electrodes are separated. The sample holder is presented in Figure S1 in the supporting information. An alternating current in the frequency range 10 mHz to 1 MHz was injected between Nickel electrodes (good resistance to corrosion) and the resulting sinusoidal voltage was measured between nonpolarizable Ag/AgCl electrodes.

For a sinusoidal voltage $U(t) = U_0 \sin(\omega t + \theta_U)$ and current $I(t) = I_0 \sin(\omega t + \theta_I)$, the electrical impedance Z is given by $U(t) = ZI(t)$, where ω is the angular frequency in radians per second, t is the time in seconds, and (U_0, θ_U) and (I_0, θ_I) are the amplitudes and phase angles of the sinusoidal voltage and current, respectively. Due to the alternating character of the electrical signal, it is convenient to write I, U, and Z as complex numbers (equation (2); Agarwal & Lang, 2005; Barsoukov & Macdonald, 2018; Sumner, 1976).

$$Z(\omega) = \frac{U_0 e^{i(\omega t + \theta_U)}}{I_0 e^{i(\omega t + \theta_I)}} = |Z(\omega)| e^{i\theta(\omega)} \tag{2}$$

where Z, U, and I are in Ω, V, and A, respectively, $|Z(\omega)|$ in Ω is the modulus of the impedance and $\theta(\omega) = \theta_I - \theta_U$ in radians is the (frequency-dependent) phase angle of the impedance, as shown in Figure 2. Most of the time, the phase angle of the impedance is negative, corresponding to a delay of the voltage relative to the current.

Impedance measurements of the electrical cell filled with water (no rock sample) at different fluid conductivities, where no polarization is expected, is shown in Appendix A. The resulting phase angle varies between 1.5 and −1 mrad in the range 0.1–1000 Hz. These values, obtained over a wide range of fluid conductivities are higher than the value of ±0.3 mrad reported (only at 0.0085 S/m) by Lesmes and Frye (2001), using a similar setup and sample holder, in the same frequency range. Our uncertainty is also significantly higher than the value of ±0.1 mrad obtained with the setup presented by Zimmermann et al. (2008), most suitable for investigation of low phase angles. However, our measurement setup presents the considerable advantage of being easy and quick to use, which allowed us to run 10 to 15 measurements per sample, including redundant measurements. Moreover, the large phase angles considered here, mostly in the range 20–200 mrad (see Figure 2), the reproducibility of our measurements over time (see Figure S3 in the supporting information),

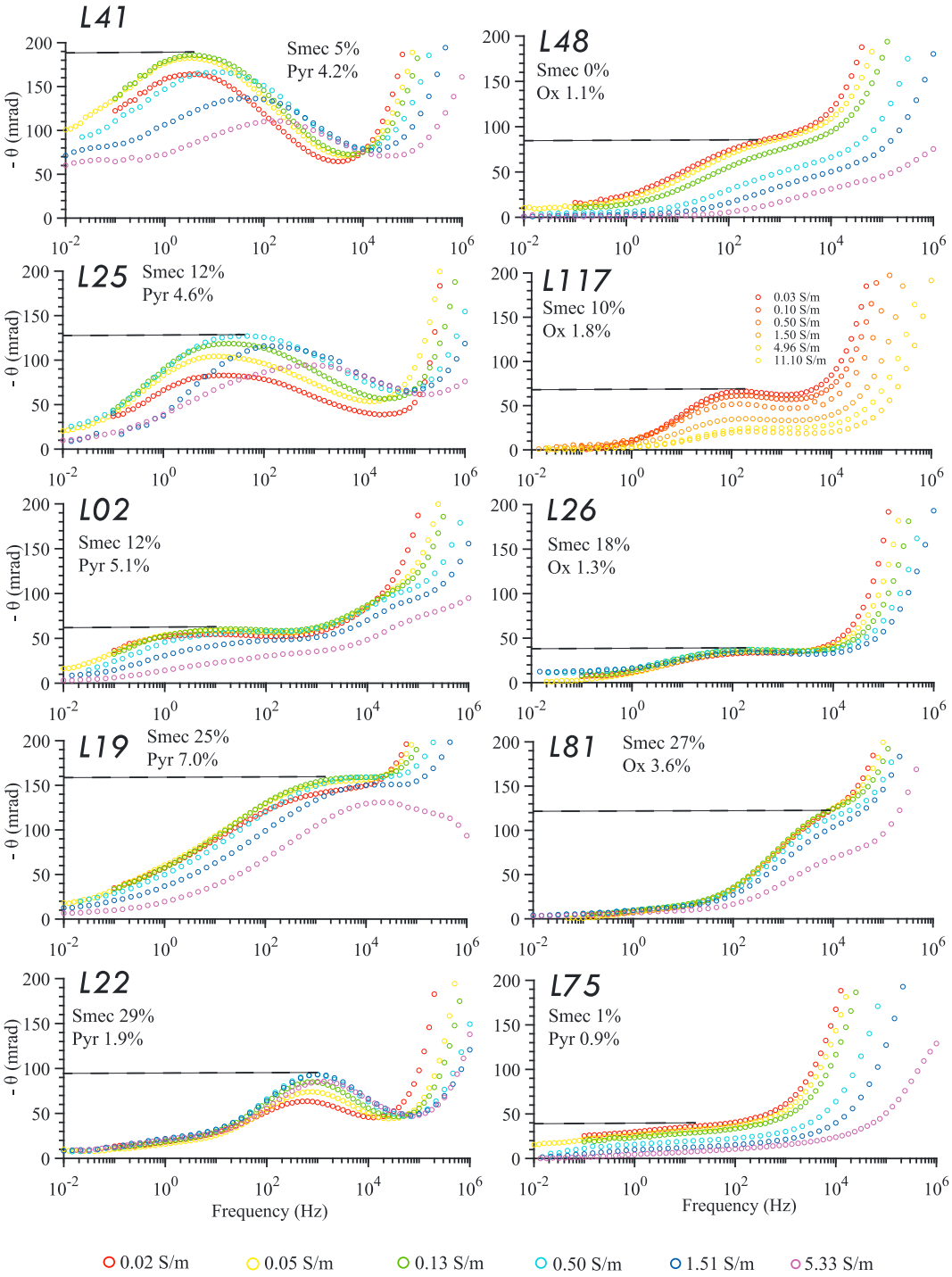

Figure 2. Phase spectra (negative phase angle θ versus alternating current frequency) from laboratory measurements of frequency domain electrical impedance for 10 samples, at different fluid conductivities (see color scale at the bottom, except for sample L117 that has separate color scale). The inferred maximum phase angle is indicated by the horizontal line. The respective smectite (Smec) and pyrite (Pyr) volume fractions are also indicated.

and the consistency of the trends observed between different samples, did not require further improvements in the measurement accuracy.

3. Results

An increase of the phase angle at frequency higher than 1–10 kHz is observed for all samples (Figure 2). This corresponds to high-frequency (HF) polarization phenomena, mostly attributed to polarization at the electrodes (Abdulsamad et al., 2016; Macdonald, 2000), although part of the observed polarization effect may also come from the so-called Maxwell-Wagner polarization (Chelidze & Gueguen, 1999). Because of these important effects, phase angle peaks due to polarization in the rock can only be observed at low frequency ($f \leq 10^4$ Hz). Polarization effects described in the rest of the study refer to low-frequency effects, unless the term HF polarization is used.

Since one objective of our study is to provide interpretations to IP parameters obtained in the field, simple parameters are required. We consider the MPA to be the simplest parameter, which can describe the amplitude of polarization in a comparable manner for all samples. It can be obtained directly from any phase spectrum and can also be inverted from field time domain IP measurements (Fiandaca et al., 2018; Madsen et al., 2017). We calculate the MPA, based on the phase angle value at the summit of spectral peaks (Figure 2), if a clear peak is observed in the phase spectrum, or the average phase angle of a linear/flat section when that is observed (e.g., L75). For samples showing two maxima (e.g., L02 at 1 and 10^5 Hz), we take the MPA at the lower frequency. Moreover, the bulk real conductivity at 1 Hz, $\sigma_{1\text{Hz}}$, is used to represent the real part of the conductivity (equation (3)). The value at 1 Hz is chosen as it is most relevant for field applications, but the bulk real conductivity is considered almost frequency independent (see, e.g., Maurya et al., 2018).

$$\sigma(\omega) = \frac{Z'(\omega)}{|Z(\omega)|^2}\frac{L}{A} \tag{3}$$

where σ and Z' are the real part of the bulk electrical conductivity and impedance, respectively. L and A are the length and cross-sectional area of the plug. $\sigma_{1\text{Hz}}$ is comparable to the conductivity measured in the field, often in the range 0.1–100 Hz.

Together, the MPA and $\sigma_{1\text{Hz}}$ provide a fair description of the complex resistivity spectra, which we use to relate IP response to mineralogy in our study. The peak frequency at which the MPA is reached, is, however, missing in this description. Since it is a more complicated and ambiguous parameter to calculate, both in field and in time domain IP studies, we do not analyze it quantitatively here (Fiandaca et al., 2018; Maurya et al., 2018).

Impedance spectra were also fitted with an electrical equivalent circuit model, based on the empirical Cole-Cole models (Cole & Cole, 1941; Davidson & Cole, 1951; Hallof & Klein, 1983; Havriliak & Negami, 1966; Macnae, 2015). This approach was not appropriate for analyzing the impedance spectra of our natural volcanic samples. (Florsch et al., 2012; Ghorbani et al., 2007). Therefore, Cole-Cole fits are not used in the rest of the paper but are, instead, presented and discussed in supporting information S2.

3.1. Identifying the Presence of Pyrite

The MPA is in the range 4–89 mrad for samples with iron oxides and in the range 7–186 mrad for samples with pyrite. Large variability with fluid conductivity is observed, with up to 70% decrease when the fluid conductivity increases from 0.02 to 5 S/m. Among the 30 samples analyzed, only 3 samples, L31, L119, and L123, contain ≤0.5% of metallic particles. These samples have a high smectite volume (≥30%) and the lowest MPA (≤20 mrad).

Samples with high MPA (≥30 mrad) contain sulfides or iron oxides in significant amounts (≥1%). Most samples with pyrite have $\sigma_{1\text{Hz}}$ higher than 10^{-2} S/m (Figure 3). More accurately, the presence of pyrite is likely if the couple MPA-$\sigma_{1\text{Hz}}$ plots to the right of the division line shown in Figure 3. The different geological matrices in which titanomagnetite and pyrite are embedded can explain this discrimination.

Iron oxides, which usually form during primary crystallization of magma (Haggerty, 1976), are found in fresh, crystalline samples, which have undergone limited hydrothermal alteration (samples L48, L26, L81, and L117 in Figure 4 and sample L48 in Figure 5). Moreover, the spatial distribution of titanomagnetite is homogeneous (samples L48, L26, L81, and L117 in Figure 4).

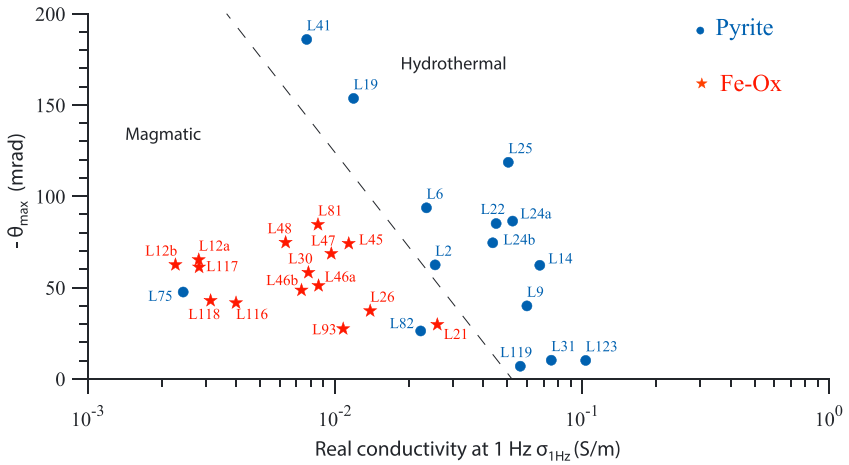

Figure 3. Maximum phase angle versus σ_{1Hz} for all samples, at pore fluid conductivity of 0.13 S/m. The black line separates hydrothermal and magmatic metallic mineralization.

The cocrystallization (in equilibrium; ; Bacon & Hirschmann, 1988) of ilmenite and titanomagnetite (at 80% ilmenite and 70% ulvospinel, respectively) in samples L30 and L46a allows calculation of the crystallization temperatures and oxidation-reduction conditions, by geothermometry and oxygen barometry. Calculated temperatures are consistent with the formation of basalt: $T = 1140$ and 1100 ± 30 °C, respectively. Corresponding oxygen partial pressures are close to the quartz-fayalite-magnetite buffer ($f_{O_2} = -8.87$ and -9.39, respectively; Ghiorso & Sack, 1991). These calculations confirm that iron oxides are magmatic minerals and that the environment of crystallization is in a relatively reduced state, according to classical calibrations (Powell & Powell, 1977).

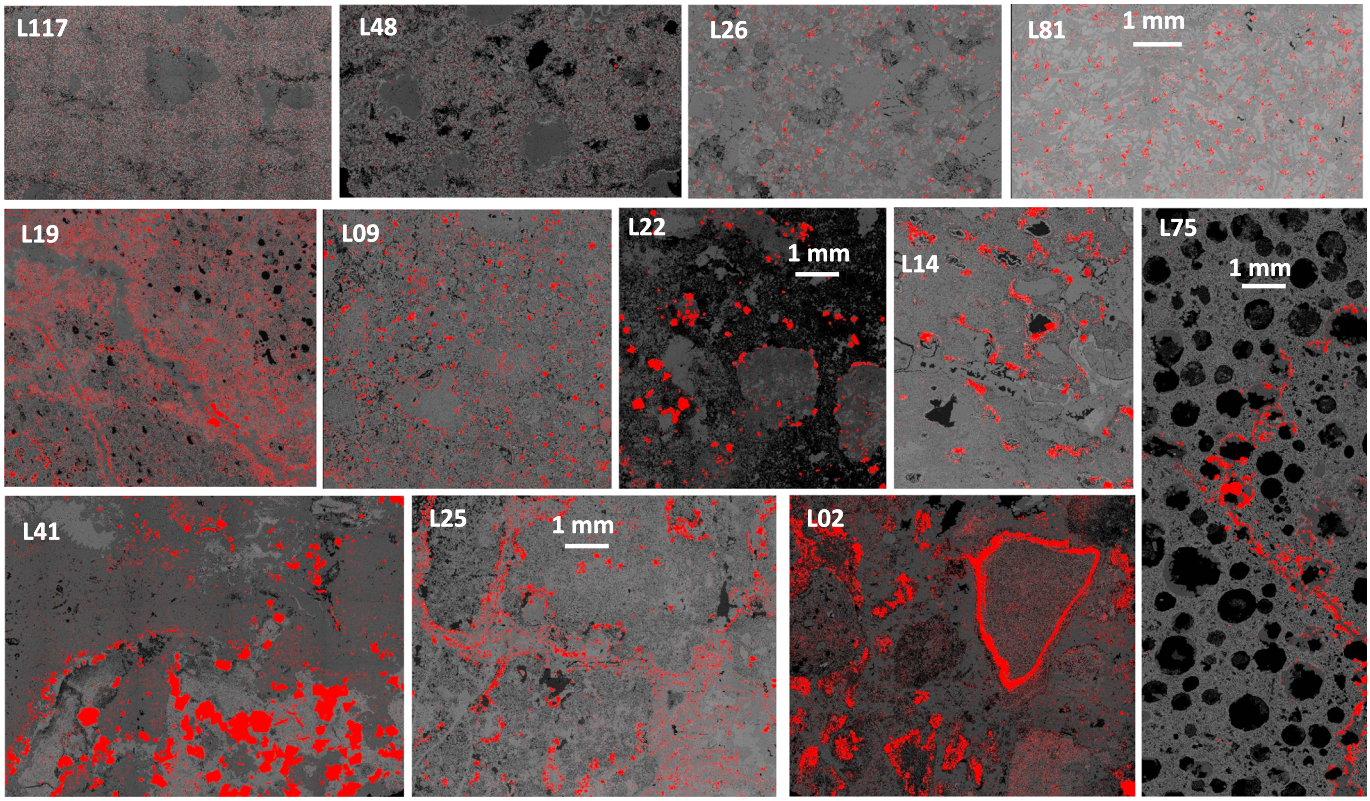

Figure 4. Scanning electron microscope images for 12 samples (all at the same scale). Red color indicates the presence of metallic particles. The top four samples (L117, L48, L26, and L81) contain iron oxides and the others pyrite.

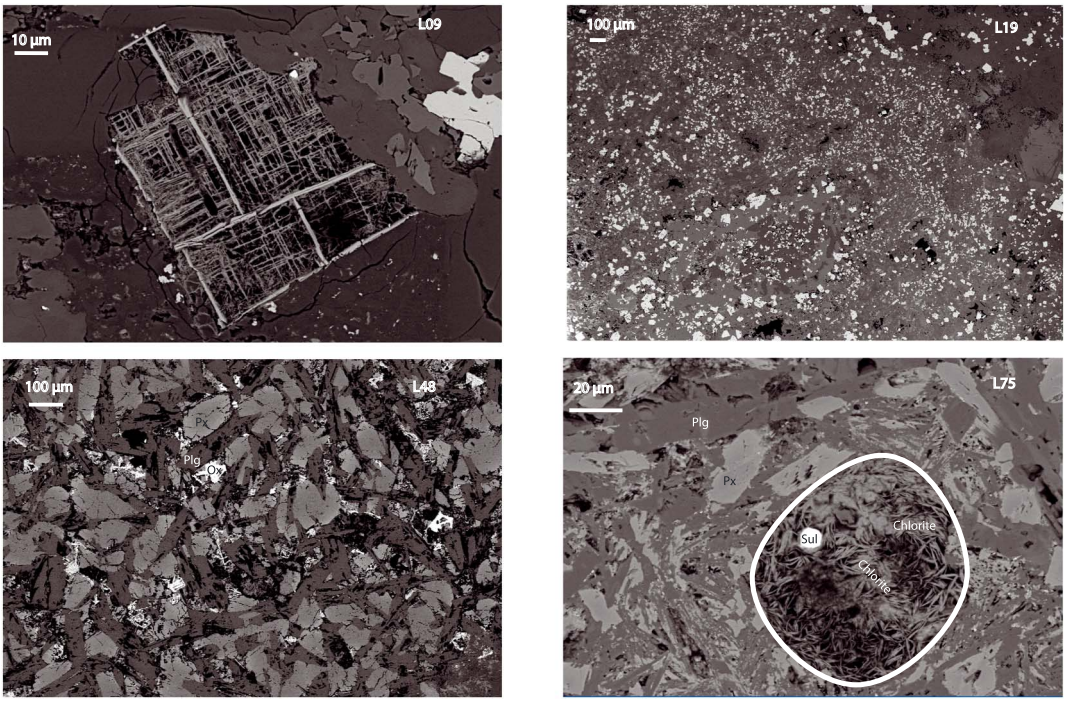

Figure 5. Scanning electron microscope pictures of polished thin section from samples L09, L19, L48, and L75. In sample L09, a former iron oxide (ilmenite), exsolved by hydrothermal circulation, is shown. In sample L19, small and abundant pyrite minerals from hydrothermal alteration are observed. In samples L48 and L75, intact primary pyroxenes (light gray, "px") and plagioclases (dark gray, "plg") are seen, showing that the surrounding matrix is well crystallized and fresh. Intact primary iron oxides (white, "ox") are also seen in L48. For sample L75, the vesicle outlined at the center of the image, is filled with chlorite. One sulfide crystal ("Sul," haycockite in this case) is also observed in the vesicle.

Sulfides (mostly pyrite) are found in hydrothermally altered samples (samples L09, L19, L14, L22, L41, L25, and L02 in Figure 4). In these samples, large smectite volumes are usually also present (Table 1), which causes a higher real conductivity (Lévy et al., 2018). In these altered samples, iron oxides have been dissolved, as illustrated in Figure 5 for sample L09. Sulfides are usually concentrated along fractures and vesicles or clasts rims (see, in particular, samples L19, L22, L14, L25, and L02 in Figure 4). In samples L41 and L75, sulfides are localized in one area of the thin section (see Figure 1 for L41).

Figure 4 demonstrates the complexity of hydrothermally altered samples. Two types of grain size (of metallic particles) distributions are shown: (i) frequency of each bin of particle sizes in terms of number of particles (classical distribution) and (ii) a distribution calculated as the surface fraction covered by each bin. Figure 4 shows that most of the metallic particles are small (cross-sectional area in the range 10–100 μm for all samples), but the few big particles (cross-sectional area greater than 10^4 μm) can represent an important, or dominant, fraction of the total area covered by metallic particles. The total area covered by metallic particles, divided by the total area of the thin section, is here our measure of the volume percentage of metallic particles. The second type of distribution shows different patterns for each sample. These patterns seem to have an influence on the phase spectrum (Figure 2). Indeed, sample L02 contains metallic particles whose section area distribution has two small maxima, at 10^2 and 10^5 μm^2, which are reflected in the two small polarization peaks observed at 1 and 10^4–10^5 Hz in Figure 2. Sample L19 contains metallic particle with one clear maximum section area at 10^3 μm^2, which is reflected by one strong polarization peak at 10^4 Hz. Finally, sample L41 contains metallic particles with a maximum section area at 10^5 μm^2, which is reflected in the polarization peak at 1 Hz. The connectivity of small pyrite grains, for example in sample L25, may also explain low peak frequencies. However, this connectivity cannot be quantified from SEM image analysis.

Two samples with sulfides, L75 and L82, lie left of the division line in Figure 3. Sample L75 contains about 0.8% sulfide but the low level of alteration indicates that sulfides may have formed during magmatic

crystallization rather than hydrothermal alteration (Figure 5). Indeed, an intact crystalline matrix is observed in this sample and the chlorite in-filling found with sulfides in closed vesicles tends to indicate late-magmatic crystallization of chlorite rather than during hydrothermal alteration (Berger et al., 2018; Meunier et al., 2012; Merle et al., 2005). The same was observed for sample L82, but in-fillings were rather of mixed-layer smectite/chlorite nature (e.g., corrensite). This type of sulfide mineralization is not detectable with the approach suggested here, but is of little interest for geothermal industry.

The discrimination between iron oxides (mostly titanomagnetite) and sulfides (mostly pyrite) shown here for a fluid conductivity of 0.13 S/m is valid at all fluid conductivities up to 0.5 S/m. Beyond 1.5 S/m, samples with titanomagnetite can be as conductive as samples with pyrite, if not more conductive, for samples with no smectite but low formation factor (Figure S11 in the supporting information). In low-salinity geothermal fields, such as Krafla (fluid conductivity 0.07 S/m at 25 °C), fluid conductivities higher than 0.5 S/m are unlikely. Indeed, even if the temperature reached 250 °C at the depths investigated, the in situ fluid conductivity would be 0.39 S/m, using a conductivity increase of 2%/°C (Arps, 1953; Hayashi, 2004). However, in saline geothermal systems, such as Reykjanes in Southwest Iceland, the discrimination may not be feasible. Finally, in contexts where pyrite is not formed by hydrothermal processes, the discrimination method suggested here may not be relevant.

3.2. Estimating the Volume of Pyrite

The volume fraction of iron oxides is in the range 1–2% in samples where iron oxides are the major metallic minerals and less in other samples. The volume fraction of sulfides ranges from ≤0.1% to 7% in all samples. The volume fraction of smectite is in the range 0–30% (Table 1).

We observe that the MPA generally increases with the volume fraction of pyrite and titanomagnetite in a linear manner (Figure 7), with a slope of 22 mrad/vol.% of metallic particles (or to 2.2 rad when the x axis is set to the interval 0–1 instead of percentages). Similar trends are observed at different pore fluid conductivities (Figure S12 in the supporting information). The linear relationship between the MPA and the volume of metallic particles may be qualitatively interpreted as an increase of the time needed for the maximum voltage to be reached, when more metallic surface is exposed to the fluid, due to more intense local displacement currents associated to longer redistribution of charges before an equilibrium is reached.

However, many samples deviate from the main trend in Figure 7. We suggest that most of the deviation is caused by the influence of interfoliar conductivity through connected smectite particles, which prevents polarization to occur (Lévy et al., 2018). Indeed, we observe a decrease of the MPA with increasing smectite content, for a given pyrite content (Figure 8a). For samples with hydrothermal pyrite and smectite, a general decreasing trend is observed between MPA and $\sigma_{1\text{Hz}}$ when considering all samples together (Figure 8a). For samples containing magmatic iron oxides, a linear trend is observed for each sample separately (Figure 8b), while their MPA are all in a narrow range (Figure 7). This indicates that varying electrolyte concentration (salinity) causes larger variations of the MPA than the different pore structures and iron oxides types and content in these magmatic unaltered samples, which is consistent with the fact that all basaltic rocks contain primarily 1–2% of iron oxides in volume. In hydrothermal samples, the MPA varies much more, due to more variable volumes of pyrite, and is also affected both by the counter influence of smectite and electrolyte concentration. We also observe that, for hydrothermal samples, the MPA reaches a maximum at a certain $\sigma_{1\text{Hz}}$ (Figure 8a). The fluid conductivity corresponding to this maximum varies from 0.13 to 1.5 S/m, depending on the sample.

As a consequence, in volcanic environments, the MPA needs to be considered together with the bulk real conductivity in order to (i) determine if the IP response corresponds to pyrite or iron oxides and (ii) estimate the pyrite content.

4. Discussion

4.1. Complexity of Natural Samples

We mentioned earlier the difficulty of fitting the impedance spectra with Cole-Cole models. We suggest this relates to the complexity of natural samples, illustrated in particular by Figure 4.

First, higher peak frequencies are observed in our samples than in studies on synthetic samples (Revil et al., 2017; Wong, 1979). This makes the discrimination between rock and apparatus polarization (as well as other

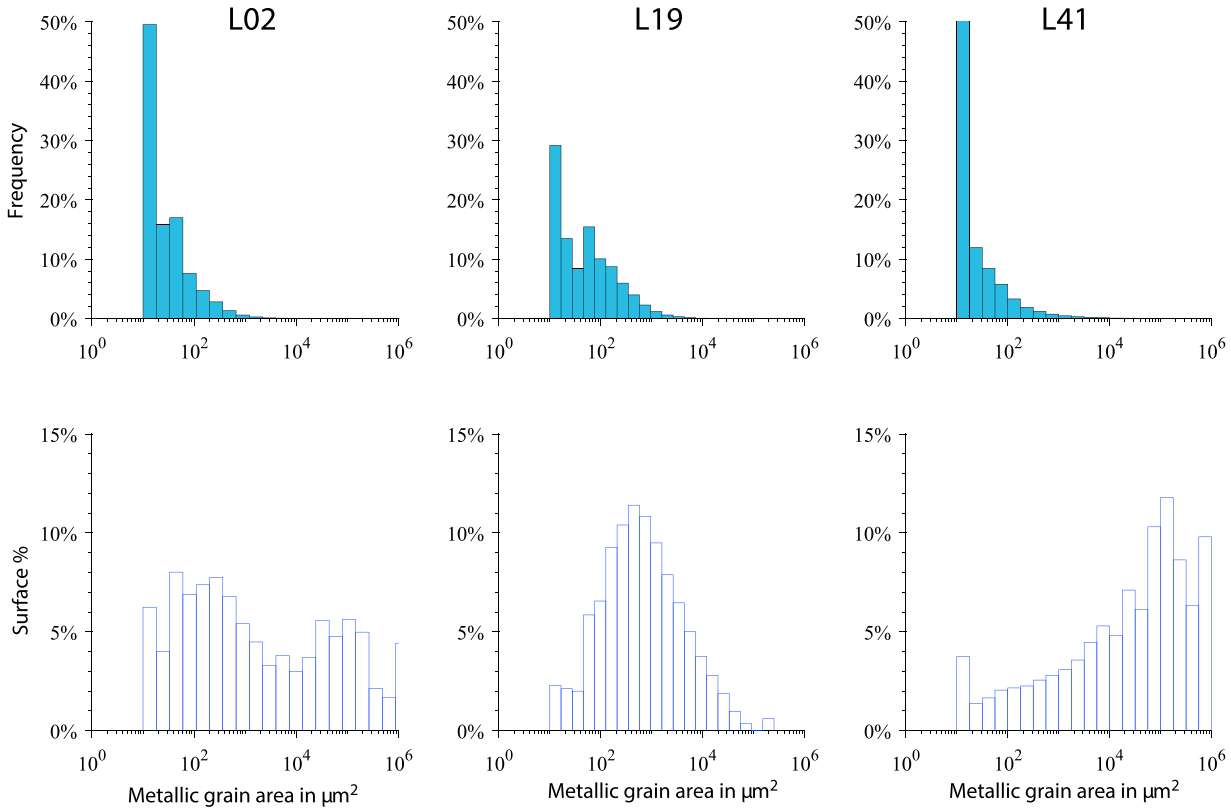

Figure 6. Distribution of metallic grain areas of sulfide minerals in samples L19, L02, and L41. The upper panels show the frequency of each area bin, while the lower panels show the surface covered by each bin, divided by the total surface covered by metallic particles. All the bins corresponding to areas greater than 10^4 μm^2 contain only one particle; they are thus invisible in the upper panels. The bin corresponding to the smallest grain areas (10 μm^2) contains about 70,000 particles for each sample.

HF effect) more difficult. This is probably due to the natural abundance of very small pyrite and iron oxides minerals in volcanic environments (see, e.g., sample L19 in Figures 5 and 6), unlike in massive sulfide ore deposits or synthetic samples with controlled grain size. Indeed, a decreasing grain size of metallic particle causes higher polarization frequency (Wong, 1979).

Second, the asymmetry of low-frequency polarization peaks, or even the presence of two clear distinct relaxation peaks (e.g., small secondary peak for L41 at high fluid conductivity around 0.1 Hz and two peaks

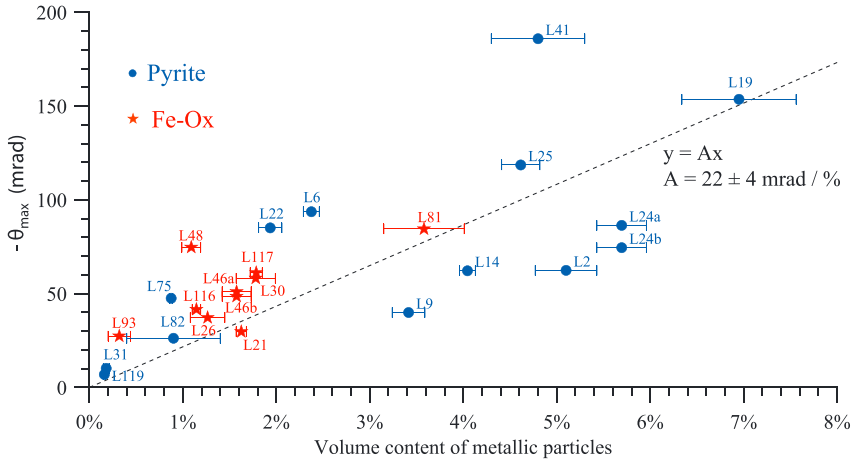

Figure 7. Maximum phase angle versus volume fraction of metallic particles, at pore fluid conductivity of 0.13 S/m. The black line corresponds to a linear fit constrained to pass through (0,0). The slope of the line is 22 ± 4 mrad/vol.%.

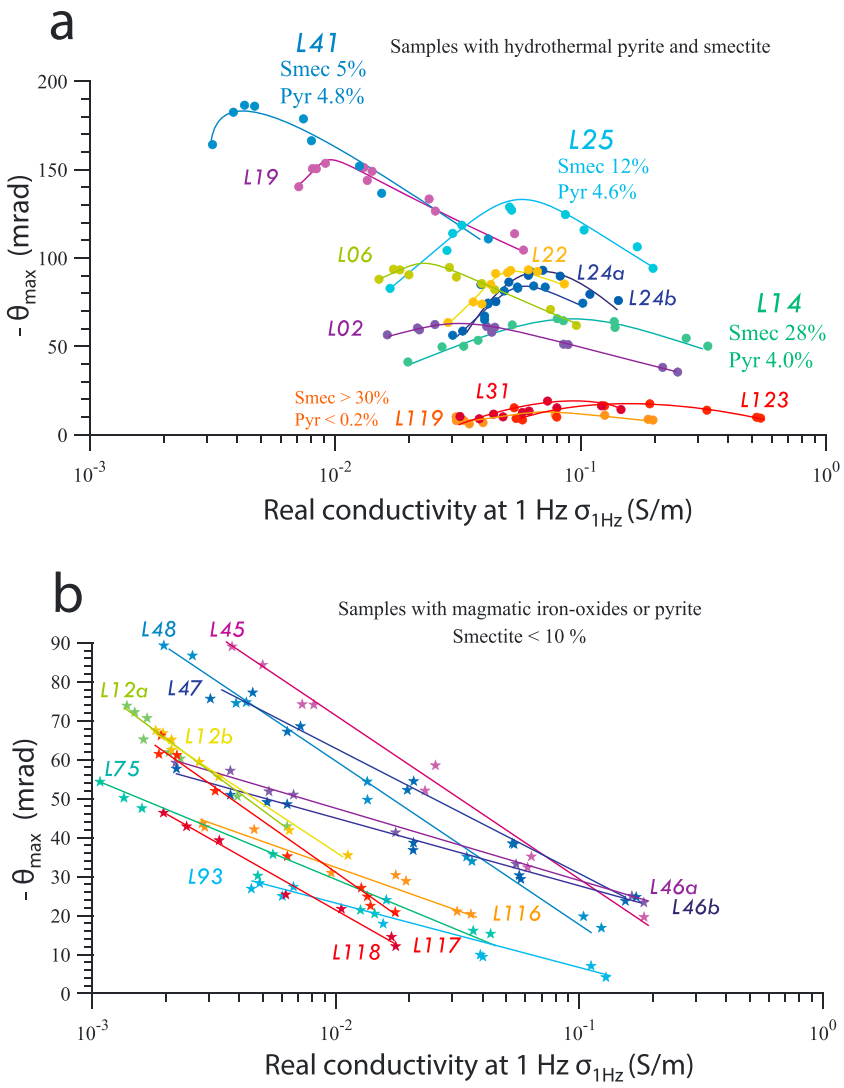

Figure 8. Maximum phase angle versus σ_{1Hz} for (a) samples with hydrothermal pyrite and smectite; (b) samples with magmatic iron oxides, besides sample L75, which contains sulfides (most likely from magmatic origin). One color corresponds to one sample (curves/lines show general trends). In (a), samples L41, L25, and L14 have similar pyrite volumes but decreasing smectite volumes.

around 1 and 10^5 Hz for L02 in Figure 2) can be explained by the large variability of grain sizes and connectivity between metallic grains, which exists in natural samples. Indeed, samples L41 and L02 have a complex distribution of grain sizes (Figures 4 and 6). On the other hand, sample L19 has a simple distribution of grain sizes (Figure 6) and can be correctly fitted with a simple Cole-Cole model (Figure S5 in the supporting information).

Less bias is introduced when calculating the MPA directly from the phase spectra than when inverting the chargeability by fitting impedance spectra with Cole-Cole models. The MPA can be slightly overestimated for samples having a maximum polarization at HF (L09, L19, L81, and L75; see Figure 2), but this does not cause deviation to the quantitative trend in Figure 7, since these samples are on the trend or below. Therefore, the MPA seems appropriate to describe the amplitude of polarization in natural samples. The MPA together with the bulk real conductivity at 1 Hz provides a convenient description of the complex electrical properties of natural samples.

The multiplicity (L02), flatness (L75), and asymmetry (L41) of polarization peaks make it difficult to determine a peak frequency or relaxation time. A qualitative comparison of the peak frequency to the metallic

grain size distribution was carried out, showing that the peak frequency seems to be controlled by the metallic particles with the largest section areas, although these particles only represent a negligible number of particles, compared to the total number of metallic particles. In order to analyze further the influence of metallic grain size on the peak frequency, a further study could be carried out to obtain a distribution of relaxation times (RTD), for example, by Debye decomposition (Florsch et al., 2014; Nordsiek & Weller, 2008; Weigand & Kemna, 2016). Different kernel functions could be tested for the decomposition (Debye, Warburg, and Cole-Cole) and the resulting total chargeability could be compared to the MPA and volume content of metallic particles, while the relaxation time distribution could be compared to the grain size distribution.

We also mentioned the difficulty of quantifying the pyrite volume, due to heterogeneity inside some samples. Despite this natural heterogeneity, we observe simple trends between the MPA and the bulk mineral content. These trends are relevant for field interpretations where the averaging of large volumes includes heterogeneous structures.

Several models predict a relationship between the chargeability, or the percentage frequency effect (PFE), and the volume percent of metallic particles. In all models, this relationship corresponds more or less to a slope of 9/2, which is verified on synthetic samples (Abdulsamad et al., 2017; Revil et al., 2017; Wong, 1979; Wait, 1983). The PFE, which is the relative variation of the real conductivity between two given frequencies, and thus an approximation of the chargeability, is supposed to be proportional to the phase angle at the geometrical mean frequency and is therefore closely related to the MPA (e.g., Revil et al., 2017). We do obtain a consistent slope of 240 $\pm$ 10 mrad between the MPA and the PFE at all salinities (see Figure S7 in the supporting information). However, this slope corresponds to a coefficient of 9.0 $\pm$ 1.5 between the PFE and the volume content of metallic particles, according to the fit in Figure 7. Therefore, our data set does not follow the trend between the PFE and the volume content of metallic particles predicted by the above-mentioned models and verified on synthetic samples (9 in our case versus 9/2 in models). Interestingly, the slope obtained in Figure 7 is very close to the value 9/4 suggested between the MPA and the volume content of metallic particles in the model by Revil et al. (2015).

4.2. Dependence of MPA Upon Bulk Electrical Conductivity

Curves in Figure 8b and the decreasing part of curves in Figure 8a, showing a decrease of MPA with increasing fluid conductivity, are consistent with other laboratory observations (e.g., Joseph et al., 2015; Kruschwitz, 2007; Lesmes & Frye, 2001) and also predictions of membrane polarization phenomena by numerical modeling (Bücker & Hördt, 2013; Hördt et al., 2016). Abdulsamad et al. (2017) suggest that the chargeability (or MPA) is independent of the electrolyte concentration, based on their observations on synthetic samples composed of sandstone with metallic particles. However, similar behavior to ours cannot be ruled out based on their Figure 4 only. Indeed, the curves corresponding to samples saturated with NaCl hint toward a similar behavior to ours, which could be confirmed by measurements on samples with larger volume content of metallic particles, saturated with a denser variation of NaCl concentrations. The x axis in Figure 8 shows the bulk real conductivity and not the fluid conductivity, but for a given sample the bulk conductivity increases monotonously with the fluid conductivity (Waxman & Smits, 1968), so that the shape of the curves is similar. The bulk conductivity is preferred because it includes a possible contribution from smectite minerals, which varies between samples. Smectite is more conductive than other clay minerals because cation exchange can occur inside the smectite crystals, between the clay tablets, and not only at the edges (Lévy et al., 2018). Therefore, the electrical current can flow through the smectite crystal, which may bypass polarization at the interface between fluid and smectite and cause a decrease in overall polarization, whereas other clay minerals would increase the overall polarization (Weller et al., 2013). Studying in more detail the conductivity within the clay tablets and polarization at the interface between fluid and connected smectite particles in volcanic rocks could improve, in the future, our understanding of the counter-effect of smectite on IP observed here.

A group of samples also reaches a maximum MPA for a certain window of fluid conductivity (Figure 8a). These samples contain pyrite and various amounts of smectite; samples with higher smectite volume seem to reach their maximum MPA at higher fluid conductivity. A similar behavior was observed for sandstones samples (Kruschwitz, 2007). This behavior is also predicted by numerical modeling of membrane polarization, in a system consisting of a sequence of narrow and wide pores, where the membrane effect is caused by different mobility of the ion species in the two pore types (Hördt et al., 2016). By analogy with the model developed by Hördt et al. (2016), we suggest that the presence of smectite with connected interfoliar spaces

creates a conduction network similar to a system of narrow and wide pores. In the range of fluid conductivity where the increase of MPA is observed, electrical conduction within connected interfoliar spaces of smectite and along the electrical double layer dominate the overall bulk conductivity. When salinity increases, the electrical double layer (e.g., at the outer surface of smectite minerals) becomes smaller. This may cause a higher mobility contrast between "regular" porosity and interfoliar spaces and thus higher membrane polarization. Interfoliar spaces would be here comparable to narrow pores in the model by Hördt et al. (2016). A possible explanation for the increasing-decreasing sequence here is that increased salinity causes an increase membrane polarization but a decrease of electrode polarization (i.e., polarization associated to metallic particles). Therefore, the overall polarization, dominated by polarization at the interface metal-electrolyte, will eventually decrease upon increasing salinity when the increase of membrane polarization becomes negligible. The model by Hördt et al. (2016) also predicts that smaller pore radii are associated to higher peak salinities for the MPA. This is consistent with the qualitative observation that the peak salinity of the MPA increases with the smectite content in Figure 8.

5. Conclusions

The amplitude of the frequency domain IP response of volcanic rocks, represented in this study by the MPA, depends in a complex manner on amounts of pyrite, iron oxides, and smectite as well as pore fluid conductivity. Natural volcanic rocks are more complex than theoretical models and synthetic samples. Despite this complexity, we observe clear trends that can constrain the location and volume of pyrite mineralization in volcanic environments, by considering together MPA and bulk resistivity without an a priori model. A MPA higher than 30 mrad in volcanic rocks corresponds to either the presence of pyrite or titanomagnetite, but a high bulk electrical conductivity or a MPA higher than 80 mrad indicates the presence of pyrite. MPA increases in general with the pyrite content. However, for a given pyrite content, the MPA decreases when the smectite content increases. This decrease is consistent with a general decrease of the MPA upon increase of bulk electrical conductivity. Adjusting numerical and analytical models to describe these observations on natural samples may be an important next step in understanding IP phenomena.

Appendix

Appendix A: Impedance Response of Water-Filled Tubes

At frequencies higher than 1 kHz, the absolute value of the phase angle of the cell filled with water increases rapidly. The increase becomes less important at higher fluid conductivity but the phase angle becomes pos-

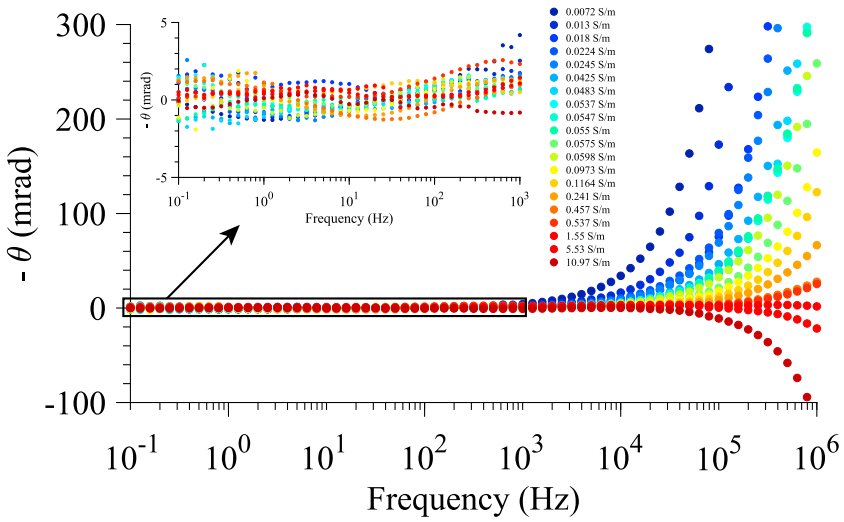

Figure A1. Phase spectra of the water-filled measuring cell in the range 100 mHz to 1 MHz. A zoom on the low phase angle at frequency below 1 kHz is also shown. The color scale corresponds to increasing water conductivity (from cold to warm colors). The *y* axis represents the negative phase angle. Most of the time, the phase angle of the complex conductivity is negative, corresponding to a phase delay of the voltage relative to the current. Positive phase angles, which are below the $x = 0$ line in this figure, can only be attributed to induction effects in the electrical circuit.

itive (whereas it is negative most of the time) at fluid conductivity higher than 1.5 S/m and the absolute value starts to increase again (Figure A1). If only dielectric absorption of water was causing the observed HF polarization, the phase angle should be only negative and much lower, considering a relative dieletric permittivity of water around $\epsilon_r = 80$ (Abdulsamad et al., 2016). A major contribution from the measuring electrodes is likely at these frequencies, as shown by previous studies (Abdulsamad et al., 2016; Lesmes & Frye, 2001; Volkmann & Klitzsch, 2015).

Appendix B: Chemical Analyses of Sulfides and Iron Oxides

Figure B1 compares the chemistry of the different sulfides and iron oxides for samples, analyzed by Electron Probe Micro-Analysis. Sulfides were analyzed in samples L02, L25, L41, L19, L24a, L75, and L31. Iron oxides were analyzed in samples L21, L26, L30, L46a, L48, L93, and L117. The detailed analyses are given in large Tables S1 and S2 (supporting information).

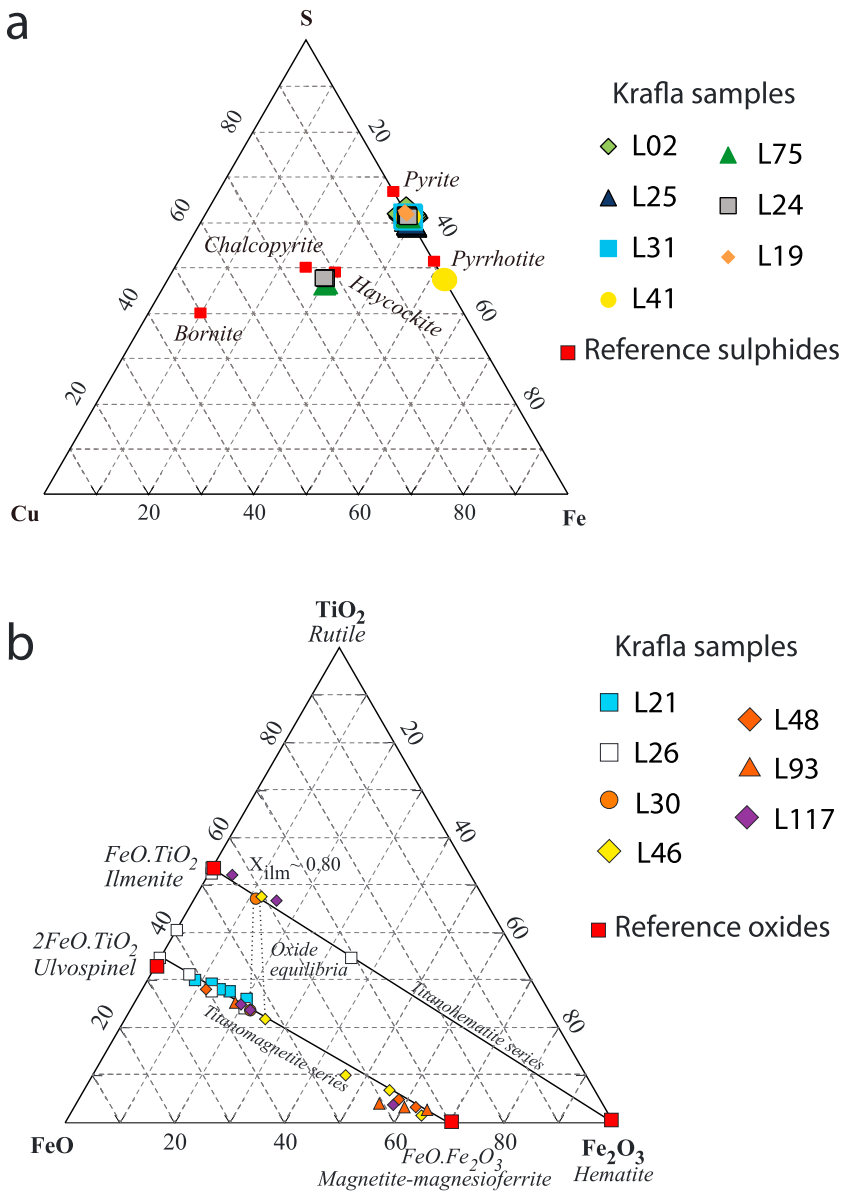

Figure B1. Sulfide and oxide composition in Krafla samples (individual analyses). (a) Cu-Fe-S ternary plot of normalized atomic proportions in sulfides. (b) TiO_2-FeO-Fe_2O_3 ternary plot of normalized weight percent of oxides in iron-titanium oxides. Titanomagnetite and titanohematite series from Lilova et al. (2012).

Acknowledgments
The complete electrical impedance files in ascii format (Data Set S1) are available online on the sip-archiv.de collaborative platform. The phase spectra for the 30 samples at six distinct pore fluid conductivities are available as supporting information (Data Set S2). The SEM images of all analyzed samples are available to anyone upon request. The authors thank Landsvirkjun for providing the core samples and Christophe Nevado and Doriane Delmas for high-quality polished thin sections. L. L. thanks Pauline Kessouri, Svetlana Byrdina, Jean Vandemeulebrouck, Knútur Árnason, Pradip Maurya, Ólafur Flóvenz, Philippe Pezard, and Pierre Briole for fruitful discussions and André Revil for recommending the use of four-electrode setup. This research was supported by the IMAGE FP7 EC and GEMex H2020 projects (grant agreements 608553 and 727550) and by a PhD grant from Paris Sciences et Lettres to Léa Lévy. We are grateful to the Editor Stephen Parman, Nicolas Florsch, and an anonymous reviewer for the efficiency of the reviewing process and valuable feedbacks, which have very much helped improve the manuscript quality.

References

Abdulsamad, F., Florsch, N., & Camerlynck, C. (2017). Spectral induced polarization in a sandy medium containing semiconductor materials: Experimental results and numerical modelling of the polarization mechanism. *Near Surface Geophysics*, *15*(6), 669–683.

Abdulsamad, F., Florsch, N., Schmutz, M., & Camerlynck, C. (2016). Assessing the high frequency behavior of non-polarizable electrodes for spectral induced polarization measurements. *Journal of Applied Geophysics*, *135*, 449–455.

Abramoff, M. D., Magalhaes, P. J., & Ram, S. J. (2004). Image processing with Image. *Journal Biophotonics International*, *11*, 36–42.

Agarwal, A., & Lang, J. (2005). *Foundations of analog and digital electronic circuits*. Elsevier.

Arps, J. J. (1953). The effect of temperature on the density and electrical resistivity of sodium chloride solutions. *Journal of Petroleum Technology*, *5*(10), 17–20.

Bacon, C. R., & Hirschmann, M. M. (1988). Mg/Mn partitioning as a test for equilibrium between coexisting Fe-Ti oxides. *American Mineralogist*, *73*, 57–61.

Barsoukov, E., & Macdonald, J. R. (2018). *Impedance spectroscopy: Theory, experiment, and applications*. Hoboken, NJ: John Wiley & Sons.

Berger, G., Beaufort, D., & Antoine, R. (2018). Clay minerals related to the late magmatic activity of the Piton des Neiges (Réunion island). Consequence for the primitive crusts. *Clay Minerals*, *51*, 1–16. https://doi.org/10.1180/clm.2018.51

Binley, A., Slater, L. D., Fukes, M., & Cassiani, G. (2005). Relationship between spectral induced polarization and hydraulic properties of saturated and unsaturated sandstone. *Water Resources Research*, *41*, W12417. https://doi.org/10.1029/2005WR004202

Börner, J. H., Girault, F., Bhattarai, M., Adhikari, L. B., Deldicque, D., Perrier, F., & Spitzer, K. (2018). Anomalous complex electrical conductivity of a graphitic black schist from the Himalayas of central Nepal. *Geophysical Research Letters*, *45*, 3984–3993. https://doi.org/10.1029/2018GL077178

Bücker, M., Flores Orozco, A., & Kemna, A. (2018). Electro-chemical polarization around metallic particles—Part 1: The role of diffuse-layer and volume-diffusion relaxation. *Geophysics*, *83*(4), 1–53.

Bücker, M., & Hördt, A. (2013). Analytical modelling of membrane polarization with explicit parametrization of pore radii and the electrical double layer. *Geophysical Journal International*, *194*(2), 804–813.

Chelidze, T. L., & Gueguen, Y. (1999). Electrical spectroscopy of porous rocks: A review—I. Theoretical models. *Geophysical Journal International*, *137*(1), 1–15.

Clennell, M. B., Josh, M., Esteban, L., Piane, C. D., Schmid, S., Verrall, M., et al. (2010). The influence of pyrite on rock electrical properties: A case study from NW Australian gas reservoirs. In *Society of Petrophysicists and Well-Log Analysts, SPWLA 51st annual logging symposium* (pp. 1–13).

Cole, K. S., & Cole, R. H. (1941). Dispersion and absorption in dielectrics. I. Alternating current characteristics. *The Journal of Chemical Physics*, *9*, 341–351.

Davidson, D. W., & Cole, R. H. (1951). Dielectric relaxation in glycerol, propylene glycol, and n-propanol. *The Journal of Chemical Physics*, *19*(12), 1484–1490.

Einaudi, F., Pezard, P. A., Ildefonse, B., & Glover, P. (2005). Electrical properties of slow-spreading ridge gabbros from ODP Hole 1105A, SW Indian Ridge. *Geological Society, London, Special Publications*, *240*(1), 179–193.

Fiandaca, G., Madsen, L. M., & Maurya, P. K. (2018). Re-parameterisations of the Cole–Cole model for improved spectral inversion of induced polarization data. *Near Surface Geophysics*, *16*(4), 385–399.

Florsch, N., Camerlynck, C., & Revil, A. (2012). Direct estimation of the distribution of relaxation times from induced-polarization spectra using a Fourier transform analysis. *Near Surface Geophysics*, *10*(6), 517–531.

Florsch, N., Revil, A., & Camerlynck, C. (2014). Inversion of generalized relaxation time distributions with optimized damping parameter. *Journal of Applied Geophysics*, *109*, 119–132.

Gautason, B., Egilson, T., Blishke, A., & Danielsen, P. E. (2007). Krafla: Borun tveggja kjarnahola, KH5 og KH6, veturinn 2006–2007. ISOR, Report in Icelandic.

Ghiorso, M. S., & Sack, O. (1991). Fe-Ti oxide geothermometry: Thermodynamic formulation and the estimation of intensive variables in silicic magmas. *Contributions to Mineralogy and Petrology*, *108*(4), 485–510.

Ghorbani, A., Camerlynck, C., Florsch, N., Cosenza, P., & Revil, A. (2007). Bayesian inference of the Cole–Cole parameters from time-and frequency-domain induced polarization. *Geophysical Prospecting*, *55*(4), 589–605.

Gudmundsson, A. (1991). Borun kjarnaholu í Sandabotnaskarð. Report in Icelandic, Orkustofnun.

Gudmundsson, A., Mortensen, A. K., Hjartarson, A., Karlsdóttir, R., & Ármannsson, H. (2010). Exploration and utilization of the Namafjall high temperature area in North Iceland. World Geothermal Congress.

Haggerty, S. E. (1976). Opaque mineral oxides in terrestrial igneous rocks. Oxide minerals. Short course notes, 3.

Hallof, P., & Klein, J. (1983). Characterization of electrical properties of metallic mineral deposits. Ontario Geological Survey Open File Report, 5468.

Havriliak, S., & Negami, S. (1966). A complex plane analysis of α-dispersions in some polymer systems. *Journal of Polymer Science: Polymer Symposia*, *14*, 99–117.

Hayashi, M. (2004). Temperature-electrical conductivity relation of water for environmental monitoring and geophysical data inversion. *Environmental Monitoring and Assessment*, *96*(1-3), 119–128.

Hördt, A., Bairlein, K., Bielefeld, A., Bücker, M., Kuhn, E., Nordsiek, S., & Stebner, H. (2016). The dependence of induced polarization on fluid salinity and pH, studied with an extended model of membrane polarization. *Journal of Applied Geophysics*, *135*, 408–417.

Jónsson, S. S., Gudmundsson, A., & Thordarson, S. (2003). Krafla borun kjarnaholu KH3 milli Jörundar og Háganga. Report in Icelandic, ISOR.

Joseph, S., Ingham, M., & Gouws, G. (2015). Spectral induced polarization measurements on New Zealand sands-dependence on fluid conductivity. *Near Surface Geophysics*, *13*(2), 169–177.

Júlíusson, B. M., Gunnarsson, I., Matthíasdóttir, K. V., Markússon, S. H., Bjarnason, B., Sveinsson, O. G., et al. (2015). Tackling the challenge of H2S emissions. In *Proceedings, World Geothermal Congress* (pp. 1–5).

Klein, J. D., & Sill, W. R. (1982). Electrical properties of artificial clay-bearing sandstone. *Geophysics*, *47*(11), 1593–1605.

Kruschwitz, S. (2007). Assessment of the complex resistivity behaviour of salt affected building materials (Doctoral dissertation), Technischen Universität Berlin. https://doi.org/10.14279/depositonce-1722

Kruschwitz, S., Binley, A., Lesmes, D., & Elshenawy, A. (2010). Textural controls on low-frequency electrical spectra of porous media. *Geophysics*, *75*(4), WA113–WA123.

Leroy, P., Weigand, M., Mériguet, G., Zimmermann, E., Tournassat, C., Fagerlund, F., et al. (2017). Spectral induced polarization of Na-montmorillonite dispersions. *Journal of Colloid and Interface Science*, *505*, 1093–1110.

Lesmes, D. P., & Frye, K. M. (2001). Influence of pore fluid chemistry on the complex conductivity and induced polarization responses of Berea sandstone. *Journal of Geophysical Research*, *106*(B3), 4079–4090.

Lévy, L., Gibert, B., Sigmundsson, F., Flóvenz, O. G., Hersir, G. P., Briole, P., & Pezard, P. A. (2018). The role of smectites in the electrical conductivity of active hydrothermal systems: Electrical properties of core samples from Krafla volcano, Iceland. *Geophysical Journal International*, *215*(3), 1558–1582.

Libbey, R. B., & Williams-Jones, A. E. (2013). Sulfide mineralization in the Reykjanes geothermal system, Iceland; Potential applications for geothermal exploration. *GRC Trans*, *37*, 417–424.

Lilova, K. I., Pearce, C. I., Gorski, C., Rosso, K. M., & Navrotsky, A. (2012). Thermodynamics of the magnetite-ulvöspinel (Fe_3O_4-Fe_2TiO_4) solid solution. *American Mineralogist*, *97*(8-9), 1330–1338.

Macdonald, J. R. (2000). Comparison of the universal dynamic response power-law fitting model for conducting systems with superior alternative models. *Solid State Ionics*, *133*(1-2), 79–97.

Macnae, J. (2015). Comment on: Tarasov, A. & Titov, K., 2013, On the use of the Cole–Cole equations in spectral induced polarization. *Geophysical Journal International*, *195*, 352–356.

Madsen, L. M., Fiandaca, G., Auken, E., & Christiansen, A. V. (2017). Time-domain induced polarization-an analysis of Cole-Cole parameter resolution and correlation using Markov Chain Monte Carlo inversion. *Geophysical Journal International*, *211*(3), 1341–1353.

Maurya, P., Fiandaca, G, Christiansen, A., & Auken, E. (2018). Field-scale comparison of frequency-and time-domain spectral induced polarization. *Geophysical Journal International*, *214*(2), 1441–1466.

Merle, R., Caroff, M., Girardeau, J., Cotten, J., & Guivel, C. (2005). Segregation vesicles, cylinders, and sheets in vapor-differentiated pillow lavas: Examples from Tore-Madeira Rise and Chile Triple Junction. *Journal of Volcanology and Geothermal Research*, *141*(1-2), 109–122. https://doi.org/10.1016/j.jvolgeores.2004.09.007

Meunier, A., Petit, S., Ehlmann, B. L., Dudoignon, P., Westall, F., Mas, A., et al. (2012). Magmatic precipitation as a possible origin of Noachian clays on Mars. *Nature Geoscience*, *5*(10), 739–743. https://doi.org/10.1038/ngeo1572

Misra, S., Torres-Verdín, C., Revil, A., Rasmus, J., & Homan, D. (2016). Interfacial polarization of disseminated conductive minerals in absence of redox-active species—Part 1: Mechanistic model and validation. *Geophysics*, *81*(2), E139–E157.

Nordsiek, S., & Weller, A. (2008). A new approach to fitting induced-polarization spectra. *Geophysics*, *73*(6), F235–F245.

Olhoeft, G. R. (1985). Low-frequency electrical properties. *Geophysics*, *50*(12), 2492–2503.

Parkhomenko, E. I. (1971). *Electrification phenomena in rocks*. New York: Springer Science & Business Media.

Pelton, W. H., Ward, S. H., Hallof, P. G., Sill, W. R., & Nelson, P. H. (1978). Mineral discrimination and removal of inductive coupling with multifrequency IP. *Geophysics*, *43*(3), 588–609.

Pezard, P. A., Howard, J. J., & Goldberg, D. (1991). Electrical conduction in oceanic gabbros, hole 735B, Southwest Indian Ridge. In *Proceedings of the ocean drilling program: Scientific results* (pp. 323).

Placencia-Gómez, E. (2015). Spectral induced polarization investigations in presence of metal sulphide minerals: Implications for monitoring the generation of acid mine drainage (Doctoral dissertation), Aalto University - Department of Civil and Environmental Engineering.

Placencia-Gómez, E., & Slater, L. D. (2016). On the pore water chemistry effect on spectral induced polarization measurements in the presence of pyrite. *Journal of Applied Geophysics*, *135*, 474–485.

Powell, R., & Powell, M. (1977). Geothermometry and oxygen barometry using coexisting iron-titanium oxides: A reappraisal. *Mineralogical Magazine*, *41*(318), 257–263.

Pridmore, D., & Shuey, R. (1976). The electrical resistivity of galena, pyrite, and chalcopyrite. *American Mineralogist*, *61*(3-4), 248–259.

Prikryl, J., Marieni, C., Gudbrandsson, S., Aradóttir, E. S., Gunnarsson, I., & Stefánsson, A. (2018). H2S sequestration process and sustainability in geothermal systems. *Geothermics*, *71*, 156–166.

Revil, A., Florsch, N., & Mao, D. (2015). Induced polarization response of porous media with metallic particles—Part 1: A theory for disseminated semiconductors. *Geophysics*, *80*, D525–D538.

Revil, A., Mao, D., Shao, Z., Sleevi, M. F., & Wang, D. (2017). Induced polarization response of porous media with metallic particles—Part 6: The case of metals and semimetals. *Geophysics*, *82*(2), E97–E110.

Revil, A., & Skold, M. (2011). Salinity dependence of spectral induced polarization in sands and sandstones. *Geophysical Journal International*, *187*(2), 813–824.

Shuey, R. (1975). *Semiconducting ore minerals*, *Developments in Economic Geology* (Vol. 4). Amsterdam: Elsevier Scientific Publishing Company.

Slater, L. D., & Sandberg, S. K. (2000). Resistivity and induced polarization monitoring of salt transport under natural hydraulic gradients. *Geophysics*, *65*(2), 408–420.

Stefánsson, A., Arnórsson, S., Gunnarsson, I., Kaasalainen, H., & Gunnlaugsson, E. (2011). The geochemistry and sequestration of H2S into the geothermal system at Hellisheidi, Iceland. *Journal of Volcanology and Geothermal Research*, *202*(3-4), 179–188.

Sumner, J. S. (1976). *Principles of induced polarization for geophysical exploration*, *Developments in Economic Geology* (Vol. 5). Amsterdam: Elsevier Scientific Publishing Company.

Telford, W. M., Geldart, L. P., & Sheriff, R. E. (1990). *Applied geophysics* (2nd ed.). Cambridge: Cambridge University Press. https://doi.org/10.1017/CBO9781139167932

Vinegar, H. J., & Waxman, M. H. (1984). Induced polarization of shaly sands. *Geophysics*, *49*(8), 1267–1287.

Volkmann, J., & Klitzsch, N. (2015). Wideband impedance spectroscopy from 1 mHz to 10 MHz by combination of four-and two-electrode methods. *Journal of Applied Geophysics*, *114*, 191–201.

Wait, J. R. (1983). Complex conductivity of disseminated spheroidal ore grains. *Gerlands Beitr. Geophys*, *92*, 49–69.

Wait, J. R. (1987). Physical model for the complex resistivity of the earth. *Electronics Letters*, *23*(19), 979–980.

Waxman, M. H., & Smits, L. J. M. (1968). Electrical conductivities in oil-bearing shaly sands. *Journal of Petroleum Science and Engineering*, *8*, 107–122.

Weigand, M., & Kemna, A. (2016). Debye decomposition of time-lapse spectral induced polarisation data. *Computers & Geosciences*, *86*, 34–45.

Weller, A., & Slater, L. (2012). Salinity dependence of complex conductivity of unconsolidated and consolidated materials: Comparisons with electrical double layer models. *Geophysics*, *77*(5), D185–D198.

Weller, A., Slater, L., & Nordsiek, S. (2013). On the relationship between induced polarization and surface conductivity: Implications for petrophysical interpretation of electrical measurements. *Geophysics*, *78*(5), D315–D325.

Wong, J. (1979). An electrochemical model of the induced-polarization phenomenon in disseminated sulfide ores. *Geophysics*, *44*(7), 1245–1265.

Zimmermann, E., Kemna, A., Berwix, J., Glaas, W., Münch, H. M., & Huisman, J. A. (2008). A high-accuracy impedance spectrometer for measuring sediments with low polarizability. *Measurement Science and Technology*, *19*(10), 105603.

Supporting Information for "Tracking magmatic hydrogen sulphur circulations using electrical impedance: complex electrical properties of core samples at the Krafla volcano, Iceland"

L. Lévy[1,2], B. Gibert[3], F. Sigmundsson[2], D. Deldicque[1], F. Parat[3], G.P. Hersir[4]

[1]Laboratoire de Géologie, Ecole Normale Supérieure - PSL, CNRS, UMR 8538, Paris, France
[2]Nordic Volcanological Center, Institute of Earth Sciences, University of Iceland, 101 Reykjavk, Iceland
[3]CNRS, Géosciences Montpellier, UM2 5243-CC60, Université de Montpellier, Montpellier, France
[4]ÍSOR-Iceland GeoSurvey, Grensásvegur 9, 108 Reykjavík, Iceland

Contents

Additional Supporting Information (Files uploaded separately)

1. Caption for Datasets S1 and S2
2. Captions for large Tables S1 to S2 (larger than 1 page)

Introduction

We present here more observations and analyses of the electrical polarization measured in our samples, both at high and low frequency. We also show how the pore fluid conductivity influences the two main results of our study: pyrite discrimination from iron-oxides and pyrite volume estimation.

S1. Impedance measurements and data quality

The 4-electrode set-up and sample holder are shown in Figure S1. The homogenization and stability of the fluid in the pore space is shown in Figure S2. Minor variations of the bulk real conductivity are observed over days, provided that samples have been soaking in the same fluid for at least one month. The reproducibility of our measurements and confidence in the actual salinity values inside the pore space can be assessed in Figure S3, where phase-angle spectra measured one year apart at similar fluid conductivity are overlapping most of the time.

S2. Problems using Cole-Cole fitting on natural samples

The impedance spectra are analyzed using an electrical equivalent circuit model, which consists in a single Cole-Cole relaxation in parallel with a capacitance (Figure S4 (a)). Cole-Cole models, originally developed for describing dielectric polarization in polymers, are often used to characterize the low-frequency IP response of geological materials (Pelton et al., 1978; Hallof & Klein, 1983). We added the capacitance in parallel to represent HF polarization effects, which can be important at the high frequencies where polarization occurs in our samples - higher than 1 kHz in many samples, e.g. L19, L47 and L81 (Abdulsamad et al., 2016; Macdonald, 2000; Kruschwitz

Corresponding author: Léa Lévy, `lea.levy@ens.fr`

et al., 2010). Our electrical equivalent circuit model has 5 parameters, as shown in the impedance function Z_{tot} (Equation 1).

$$\frac{1}{Z_{tot}} = \frac{1}{Z_{C_\infty}} + \frac{1}{Z_{CC}} = jC_\infty\omega + \frac{1 + (j\omega\tau)^c}{R_0 - R_\infty} \tag{1}$$

where ω is the angular frequency, C_∞ is the capacitance associated to high-frequency dielectric effects and the four other parameters are associated to the low-frequency Cole-Cole relaxation: R_0 being the DC resistance, R_∞ the resistance at infinite frequency, τ the average relaxation time and c the width of distribution of relaxation times.

We use the complex non-linear least square frequency-response fitting software "LEVMW" to optimize the fit between model and data (Macdonald, 2000).

The chargeability, a parameter commonly used to represent the magnitude of the polarization, is calculated with Equation 2, based on the values of R_0 and R_∞ obtained from the fit (see fitting curves in Figure S5).

$$m = \frac{R_0 - R_\infty}{R_0} \tag{2}$$

When the frequency tends towards 0, polarization phenomena disappear (Olhoeft, 1985). Therefore the DC conductivity is used to analyze the conductivity without influence of polarization phenomena, and calculated with Equation 3.

$$\sigma_{DC} = \frac{1}{R_0} \tag{3}$$

The Cole-Cole model used here is an adaptation of the original Cole-Cole model (Cole & Cole, 1941), applicable to fitting impedance or resistivity spectra (Macnae, 2015). In samples where two distinct low-frequency dispersions are observed (see sample L02 in Figure S5), a "Double Cole-Cole" model can be used, as suggested by Hallof and Klein (1983) (see Figure S4 (b)). However, the parameters retrieved from the model cannot be directly compared to parameters obtained with a "Simple Cole-Cole" model.

The capacitance in parallel represents all the high-frequency dielectric effects. It includes dielectric absorption by reorientation of water molecules, accumulation of ions at all interfaces between two different phases (e.g. liquid/solid or liquid1/liquid2), also known as the Maxwell-Wagner polarization (Chelidze et al., 1999) and polarization at the measuring electrodes. In order to correctly fit the low-frequency relaxation, of main interest in our study, it is necessary to fit the high frequency dielectric contribution of the spectra (Florsch et al., 2012; Hallof & Klein, 1983). A single capacitance is preferred to represent these effects because the resulting relaxation is only partially resolved in the frequency range analyzed here (Kruschwitz et al., 2010). However, this single capacitance in parallel did not always provide a good fit of the HF part of the phase spectra. Therefore, another model was tested: a circuit representing the electrodes contribution to both the resistance and the capacitance is added in series to the main circuit representing the rock contribution, as suggested by Macdonald (2000). This model could better fit the phase spectra at high frequency, but a correlation between the parameters R_{el} and R_∞ (see Figure S4 (c)) was observed and the parameter R_∞ could not be resolved.

The complex function presented in Equation 1 provides a good fit to the real part of the impedance Z' and to the phase-angle θ for a few samples (see L19, L22, L25 in Figure S5) but not for most samples (see e.g. L41, L46a and L117 in Figure S6).

We also tested the modification suggested by Havriliak and Negami (1966) to fit the asymmetric peaks at low frequency, as it was observed in many samples (e.g. L25, L41). It cannot be represented with an equivalent circuit and is therefore not shown in Figure S4. Its impedance is given in Equation 4.

$$Z_{GCC} = \frac{R_0 - R_\infty}{(1 + (j\omega\tau)^c)^\gamma} \tag{4}$$

where GCC means Generalized Cole-Cole and γ is an additional exponent, originally introduced by Davidson and Cole (1951) to fit the asymmetric shape of polarization peaks.

The use of this function did improve the fitting quality for some samples (e.g. L41) but the additional parameter γ has no clear physical meaning. It can be observed in Figure S6 that sample L41 shows, for the two highest fluid conductivities, a second small polarization peak at frequency lower than 1 Hz. This peak is also probably present at other fluid conductivities and contributes to the asymmetry.

S3. Maximum phase angle vs. chargeability

The Percentage Frequency Effect (PFE) was also computed at each fluid conductivity, using Equation 5. The PFE is an approximation of the chargeability but can be significantly lower for samples where the real part of the impedance Z' is still increasing at the cut-off frequency of 100 mHz taken here (see e.g. L25 in Figure S5 (c)).

$$PFE = \frac{\rho_{100mHz} - \rho_{10kHz}}{\rho_{100mHz}} \tag{5}$$

where ρ_{100mHz} is the real part of the resistivity at 100 mHz and ρ_{10kHz} is the real part of the resistivity at 10 kHz. The cut-off frequency of 100 mHz was chosen because the data quality drastically decreases at lower frequencies.

The PFE and fitted IP parameters by the Cole-Cole simple model are given in Table S1 for all analyzed samples, at the lowest fluid conductivity 0.02 S/m.

The PFE is proportional to the MPA, at all pore fluid conductivities, as illustrated in Figure S7.

S4. Maximum imaginary conductivity

Induced Polarization studies on sandstones often use the imaginary conductivity rather than the phase angle to measure the amplitude of polarization phenomena. We show here that the maximum imaginary conductivity is proportional to the bulk real conductivity at 1 Hz (the real conductivity is frequency-dependent as first approximation) (Figure S8). This proportionality relationship is true for one sample at different fluid conductivities, but also when considering all the samples together, especially those without smectite (samples with iron-oxides represented with filled stars). The maximum imaginary conductivity of samples with large smectite volumes but rather small pyrite volumes (represented by filled circles with red/orange color have the largest smectite volumes), have a lower maximum imaginary conductivity than the other pyrite-rich samples. The maximum imaginary conductivity is also correlated to the volume fraction of metallic particles, to some extent (Figure S9). However, no direct correlation exists between the maximum phase angle and the maximum imaginary conductivity, because the real conductivity is more variable amongst samples and across salinities than the maximum phase angle (Figure S10).

References

Abdulsamad, F., Florsch, N., Schmutz, M., & Camerlynck, C. (2016). Assessing the high frequency behavior of non-polarizable electrodes for spectral induced polarization measurements. *Journal of Applied Geophysics*, *135*, 449–455.

Chelidze, T. L., Gueguen, Y., & Ruffet, C. (1999). Electrical spectroscopy of porous rocks: A review–ii. experimental results and interpretation. *Geophysical Journal International*, *137*(1), 16–34.

Cole, K. S., & Cole, R. H. (1941). Dispersion and absorption in dielectrics i. alternating current characteristics. *The Journal of chemical physics*, *9*(4), 341–351.

Davidson, D. W., & Cole, R. H. (1951). Dielectric relaxation in glycerol, propylene glycol, and n-propanol. *The Journal of Chemical Physics*, *19*(12), 1484–1490.

Florsch, N., Camerlynck, C., & Revil, A. (2012). Direct estimation of the distribution of relaxation times from induced-polarization spectra using a fourier transform analysis. *Near Surface Geophysics*, *10*(6), 517–531.

Hallof, P., & Klein, J. (1983). Characterization of electrical properties of metallic mineral deposits. *Ontario Geological Survey Open File Report*, *5468*.

Havriliak, S., & Negami, S. (1966). A complex plane analysis of α-dispersions in some polymer systems. In *Journal of polymer science: Polymer symposia* (Vol. 14, pp. 99–117).

Kruschwitz, S., Binley, A., Lesmes, D., & Elshenawy, A. (2010). Textural controls on low-frequency electrical spectra of porous media. *Geophysics*, *75*(4), WA113–WA123.

Lesmes, D. P., & Frye, K. M. (2001). Influence of pore fluid chemistry on the complex conductivity and induced polarization responses of Berea sandstone. *Journal of Geophysical Research: Solid Earth*, *106*(B3), 4079-4090.

Macdonald, J. R. (2000). Comparison of the universal dynamic response power-law fitting model for conducting systems with superior alternative models. *Solid State Ionics*, *133*(1-2), 79–97.

Macnae, J. (2015). Comment on: Tarasov, a. & titov, k., 2013, on the use of the cole–cole equations in spectral induced polarization. *Geophysical Journal International*, *195*, 352–356.

Olhoeft, G. R. (1985). Low-frequency electrical properties [Journal Article]. *Geophysics*, *50*(12), 2492-2503.

Pelton, W. H., Ward, S. H., Hallof, P. G., Sill, W. R., & Nelson, P. H. (1978). Mineral discrimination and removal of inductive coupling with multifrequency IP. *Geophysics*, *43*(3), 588–609.

Vinegar, H., & Waxman, M. (1984). Induced polarization of shaly sands [Journal Article]. *Geophysics*, *49*(8), 1267-1287.

Data Set S1.

Electrical impedance raw files in the native ".z" format (ASCII) for the 30 samples analyzed in the article, at six distinct pore water conductivities. These files, as well as relevant petrophysical data for these samples are available online on the platform www.sip-archiv.de.

Data Set S2.

Phase spectra in the frequency-range $10^{-2} - 10^{6}$ Hz for the 30 samples analyzed in the article, at six distinct pore water conductivities.

Table S1: IP parameters for measured sample. First column shows ID number of samples and the second and third columns show the Percentage Frequency Effect (PFE), calculated between 10^{-1} and 10^{4} Hz (see Equation 5). Since the PFE varies with fluid conductivity, the two extreme values are given. The next four columns are parameters obtained by fitting, when possible, impedance spectra at the lowest fluid conductivity (0.02 S/m) with the model presented in Equation 1. Exception is L02, where a Double Cole-Cole is used. m is the chargeability, τ is the relaxation time, c is the Cole-Cole exponent and C_∞ is the HF capacitance.

ID	Min PFE	Max PFE	m	τ	c	C_∞
	Ω/Ω	Ω/Ω	Ω/Ω	s	no unit	nF
L02	0.17	0.37	0.50	3.7E-02	0.30	0.08
L06	0.30	0.45	no fit	no fit	no fit	no fit
L09	0.13	0.19	0.25	1.1E-04	0.30	0.09
L14	0.20	0.30	0.30	2.6E-03	0.34	0.11
L19	0.35	0.54	0.73	9.4E-04	0.28	0.07
L22	0.25	0.35	0.29	5.4E-04	0.44	0.09
L24a	0.23	0.32	0.28	3.3E-04	0.41	0.10
L24b	0.22	0.36	0.30	3.1E-04	0.36	0.10
L25	0.40	0.53	0.48	2.1E-02	0.35	0.06
L31	0.04	0.10	no fit	no fit	no fit	no fit
L41	0.46	0.58	0.73	4.5E-01	0.30	0.06
L75	0.07	0.26	no fit	no fit	no fit	no fit
L82	0.06	0.15	0.23	3.8E-04	0.23	0.04
L119	0.04	0.07	0.12	2.7E-04	0.16	0.09
L123	0.04	0.09	no fit	no fit	no fit	no fit
L12a	0.24	0.42	no fit	no fit	no fit	no fit
L12b	0.21	0.32	no fit	no fit	no fit	no fit
L21	0.10	0.13	no fit	no fit	no fit	no fit
L26	0.17	0.19	0.23	4.4E-04	0.34	0.05
L30	0.08	0.33	no fit	no fit	no fit	no fit
L45	0.08	0.35	0.59	1.0E-04	0.27	0.04
L46a	0.09	2.47	0.41	4.8E-04	0.30	0.02
L46b	0.10	0.28	0.42	4.1E-04	0.28	0.02
L47	0.07	0.41	0.50	5.1E-04	0.30	0.03
L48	0.06	0.34	0.54	1.7E-04	0.31	0.03
L81	0.15	0.26	0.52	1.2E-05	0.39	0.04
L93	0.03	0.16	0.35	1.2E-04	0.16	0.04
L116	0.15	0.21	no fit	no fit	no fit	no fit
L117	0.11	0.29	0.32	4.7E-04	0.47	0.02
L118	0.10	0.20	no fit	no fit	no fit	no fit

Large Table S1.

Results of sulphides analyses by EPMA on 7 samples: L02, L25, L41, L19, L24a, L75 and L31. Between 3 and 17 analyses by sample are given. Not all samples were analyzed by EPMA but the dominant mineralogy of the others was determined qualitatively by SEM analyses.

Large Table S2.

Results of iron-titanium oxides analyses by EPMA on 7 samples: L21, L26, L30, L46a, L48, L93 and L117. Between 2 and 6 analyses by sample are given. Not all samples were analyzed by EPMA but the dominant mineralogy of the others was determined qualitatively by SEM analyses.

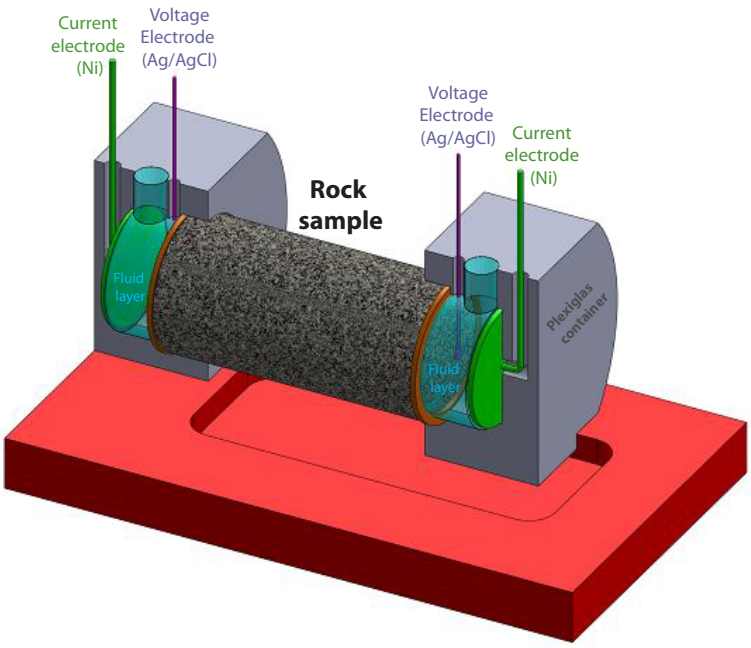

Figure S1: Sample holder and electrodes set-up for complex electrical resistivity measurements in this study. Manufactured according to descriptions in Vinegar and Waxman (1984) and Lesmes and Frye (2001).

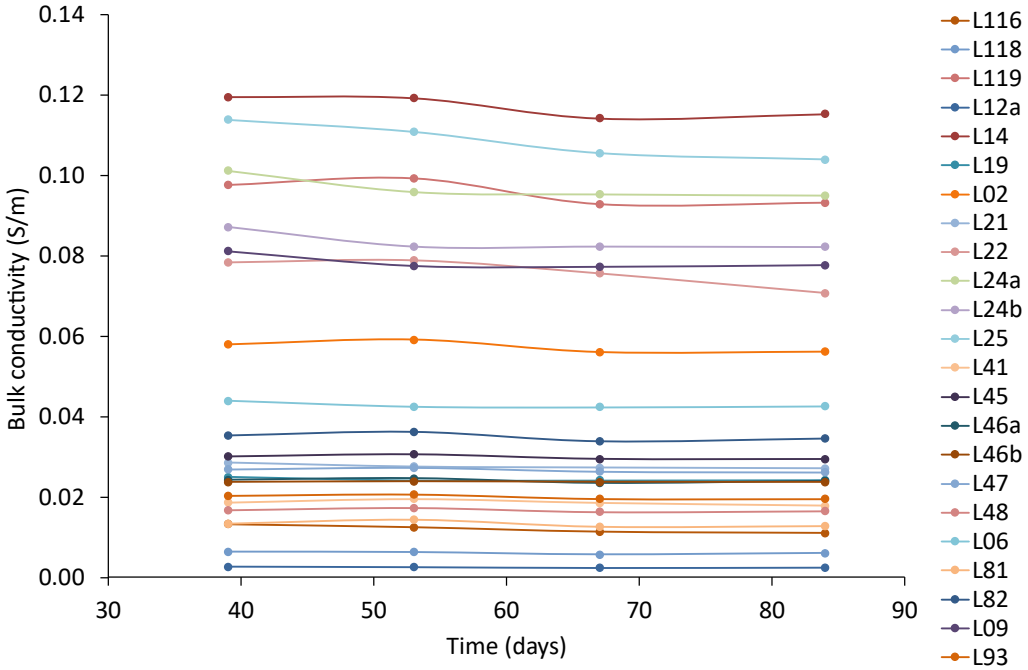

Figure S2: Bulk electrical conductivity measurements (at 10 kHz) of samples used in this study, saturated with a pore fluid conductivity of about 0.1 S/m, repeated over time after 39 days of saturation and homogenization.

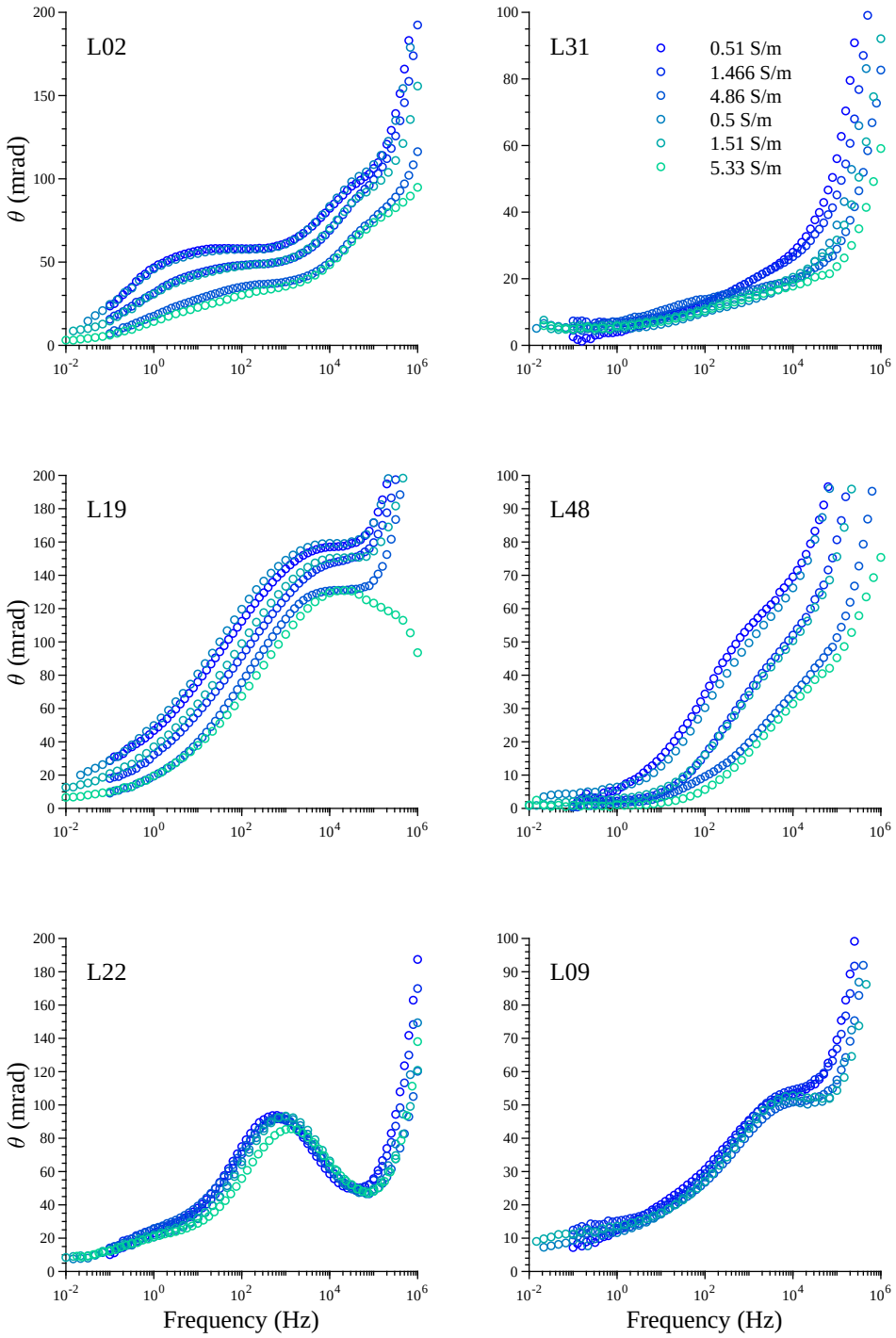

Figure S3: Phase angle of the impedance for six samples saturated with pore water at three distinct conductivities. Two runs of measurements (about one year apart) are shown: the blue colors indicate the first run and the green colors indicate the second run. The corresponding pore fluid conductivities are the same for all samples and indicated as legend of sample L31.

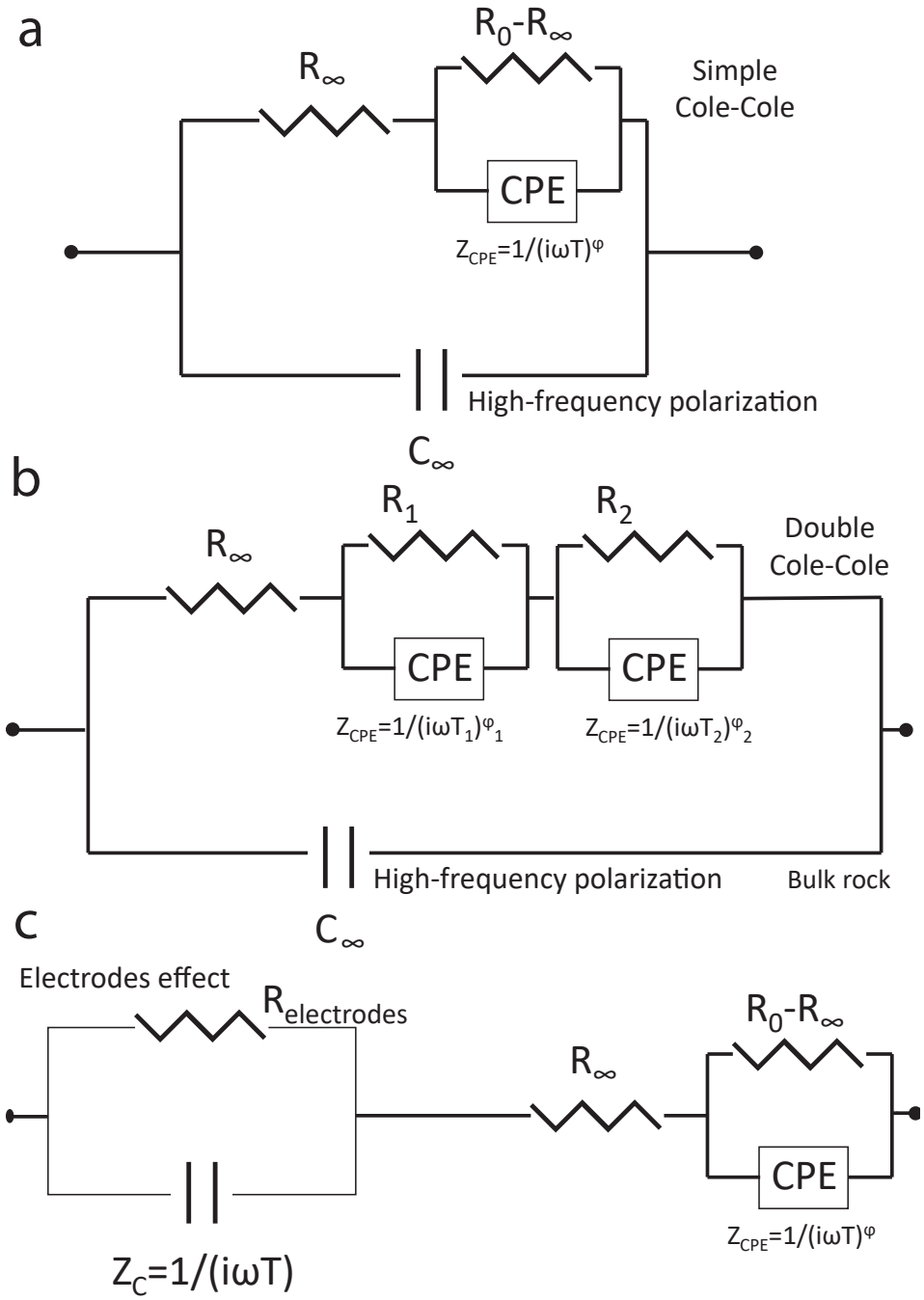

Figure S4: Equivalent circuit models used to analyze the impedance spectra: (a) Simple Cole-Cole in parallel with a capacitance (for HF polarization), corresponding to Equation 1, (b) Double Cole-Cole in parallel with a capacitance and (c) Simple Cole-Cole in series with a R-C circuit (representing the electrodes). R is a resistance, C is a capacitance, CPE stands for constant phase element and is an imperfect capacitance.

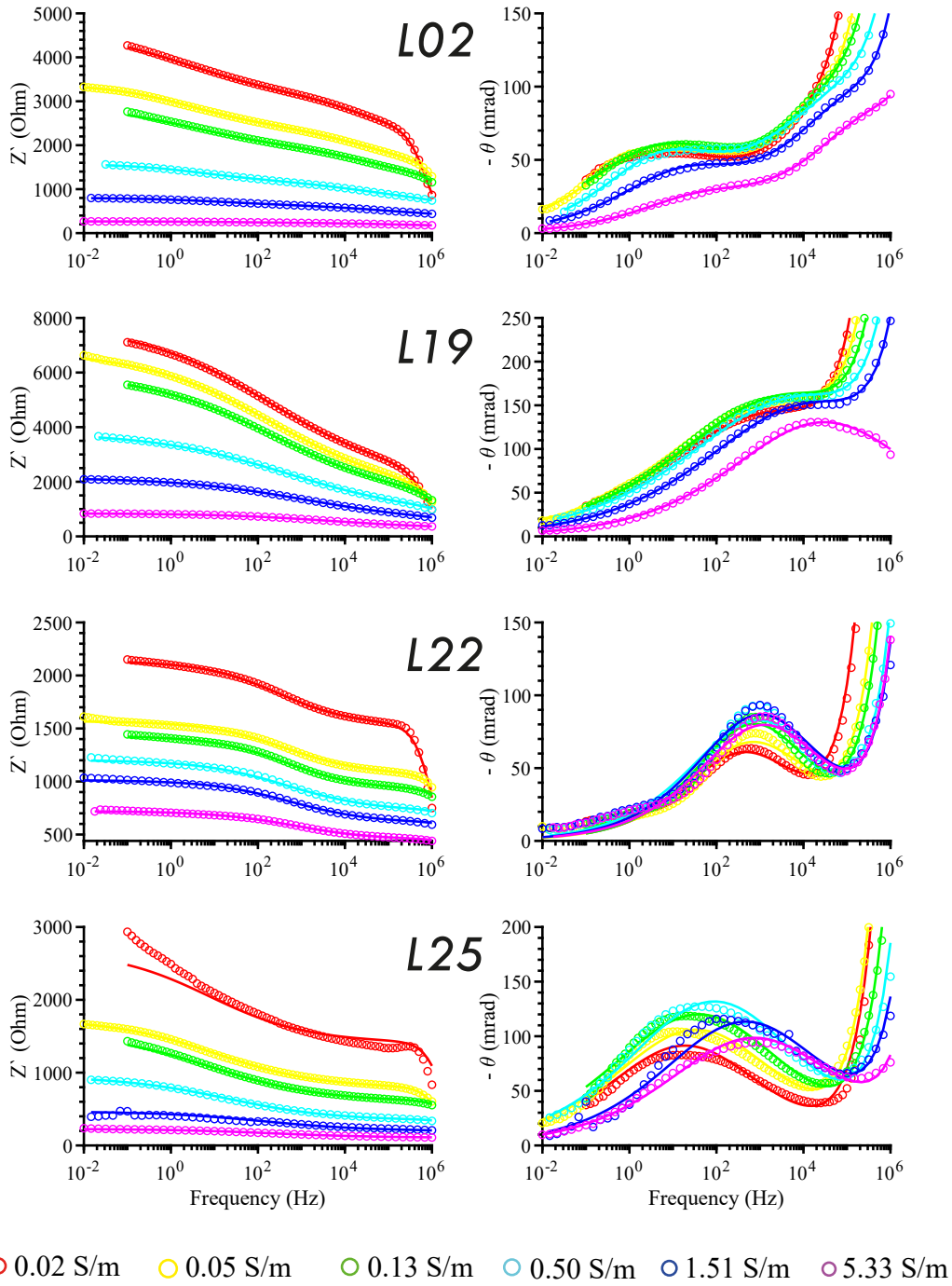

Figure S5: Impedance spectra of four samples, correctly fitted with the model presented in Equation 1. The real impedance Z' and the negative phase-angle θ are shown in the left and right parts, respectively. The circles are the measured data points and the lines are the fits. The same color scale, corresponding to different fluid conductivities, is used for all samples. The phase spectrum of sample L02 is fitted with a Double Cole-Cole circuit (see Figure S4 (b)).

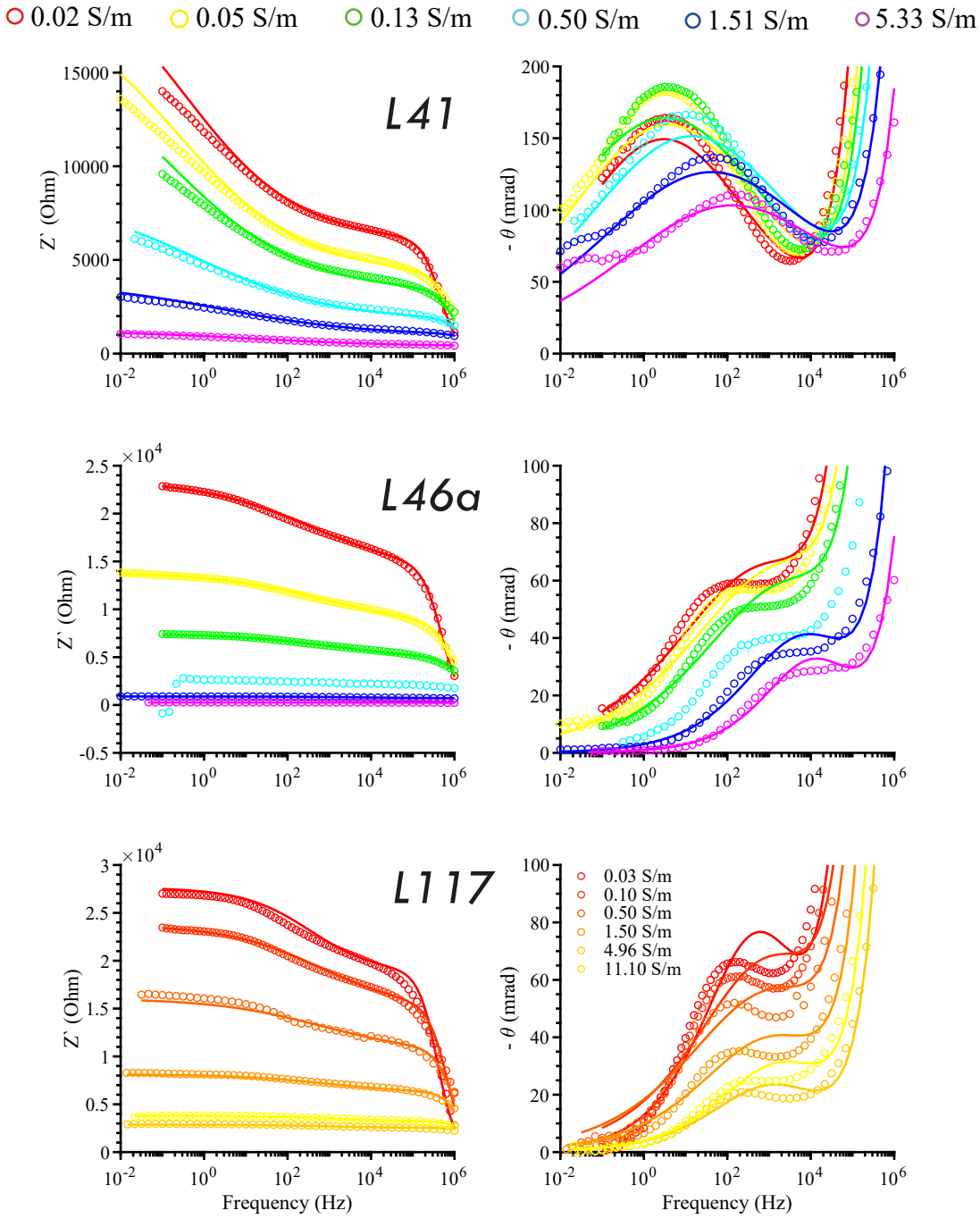

Figure S6: Impedance spectra of three samples, not correctly fitted with the model represented by Equation 1. The real impedance Z' and the negative phase-angle θ are shown in the left and right parts, respectively. The circles are the measured data points and the lines are the fits. The color scale, corresponding to the different pore fluid conductivities, is displayed at the top of the figure for samples L41 and L46a (same scale), and at the bottom for sample L117.

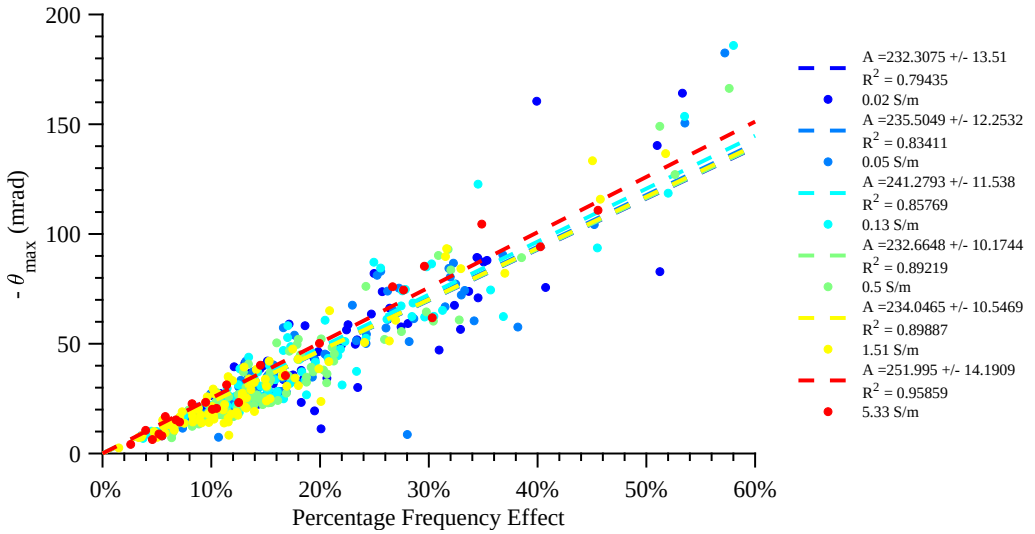

Figure S7: Maximum Phase Angle versus Percentage Frequency Effect, at five pore water conductivities, represented by five colors. The filled circles represent the data and the broken line are the best fitting linear fit (y = Ax), whose slope and regression coefficient are given in the legend. A slope of 242 ± 10 mrad is found at all fluid conductivities.

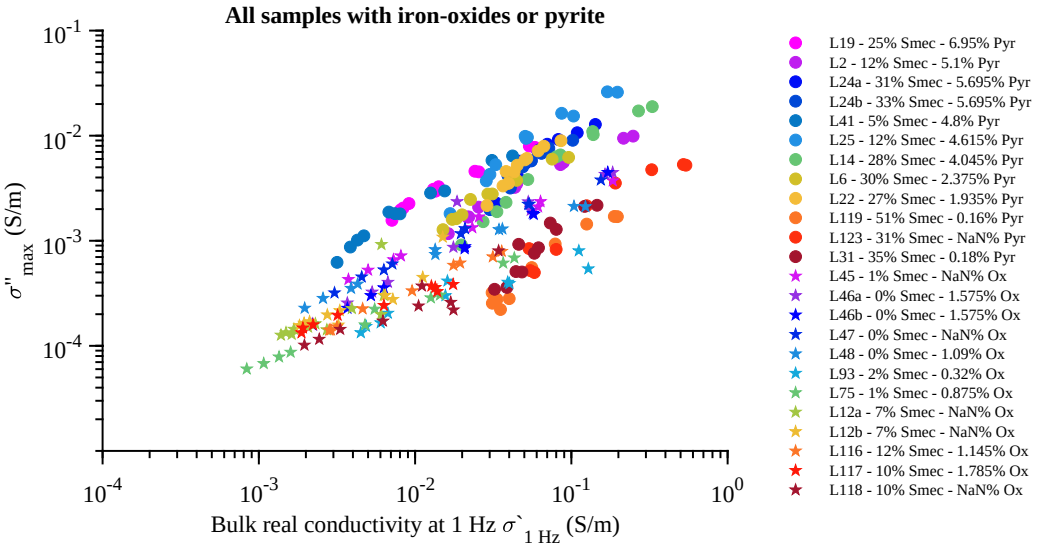

Figure S8: Maximum imaginary conductivity versus bulk real conductivity at 1 Hz for all samples analyzed in the present study and all salinities. Samples containing iron-titanium-oxides (and no or little smectite content) are shown with filled stars, while samples containing sulphides (and very variable smectite volumes) are shown with filled circles.

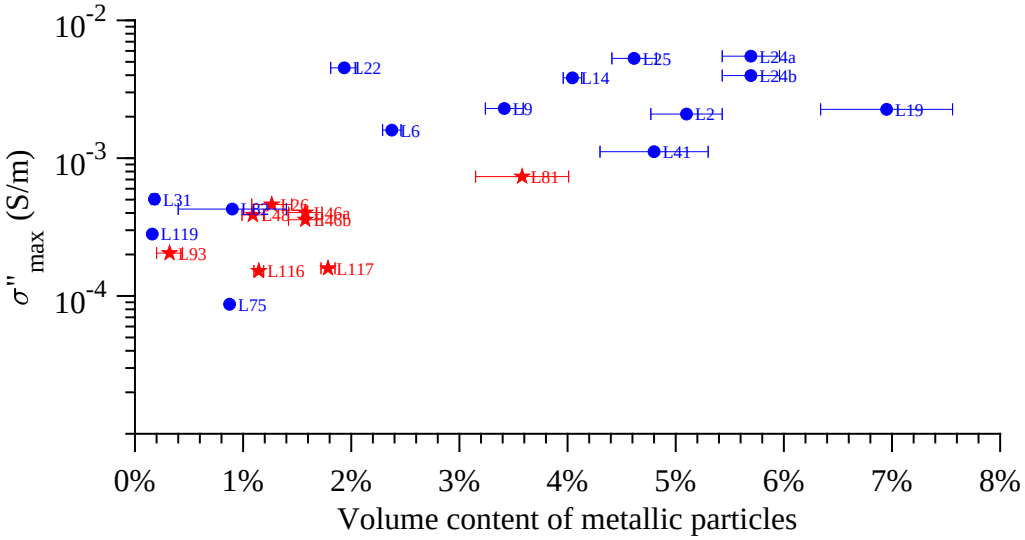

Figure S9: Maximum imaginary conductivity versus volume fraction of metallic particles for samples saturated with pore fluid at 0.13 S/m.

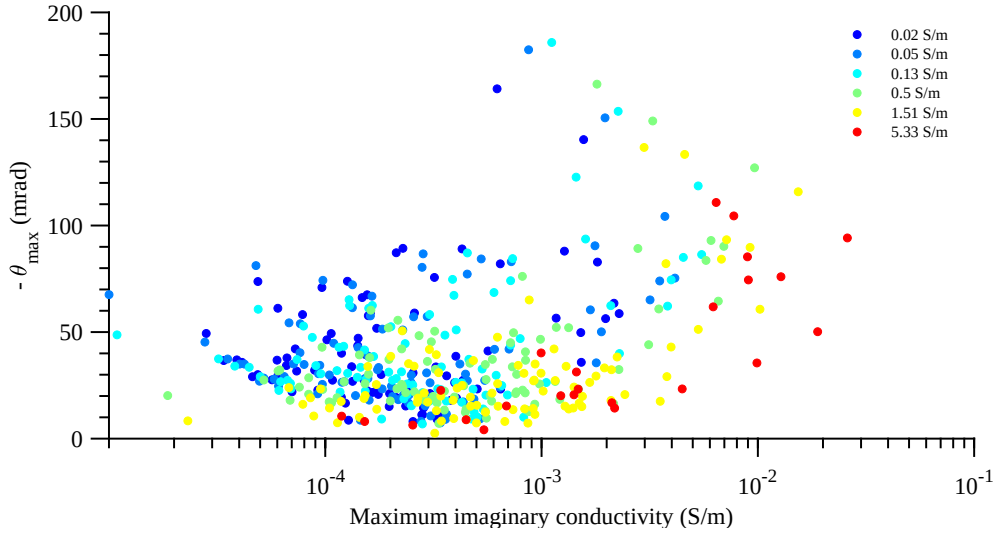

Figure S10: Maximum phase angle versus maximum imaginary conductivity for all samples and all salinities considered in this study.

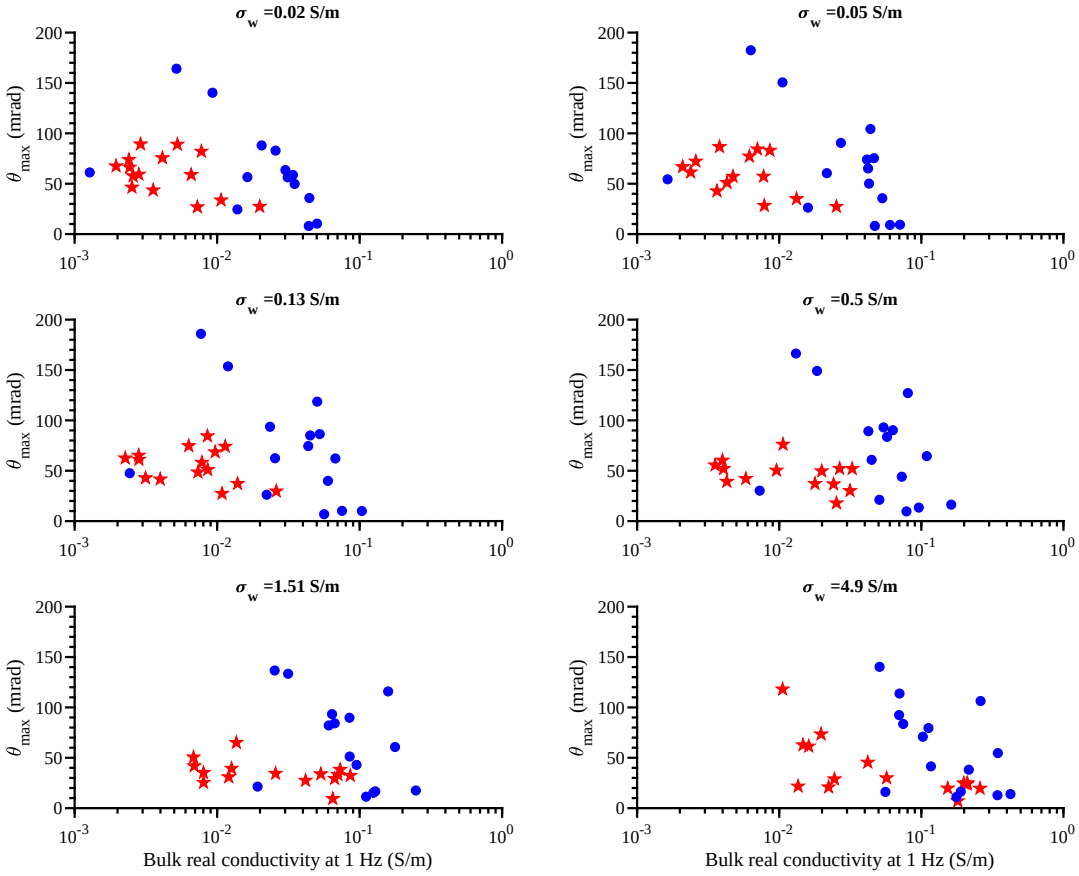

Figure S11: Maximum Phase Angle versus bulk real conductivity at 1 Hz at six distinct pore fluid conductivities. The samples ID are removed for clarity purpose. The discrimination between pyrite and iron-oxides works well for fluid conductivity up to 0.5 S/m.

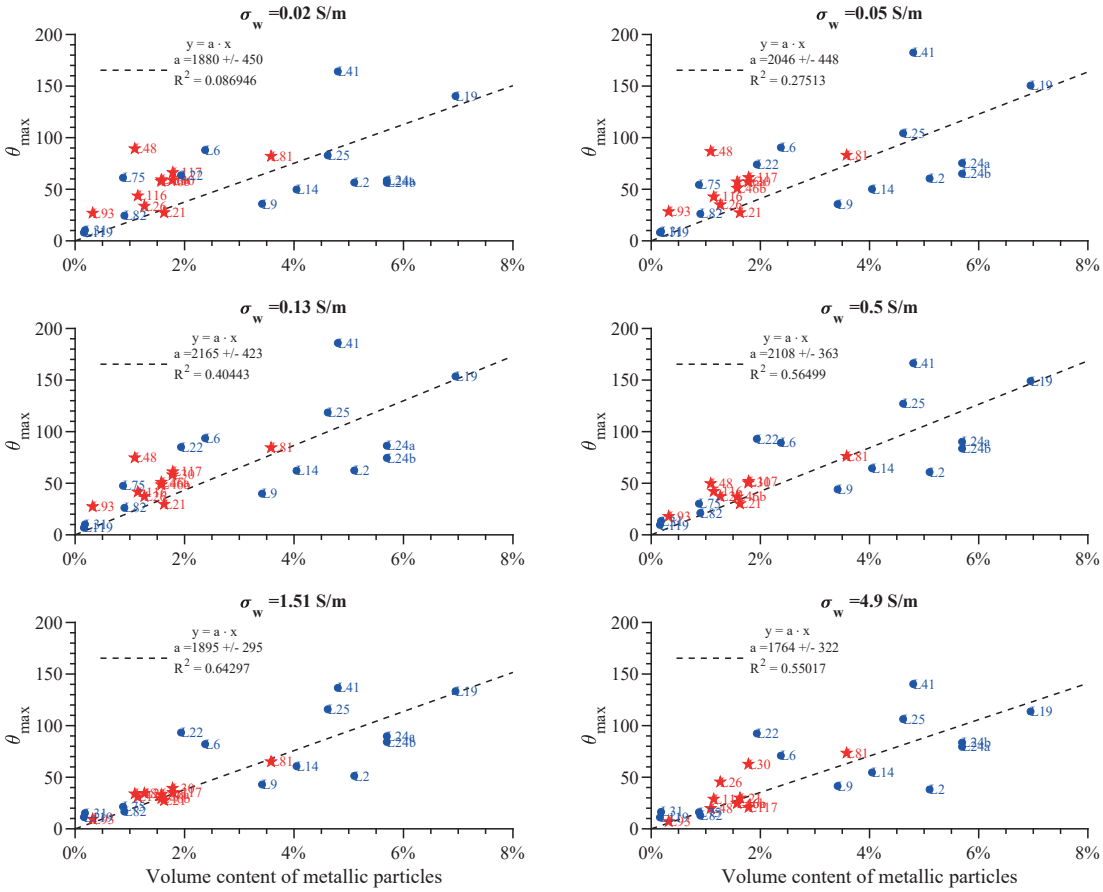

Figure S12: Maximum Phase Angle versus volume of metallic particles at six distinct pore fluid conductivities. The slope and regression coefficients of each fitting line are given on each subplot. The best fitting curve is obtained at the pore fluid conductivity 1.51 S/m

submitted to *Geophys. J. Int.*

Electrical Resistivity Tomography and Time-Domain Induced Polarization field investigations of geothermal areas at Krafla, Iceland: comparison to borehole and laboratory frequency-domain electrical observations

L. Lévy[1 2⋆], P.K. Maurya[3], S. Byrdina[4], J. Vandemeulebrouck[4], F. Sigmundsson[2], K. Árnason[5], T. Ricci[6], D. Deldicque[1], M. Roger[1], B. Gibert[7] and P. Labazuy[8]

[1] *Laboratoire de Géologie, Ecole Normale Supérieure - PSL, CNRS, UMR 8538, Paris 75005, France*

[2] *Nordic Volcanological Center, Institute of Earth Sciences, University of Iceland, 101 Reykjavík, Iceland*

[3] *Institute of Geoscience, HydroGeophysics Group, Aarhus University, Aarhus, Denmark*

[4] *Université Grenoble Alpes, Université Savoie Mont Blanc, CNRS, IRD, IFSTTAR, ISTerre, Grenoble, France*

[5] *ÍSOR - Iceland GeoSurvey, Reykjavik, Iceland*

[6] *Istituto Nazionale di Geofisica e Vulcanologia, Roma, Italy*

[7] *Géosciences Montpellier, Université de Montpellier, Université des Antilles, CNRS, France*

[8] *Université Clermont Auvergne, CNRS, IRD, OPGC, Laboratoire Magmas et Volcans, F-63000 Clermont-Ferrand, France*

Received XX; in original form XX

SUMMARY

Interaction of H_2S and basaltic rocks in volcanic geothermal areas can originate from natural up-flow of magmatic fluids or H_2S artificial re-injection in relation to geothermal exploitation, both causing pyrite mineralisation. We study the possibility to track these processes with electrical impedance field measurements. Electrical Resistivity Tomography (ERT) and Time-Domain Induced Polarization (TDIP) soundings were performed along thirteen 1.24 km-long

profiles, at three different sites around the eastern caldera rim of the Krafla caldera: (i) a "cold altered" site affected by past hydrothermal circulations, (ii) a hot active site and (iii) a "cold unaltered" site, unaffected by hydrothermal circulations. We present two-dimensional inversions of direct current (DC) resistivity, maximum phase angle of the electrical impedance (MPA) and its relaxation time. The maximum depth of investigation for the MPA is 200 m, obtained in zones of high resistivity, corresponding to fresh and recent unaltered basalt. At the hot and cold altered sites, the field resistivities are compared to in-situ borehole logs and laboratory complex resistivity measurements on rock samples from the boreholes. The laboratory complex resistivity was measured at six different pore water conductivities, ranging from 0.02 to 5 S/m, and frequency in the range $10^{-2} - 10^{6}$ Hz. The time-range investigated in our field TDIP measurements was approximately 0.01-8 s.

At the cold altered site, the inverted resistivity is consistent with both borehole observations and laboratory measurements. At the hot site, resistivity from field inversion and borehole logs are consistent. Comparing inversion results and borehole logs to laboratory resistivity measured on core samples at room temperature reveals that a correction coefficient for the effect of temperature on resistivity of 6% per $^{\circ}C$ is appropriate at investigated depths. This exceptionally high temperature-correction coefficient suggests a dominant influence of interface and interfoliar conduction, characteristic of smectite-rich rocks, compared to electrolyte conduction. High MPA is attributed to the presence of pyrite at the hot site and of iron-oxides at the cold unaltered site, through joint consideration of MPA together with DC resistivity and relaxation time. TDIP measurements offer the possibility to detect the presence of metallic minerals at shallow depth and distinguish between pyrite and iron-oxides. The abundance of highly conductive smectite in altered volcanic rocks represents a challenge for resolving IP parameters, as low resistivity created by abundant smectite limits the data quality of the measured voltage decays.

Key words: Induced Polarization – Hydrothermal Systems – Electrical Resistivity Tomography – Hydrogeophysics

⋆ Corresponding author: lea.levy@ens.fr

1 INTRODUCTION

Iron-sulphides (e.g. pyrite) and expandable clays (e.g. smectite) are common secondary minerals in magmatic-hydrothermal systems (Meunier 2005). Their abundant presence is an indication of sustained hydrothermal activity (Patrier et al. 1996; Beaufort et al. 1995; Libbey & Williams-Jones 2013; Gudmundsson et al. 2010). Therefore, mapping underground smectite and pyrite distribution can constrain the location of hydrothermal circulations. Electrical Resistivity Tomography (ERT) is a method of subsurface investigation, which maps the electrical resistivity of the rock matrix filled with pore fluids. The measured conductivity (and its inverse, resistivity) is particularly sensitive to the salinity and temperature of the fluids, but also to the presence of minerals with significant surface or interfoliar conduction, such as smectite (Waxman & Smits 1968; Flóvenz et al. 2005; Lévy et al. 2018). Induced Polarization (IP) is a complementary method, which investigates the electrical charge storage capability of the rock matrix, in addition to the electrical conductivity. IP is particularly sensitive to the presence of sulphides and iron-oxides (Pelton et al. 1978; Gurin et al. 2015) but also to the presence of conductive fluid and clay minerals (Lesmes & Frye 2001; Weller et al. 2013; Gurin et al. 2015). Several studies also suggest that clay minerals, including smectite, have an important IP signal and could be mapped using IP methods (Slater & Sandberg 2000; Leroy et al. 2017; Revil et al. 2017a,b)). However, according to Parkhomenko (1971) and Vinegar & Waxman (1984), the largest induced polarization effects are observed for clay contents in the range 3–10%. Moreover, the recent study by Lévy et al. (2019) on volcanic rocks shows that the polarization associated to altered volcanic rocks decreases when the smectite volume increases, for a given volume of metallic particles. Indeed, electrical conduction occurring through connected smectite particles would prevent polarization to occur (Lévy et al. 2018).

IP can be either measured in frequency-domain (FDIP) or in time-domain (TDIP). In both cases, it is possible to obtain the average relaxation time, in addition to the amplitude of the polarization, usually represented by the chargeability or the phase angle (Orozco et al. 2012; Kemna et al. 2012; Orozco et al. 2018; Maurya et al. 2018; Fiandaca 2018). The relaxation time is the time taken by the charge carriers (ions, electrons or holes, responsible for polarization) to relax,

that is to return to their initial position (Abdulsamad et al. 2017; Bücker et al. 2018; Misra et al. 2016; Revil et al. 2015).

Volcanic rocks can contain iron-oxides, sulphides and clay minerals. Iron-oxides, formed during primary magmatic crystallisation, are mostly present in fresh unaltered basalts, whereas pyrite, smectite (and clay minerals in general) are secondary minerals, more abundant in altered volcanic rocks. Laboratory frequency-domain electrical measurements on core samples from the Krafla volcano (Iceland) show that pyrite can be distinguished from iron-oxides in volcanic environments, because pyrite is associated to low-resistivity (smectite-rich) rocks, whereas iron-oxides are associated to high-resistivity (crystalline and dense) rocks (Lévy et al. 2019). Moreover, pyrite crystals formed by hydrothermal alteration tend to be larger and more connected than iron-oxides, which are usually small and homogeneously disseminated in volcanic rocks. The presence of larger or connected metallic particles leads to longer relaxation times than small and disseminated metallic particles so that relaxation time is another possible discrimination parameter between pyrite and iron-oxides (Pelton et al. 1978; Gurin et al. 2015, 2018; Hupfer et al. 2016). Here, we investigate to what extent results obtained with frequency-domain IP measurements can be used, in practice, to interpret time-domain IP (TDIP) field measurements in volcanic environments.

The Krafla area is well suited for this type of investigation since it is the site of a significant geothermal production and smectites, sulphides and iron oxides can be observed at variable concentrations in the geological formations of the geothermal reservoir. The Krafla volcano is composed of a 15 km diameter central volcano and a 100 km long (and 4 to 19 km-wide) NNE-SSW trending fissure swarm running through it (Ármannsson et al. 1987; Hjartardóttir et al. 2012, 2016). Caldera rims, shown in Figure 1, have been defined by mapping a reddish welded ash flow, of dacitic composition, whose formation is related to the first collapse of the caldera during the early part of the last interglacial period, about 100.000 years ago (Jónasson 1994; Sæmundsson 1983, 1991). About 24.000 years ago, a rhyolitic fissure eruption beneath thin ice inside the caldera formed Hrafntinnuhryggur (1), a 2.5-km-long NNE-SSW trending ridge of obsidian (Sæmundsson et al. 2000; Tuffen & Castro 2009). Except for isolated episodes of rhyolitic volcanism, most of volcanic deposits at Krafla originate from tholeiitic basaltic magmas, with a mineral composition

dominated by olivine, clinopyroxene, plagioclase and minor iron-titanium oxides (e.g. Sigmarsson & Steinthórsson 2007). In general, the geology and tectonics at the Krafla caldera have been extensively studied (Sigmundsson 2006) and allow to put in context the inversion results from near-surface geophysics investigations. Finally, numerous Transient Electromagnetic (TEM) and Magnetotelluric (MT) campaigns have been carried out at Krafla (Gasperikova et al. 2011; Árnason et al. 2007).

The aim of this study is to determine the usefulness of combining ERT and TDIP measurements in volcanic environments for geothermal exploration. The comparative analysis conducted here is based, in an original way, on both ERT and TDIP field measurements around three boreholes, as well as in-situ borehole resistivity observations and laboratory frequency-domain IP measurements on borehole samples. In addition, knowledge of the lithology and mineral composition at the investigated sites, thanks to borehole samples, allows validating the interpretations.

2 MATERIALS AND METHODS

2.1 Study sites

The Krafla high-temperature geothermal field has about 40 production boreholes and several exploration boreholes (including KH1, KS1 and KH3) have also been drilled. Our study focuses on three sites, centred around the KS1, KH1 and KH3 boreholes, which are all on the eastern side of the Krafla caldera. We named the sites according to these boreholes (Figure 1). A total of 13 1.2-km-long profiles were measured with ERT and TDIP: four profiles at KS1 (ISL-1 to ISL-4), all of them parallel, with 100 m spacing in-between; four profiles at KH1, three of them parallel, with 100 m spacing in-between and one of them perpendicular to the others (ISL-10 to ISL-13); five profiles at KH3, all of them parallel, with 50 m spacing in-between (ISL-5 to ISL-9). An additional long ERT profile (LONG) was measured in the continuation of ISL-9 profile all the way to KS1 site. Boreholes KH1 and KH3 were cored down to 200 and 400 m, respectively, while borehole KS1 was drilled down to 2.5 km and drill-cuttings were retrieved. Steel casings are present in boreholes KS1, KH3 and KH1, down to 900, 30 and 12 m, respectively.

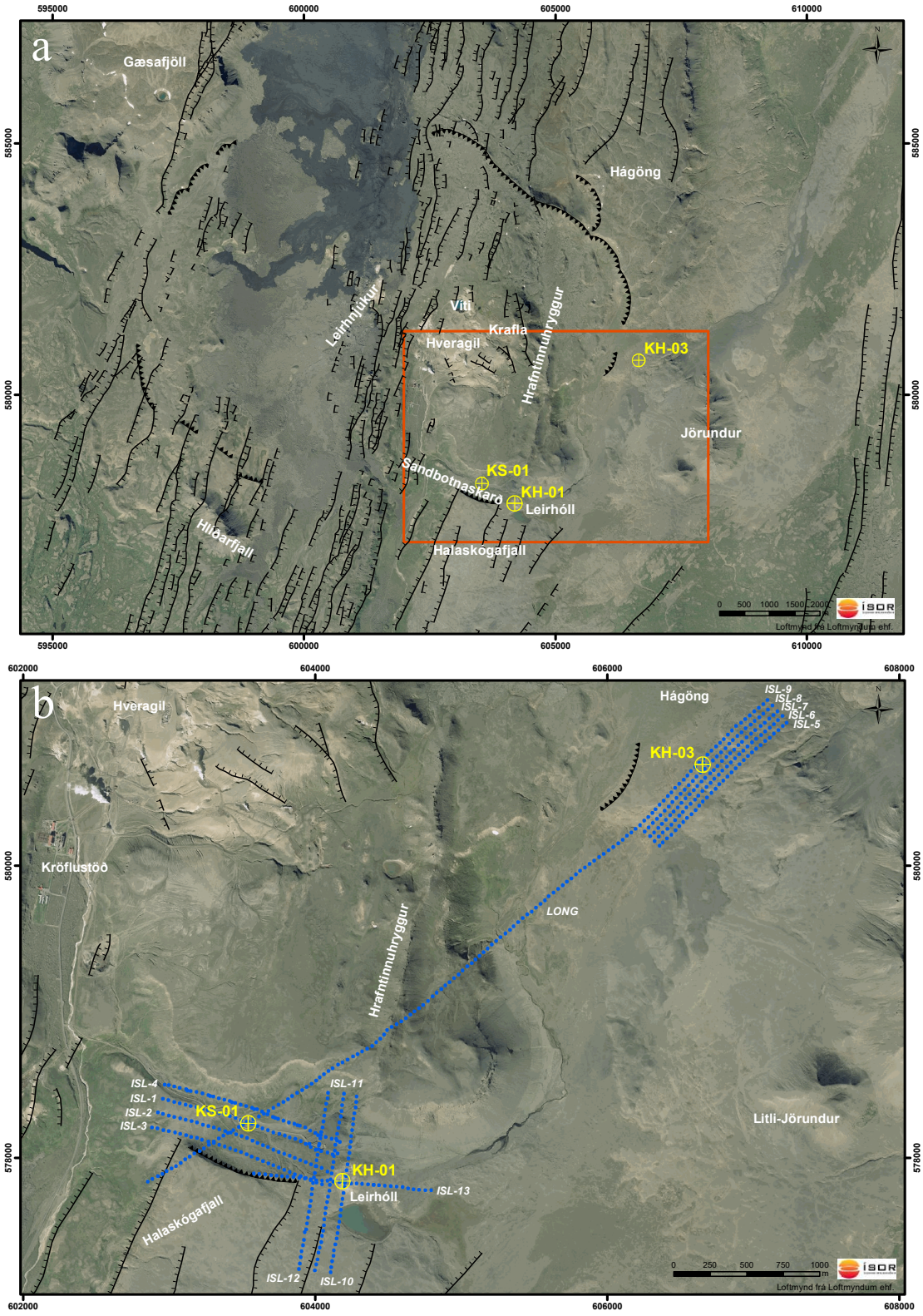

Figure 1. Krafla caldera: (a) aerial map of the Krafla central volcano, with known caldera rims and faults represented as black lines (Saemundsson et al. 2012) and boreholes used in this study as yellow circles with crosses; (b) zoom on the eastern part where the geoelectric soundings were performed. The blue markers indicate the position of electrodes along the profiles. The geothermal power plant operated by Landsvirkjun is marked by the white name Kröflustöð.

2.2 Laboratory observations

A total of 25 and 13 core samples from boreholes KH1 and KH3, respectively, were available for comparison to field measurements (Table 1). Amongst the 25 samples from KH1 used in this study, F58 and F61 were analysed by Flóvenz et al. (2005) and Kristinsdóttir et al. (2010). The rest of the samples were analysed by Lévy et al. (2018) and Lévy et al. (2019), who provide estimates of the overall mineral distribution, influence of clay minerals on in-phase electrical conductivity at 1 kHz and influence of sulphides and iron-oxides on the spectral measurements of the phase angle and the real part of the impedance.. The host rock of the cores varies from volcanic glass (sub-glacial eruptions) to crystalline basalt (centre of lava layers or dykes).

Table 1: Main characteristics of the 38 samples used for comparison to field data. BH = borehole. Columns 4 to 7 give the measured conductivity at different pore fluid conductivities, in S/m.

Sample	BH	Depth (m)	$\sigma_{0.02S/m}$	$\sigma_{0.05S/m}$	$\sigma_{0.1S/m}$	$\sigma_{0.5S/m}$	Lithology
L12a	KH1	70	1.39E-03	1.49E-03	1.62E-03	2.30E-03	dense lava
L12b	KH1	70	1.82E-03	1.95E-03	2.11E-03	3.30E-03	dense lava
F58	KH1	187.5	2.06E-03	1.96E-03	2.41E-03	3.30E-03	dyke
L5b	KH1	45.3	2.59E-03	2.86E-03	2.93E-03	4.24E-03	ignimbrite
L30	KH1	185.1	4.13E-03	4.87E-03	4.91E-03	6.01E-03	dyke
L19	KH1	120.3	7.11E-03	8.08E-03	9.13E-03	1.41E-02	dense basalt
L5a	KH1	45.3	7.61E-03	8.76E-03	9.27E-03	1.41E-02	ignimbrite
L26	KH1	157.9	8.53E-03	1.06E-02	1.11E-02	1.43E-02	lava layer
L28	KH1	167.1	8.89E-03	1.06E-02	1.09E-02	1.26E-02	dense basalt
L29	KH1	174.3	1.14E-02	1.36E-02	1.49E-02	1.98E-02	lava layer
L15	KH1	79.5	1.29E-02	1.58E-02	1.54E-02	1.95E-02	lava layer
L16	KH1	99	1.44E-02	1.59E-02	1.55E-02	1.90E-02	lava layer
L21	KH1	125.5	1.50E-02	1.90E-02	1.96E-02	2.37E-02	lava layer

L6	KH1	48.8	1.51E-02	2.00E-02	1.73E-02	3.12E-02	welded breccia
L2	KH1	39.5	1.63E-02	2.16E-02	2.55E-02	4.47E-02	welded breccia
L25	KH1	151.3	1.67E-02	2.85E-02	3.28E-02	5.23E-02	dense altered basalt
L11	KH1	68.7	2.04E-02	2.54E-02	2.61E-02	3.31E-02	lava layer
L10	KH1	66	2.05E-02	2.53E-02	2.42E-02	4.05E-02	lava layer
L14	KH1	74.5	2.72E-02	3.34E-02	5.26E-02	8.50E-02	altered hyaloclastite
L22	KH1	131.1	2.88E-02	3.96E-02	4.30E-02	5.19E-02	lava layer
L24b	KH1	144.1	3.01E-02	4.06E-02	4.20E-02	5.52E-02	altered hyaloclastite
F61	KH1	195	3.19E-02	3.03E-02	3.28E-02	4.04E-02	altered hyaloclastite
L31	KH1	188.5	3.23E-02	3.86E-02	4.83E-02	6.16E-02	altered hyaloclastite
L24a	KH1	144.1	3.31E-02	4.51E-02	5.10E-02	6.13E-02	altered hyaloclastite
L9	KH1	60	3.89E-02	4.65E-02	5.25E-02	6.38E-02	altered hyaloclastite
L116	KH3	41.75	2.82E-03	2.89E-03	3.16E-03	4.62E-03	dense and fresh basalt
L117	KH3	47.8	1.91E-03	NaN	2.22E-03	3.19E-03	dense and fresh basalt
L118	KH3	54.25	1.96E-03	NaN	2.44E-03	3.32E-03	dense and fresh basalt
L119	KH3	60.4	3.12E-02	3.34E-02	4.00E-02	5.58E-02	altered hyaloclastite
L120	KH3	70.8	1.35E-02	1.50E-02	1.95E-02	3.49E-02	altered hyaloclastite
L121	KH3	72.7	2.40E-02	2.79E-02	3.80E-02	6.21E-02	altered hyaloclastite
L122	KH3	83.1	2.00E-02	2.40E-02	3.17E-02	5.83E-02	altered hyaloclastite
L123	KH3	91.8	-	5.46E-02	7.99E-02	1.25E-01	altered hyaloclastite
L157	KH3	100	-	1.41E-02	-	-	basaltic breccia
L158	KH3	114	-	8.93E-03	-	-	basaltic breccia
L35	KH3	151.2	9.59E-03	1.33E-02	1.54E-02	1.93E-02	basaltic tuff
L36	KH3	273.4	1.91E-03	2.28E-03	2.74E-03	5.97E-03	buried fine grained lava
L37	KH3	325.1	7.03E-03	7.65E-03	9.36E-03	1.92E-02	buried fine grained lava

Borehole KH1 shows alternating layers of very altered volcanic glass, altered basaltic breccia and dense crystallised layers. The rock is overall very fractured and evidence of boiling (e.g.

platy calcite, amorphous silica) is found in fractures. The dominant mineralogy is composed of secondary minerals: smectite, zeolites, quartz, calcite and pyrite. Primary minerals, such as plagioclases, pyroxenes and iron-oxides are, however, sometimes observed in crystalline samples with little alteration (centre of lava flows or dykes, less exposed to fluid flow).

Borehole KH3 has an uppermost dense layer (31-58 m), composed of fresh and crystalline basaltic lava, which mostly contains pyroxenes, plagioclases and iron-oxides (formed during magmatic crystallisation), followed by a very altered layer (58-96 m) of former volcanic glass, named hyaloclastite. This second layer contains up to 50 wt. % of smectite. Below this layer, basaltic breccia and lava flows are observed, mostly unaltered below 150 m. In general, little fracturation is observed.

No cores were available in borehole KS1 but geological observations of drill-cuttings indicate that the first 350 m are mostly composed of fresh volcanic glass and fresh basaltic lava containing abundant iron-oxides. No evidence of hydrothermal alteration is found above 350 m (Gudmundsson et al. 2007).

The frequency-domain electrical impedance of the core samples was measured in the laboratory with a Solartron 1260 impedance-meter and a 4-electrode set-up, where the voltage (non-polarizable Ag/AgCl) and current (nickel) electrodes are separated. The quality of the impedance-meter calibration is illustrated in Supporting Information (Figure S1) with a comparison between measurements and predictions for three networks of ideal resistors and capacitors of known impedance. The uncertainty of the phase-angle measurement is estimated to be 1 mrad, based on measurements of water-filled sample-holder with water at different salinities (Supporting Information, Figure S2). More details on the saturation procedure and electrical measurements can be found in Lévy et al. (2018) and Lévy et al. (2019).

2.3 In-situ borehole observations

In-situ temperature logs were obtained shortly after drilling, in 1991, 2003 and 2007 for KH1, KH3 and KS1, respectively. We consider that the temperatures are similar at the time of our experiments. In borehole KS1, a temperature below 40°C is observed in the first 300 m but reaches 300°C at

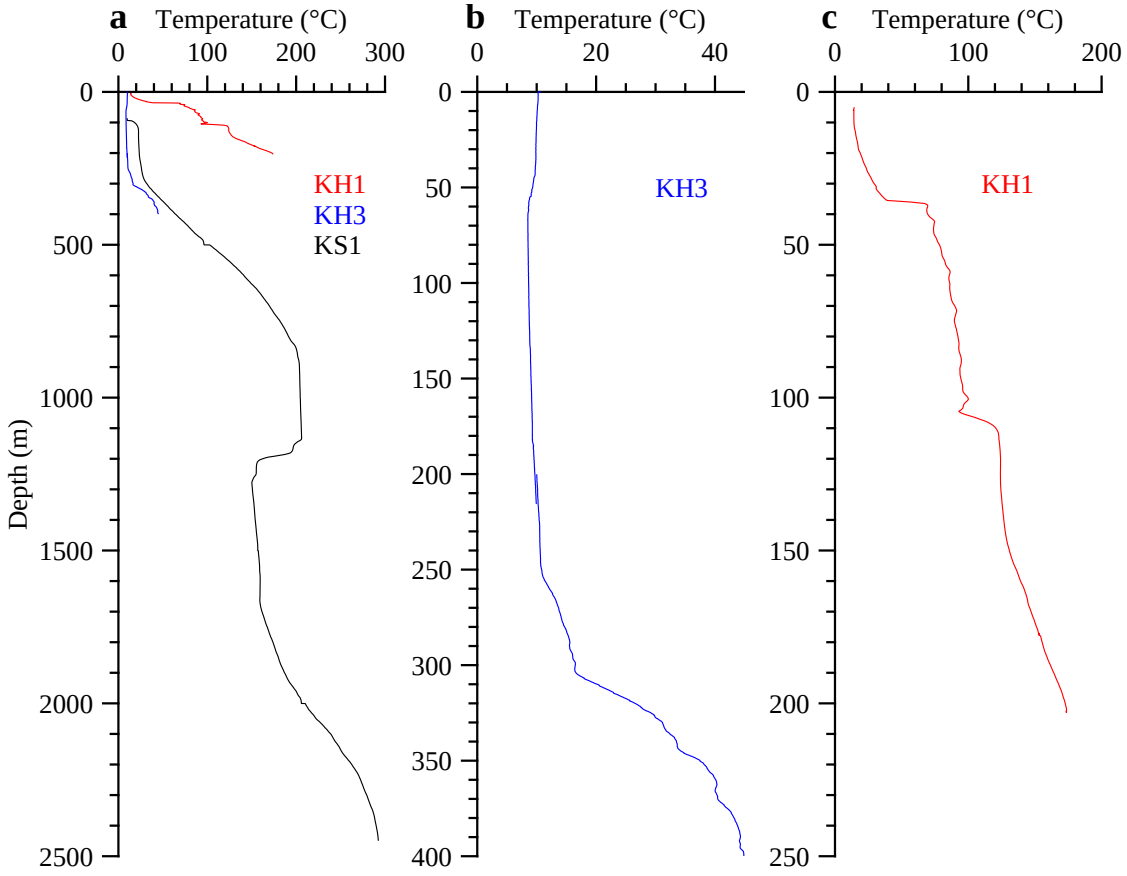

Figure 2. Temperature profiles in (a) boreholes KH1, KH3 and KS1, (b) borehole KH3 and (c) borehole KH1. Note the different scales in depth and temperature in the three figures. The temperature profiles of KH1 (hot) and KH3 (cold) are shown in red and blue, respectively.

2500 m depth (Figure 2). In KH3, the temperature is about 10°C in the first 250 m. On the other hand, a strong temperature gradient is observed in KH1, with the temperature reaching 175°C at 200 m depth.

Electrical logs were measured with a 16/64 probing tool along the entire depth-range in KH1 (200 m) but only above 140 m in KH3 and only below 300 m in KS1 (Gudmundsson 1991; Jónsson et al. 2003; Gudmundsson et al. 2007). The 16/64 probing tool measures the electrical resistivity every 50 cm. It uses the so-called normal electrode configuration, where the current electrode B is connected to the ground at the surface and current electrode A is at the bottom of the probe. Potential electrodes M an N are both in the borehole and the fixed distance of 22 meters between M and N is considered to be infinite. The electrode spacing is defined as the distance between A

(current) and M (potential) and can be either 16 inches or 64 inches. (Helander 1983). The 16-inch measurement is more sensitive to local heterogeneity than the 64-inch measurement. The names "shallow" and "deep", commonly used for 16-inch and 64-inch, respectively, refer to the horizontal distance of penetration into the rock matrix. The true resistivity, corrected for the resistivity of the water inside the borehole, is not considered in our case so that there is a possible constant shift in the resistivity values obtained from logging. Neutron-Neutron (NN) logs were measured along the whole depth-range in KH1 and KH3 but only below 300 m in KS1. The NN logging tool is composed of a neutron-source (radioactive Americium-Beryllium in our case) and a neutron-receiver, which measures the number of counts (number of neutrons arriving) per second (cps) (Scott 1984).

2.4 Field measurements

2.4.1 Background on ERT and TDIP

Electrical Resistivity Tomography (ERT) consists of injecting a Direct Current (DC) along a profile, through grounded electrodes (A and B) and measuring the resulting voltage at two other electrodes (M and N), as presented in Figure 3. The quadrupole A-B-M-N is selected at each step of the acquisition protocol from the electrodes available on the profile. For each quadrupole, the apparent resistivity ρ_a is calculated by Equation 1.

$$\rho_a = k\frac{V_M - V_N}{I_{AB}} \tag{1}$$

where I_{AB} is the current injected between electrodes AB, V_M and V_N the potentials measured at electrodes M and N, respectively, and k the so-called geometrical factor, defined in Equation 2 (e.g. Bertin & Loeb 1976).

$$k = \frac{2\pi}{\frac{1}{AM} - \frac{1}{AN} - \frac{1}{BM} + \frac{1}{BN}} \tag{2}$$

Each apparent resistivity measurement averages the true resistivity of the Earth down to the penetration depth of the electrical current, which depends on the intensity of the current injected, the electrode configuration, but also the conductivity of the medium and the period of the electrical

signal in case of a sinuisoidal current (e.g. Telford et al. 1990). A convenient means to display results of ERT measurements at a profile is a two-dimensional "pseudo-section" plot, which is obtained by placing each apparent resistivity measurement at a horizontal mid-point and a pseudo-depth (Loke & Barker 1996). The pseudo-depth is defined as the median "effective" depth of investigation of the array and is calculated based on the Frechet derivatives for a homogeneous half space (Loke 2004; Edwards 1977; Menke 2012). It can be understood as the depth at which one half of the signal originates from above and the other half from below (Okpoli 2013).

Time-Domain Induced Polarization (TDIP) consists of analysing the time-dependent voltage signal, recorded with an appropriate sampling rate (e.g. 1000 Hz or more). Upon injection of a square-wave current, a voltage progressively builds up when the current is on, during the "charge" T_{on}, and progressively decreases to zero when the current is turned off, during the "discharge" T_{off}. The integral apparent chargeability <M> in msec, in a given time-window, is calculated with Equation 3 (e.g. Bertin & Loeb 1976; Sumner 1976). <M> represents the area enclosed by the discharge curve and its zero asymptote during this time-window, divided by the primary voltage V_p.

$$< M >= \int_{t_1}^{t_2} \frac{V(t)}{V_p} dt \tag{3}$$

where t_1 and t_2 delimits the integration window and $m_0 = \frac{V(t)}{V_p}$ (mV/V) is the apparent chargeability at a time t.

Smaller integral apparent chargeability are observed when smaller injection times are used, due to the finite length of the current pulse and in particular the fact that the voltage at the end of T_{on} is not yet maximum (Olsson et al. 2015; Fiandaca et al. 2012). An example of this effect is illustrated with our field data in Supporting Information (Figure S3). Therefore, the exact waveform of the transmitted current needs to be taken into account in the inversion, including in particular T_{on} and the number of pulses (Bertin & Loeb 1976).

Capacitive and inductive coupling are common sources of noise in TDIP. Capacitive coupling can be reduced by using two distinct cables for current injection and potential measurement (Dahlin & Leroux 2012). Inductive coupling is particularly important in nested arrays and increases with the distance between electrodes and the conductivity of the ground, but mostly takes

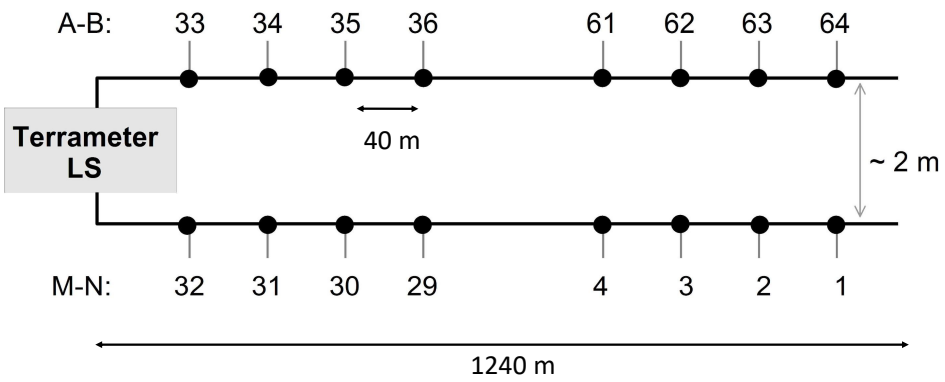

Figure 3. Multicable setup for ERT - TDIP measurements with cable separation to reduce the capacitive coupling. The electrodes 1-32 are used as potential electrodes (M-N), while electrodes 33-64 are used as injection electrodes (A-B). Some sets of measurements were recorded with the reciprocal configuration: 1-32 for current and 33-64 for voltage, in order to verify the symmetry of the measurement. As an example, the ABMN electrode numbers of the first measurement for a Wenner configuration are: 64 61 2 3.

place in the early times after current turn-off (Ingeman-Nielsen & Baumgartner 2006; Dahlin & Leroux 2012).

The spectral IP signal can be obtained from both frequency-domain (FDIP) and time-domain measurements (TDIP) in the field (e.g. Maurya et al. 2018). The former is more time-consuming and thus can only cover small areas The latter contains noise from more sources (Olsson et al. 2016; Gazoty et al. 2013). Moreover, the spectral content of the latter is more difficult to obtain, although this is currently debated (Fiandaca 2018).

2.4.2 Data acquisition

Two 1.24 km-long parallel cables, with 50 cm-long steel electrodes grounded every 40 meters, were connected to an ABEM Terrameter LS instrument: one cable for current injection and another one for voltage measurement (Figure 3). The setup, adapted from Dahlin & Leroux (2012), avoids most of the capacitive coupling effects while working with a single instrument.

A square-wave current, ranging from 15 to 300 mA, was injected by the ABEM Terrameter instrument through electrodes A and B, using different current-on times (T_{on}), in the range 0.4-

4 s and current-off times (T_{off}), in the range 1-8 s. The on-off pulse was repeated with reverse orientation (negative current) and the whole cycle was repeated (stacked) five times, in average. The voltage was measured at electrodes M an N by the Terrameter instrument, both in the on-time for direct current (DC) resistivity measurement and in the off-time for voltage decay acquisition (1000 Hz sampling rate). Two types of electrode configurations were used for each profile: Wenner for its best signal-to-noise ratio and multi-gradient for its redundancy and efficiency when using a multi-channel instrument (Dahlin & Zhou 2006). The particular mid-point and pseudo-depth definitions for the multi-gradient array can be found in Dahlin & Zhou (2006). Different injection times were used: 0.4, 1.5 and 4 s, in order to better resolve the relaxation times (see Supporting Information, Figure S3) and reciprocal measurements were carried out with the 0.4 s injection time. The response of up to 264 quadrupoles was measured for each injection time, where one quadrupole corresponds to one position of electrodes A-B-M-N.

Water mixed with large amounts of dissolved sodium chloride was added around the electrodes to lower the contact resistance between ground and electrodes. For profiles at KH1, bentonite was also used for the same reason. Contact resistances of electrodes were tested before each acquisition, using a current of 20 mA, and were below 1 kΩ most of the time.

2.4.3 Data processing and inversion

Current is injected for a limited time only and does not follow an infinite step function, as assumed by theory (Olsson et al. 2015). Different acquisition settings cause different decays: smaller integral chargeability are observed when smaller injection times are used (Supporting Information, Figure S3). For this reason, the waveform of the transmitted current needs to be taken into account in the inversion. The 2D inversion code developed by Fiandaca et al. (2013) has incorporated this option, as well as the possibility to model the full voltage decay in order to retrieve the spectral content of the IP signal from time-domain data sets, instead of only the integral chargeability. This code, integrated in the software AarhusInv (Auken et al. 2014), was chosen for the inversions of TDIP data. Since the topography is considered in the inversions, the vertical axes of the two-dimensional profiles are displayed in terms of meters above sea level (m a.s.l) instead of depth.

The recorded full waveform data sets were re-processed using the signal processing scheme presented by Olsson et al. (2016). Re-processing full waveform data includes: (i) integrating the DC resistivity during the last 10 or 100 msec of the on-time, instead of the entire on-time; (ii) gating the voltage decay in the off-time starting at 1 msec, instead of 80 msec; (iii) correcting for background drift due to spontaneous polarization and electrode polarization, using a Cole-Cole model, instead of a linear model and (iv) spikes removal at early recording times to increase the time window of usable IP signal. A high background drift was observed at late recording times (after one second), probably due to a spontaneous potential generated by hydrothermal circulation. Flows of salty water could explain the background drift if the volumes investigated (electrode spacing) were small compared to the volume where the salty water penetrated. In the present field setup, where 40 m spacing between electrodes is used, the influence of salty water seems unlikely. Following Olsson et al. (2016), we used a drift model based on Cole-Cole model that describes the depolarization phenomenon, to remove the background drift from the IP signal. We use the time-domain expression of Cole-Cole model by Pelton et al. (1978) to model the drift potential in full waveform data.

The re-processed tasks were then filtered, using the software Aarhus Workbench, in order to remove outliers. For each quadrupole of each profile, apparent chargeability curves or part of the curves showing a non-decaying behaviour, were filtered out manually. After manual processing, the time of the earliest usable signal varied from 10 to 100 ms. No removal of electromagnetic coupling was performed, since the first milliseconds of the recorded signal were always unused.

At KH3, most of the discharge curves recorded were noisy, over the whole time-range and along the five profiles. A conductive near-horizontal body seems to be associated with particularly noisy voltage discharge curves, while clean IP decays are observed outside this body (Figure 4). Below the conductive body, IP data were unusable. The remaining IP pseudo-sections after filtering the noisy voltage discharge curves, over the fives profiles at KH3, were considered not sufficient to resolve the IP parameters and only DC resistivity was inverted at this site.

For IP inversions at the other sites (KH1 and KS1), the following acquisitions settings were retrieved for each quadrupole and used to model the waveform of the transmitted current in the

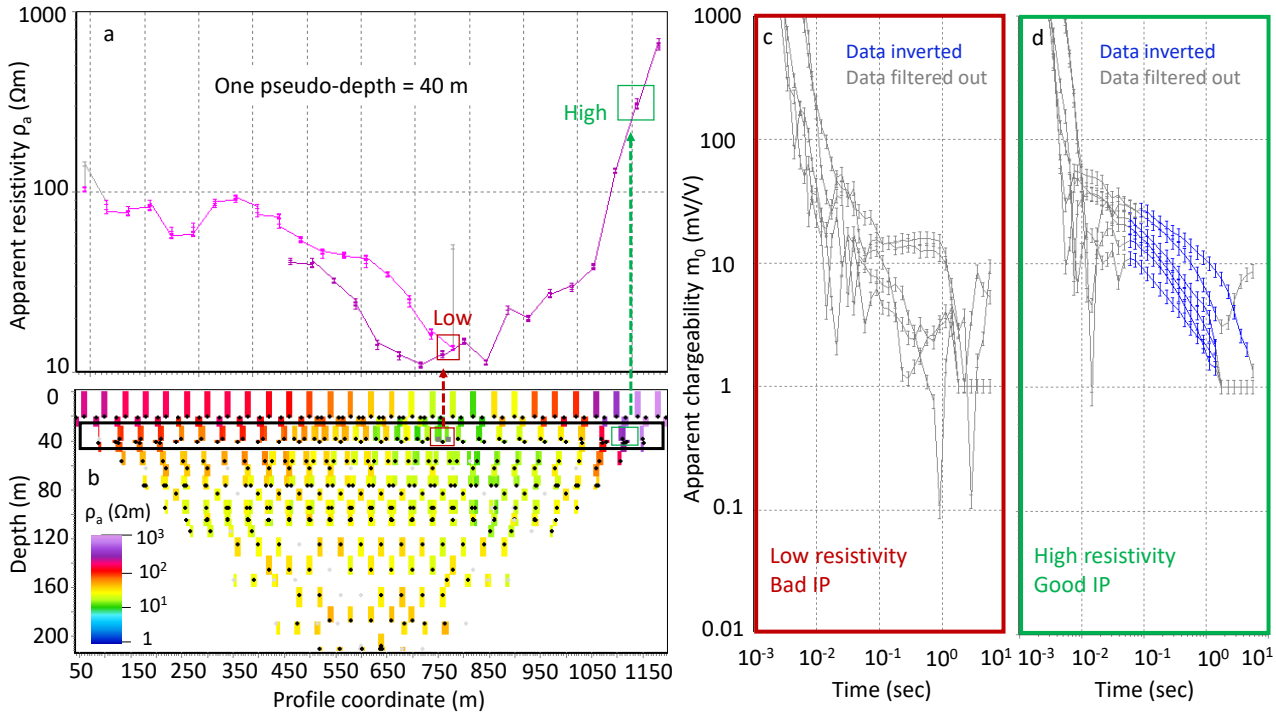

Figure 4. Visualisation of the apparent resistivity and chargeability data at profile ISL-5, using the software Aarhus Workbench. Panels (a) and (b) show apparent resistivity, at one pseudo-depth and over the complete pseudo-section, respectively.Panels (c) and (d) show the chargeability as a function of time, for data points selected in (a). Panel (d) corresponds to datapoints with high resistivity and good quality voltage decays (green rectangle in panel (a)). Panel (c) corresponds to data points with low resistivity and noisy voltage decays (red rectangle in panel (a)).

inversion: number of pulses, injected current, on-time, off-time, DC integration starting time, DC integration end time.

Inversion of TDIP data was performed using the re-parametrised "maximum phase angle" (MPA) model suggested by Fiandaca et al. (2018) because less correlation exists between IP parameters in this model compared to the standard Cole-Cole model. The MPA is a more straightforward parameter to obtain from laboratory measurements than the chargeability since no a priori model is required (see discussion in Lévy et al. (2019)). The polarization phase angle is negative because the IP voltage lags the current. The phase angle represents polarization as a momentarily "frozen" impedance vector (Sumner 1976). With MPA parametrisation, the model space consists of DC resistivity, ρ_0, maximum phase angle, ϕ_{max}, relaxation time, τ_ϕ (inverse of the angular frequency at which the phase angle reaches a maximum) and frequency exponent, c. The exponent

c was not used for interpretations. We also carried out inversions using the classical Resistivity Cole-Cole parameterization, in order to compute the normalized chargeability. We show inversion results using this parametrization for one profile at KH1 site in Supporting Information (Figure S4).

The depth of investigation (DOI) computation in AarhusInv is based on approximate covariance analysis, following Fiandaca et al. (2015). The analysis takes the noise in the data and the final derived model into account. In the results sections, DOI is shown as conservative (shallow) and less conservative (deeper). For each inversion, a dimensionless data misfit χ is calculated, using Equation 4.

$$\chi = \sqrt{\frac{1}{N}\sum_{i=1}^{N}\frac{(d_{obs,i} - d_{fwd,i})^2}{\delta_{d_i}^2}} \tag{4}$$

where d_{obs}, d_{fwd}, δ_d and N are the logarithm of the observed (measured) data, logarithm of the forward prediction, standard deviation of the observed data and number of data points, respectively. Standard deviation of resistivity is estimated as 2% of the resistivity value and is calculated by Equation 5 for IP parameters.

$$\delta_{d_{IP}} = \frac{V_{threshold}}{V_{IP}}\frac{1}{\sqrt{stk}}\frac{1}{\sqrt{\frac{gwd}{10}}} \tag{5}$$

where $\delta_{d_{IP}}$, $V_{threshold}$, V_{IP}, stk and gwd are the standard deviation of IP parameters in a given gate, the nominal noise floor for 10 ms integration time (gate width) and one stack (in mV), the voltage value for a given gate (in mV), the stack size (dimensionless) and the gate width (in msec but normalized to 10 msec so that gwd/10 is dimensionless), respectively. The parameter $V_{threshold}$ is adjusted manually until a suitable noise model is obtained for each IP gate.

In TDIP, negative voltage decays can be observed and modelled by AarhusInv (Fiandaca et al. 2019). However in our field measurements, negative voltage decays could not be correctly fitted with IP inversion. Therefore, we attributed these negative data to poor data quality and did not include them in the inversions.

3 RESULTS

Different types of data sets are analysed in this section. The complex resistivity inversion models from time-domain field data are presented for each of the three sites separately. KS1, where IP data of best quality are recorded, is presented first. KH3, where the noisiest IP discharge curves are recorded, is presented at last. At KH1 and KH3, resistivity inversions are compared to in-situ resistivity measured in the boreholes with the 16/64 logging tool. Then, laboratory measurement of resistivity and phase-angle, at room temperature, are presented. These laboratory measurements are compared to field inversions and in-situ logs, in order to evaluate the consistency between laboratory and field values. Finally, relationships between resistivity, maximum phase angle (MPA), relaxation time and mineralogy, resulting from frequency-domain laboratory observations, are used to support the interpretation of field inversions.

The investigated area is characterised by a caldera boundary, hydrothermal alteration, large groundwater flow, and is affected by both basaltic and rhyolitic fissure eruptions and volcano-tectonic rifting episodes. These features result in large resistivity contrasts, with resistivity as low as a few Ωm where active hydrothermal circulations take place, and up to 10^4 Ωm, corresponding either to the obsidian ridge "Hrafntinnuhryggur" or to a near-surface layer above the ground water level (Figure 5). The colour scale used here shows low resistivity in blue.

3.1 KS1 site: cold and unaltered

Profiles ISL-1 and ISL-4 (north of borehole KS1) show a high-resistivity body over the whole section, down to the DOI. Profile ISL-2 (south of borehole KS1) shows a low-resistivity structure on their southeastern edge (Figure 6). Profile ISL-3 is very similar to ISL-2 both in terms of data pseudo-section and inversion models. The inversion results can be seen in the three-dimensional view presented in subsection 3.5.

A high MPA is observed at the centre and western edge of ISL-1 and ISL-4: up to 80 mrad at 120 m depth and 50 mrad at 140 m depth, respectively (Figure 6). ISL-2 and ISL-3 show less MPA contrast than ISL-1 and ISL-4. The low MPA observed at the centre of ISL-1 profile is local

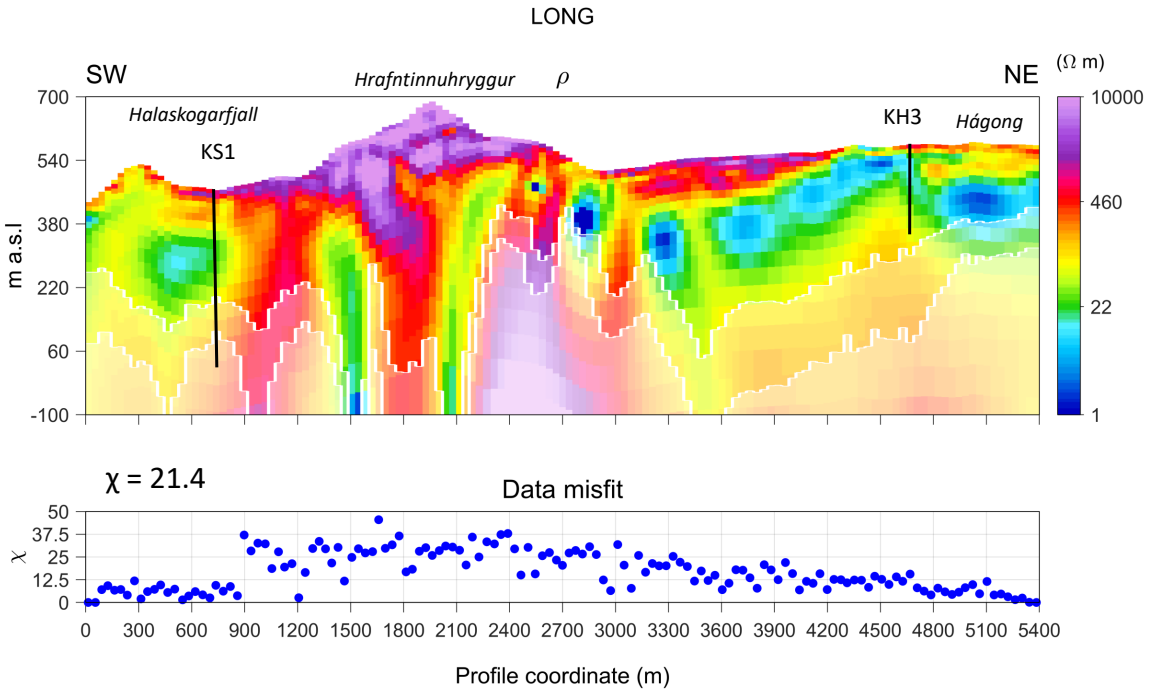

Figure 5. Two-dimensional resistivity inversion of the LONG profile, showing the overall resistivity structure of the area. The lower panels give the data misfit χ for each vertical section of the model (spaced every 40 m). The two white lines in the lower part of the figure represent the shallow and deep DOI.

features not seen at neighbouring profiles. As ISL-1 profile is the closest to KS1 borehole, we cannot rule out an artefact related to the 900 m long steel casing in this hole.

Short relaxation times, down to 0.02 s at elevation 400 m (depth 50 m) are observed on profile ISL-1 and, to some extent, ISL-2 and ISL-4 (Figure 6).

The IP data quality at site KS1 is the best of the three sites, as can be observed on the IP data pseudo-sections, the DOI and the residuals of all profiles. Unfortunately, neither cores nor borehole observations, at depths relevant for comparison to field data, are available at KS1.

3.2 Site KH1: hot and altered

The inverted resistivity models from profiles ISL-10, ISL-11 and ISL-12 highlight a central low-resistivity body from the surface to the DOI (Figure 7), with a resistivity in the range 5-10 Ωm over the whole body. In comparison, the surrounding region is very resistive, up to 10^4 Ωm at the surface, where dry basaltic rocks dominate. The resistivity values obtained from the inversions of

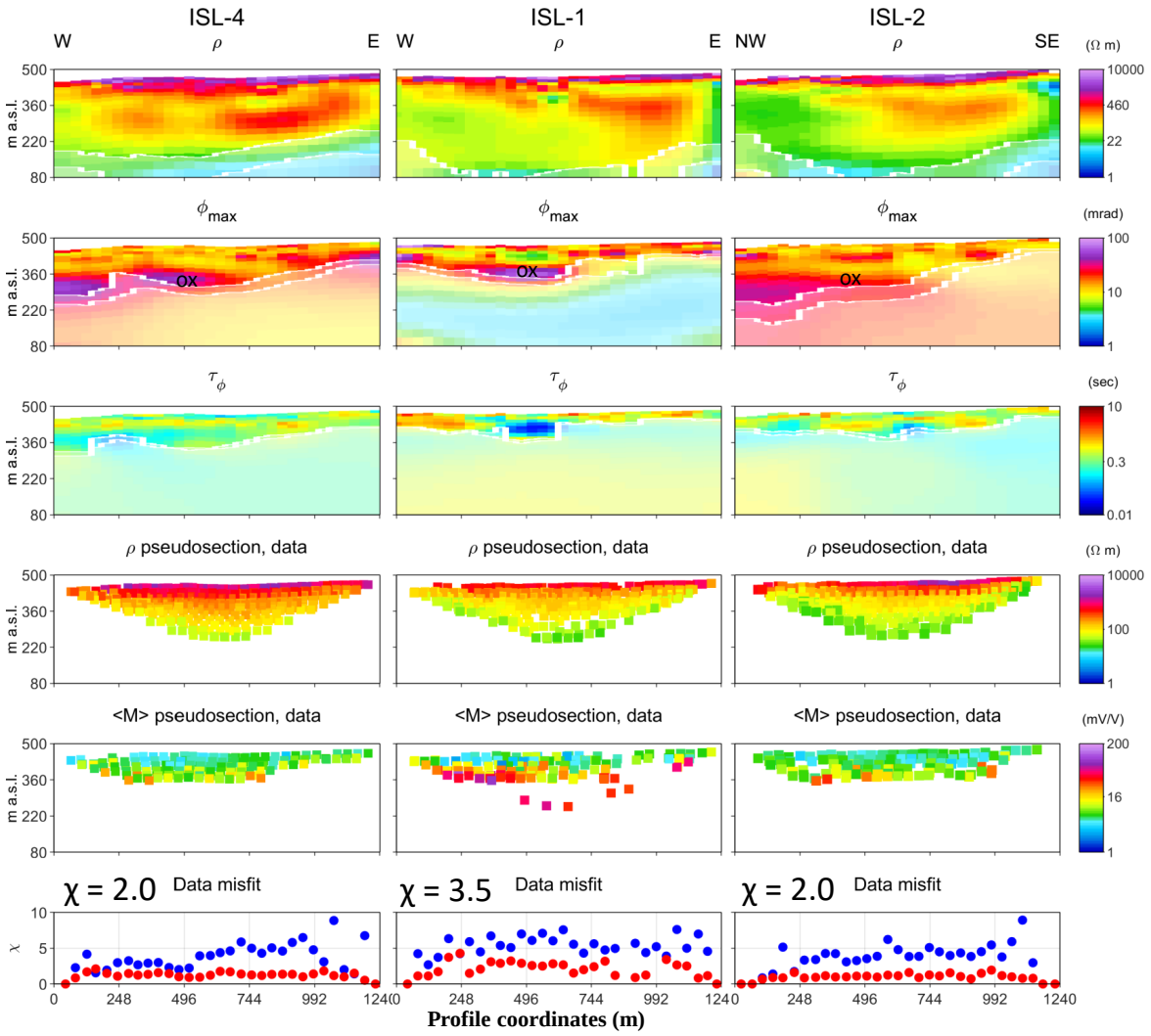

Figure 6. Inversion models for profiles ISL-4, ISL-1 and ISL-2. Six figures are shown by profile, from top to bottom: resistivity ρ inversion model, MPA inversion model (ϕ_{max} is the opposite of the maximum phase angle), relaxation time τ inversion model, resistivity data (ρ) pseudo-section, IP data (represented by integral apparent chargeability, <M>) pseudo-section, data misfit for resistivity (blue) and IP decays (red). The average data misfits χ for each profile, including resistivity and IP data misfits are also shown in the bottom panel. The inferred presence of iron-oxides in the high-MPA zones is indicated by "ox".

ISL-10 and ISL-11 are consistent with electrical logs (16/64) in borehole KH1, located at 17 and 84 m from the centre of ISL-10 and ISL-11, respectively (Figure 7).

A layer with high MPA is observed in profiles ISL-11, ISL-12 and to some extent, ISL-10 (Figure 7). The high MPA layer is less clear in ISL-10 because the DOI of the MPA model is shallower for this profile. The DOI of the MPA for the three profiles is shallowest at the centre. All the IP data in the low-resistivity body had to be filtered out, due to poor signal quality and the

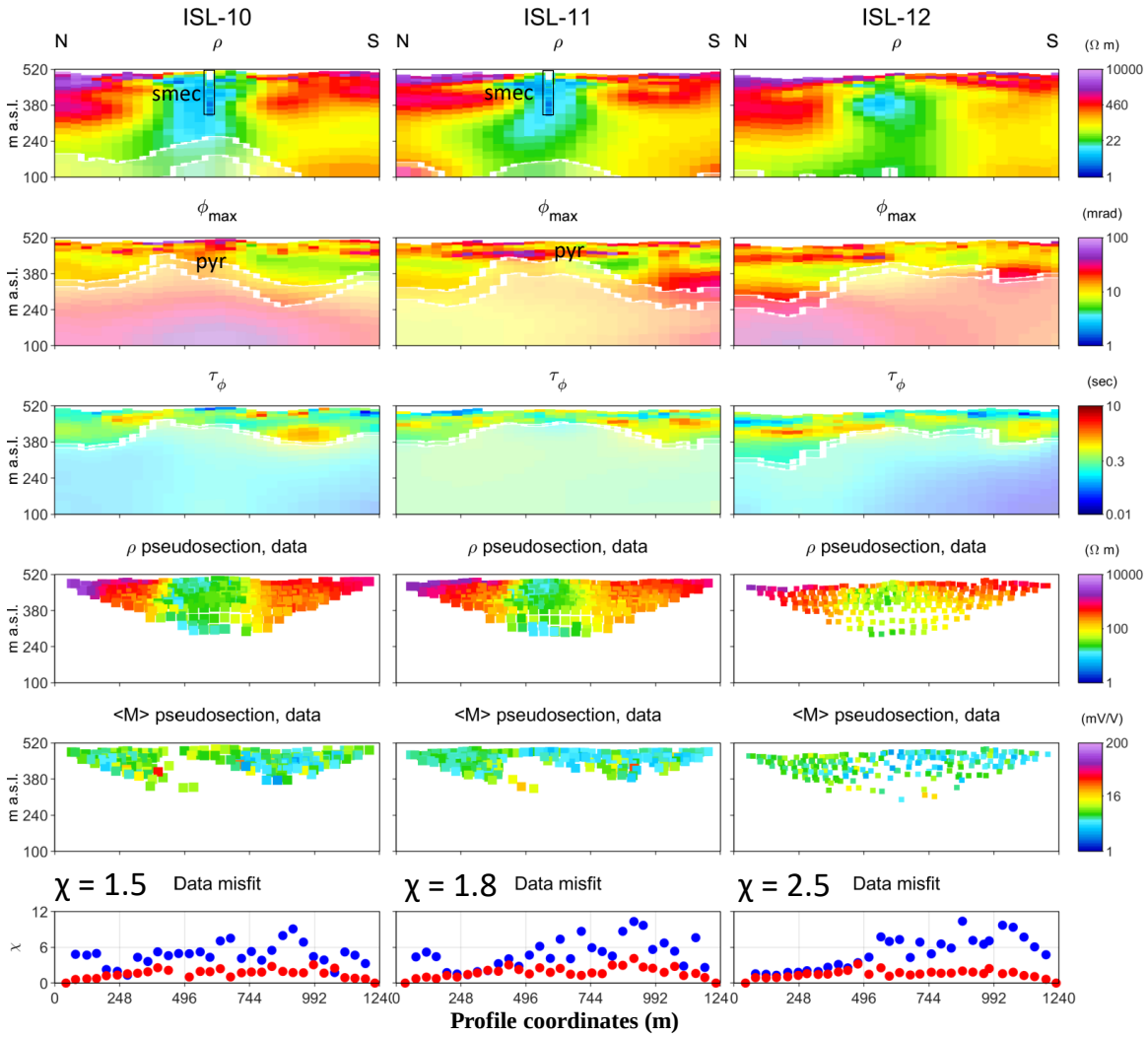

Figure 7. Inversion models for profiles ISL-10, ISL-11 and ISL-12. Six figures are shown by profile, from top to bottom: resistivity ρ inversion model, MPA inversion model (ϕ_{max} is the opposite of the maximum phase angle), relaxation time τ inversion model, resistivity data (ρ) pseudo-section, IP data (represented by integral apparent chargeability, <M>) pseudo-section, data misfit for resistivity (blue) and IP decays (red). The average data misfits χ for each profile, including resistivity and IP data misfits are also shown in the bottom panel. The borehole resistivity log (16-inch) in KH1 is shown at the centre of ISL-10 and ISL-11 resistivity inversion models (real distances are 17 and 84 m, respectively). The inferred presence of smectite and pyrite in the low-resistivity and high-MPA zones is indicated by "smec" and "pyr", respectively.

impossibility to fit the voltage discharge curves with IP decays. This explains the "hole" in the apparent chargeability pseudo-sections of profiles ISL-10, ISL-11 and, to some extent, ISL-12, while the resistivity pseudo-sections are complete (Figure 7). The lack of IP data is less pronounced in

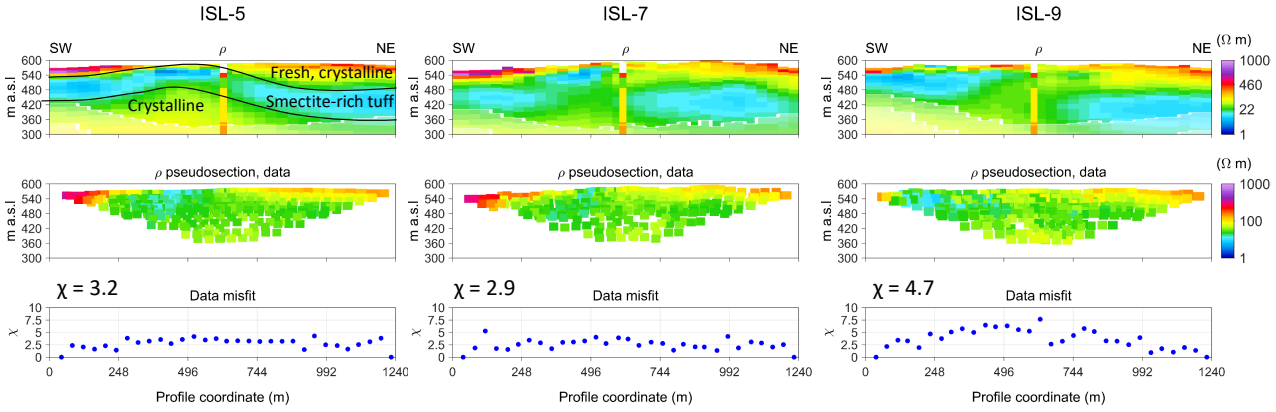

Figure 8. Resistivity inversion models, comparison to borehole data and interpretation at KH3 for parallel profiles ISL-5, 7 and 9, with 100 m in-between. The two black lines delimit a low-resistivity layer, interpreted as smectite-rich tuff. The data misfit χ for each vertical section of the model (spaced every 40 m) is given in the lower part of the figure and the average data misfit is also written (see Equation 4). The lithological resistivity log of borehole KH3 is placed at the centre of profile ISL-5, with the same resistivity colour scale. The green layer corresponds to the low-resistivity layer in the borehole. The real distance between the centre of ISL-5 and borehole KH3 is 174 m. The white rectangle indicates that no cores were available.

profile ISL-12, where the resistivity anomaly is slightly reduced compared to profiles ISL-10 and ISL-11.

Rather long relaxation times are observed in profiles ISL-10, ISL-11 and ISL-12: up to one second in the depth range 50-100 m (elevation 400-450 m) in profile ISL-12 (Figure 7).

3.3 KH3: field results at cold altered site

A low-resistivity layer is evidenced in the inversion models at site KH3 and more generally in the northeastern part of the studied area (Figure 8 for ISL-5, ISL-7 and ISL-9 and Supporting Information (Figure S5) for ISL-6 and ISL-8). The in-situ resistivity logs 16/64, available between 40 and 120 m, as well as the laboratory resistivity show a similar low-resistivity layer (10-30 Ωm) at the same depth but thinner (Figure 10).

3.4 Comparison to laboratory results

3.4.1 Presentation of frequency-domain laboratory results

The phase-angle of the electrical impedance is the delay between the voltage and the injected current. The phase spectra presented in Figure 9 show the variations of phase-angle over the frequency range $0.01 - 10^4$ Hz, for three samples from borehole KH1 (samples L2, L6 and L9) and three from borehole KH3 (samples L117, L119 and L123). The three samples from KH1 are smectite- and pyrite-rich, while the samples from KH3 contain either iron-oxides with no smectite (L117) or less than 0.5% pyrite but $\geq 30\%$ smectite (L119, L123). For each sample, the frequency-domain maximum phase angle (MPA) is the maximum of the phase-angle spectrum, at frequencies lower than 10^4 Hz. In natural volcanic samples presenting a wide variety of mineral textures, with in particular variable grain sizes for metallic minerals, this maximum includes contributions from different polarization processes occurring over different length-scales. The frequency at which maximum polarization occurs may be related to the grain size distribution of metallic particles (e.g. Gurin et al. 2018; Wait 1987; Wong 1979). Figures S6 and S7 in Supporting Information illustrate the variability of peak frequency (or its inverse, the relaxation time) and grain size distribution of metallic particles among the samples used for comparison in this study.

3.4.2 Consistent field and laboratory resistivity values at the cold altered site (KH3)

A low-resistivity layer is consistently observed in the depth range 55-95 m (corresponding to elevations 500-540 m) in borehole and laboratory measurements and at elevations 450-550 m in inversion of field data (Figure 10). The discrepancy in thickness and resistivity value of this layer between borehole and laboratory measurements on one side, and inversion of field data on the other side can be explained, to some extent, by a scale effect: the smallest distance between electrodes are a few centimetres in laboratory and boreholes measurements, whereas it is 40 m in the field. In addition, the equivalence between thickness and resistivity, which is intrinsic to ERT and more generally to geophysical inversion (e.g Johansen 1977; Menke 2012), may also partly explain the different thickness of the conductive layer in the field inversion, compared to borehole logs and laboratory measurements.

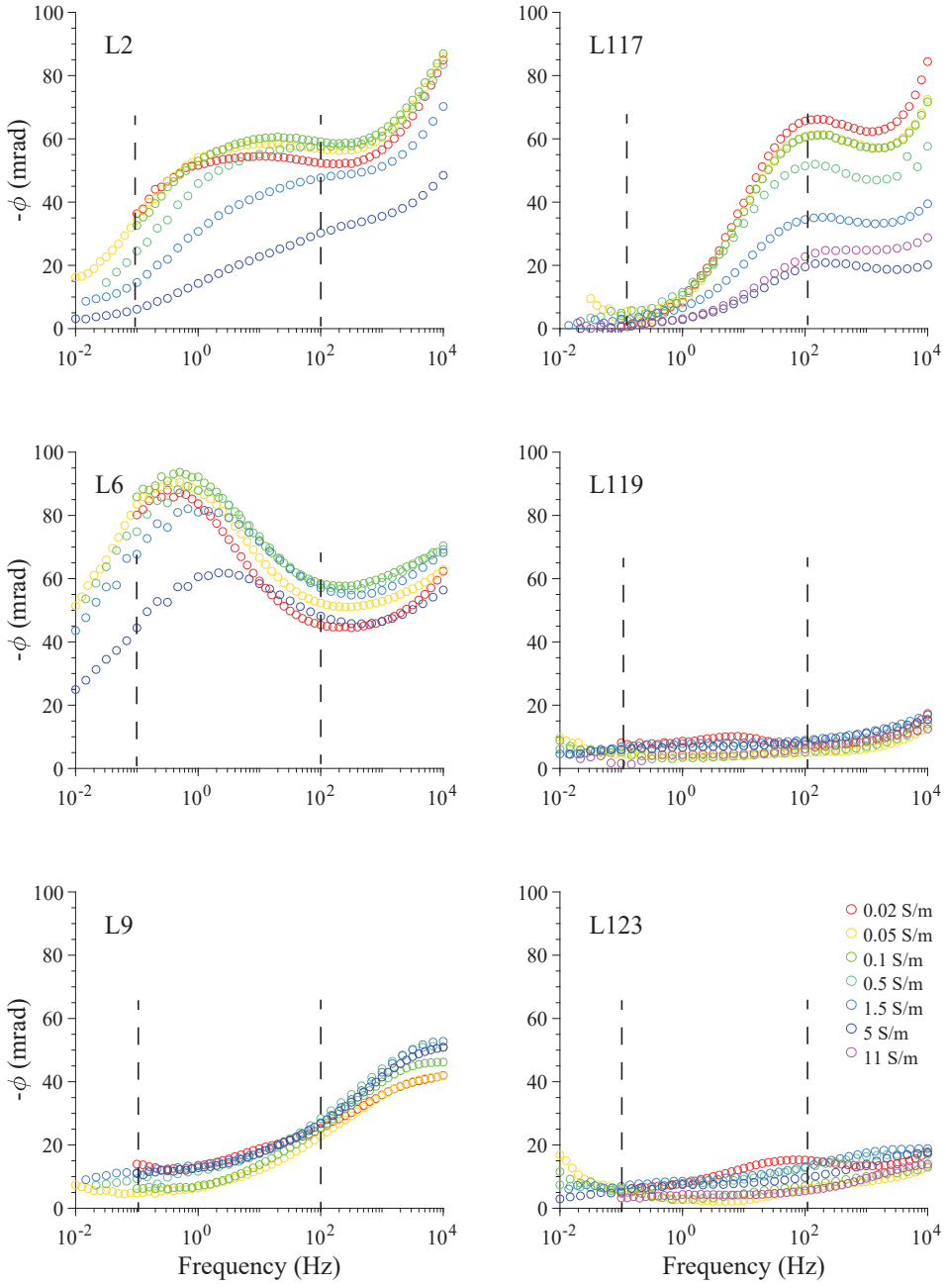

Figure 9. Phase spectra for samples L2, L6, L9 (KH1) and L117, L119, L123 (KH3) measured with laboratory frequency-domain IP. The different colours correspond to different pore fluid conductivities. The same colour scale as for L123 is used for all samples. The vertical lines indicate the range of frequency investigated in the field, in the most optimistic scenario: 0.1-100 Hz, corresponding approximately to the time-range from 10 msec to 8 s. Samples L119 and L123 contain less than 0.5 vol.% of metallic particles (pyrite) but more than 30 vol.% smectite. Sample L117 contains 1.8 vol.% iron-oxides while samples L2, L6 and L9 contain 2.5-5.5 vol.% pyrite

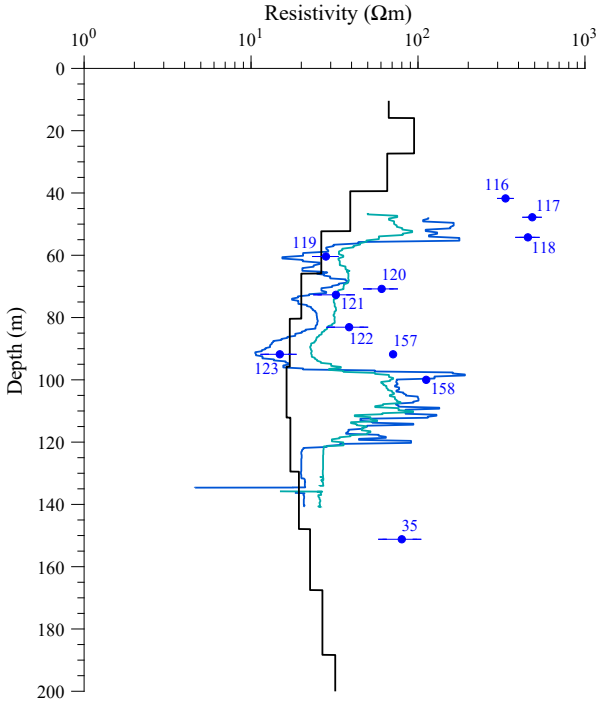

Figure 10. Comparison of resistivity values obtained from laboratory, in-situ borehole logs and inversion of profile ISL-5. The laboratory resistivity measurements at 1 Hz (blue circles) are given with an error bar corresponding to variations of pore water conductivity in the range 0.02-0.1 S/m. No error bars are shown for samples 157 and 158 because only one measurement, at pore fluid conductivity 0.07 S/m, was made. The 16-inch and 64-inch borehole resistivity logs are represented by blue and green lines, respectively. The inversion model is shown with the black line.

3.4.3 Large resistivity offset at the hot altered site (KH1)

An offset of about one order of magnitude between laboratory resistivity measurements at room temperature and in-situ borehole logs is observed at KH1 (Figure 11, left panel). In order to investigate the reason for this offset between laboratory and in-situ resistivity measurements, we build a "room temperature" resistivity model of the borehole, based on the lithology and the NN logs. The analysed samples at KH1 are classified into five types of lithological layers, using petrographic observations of the core samples, as well as lithological logs presented by Gudmundsson (1991). This classification has resulted in a simplified lithological model of the borehole geology, presented in Supporting Information (Figure S8).

We observe that laboratory resistivity values of core samples fall in a similar range for samples sharing a common lithological type (Table 2). This can be explained by the fact that, for these sam-

Table 2. Five types of lithological layers in borehole KH1 and their electrical resistivity. Average values and standard deviation within each group are given, based on laboratory resistivity of three to six samples, measured at room temperature (22-25°C) and at pore water conductivity in the range 0.02-0.1 S/m, to evaluate the influence of possible local variations in salinity around the average salinity at Krafla (corresponding to a pore water conductivity at 25°C of 0.078 S/m according to Flóvenz et al. (2005)).

Litho Layer	Type	ρ_{avg} (Ωm)	ρ_{std} (Ωm)
A	Dyke, ignimbrite	289	58
B	Basaltic intrusion	94	24
C	Unaltered lava/breccia	57	14
D	Altered lava/breccia	37	13
E	Hyaloclastite / tuff	19	7

ples, the electrical resistivity is controlled by the quantity of smectite and the porosity, which are themselves mainly controlled by the original lithology. In other words, the fracture system allows hot water to flow everywhere but, in the end, the glassy and porous layers (tuff, hyaloclastite) are the most altered while the crystalline and dense layers (basaltic intrusion, central lava flow, ignimbrite) are the least altered. A conductivity value was estimated for each layer, using the average conductivity of three to six samples belonging to each lithological layer. An average resistivity, with associated standard deviation, is then calculated for each layer (Table 2) and used to build the lithological resistivity log at room temperature.

We observe that the lithological resistivity log at room temperature (22-25°C) has an average resistivity about one order of magnitude higher than the in-situ borehole observations and the inversion results (3-6 Ωm). This holds true even when a large range of pore fluid conductivity is considered (see Figure 11(a) for the range 0.02-0.1 S/m represented by errorbars).

3.4.4 Qualitative comparison of IP parameters at KH1

The time-scale of polarization phenomena investigated with field measurements falls in the range 0.01-8 s. This means that only polarization processes with a time constant within this interval can be observed. This range is limited by (i) the high-frequency noise in the early recording times, mostly due to electromagnetic induction effects and (ii) the maximum T_{off} = 8 s, which was

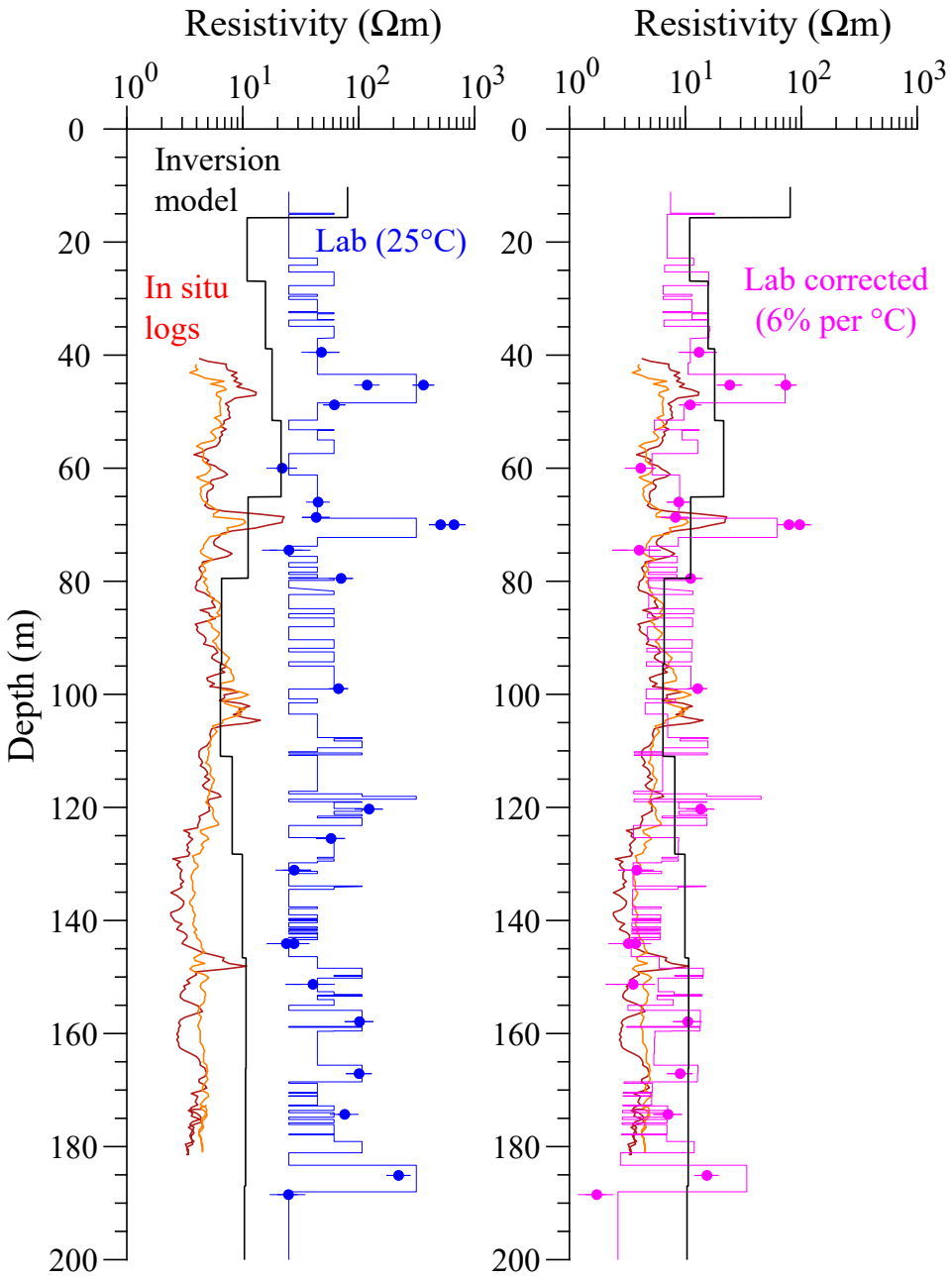

Figure 11. Comparison of resistivity values from laboratory, lithological resistivity logs, borehole logs and inversion of field data at KH1 site. The left panel shows original laboratory resistivity values for each sample, measured at 1 Hz, at pore fluid conductivity in the range 0.02-0.1 S/m (blue filled circles with error bars), together with the lithological resistivity log at 25°C and pore fluid conductivity 0.05 S/m (blue line), as described in section 2.3.3 and Table 2. Also shown are in-situ borehole logs 16/64 (dark red and orange lines). The right panel shows laboratory resistivity values and lithological resistivity log after correction of the effect of temperature using the coefficient $0.06°C^{-1}$, obtained by fitting in-situ data using Equation 6 (red line).

used in the field. The frequency-range corresponding to this time-range is approximately 0.1- 100 Hz. The maximum polarization of core samples from borehole KH1 (hot site), measured in the laboratory in the frequency range $10^{-2} - 10^{4}$ Hz, occurs at higher frequencies for many samples, reaching 10 kHz in some cases (e.g. sample L9 in Figure 9). Therefore, the polarization observed in the field can be significantly lower than the maximum polarization.

This is a drawback of field IP measurements (time-domain [TDIP] or frequency-domain [FDIP]), compared to laboratory frequency-domain IP measurements. The frequency-range which can be investigated by field FDIP is also limited by the presence of electromagnetic effects above a certain frequency. In the field study by Pelton et al. (1978), a frequency-range as large as $10^{-2} - 10^{5}$ Hz was investigated with FDIP but using one meter spacing between electrodes and thus targeting only exposed mineralization at the surface. Increasing the distance between electrodes, necessary to target deeper levels, enlarges the frequency- and time-ranges in which EM effects are dominant, in FDIP and TDIP respectively (Fiandaca 2018).

Profile ISL-11 is chosen for comparison between field and laboratory MPA measurements, because the DOI at the center of ISL-11 is deeper than in ISL-10 (Figure 7). Many samples in borehole KH1 reach their maximum polarization at times shorter than 10 msec (frequency higher than 100 Hz, Figure 9). Since only polarization occurring on time-scales larger than 10-20 msec can be resolved by our TDIP field measurements, we can only observe a part of the maximum polarization with these measurements. Therefore, the laboratory MPA taken at frequencies below 100 Hz is used for comparison to the inverted MPA.

In the depth-range investigated (above DOI), the inverted MPA is fairly consistent with the laboratory MPA taken below 100 Hz (Figure 12). In particular, the high MPA layer at 40-50 m depth corresponds to the high MPA observed in samples L2 and L6. However, frequency-domain laboratory MPA are generally higher than inverted MPA, at a given depth. The laboratory MPA are shown with error bars, corresponding to a large range of pore fluid conductivity (0.02-0.5 S/m), to account for possible variations of local pore water conductivity. Note that the typical in-situ fluid conductivity at Krafla is 0.078 S/m, according to Flóvenz et al. (2005).

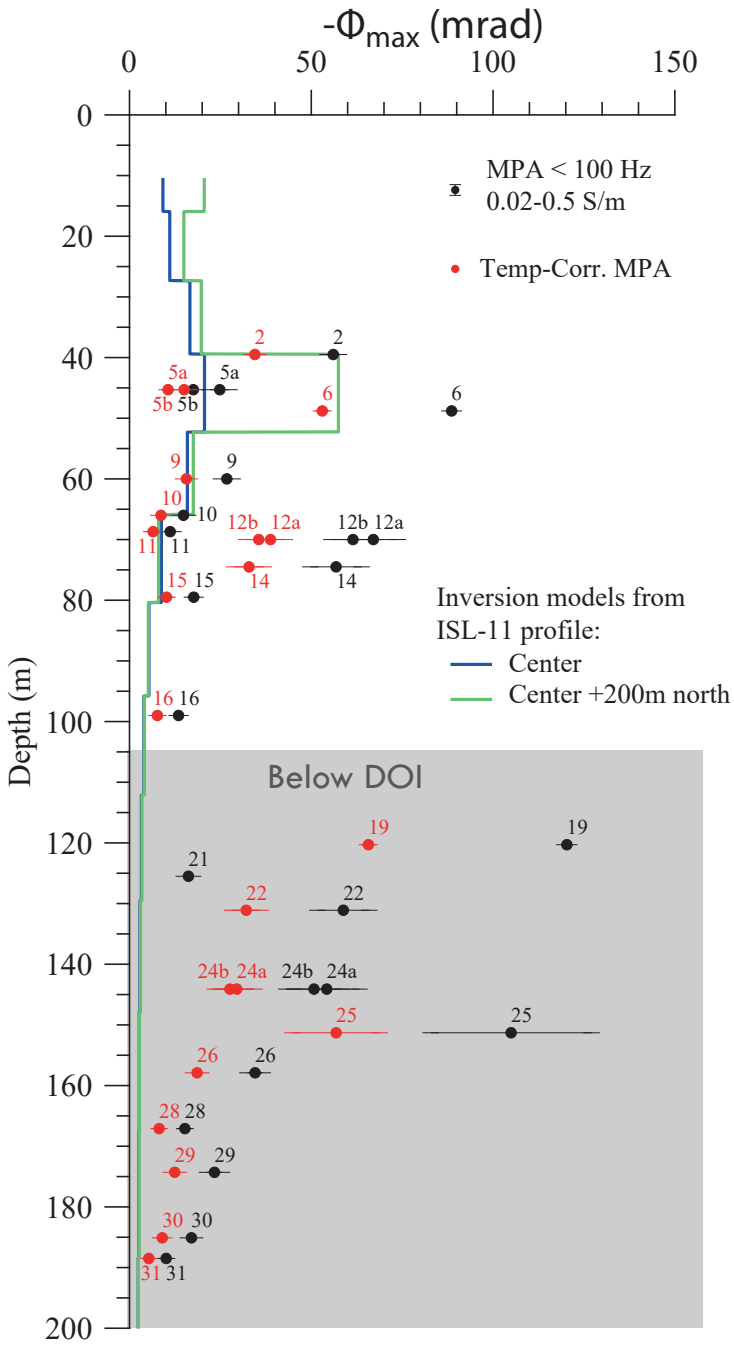

Figure 12. Comparison of MPA obtained with laboratory frequency-domain measurements of samples from borehole KH1 and inversion of profile ISL-11 (time-domain). The two coloured lines correspond to the vertical models at the center and 200 m to the North, along profile ISL-11. The laboratory MPA, determined in the range $0.1 - 100$ Hz (filled black circles with horizontal error bars corresponding to variations with fluid conductivity, in the range 0.02-0.5 S/m) are shown together with temperature-corrected laboratory MPA, using Equation A.2.

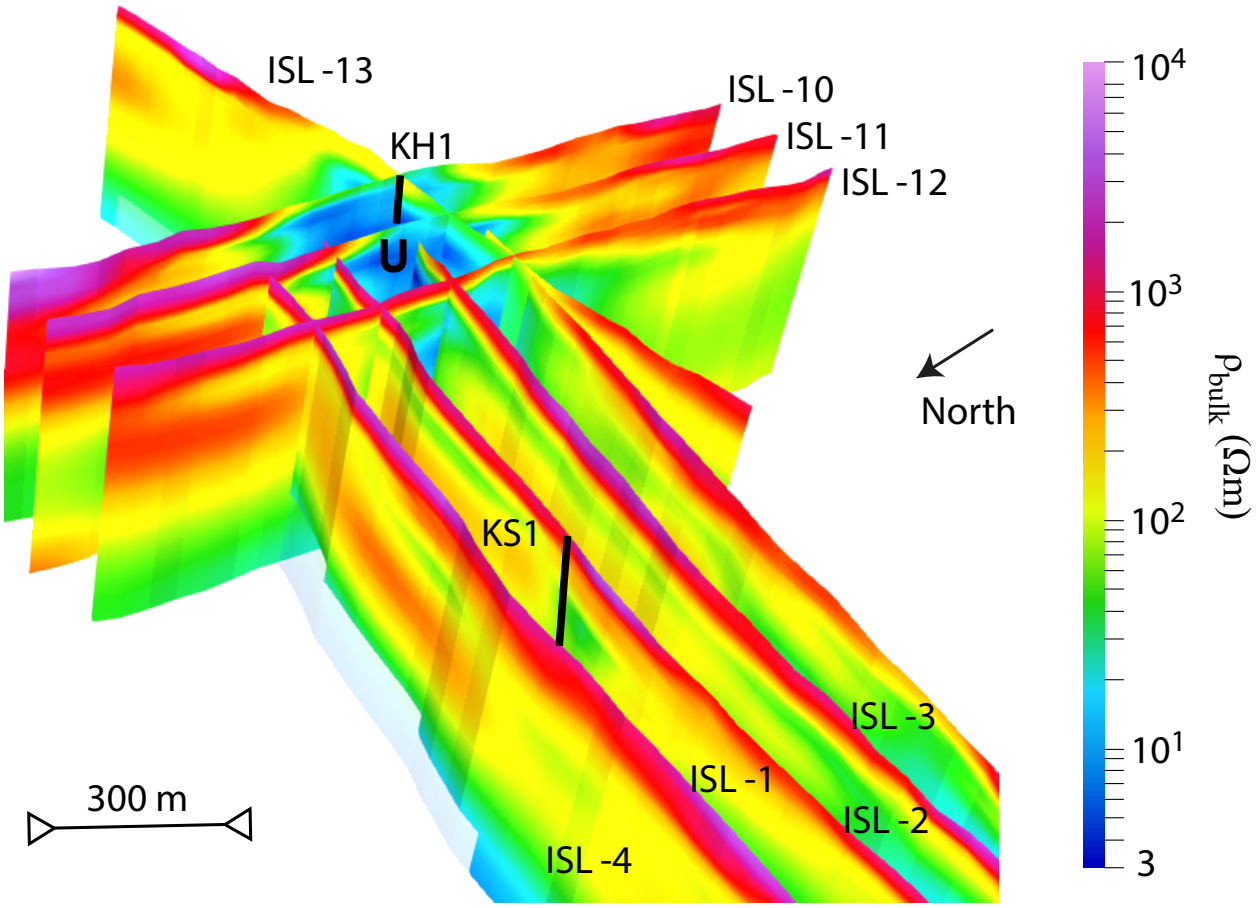

Figure 13. Three-dimensional visualisation of the four resistivity profiles at KH1 (ISL-10, 11, 12 and 13) and four intersecting resistivity profiles at KS1 (ISL-4, 1, 2 and 3). . The zone marked "U" corresponds to the smectite-rich low-resistivity plume-like structure, interpreted as an upflow zone. The inversion results below DOI are transparent. All sections displayed are about 300 m high.

3.5 Joint consideration of the results at KH1 and KS1 sites

We interpret the low-resistivity body observed at KH1 site as a hydrothermal plume (Figure 13 on ISL-10, ISL-11 and ISL-12 and Supporting Information, Figure S9, for ISL-13). At KS1, inversion models from the four parallel profiles indicate an overall resistive environment. A low-resistivity structure is observed in the southeastern edge of ISL-2 and ISL-3 and corresponds to the upflow zone at KH1 site, under Leirholl (Figures 1(b) and 13).

As opposed to resistivity, MPA inversions do not indicate a clear difference between KH1 and KS1 sites. A high MPA is consistently observed on the three parallel profiles at KH1, at shallow depth, as well as on two of four parallel profiles at KS1 (red to purple color in Figure 14). Inversions of the relaxation time show that the high MPA layers at KH1 are generally associated

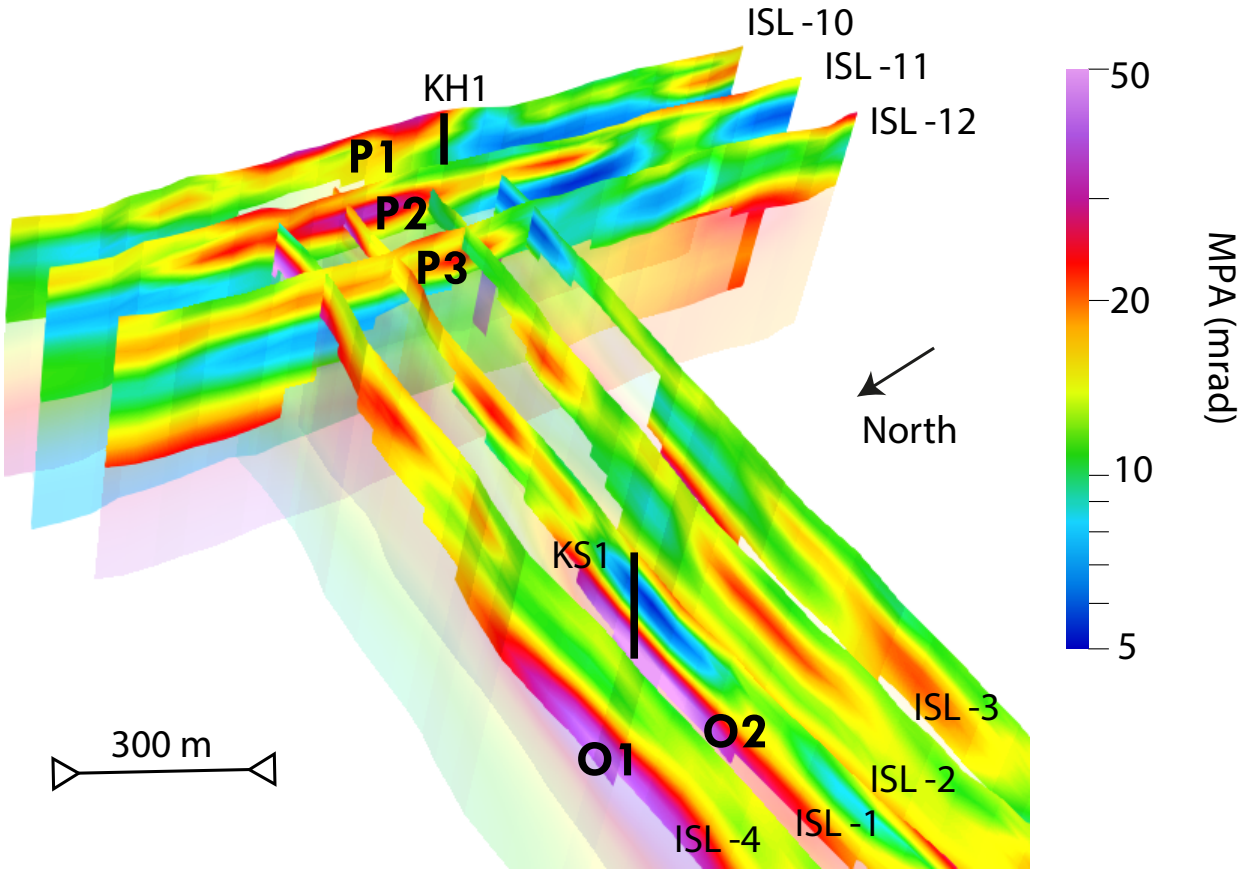

Figure 14. Three-dimensional visualisation of the three parallel MPA profiles at KH1 (ISL-10, 11 and 12) and four intersecting MPA profiles at KS1 (ISL-4, 1, 2 and 3). The areas marked P1 to P3 indicate the inferred presence of pyrite, while the areas marked O1 and O2 indicate the inferred presence of iron-oxides.

to long relaxation times (1 s, in red), whereas layers of very short relaxation time (0.01 s, in blue) are observed at KS1 site (Figure 15). Although a contrast exists between the two sites, care must be taken when interpreting the relaxation time values, due to the limited time-range resolved with the TDIP measurements, and the limited depth of investigation of the relaxation time (shallower than for the resistivity and the MPA).

A classification of the three different sites, based on their complex electrical structure, mineralogy and hydrothermal activity, is summarised in Table 3.

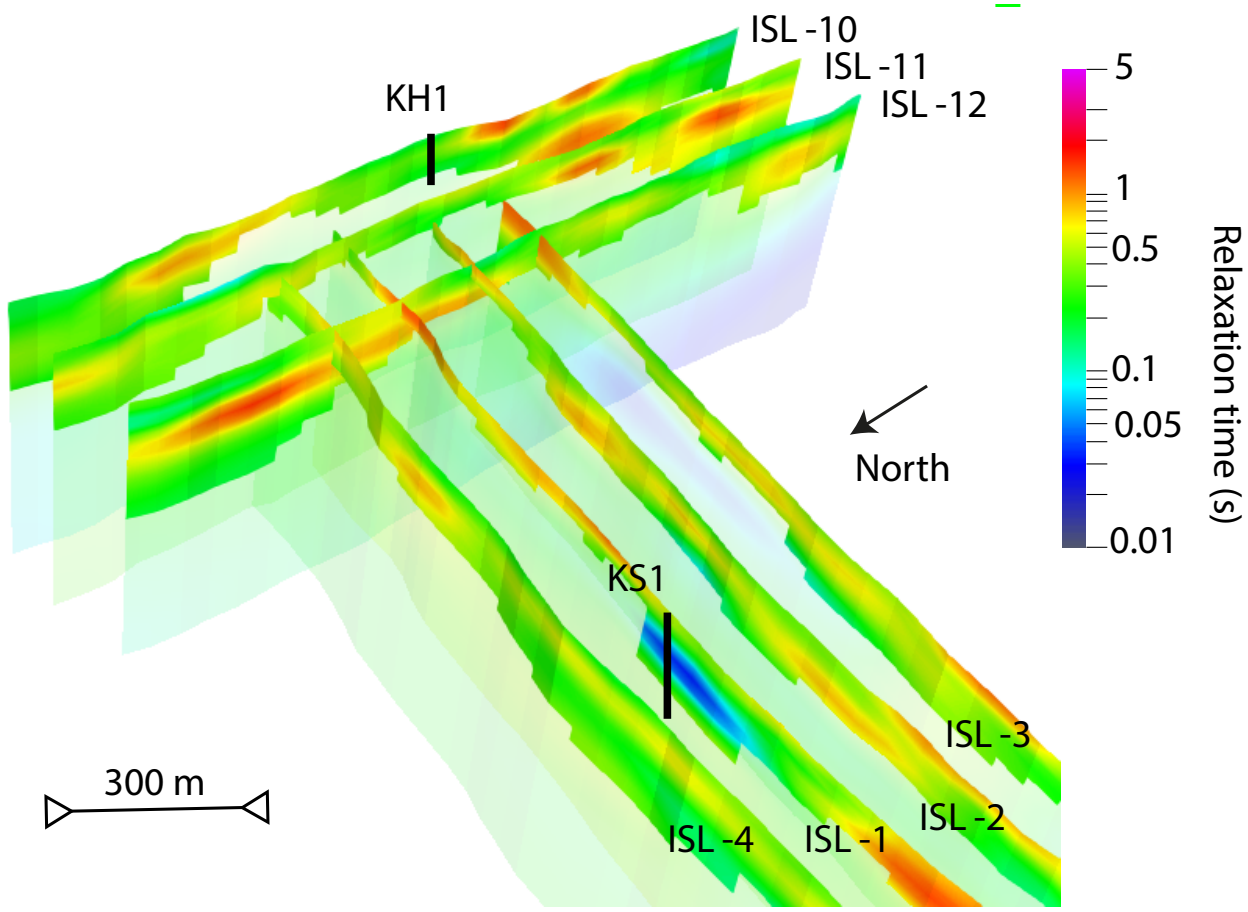

Figure 15. Three-dimensional visualisation of the relaxation time inversions, for the same profiles as in Figure 14. Three parallel at KH1 (ISL-10, 11 and 12) and four intersecting profiles at KS1 (ISL-4, 1, 2 and 3).

4 INTERPRETATIONS AND DISCUSSION

4.1 Rapid spatial variations of resistivity signatures along the caldera boundary

At KH3, the low-resistivity body is attributed to an abundance of smectite, with up to 50 wt.% smectite found in the samples corresponding to the low-resistivity layer observed with borehole logs and laboratory measurements (Lévy et al. 2018). The present temperature in borehole KH3 is

Table 3. Summary of the ERT and IP signatures of the three sites investigated and comparison to known mineralogy and hydrothermal activity.

	KH3	KH1	KS1
ERT	Conductive layer	Conductive plume	Overall resistive
IP	IP signal too noisy	High MPA with long relaxation time. IP noisy in the plume.	High MPA with short relaxation time
Mineralogy	Altered hyaloclastite (smectite and little pyrite)	Overall very altered, evidences of boiling, smectite and pyrite abundant	Fresh basalt, iron-oxides abundant
Activity	Cold, possible former regional circulation	Hot, active	Cold at shallow depth

lower than 50°C down to 400 m (Figure 2 (b)) but smectite could have formed during past regional hydrothermal circulations with a rather horizontal flow direction, coming from inside the caldera, or simply by slow glass replacement without any active circulation. Pyrite and calcite are sporadically observed in fracture fillings in the low-resistivity layer, indicating that hydrothermal activity has occurred, but to a small extent only. We thus interpret the low-resistivity layer, observed in all profiles of the northeastern part of the studied area (Figures 5, 8 and Supporting Information, Figure S5), as a consistent geological layer composed of very altered volcanic glass.

At KH1, a low-resistivity body with a cylindrical geometry is observed (Figure 13). We interpret this shape as the result of the crossing of two orthogonal faulting directions (Figure 1) : the rifting NNE-SSW direction, consistent with the rhyolite eruption forming the obsidian ridge Hrafntinnuhryggur, and a concentric faulting system, typical of caldera rim structures, at the southern edge of the caldera (see e.g. Sigmundsson (2006) for more details on the geology). We thus suggest that the intersection of these two geological features at KH1 site has created a high-permeability up-flow zone. Intense alteration and large smectite volumes could be the primary cause for the low-resistivity. Hydrothermal plumes of similar shape have been observed at the intersection of orthogonal faulting structures at other volcanoes (Gresse et al. 2017). Moreover, surface alteration at this site suggests the presence of hot springs and even fumaroles at some point: white soft clays, gypsum and silica sinters are found at Leirholl ("clay-hill" in Icelandic), around borehole KH1. These minerals are witnesses of steam upflow reaching the surface. The hydrothermal plume at KH1 may relate to a deep low-resitivity anomaly observed at 1750 m depth in 3D inversions of MT data in the same area, named Sandabotnaskarð, around the southern caldera rim (Árnason & Magnússon 2001). However, the shallow up-flow observed with ERT data, and correlated to geological and tectonic features, is not resolved with one-dimensional inversion of TEM data (Rosenkjaer et al. 2015). Although hydrothermal activity has faded out, KH1 is still relatively hot today at the shallow depths investigated (170°C at 200 m depth, Figure 2(c)).

At KS1, the overall high resistivity observed at the shallow depths investigated (down to 300 m) coincides with the presence of fresh, recent and unaltered basalt and low temperature (Gudmundsson et al. 2007). Intense hydrothermal activity is yet present at KS1 site below one kilometer: the

temperature reaches 300°C at 1.2 km and 350°C at 2.5 km (Figure 2(a)). These deep hydrothermal circulations, buried under recent lava layers at KS1 site, are probably connected to the up-flow at KH1 site. The recent lava flow at KS1 site, which is not observed at KH1 site, might have been stopped before reaching KH1. In this case, it could have caused subsidence of the ground at KS1 site but up-lift at KH1 site. Finally, a low-resistivity body below 250 m depth is observed in resistivity inversions at KS1 site and is particularly visible in the southeastern part of the LONG profile (Figure 5). Future ERT studies in the area of Hvíthólar (west of Sandabotnaskarð) could help characterise the tectonic features in the southern Krafla caldera.

4.2 Interpretation of observed high MPA (KS1 and KH1)

In the southern part of the caldera, we observe two high-MPA formations but associated with a different range of resistivity (Figures 13 and 14). These two types of complex electrical structures correspond, based on laboratory observations, to pyrite-rich versus magnetite-rich zones (Figure 16). An abundance of iron-oxides, such as magnetite, corresponds to fresh unaltered basalts, whereas an abundance of pyrite mostly corresponds to basaltic rocks affected by hydrothermal circulation (e.g. Lévy et al. 2019). These two different geological contexts would be responsible for the different resistivity range, despite the similar semi-conducting properties of pyrite and magnetite. Based on this discrimination method, we attribute the high-MPA and low-resistivity observed at KH1 to the presence of pyrite, and the high-MPA and high-resistivity at KS1 to iron-oxides.

The presence of pyrite in the high-MPA layer of KH1 is confirmed by three samples coming from KH1 at the relevant depths and analysed in the laboratory: L2, L6 and L9 have a volume fraction of pyrite ranging from 2.5 to 5.5%. The presence of iron-oxides and absence of pyrite in borehole KS1 above 350 m is confirmed by the drill-cutting analyses (Gudmundsson et al. 2007).

The relaxation time can also be used, to some extent, as a discriminating factor between pyrite and iron-oxides. Pyrite crystals formed by hydrothermal circulations are usually more connected than small and disseminated iron-oxides formed during primary magmatic crystallisation. Since connected metallic particles are expected to have longer relaxation time than disseminated metallic particles (Pelton et al. 1978), pyrite-rich layers are expected to be have longer relaxation times than

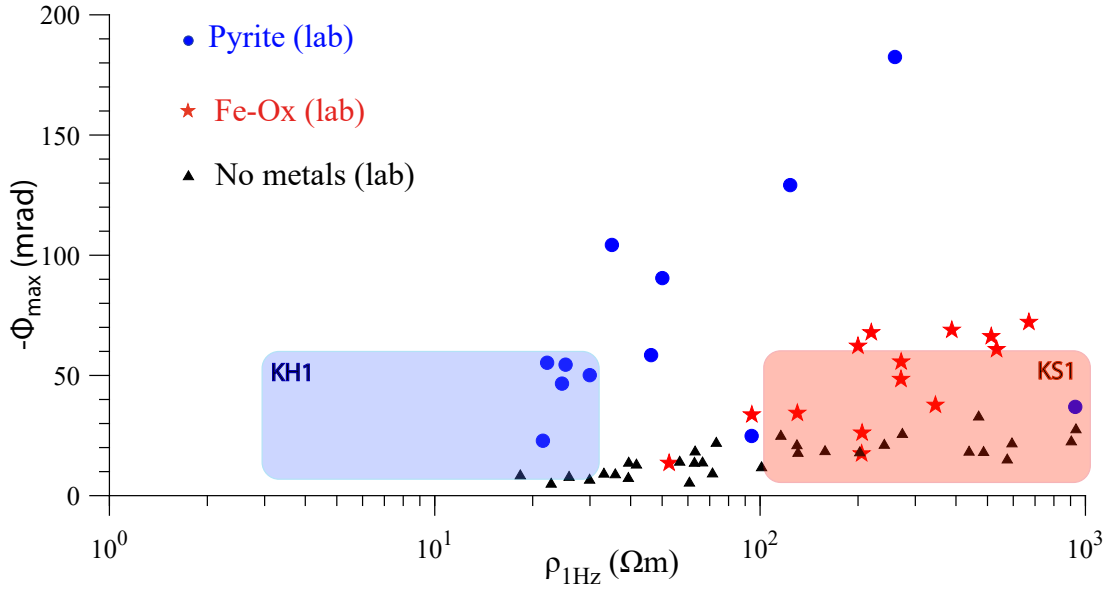

Figure 16. MPA vs. DC resistivity from laboratory measurements on core samples and from inversion of field data. Laboratory measurements, at room temperature, are carried out on samples from boreholes KH1 and KH3, as well as two other boreholes in the western side of the Krafla caldera (KH5 and KH6). The laboratory DC resistivity is approximated by the resistivity measured at 1 Hz. Blue circles and red stars correspond to pyrite-rich and magnetite-rich samples, respectively, while black triangles correspond to samples with less than 1% metallic particles. The blue and red rectangles show the ranges of MPA and DC resistivity resulting from inversions at KH1 and KS1 site, respectively.

magnetite-rich layers (see e.g. Figures S6 and S7 in Supporting Information). Relaxation times are generally shorter at KS1 site than KH1 site (Figure 15), so that we suggest pyrite as the main element responsible for high MPA at KH1, while magnetite plays the same role at KS1,based on the relaxation time values. However, the DOI for the relaxation time is always the shallowest of all the IP parameters (Madsen et al. 2017), so that this parameter is not very constrained by the model in the conductive plume area (Figures 7 and 15).

An effect of the 900 m deep casing on the inversion parameters at KS1 cannot be ruled out. For example the low-MPA anomaly, only observed in one profile (ISL-1, see Figure 14), suggests the presence of a small structure, such as conductive steel casing. With 40 m spacing between electrodes, the resolution is much coarser than the casing size (few centimetres). Forward calculation of the casing effect requires a refined mesh around the casing. This might be possible with finite elements modelling.

4.3 Influence of in-situ temperature on resistivity and MPA

At KH3, resistivity resulting from field inversions, borehole logs and laboratory are consistent (Figure 10). At KH1, resistivity values obtained from field inversions fall in the same range as borehole logs but a significant offset exists between field and in-situ borehole logs on one hand and laboratory measurements on the other hand (Figures 7 and 11). The range of resistivity observed in the field is also lower than resistivity measurements on pyrite-rich samples at room temperature (Figure 16).

We first investigate the possible effect of a hot pore fluid at KH1, with a fluid composition realistic for a low-salinity geothermal system (corresponding to a fluid conductivity σ_f of up to 0.1 S/m at 25°C). We use Equation 6 to estimate the temperature effect on resistivity (e.g. Arps 1953; Kristinsdóttir et al. 2010).

$$\frac{\rho'(T_0)}{\rho'(T)} = 1 + \alpha_{\rho'}(T - T_0) \tag{6}$$

where T and T_0 are the in-situ temperatures (presented in Figure 2) and room temperature in °C, respectively, $\alpha_{\rho'}$ is the correction coefficient in $^\circ C^{-1}$ and ρ is the resistivity in Ωm.

The coefficient $\alpha_{\rho'} = 0.02^\circ C^{-1}$ suggested by Arps (1953) for water, corresponding to a decrease of resistivity of 2% per °C, would correspond to ρ_f = 2.5 Ωm for a temperature of 180°C. With formation factors F mostly in the range 30-200 (Lévy et al. 2018), the minimum ρ_f would correspond to a minimum rock resistivity ρ_{bulk} of at least 50 Ωm, using Archie's law $\rho_{bulk} = F\rho_f$ (Archie 1942), which is much higher than the 3-6 Ωm observed. On the other hand, if a local increase of salinity was the explanation for an average rock resistivity of 5 Ωm, the fluid would need to have a resistivity of at most $\rho_f = \frac{\rho_{bulk}}{F} = \frac{5}{30} = 0.17$ Ωm in average. It would correspond to a fluid resistivity of 0.4 Ωm at 25°C, considering an average in-situ temperature of 100°C, which is much smaller than the 13 Ωm (conductivity 0.078 S/m) measured by Flóvenz et al. (2005). Thus the sole effect of a hot pore fluid cannot explain the lower resistivity observed in the field.

As a consequence, we suggest that the observed lower in-situ resistivity is also due to a temperature effect on the clay minerals and not only on the fluid. The experimental value of temperature-

correction factor, compiled from data on clay-rich sands measured by Vinegar & Waxman (1984), $0.033°C^{-1}$, is yet not sufficient to explain the resistivity offset between laboratory and field. We calculated that a coefficient of $0.06°C^{-1}$ is necessary to explain the resistivity offset, by adjusting the lithological resistivity log at room temperature to the in-situ borehole logs (Figure 11 (b)). Variations of this coefficient with lithological differences could be expected but this value is generally consistent with experimental results by Kristinsdóttir et al. (2010) on core samples from borehole KH1, heated up to 250°C, as well as experimental results by Flóvenz et al. (1985) and Nono et al. (2018) on core samples from the Icelandic geothermal fields of Laugar, Reykjanes and Nesjavellir. We thus suggest that the low-resistivity plume-like structure observed at KH1 site is caused by an intense clay alteration (mostly smectite), hence interface conduction, as well as interfoliar conduction within smectite crystals, whose high electrical conductivity is enhanced by high temperature. A strong temperature-dependence of interface conduction has been observed by Nono et al. (2018) on cores from Nesjavellir and Reykjanes, two high-temperature areas in Iceland, with a change of conductivity of one order of magnitude between 0 and 100°C. A temperature-dependence of smectite interfoliar conduction can also be expected since an increase of temperature could cause an increase of interfoliar distance in smectite crystals by dilatation, which would enhance the mobility of ions (charge carriers) throughout connected interfoliar spaces of smectite crystals. Laboratory measurements on single-crystal vermiculite confirm that interfoliar conduction increases with temperature (Maraqah et al. 1990).

The field MPA are lower than the laboratory MPA, even after the difference of frequency-range has been accounted for (Figure 12). We briefly explore the possible effect of in-situ temperature on the MPA. The temperature-dependence of IP parameters is not well known, and especially not at these high temperatures (Bairlein et al. 2016; Treichel et al. 2014). We suggest in Appendix A a procedure to correct the phase-angle for the effect of temperature, which results in corrected laboratory MPA falling in the same range as field MPA for ISL-11, down to the DOI (Figure 12). However, this comparison is only qualitative and the use of different correction coefficients could also work. The high MPA measured in the laboratory at depths between 120 and 150 m

corresponds to layers below the DOI, so that the field MPA at these depths cannot be used for comparison to laboratory MPA.

There is also a possible effect of temperature on the relaxation time since τ is sensitive to fluid conductivity (e.g. Gurin et al. 2015; Wait 1983). However, the relaxation time values obtained from the inversion cannot be quantitatively compared to the relaxation time obtained in the laboratory, in particular due to the limited time-range investigated in the field.

4.4 Influence of smectite on IP data quality (KH1 and KH3)

Field data at KH3 and KH1 sites are characterised by noisy voltage discharge curves, which cannot be included in the inversion input data.

At KH3, noisy voltage discharge curves are systematically associated with low apparent resistivity, whereas clean IP decays are associated with high apparent resistivity (Figure 4). The near-horizontal low-resistivity body, observed on the ERT inversions of all profiles at KH3, is interpreted as a smectite-rich layer, based on comparison to borehole logs and laboratory analyses.

At KH1, a cylindrical low-resistivity body is observed and attributed to a up-flow causing extensive hydrothermal alteration, with in particular abundant formation of smectite. Noisy voltage discharge curves are associated to this central low-resistivity body at profiles ISL-10 and ISL-11, and to some extent ISL-12. Yet, the spatial distribution of the smectite-rich body does not obstruct the IP measurements as much as at KH3 site. The resistive structures on the sides of the profiles at KH1 site allow resolving IP parameters in these zones and thus in parts of the central zone, thanks to lateral constraints in the inversion. On the other hand, at KH3 site, the low-resistivity layer completely screens the IP signal.

These observations suggest that an abundance of smectite, especially as a thick layer, is a major obstacle to retrieve good IP data quality in volcanic environments. The conductive properties of smectite, especially the diffusion of ions through interfoliar spaces, might prevent the creation of high voltages in the ground (Lévy et al. 2018, 2019), which are a pre-requisite for good quality IP data (Gazoty et al. 2013). More generally, low or even negative apparent chargeability have been observed over conductive and polarisable bodies and interpreted as the effect of

conduction, preventing relaxation (Sumner 1976). This emphasises the importance of fitting the voltage discharge curves with IP decays to ensure that discharge curves contain information about the electrical charge storage capabilities of the rock and not about other sources of polarization (e.g. cross-talking between cables or spontaneous polarization). A recent study by Fiandaca et al. (2019) lists the shapes of voltage decays which can be fitted by IP decays.

The creation of larger voltage in smectite-rich environments would require injection of larger currents. Instruments including independent dipoles for injection and potential measurements could be adapted for this purpose. Induction-based soundings, such as Transient Electromagnetic (TEM), could also be a solution to obtain a deeper IP signal in conductive environments. Yet, a strong IP anomaly needs to be present in the ground to be imaged by TEM soundings, especially if the host rock is conductive (Flis et al. 1989).

4.5 Interest of shallow ERT/TDIP investigations for geothermal exploration

The very different resistivity signatures of KH1 and KS1 sites at shallow depths illustrate the spatial variability of lithological and tectonic features, which can exist along caldera boundaries over short distances (see Table 3 for a summary of these different features). ERT soundings allow identifying shallow structures, such as a localised up-flow zones, relevant for geothermal exploration, as well as for understanding better the shallow structure of calderas. Therefore, ERT soundings bring complementary information to electromagnetic soundings, which are usually inverted in a larger grid and overlook these shallow localised structures.

IP measurements bring more details about the mineralogy at shallow depth, compared to structures imaged by DC resistivity only. Our study shows that pyrite and iron-oxides can be identified with DCIP soundings in volcanic environments. However, the presence of clay minerals such as smectite is difficult to detect with IP soundings, due to high electrical conduction associated with smectite alteration in these environments, concurring with polarization. The best IP signal is obtained in resistive zones, which can either correspond to fresh unaltered basalt or to altered basalt without smectite, e.g. when smectite has been replaced by chlorite. This last case was not observed in our study.

Although the depth range investigated is large compared to many IP campaigns, it remains small compared to common target depths of interest for geothermal targets (more than one km). A joint analysis of TEM and ERT/TDIP (with higher injected current) could possibly allow obtaining the IP signal down to one kilometre depth.

5 CONCLUSIONS

Here, we have used the eastern Krafla caldera boundary as a laboratory to better understand the spatial variations in lithology, mineralogy and volcano-tectonic structures, which can be expected over short distances at caldera boundaries. Electrical Resistivity Tomography (ERT) at an active volcano (Krafla, Iceland) has highlighted an up-flow zone of cylindrical shape, located at the intersection of two tectonic features : the southern caldera rim and NNE-SSW faults associated with the main rifting axis. This shallow low-resistivity anomaly was not detected in previous electromagnetic soundings, conventionally used for geothermal exploration. Time-Domain Induced Polarization (TDIP) has allowed identifying a region with high maximum phase angle (MPA) and long relaxation time associated with this low-resistivity anomaly, which we thus interpreted as pyrite-rich. TDIP measurements appear to be useful to detect and discriminate pyrite and iron-oxides but seem to be rather not sensitive to the presence of smectite. Our results confirm that the abundance of smectite, a clay mineral common at shallow depths in volcanic environments, leads to high conduction and low polarization. The abundance of smectite is an obstacle for the transformation of injected currents into high voltage and thus to the retrieval of good quality IP data. The naturally high conductivity of smectite is enhanced by high temperatures: at the hot site, the temperature difference between in-situ and laboratory resistivity measurements corresponds to an overall increase of the electrical conductivity of 6 % per $^{\circ}C$. The inverted MPA from time-domain field measurements at the hot site are consistent with laboratory frequency-domain measurements on borehole samples from this site, down to the depth of investigation of about 120 m, provided that the frequency-range where the MPA is retrieved in laboratory measurements is reduced to approximately match the time-range investigated in the field. A decrease of MPA with temperature is also possible. At the cold altered site, resistivity from laboratory measurements, borehole logs and

inversion of field data are consistent but the IP data could not be inverted, due to a near-horizontal smectite-rich conductive layer affecting the quality of IP data. At the cold unaltered site (the most resistive of the three sites), the best IP signal was obtained and a high MPA associated with short relaxation time was attributed to the presence of iron-oxides.

ACKNOWLEDGMENTS

Editor Alexis Maineult and reviewers Tina Martin and Konstantyn Titov are thanked for improving the clarity and scientific quality of the manuscript, through an efficient review process. The power company Landsvirkjun is thanked for providing with on-site accommodation and facilities during the field campaign. Anthony Finizola, Renaud Trinquier and Anna Kristín Árnadóttir are thanked for helping with material transportation issues. André Revil, Sveinbjorn Steinthórsson, Daniel Juncu and Vincent Drouin are thanked for their help in the field, and Stefán Auðunn Stefánsson for the logistical support. Völker Rath is thanked for constructive discussion. L.L. thanks Gylfi Páll Hersir for his constructive comments on the manuscript and his general support and Lee Slater for valuable feedbacks and discussions on the manuscript. L.L. also thanks Pierre Briole and Ólafur G. Flóvenz for their support with the organisation of the field campaign. The company Jarðboranir is thanked for providing bentonite for field measurements. The company Aarhus GeoSoftware is thanked for providing a free trial license for Aarhus Workbench to L.L. Three-dimensional figures were made with the freeware Paraview. This work was supported by a PhD grant from Paris Sciences et Lettres to Léa Lévy and the IMAGE FP7 EC and GEMex H2020 projects (grant agreements 608553 and 727550). Fundings for the field measurements were provided by the French Ministries of Foreign Affairs and International Development and of Education, Teaching and Research, through the PHC program Jules Verne, granted to Ecole Normale Supérieure and University of Iceland, as well as by a CNRS-INSU grant to University of Savoie-Mont Blanc. Equipment transportation expenses were covered by University of Montpellier and also supported by University of La Réunion.

REFERENCES

Abdulsamad, F., Florsch, N., & Camerlynck, C., 2017. Spectral induced polarization in a sandy medium containing semiconductor materials: experimental results and numerical modelling of the polarization mechanism, *Near Surface Geophysics*, **15**(6), 669–683.

Archie, G. E., 1942. The electrical resistivity log as an aid in determining some reservoir characteristics, *Transactions of the AIME*, **146**(01), 54–62.

Ármannsson, H., Gudmundsson, A., & Steingrímsson, B. S., 1987. Exploration and development of the Krafla geothermal area, *Jökull*, **37**, 13–30.

Árnason, K. & Magnússon, I. T., 2001. Niðurstöður við námsmælinga í Kröflu, Report OS-2001/062, Orkustofnun.

Árnason, K., Vilhjálmsson, A., & Björnsdóttir, T., 2007. A study of the Krafla volcano using gravity, micro earthquake and MT data, KenGen, Lake Naivasha, Kenya, 14 pp.

Arps, J. J., 1953. The effect of temperature on the density and electrical resistivity of sodium chloride solutions, *Journal of Petroleum Technology*, **5**(10), 17–20.

Auken, E., Christiansen, A. V., Kirkegaard, C., Fiandaca, G., Schamper, C., Behroozmand, A. A., Binley, A., Nielsen, E., Effersø, F., Christensen, N. B., et al., 2014. An overview of a highly versatile forward and stable inverse algorithm for airborne, ground-based and borehole electromagnetic and electric data, *Exploration Geophysics*, **46**(3), 223–235.

Bairlein, K., Bücker, M., Hördt, A., & Hinze, B., 2016. Temperature dependence of spectral induced polarization data: experimental results and membrane polarization theory, *Geophysical Supplements to the Monthly Notices of the Royal Astronomical Society*, **205**(1), 440–453.

Beaufort, D., Papapanagiotou, P., Patrier, P., Fujimoto, K., & Kasai, K., 1995. High-temperature smectites in active geothermal systems, in *Proceedings 8th Water-Rock Interaction Symposium, Vladivostok*, pp. 1071 – 1076, Balkema, Rotterdam.

Bertin, J. & Loeb, J., 1976. *Experimental and Theoretical aspects of induced polarization, Vol. 1*, Schweizerbart Science Publishers, Stuttgart, Germany.

Bücker, M., Flores Orozco, A., & Kemna, A., 2018. Electro-chemical polarization around metallic particles–part 1: The role of diffuse-layer and volume-diffusion relaxation, *Geophysics*, **83**(4), 1–53.

Dahlin, T. & Leroux, V., 2012. Improvement in time-domain induced polarization data quality with multi-electrode systems by separating current and potential cables, *Near Surface Geophysics*, **10**(6), 545–565.

Dahlin, T. & Zhou, B., 2006. Multiple-gradient array measurements for multichannel 2d resistivity imaging, *Near Surface Geophysics*, **4**(2), 113–123.

Edwards, L., 1977. A modified pseudosection for resistivity and ip, *Geophysics*, **42**(5), 1020–1036.

Fiandaca, G., 2018. Induction-free acquisition range in spectral time- and frequency-domain induced polarization at field scale, *Geophysical Journal International*.

731 Fiandaca, G., Auken, E., Christiansen, A. V., & Gazoty, A., 2012. Time-domain-induced polarization:
732 Full-decay forward modeling and 1d laterally constrained inversion of cole-cole parameters, *Geophysics*,
733 **77**(3), E213–E225.
734 Fiandaca, G., Ramm, J., Binley, A., Gazoty, A., Christiansen, A. V., & Auken, E., 2013. Resolving spectral
735 information from time domain induced polarization data through 2-d inversion, *Geophys. J. Int*, **192**,
736 631–646.
737 Fiandaca, G., Christiansen, A., & Auken, E., 2015. Depth of investigation for multi-parameters inversions,
738 in *Near Surface Geoscience 2015-21st European Meeting of Environmental and Engineering Geophysics*.
739 Fiandaca, G., Madsen, L. M., & Maurya, P. K., 2018. Re-parameterisations of the cole–cole model for
740 improved spectral inversion of induced polarization data, *Near Surface Geophysics*, **16**(4), 385–399.
741 Fiandaca, G., Olsson, P., Maurya, P. K., Dahlin, T., & Auken, E., 2019. Non-standard responses in time-
742 domain induced polarization measurements, *Geophysical Journal International (under review)*.
743 Flis, M. F., Newman, G. A., & Hohmann, G. W., 1989. Induced-polarization effects in time-domain
744 electromagnetic measurements, *Geophysics*, **54**(4), 514–523.
745 Flóvenz, O., Georgsson, L., & Árnason, K., 1985. Resistivity structure of the upper crust in iceland,
746 *Journal of Geophysical Research*, **90**(B12), 10136–10150.
747 Flóvenz, O., Spangenberg, E., Kulenkampf, J., Árnason, K., Karlsdóttir, R., & Huenges, E., 2005. The
748 role of electrical interface conduction in geothermal exploration, in *World Geothermal Congress*.
749 Gasperikova, E., Newman, G., Feucht, D., & Árnason, K., 2011. 3D MT characterization of two geother-
750 mal fields in Iceland, *GRC Transactions*, **35**.
751 Gazoty, A., Fiandaca, G., Pedersen, J., Auken, E., & Christiansen, A. V., 2013. Data repeatability and
752 acquisition techniques for time-domain spectral induced polarization, *Near Surface Geophysics*, **11**(4),
753 391–406.
754 Ghorbani, A., Revil, A., Coperey, A., Ahmed, A. S., Roque, S., Heap, M., Grandis, H., & Viveiros, F.,
755 2018. Complex conductivity of volcanic rocks and the geophysical mapping of alteration in volcanoes,
756 *Journal of Volcanology and Geothermal Research*, **357**, 106–127.
757 Gresse, M., Vandemeulebrouck, J., Byrdina, S., Chiodini, G., Revil, A., Johnson, T. C., Ricci, T., Vilardo,
758 G., Lebourg, T., Grangeon, J., et al., 2017. 3-D resistivity tomography of the Solfatara crater (Italy):
759 implication for the multiphase flow structure of the shallow hydrothermal system, *Journal of Geophysical*
760 *Research*, **122**.
761 Gudmundsson, A., 1991. Borun kjarnaholu í Sandabotnaskarð, Report in icelandic, Orkustofnun.
762 Gudmundsson, A., Egilson, T., & Haraldson, K., 2007. Krafla - Hola KS-01. forborun og 1. áfangi., Tech.
763 Rep. LV-2007/055, Landsvirkjun.
764 Gudmundsson, A., Mortensen, A. K., Hjartarson, A., Karlsdóttir, R., & Ármannsson, H., 2010. Exploration
765 and utilization of the Namafjall high temperature area in North Iceland, in *World Geothermal Congress*.

766 Gurin, G., Titov, K., Ilyin, Y., & Tarasov, A., 2015. Induced polarization of disseminated electronically
767 conductive minerals: a semi-empirical model, *Geophysical Journal International*, **200**(3), 1555–1565.
768 Gurin, G., Ilyin, Y., Nilov, S., Ivanov, D., Kozlov, E., & Titov, K., 2018. Induced polarization of rocks
769 containing pyrite: Interpretation based on x-ray computed tomography, *Journal of Applied Geophysics*,
770 **154**, 50–63.
771 Helander, D. P., 1983. *Fundamentals of formation evaluation*, OGCI Publications Tulsa.
772 Hjartardóttir, Á., Einarsson, P., Magnúsdóttir, S., Björnsdóttir, Þ., & Brandsdóttir, B., 2016. Fracture
773 systems of the northern volcanic rift zone, Iceland: An onshore part of the mid-atlantic plate boundary,
774 *Geological Society, London, Special Publications*, **420**(1), 297–314.
775 Hjartardóttir, Á. R., Einarsson, P., Bramham, E., & Wright, T. J., 2012. The krafla fissure swarm, iceland,
776 and its formation by rifting events, *Bulletin of Volcanology*, **74**(9), 2139–2153.
777 Hupfer, S., Martin, T., Weller, A., Günther, T., Kuhn, K., Ngninjio, V. D. N., & Noell, U., 2016. Polariza-
778 tion effects of unconsolidated sulphide-sand-mixtures, *Journal of Applied Geophysics*, **135**, 456–465.
779 Ingeman-Nielsen, T. & Baumgartner, F., 2006. Numerical modelling of complex resistivity effects on a
780 homogenous half-space at low frequencies, *Geophysical prospecting*, **54**(3), 261–271.
781 Johansen, H., 1977. A man/computer interpretation system for resistivity soundings over a horizontally
782 strafified earth, *Geophysical Prospecting*, **25**(4), 667–691.
783 Jónasson, K., 1994. Rhyolite volcanism in the krafla central volcano, north-east iceland, *Bulletin of Vol-*
784 *canology*, **56**(6-7), 516–528.
785 Jónsson, S. S., Gudmundsson, A., & Thordarson, S., 2003. Krafla borun kjarnaholu KH3 milli Jörundar
786 og Háganga., Report in icelandic, ISOR.
787 Kemna, A., Binley, A., Cassiani, G., Niederleithinger, E., Revil, A., Slater, L., Williams, K. H., Orozco,
788 A. F., Haegel, F.-H., Hoerdt, A., et al., 2012. An overview of the spectral induced polarization method
789 for near-surface applications, *Near Surface Geophysics*, **10**(6), 453–468.
790 Kristinsdóttir, L. H., Flóvenz, O. G., Árnason, K., Bruhn, D., Milsch, H., Spangenberg, E., & Kulenkampff,
791 J., 2010. Electrical conductivity and p-wave velocity in rock samples from high-temperature icelandic
792 geothermal fields, *Geothermics*, **39**(1), 94–105.
793 Leroy, P., Weigand, M., Mériguet, G., Zimmermann, E., Tournassat, C., Fagerlund, F., Kemna, A., &
794 Huisman, J. A., 2017. Spectral induced polarization of na-montmorillonite dispersions, *Journal of colloid*
795 *and interface science*, **505**, 1093–1110.
796 Lesmes, D. P. & Frye, K. M., 2001. Influence of pore fluid chemistry on the complex conductivity
797 and induced polarization responses of Berea sandstone, *Journal of Geophysical Research: Solid Earth*,
798 **106**(B3), 4079–4090.
799 Lévy, L., Gibert, B., Sigmundsson, F., Flóvenz, O. G., Hersir, G. P., Briole, P., & Pezard, P. A., 2018. The
800 role of smectites in the electrical conductivity of active hydrothermal systems: electrical properties of

core samples from Krafla volcano, Iceland, *Geophysical Journal International*, **215**(3), 1558–1582.

Lévy, L., Gibert, B., Sigmundsson, F., Parat, F., Deldicque, D., & Hersir, G. P., 2019. Tracking magmatic hydrogen sulphur circulations using electrical impedance : complex electrical properties of core samples at the Krafla volcano, Iceland, *Journal of Geophysical Research: Solid Earth*, **124**.

Libbey, R. B. & Williams-Jones, A. E., 2013. Sulfide mineralization in the Reykjanes geothermal system, Iceland; potential applications for geothermal exploration, *GRC Trans*, **37**, 417–424.

Loke, M. H., 2004. Tutorial: 2-d and 3-d electrical imaging surveys, Set of notes available online.

Loke, M. H. & Barker, R., 1996. Rapid least-squares inversion of apparent resistivity pseudosections by a quasi-newton method 1, *Geophysical prospecting*, **44**(1), 131–152.

Madsen, L. M., Fiandaca, G., Auken, E., & Christiansen, A. V., 2017. Time-domain induced polarization-an analysis of cole-cole parameter resolution and correlation using markov chain monte carlo inversion, *Geophysical Journal International*, **211**(3), 1341–1353.

Maraqah, H., Li, J., & Whittingham, M. S., 1990. Ion transport in single crystals of the clay-like aluminosilicate, vermiculite, *MRS Online Proceedings Library Archive*, **210**.

Maurya, P., Fiandaca, G., Christiansen, A., & Auken, E., 2018. Field-scale comparison of frequency-and time-domain spectral induced polarization, *Geophysical Journal International*.

Menke, W., 2012. Chapter 9 - Nonlinear inverse problems, in *Geophysical Data Analysis: Discrete Inverse Theory (Third Edition)*, pp. 163 – 188, ed. Menke, W., Academic Press, Boston, third edition edn.

Meunier, A., 2005. *Clays*, Springer Science & Business Media.

Misra, S., Torres-Verdín, C., Revil, A., Rasmus, J., & Homan, D., 2016. Interfacial polarization of disseminated conductive minerals in absence of redox-active species–part 1: Mechanistic model and validation, *Geophysics*, **81**(2), E139–E157.

Nono, F., Gibert, B., Parat, F., Loggia, D., Cichy, S. B., & Violay, M., 2018. Electrical conductivity of icelandic deep geothermal reservoirs up to supercritical conditions: Insight from laboratory experiments, *Journal of Volcanology and Geothermal Research*.

Okpoli, C. C., 2013. Sensitivity and resolution capacity of electrode configurations, *International Journal of Geophysics*, **2013**.

Olsson, P.-I., Fiandaca, G., Dahlin, T., & Auken, E., 2015. Impact of time-domain IP pulse length on measured data and inverted models, in *Near Surface Geoscience 2015-21st European Meeting of Environmental and Engineering Geophysics*.

Olsson, P.-I., Fiandaca, G., Larsen, J. J., Dahlin, T., & Auken, E., 2016. Doubling the spectrum of time-domain induced polarization by harmonic de-noising, drift correction, spike removal, tapered gating and data uncertainty estimation, *Geophysical Supplements to the Monthly Notices of the Royal Astronomical Society*, **207**(2), 774–784.

Orozco, A. F., Kemna, A., Oberdörster, C., Zschornack, L., Leven, C., Dietrich, P., & Weiss, H., 2012.

Delineation of subsurface hydrocarbon contamination at a former hydrogenation plant using spectral induced polarization imaging, *Journal of contaminant hydrology*, **136**, 131–144.

Orozco, A. F., Bücker, M., Steiner, M., & Malet, J.-P., 2018. Complex-conductivity imaging for the understanding of landslide architecture, *Engineering Geology*, **243**, 241–252.

Parkhomenko, E. I., 1971. *Electrification phenomena in rocks*, Springer Science & Business Media New York.

Patrier, P., Papapanagiotou, P., Beaufort, D., Traineau, H., Bril, H., & Rojas, J., 1996. Role of permeability versus temperature in the distribution of the fine (≤ 0.2 μ m) clay fraction in the Chipilapa geothermal system (El Salvador, Central America), *Journal of Volcanology and Geothermal Research*, **72**(1), 101–120.

Pelton, W. H., Ward, S. H., Hallof, P. G., Sill, W. R., & Nelson, P. H., 1978. Mineral discrimination and removal of inductive coupling with multifrequency IP, *Geophysics*, **43**(3), 588–609.

Revil, A., Florsch, N., & Mao, D., 2015. Induced polarization response of porous media with metallic particles - Part 1: a theory for disseminated semiconductors, *Geophysics*.

Revil, A., Le Breton, M., Niu, Q., Wallin, E., Haskins, E., & Thomas, D. M., 2017a. Induced polarization of volcanic rocks.1. surface versus quadrature conductivity, *Geophysical Journal International*, **208**(2), 826–844.

Revil, A., Murugesu, M., Prasad, M., & Le Breton, M., 2017b. Alteration of volcanic rocks: A new non-intrusive indicator based on induced polarization measurements, *Journal of Volcanology and Geothermal Research*, **341**, 351–362.

Rosenkjaer, G. K., Gasperikova, E., Newman, G. A., Árnason, K., & Lindsey, N. J., 2015. Comparison of 3D MT inversions for geothermal exploration: case studies for Krafla and Hengill geothermal systems in Iceland., *Geothermics*, **57**, 258–274.

Sæmundsson, K., 1983. The eruption history of the krafla volcano during the last 3000 years, *Ravens Congregations*, pp. 1–2.

Sæmundsson, K., 1991. *Náttúra Mývatns*, chap. Jarðfræði Kröflukerfisins., pp. 25–95, Reykjavík: Hið íslenska náttúrufræðifélag.

Sæmundsson, K., Pringle, M., & Hardarson, B., 2000. About the age of strata in the krafla volcanic system, in *Geoscience Society of Iceland, Spring Meeting*, pp. 26–27.

Saemundsson, K., Hjartarson, A., Kaldal, I., Sigurgeirsson, M. A., Kristinsson, S. G., & Víkingsson, S., 2012. Geological map of the northern volcanic zone, Iceland. Northern part 1:100 000, Reykjavík: Iceland Geosurvey and Landsvirkjun.

Scott, J. H., 1984. *Computer analysis of digital well logs*, no. 879-882, US Department of the Interior, Geological Survey.

Sigmarsson, O. & Steinthórsson, S., 2007. Origin of icelandic basalts: A review of their petrology and

geochemistry, *Journal of Geodynamics*, **43**(1), 87–100.

Sigmundsson, F., 2006. *Iceland geodynamics: crustal deformation and divergent plate tectonics*, Springer Science & Business Media.

Slater, L. D. & Sandberg, S. K., 2000. Resistivity and induced polarization monitoring of salt transport under natural hydraulic gradients, *Geophysics*, **65**(2), 408–420.

Sumner, J. S., 1976. *Principles of induced polarization for geophysical exploration*, vol. 5 of **Developments in Economic Geology**, Elsevier Scientific Publishing Company Amsterdam.

Telford, W. M., Geldart, L. P., & Sheriff, R. E., 1990. *Applied Geophysics*, Cambridge University Press, 2nd edn.

Treichel, A., Binley, A., Kemna, A., Esser, O., Zimmermann, E., Vereecken, H., & Huismann, J., 2014. Temperature dependence of broadband complex electrical conductivity in unconsolidated porous media with variable clay content, in *3rd International Workshop on Induced Polarization*, pp. 38–39, Ile d'Oleron France.

Tuffen, H. & Castro, J. M., 2009. The emplacement of an obsidian dyke through thin ice: Hrafntinnuhryggur, Krafla Iceland, *Journal of Volcanology and Geothermal Research*, **185**(4), 352–366.

Vinegar, H. & Waxman, M., 1984. Induced polarization of shaly sands, *Geophysics*, **49**(8), 1267–1287.

Wait, J. R., 1983. Complex conductivity of disseminated spheroidal ore grains, *Gerlands Beitr. Geophys*, **92**, 49–69.

Wait, J. R., 1987. Physical model for the complex resistivity of the earth, *Electronics letters*, **23**(19), 979–980.

Waxman, M. H. & Smits, L. J. M., 1968. Electrical conductivities in oil-bearing shaly sands, *Soc. Pet. Eng. J.*, **8**, 107–122.

Weller, A., Slater, L., & Nordsiek, S., 2013. On the relationship between induced polarization and surface conductivity: Implications for petrophysical interpretation of electrical measurements, *Geophysics*, **78**(5), D315–D325.

Wong, J., 1979. An electrochemical model of the induced-polarization phenomenon in disseminated sulfide ores, *Geophysics*, **44**(7), 1245–1265.

APPENDIX A: TEMPERATURE-DEPENDENCE OF THE PHASE-ANGLE

We build here an empirical equation to estimate the temperature-dependence of the phase-angle, assuming that in-phase and quadrature conductivity depend on temperature in a similar manner (Equation A.1), following an Arps' relationship (Arps 1953).

$$\frac{\rho'(T_0)}{\rho'(T)} = 1 + \alpha_{\rho'}(T - T_0) \iff \frac{\sigma'(T)}{\sigma'(T_0)} = 1 + \alpha_{\sigma'}(T - T_0)$$
$$\frac{\sigma"(T)}{\sigma"(T_0)} = 1 + \alpha_{\sigma"}(T - T_0) \tag{A.1}$$

where T and T_0 are the in-situ (from log) and reference temperature in °C, respectively, σ' and $\sigma"$ are the in-phase and quadrature conductivity in S/m, respectively, $\alpha_{\sigma'}$ and $\alpha_{\sigma"}$ are the correction coefficient for the in-phase and quadrature conductivity in $^\circ C^{-1}$, respectively, with $\alpha_{\sigma'} = \alpha_{\rho'}$.

Small phase angles ($\phi \leq 200$ mrad in our measurements) can be approximated by the ratio between quadrature and in-phase conductivity. Equation A.2 presents the corresponding temperature-dependence for the phase-angle.

$$\frac{\phi(T)}{\phi(T_0)} = \frac{\frac{\sigma"(T)}{\sigma"(T_0)}}{\frac{\sigma'(T)}{\sigma'(T_0)}} = \frac{1 + \alpha_{\sigma"}(T - T_0)}{1 + \alpha_{\sigma'}(T - T_0)} \tag{A.2}$$

Using Equation A.1 and laboratory measurements of the quadrature conductivity at temperatures 25°C, 50°C, 75°C and 100°C by Vinegar & Waxman (1984), we obtain the coefficients $\alpha_{\sigma"}$ = 0.0282$^\circ C^{-1}$ and 0.028$^\circ C^{-1}$ for a clay-rich sample and a sandstone sample. Using Equation A.1 as well and laboratory measurements of the quadrature conductivity of two volcanic samples heated up to 50°C by Ghorbani et al. (2018), we obtain a correction coefficient of 0.0213$^\circ C^{-1}$. We consider that $\alpha_{\sigma"} = 0.0282^\circ C^{-1}$ is the closest value to our conditions, given that it is fitted to measurements up to 100 °C and corresponds to a clay-rich sample.

Then, we consider two distinct values for the temperature-dependence of the in-phase conductivity: $\alpha_{\sigma'}$ = 0.033$^\circ C^{-1}$, inferred from in-phase conductivity measurements by Vinegar & Waxman (1984), and $\alpha_{\sigma'}$ =0.06$^\circ C^{-1}$, fitted to our results and consistent with other studies on Icelandic volcanic samples, as mentioned earlier.

Samples from KH1 analysed here were extracted from depths corresponding to the temperature range 75-165°C. In this range of temperatures and considering the coefficients $\alpha_{\sigma'}$ and $\alpha_{\sigma"}$ inferred above, we find that the ratio $\frac{\phi(T)}{\phi(T_0)}$ is close to 0.9 in the case $\alpha_{\sigma'}$ = 0.033$^\circ C^{-1}$ but decreases from 0.6 to 0.5 in the case $\alpha_{\sigma'}$ =0.06$^\circ C^{-1}$ with increasing temperature (Figure A1). We use the latter temperature-dependence to estimate the temperature-corrected laboratory MPA in our study. If the

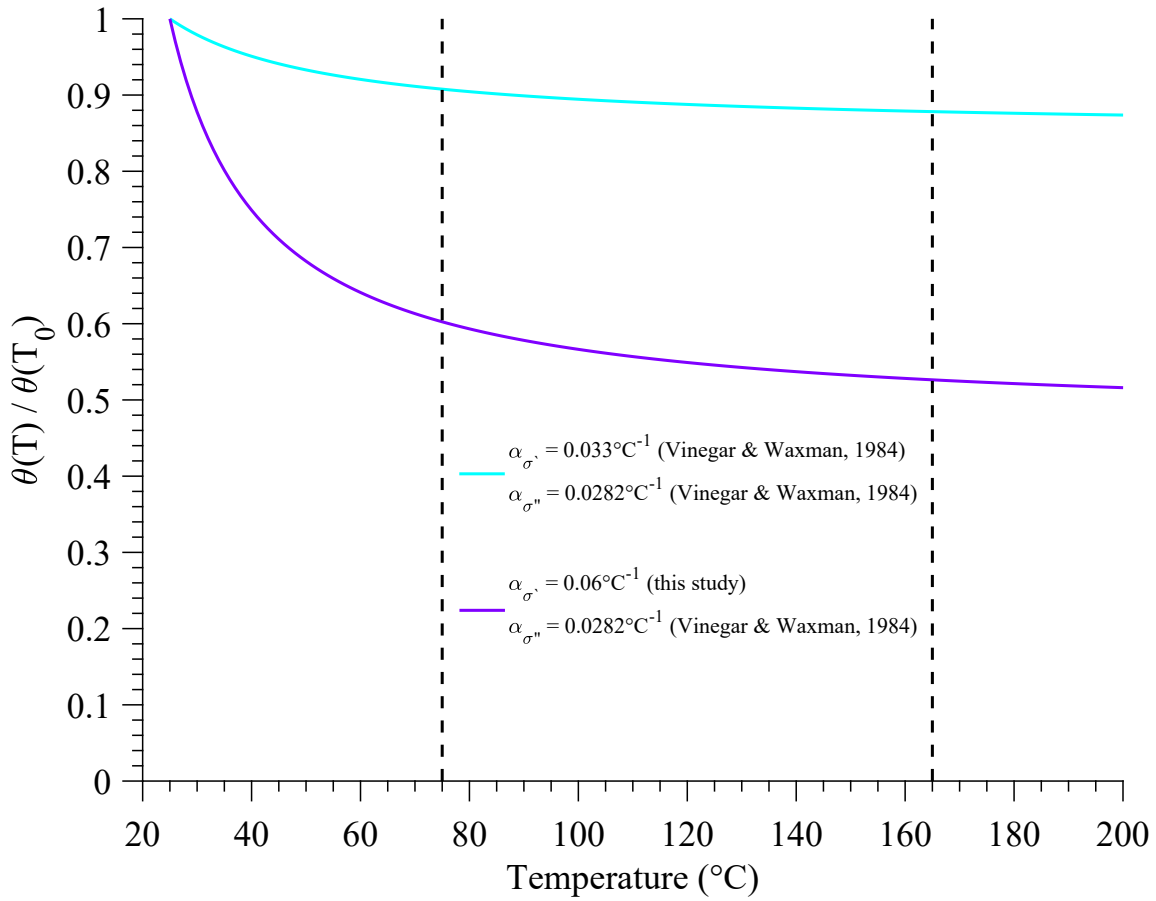

Figure A1. Decrease of phase angle with temperature increasing from 25°C to 200°C, based on Equation A.2. The correction coefficient $\alpha_{\sigma''} = 0.0282°C^{-1}$ is used for the quadrature conductivity and two different correction coefficients are used for the in-phase conductivity: $\alpha_{\sigma'} = 0.06°C^{-1}$ (magenta line, based on temperature-dependence observed on samples from this area) and $\alpha_{\sigma'} = 0.033°C^{-1}$ (cyan line, based on samples from Vinegar & Waxman (1984)). The range of temperatures relevant for samples in borehole KH1 is within the two black broken lines.

coefficient $\alpha_{\sigma''} = 0.0213°C^{-1}$, inferred from data presented by Ghorbani et al. (2018), were to be used instead of $\alpha_{\sigma''} = 0.0282°C^{-1}$ inferred from data presented by (Vinegar & Waxman 1984), it would lead to excessive correction (temperature-corrected laboratory MPA would become smaller than field MPA).

submitted to *Geophys. J. Int.*

Supporting Information for: Electrical Resistivity Tomography and Time-Domain Induced Polarization field investigations of geothermal areas at Krafla, Iceland: comparison to borehole and laboratory frequency-domain electrical observations

L. Lévy[1 2⋆], P.K. Maurya[3], S. Byrdina[4], J. Vandemeulebrouck[4], F. Sigmundsson[2], K. Árnason[5], T. Ricci[6], D. Deldicque[1], M. Roger[1], B. Gibert[7] and P. Labazuy[8]

[1] *Laboratoire de Géologie, Ecole Normale Supérieure - PSL, CNRS, UMR 8538,, Paris 75005, France*

[2] *Nordic Volcanological Center, Institute of Earth Sciences, University of Iceland, 101 Reykjavík, Iceland*

[3] *Hydrogeophysics Group, Aarhus University, Aarhus, Denmark*

[4] *Université de Savoie Mont-Blanc, ISTerre, Le Bourget du Lac, France*

[5] *ÍSOR - Iceland GeoSurvey, Reykjavik, Iceland*

[6] *Istituto Nazionale di Geofisica e Vulcanologia, Roma, Italy*

[7] *Géosciences Montpellier, Université de Montpellier, Université des Antilles, CNRS, France*

[8] *Université Clermont Auvergne, CNRS, IRD, OPGC, Laboratoire Magmas et Volcans, F-63000 Clermont-Ferrand, France*

8 April 2019

S1. Quality of laboratory measurements

The calibration of the impedance-meter used for laboratory measurements is illustrated in Figure S1. The impedance response of the apparatus when the sample holder is filled with water is shown in Figure S2 for different salinities. These two figures suggest that an overall 1 mrad uncertainty exists on the measured phase-angles.

S2. Impact of pulse length

It can be observed in Figure S3 that the voltage discharge curves depend on the current injection time: the longer the injection, the larger is the area under the decay curve. This shows that the integral chargeability (integer under the decay curve) depends on the injection time, as already underlined by Fiandaca et al. (2012) and Olsson et al. (2015). It illustrates the importance of taking into account the waveform of the transmitted current in the inversion but also to fit the whole decay curve rather than considering only the integral chargeability. Without taking the waveform of the transmitted current into account, smaller injection time give smaller values of integral chargeability. We used together all the different injection times for a single inversion.

S3. Normalized chargeability

Recent studies suggest that the normalized chargeability, or more generally "normalized IP parameters", can help visualise the contribution of clay minerals to the Induced Polarization response. Here, we show that the distribution of chargeability is more or less the same as the distribution of resistivity (Figure S4). This was expected given the several orders of magnitude of variation of resistivity, as opposed to the slight variations of chargeability (or MPA). The normalized chargeability, which is the product between conductivity and chargeability, is controlled by the variations of conductivity (resistivity), since resistivity ranges from 1 to 10^4, while chargeability only from 1 to 200. Figure S4 illustrates that normalized chargeability does not bring any additional information compared to resistivity.

S4. Resistivity inversion for profiles ISL-6 and ISL-8 (KH3 site)

The resistivity inversion models and resistivity data pseudo-section for profiles ISL-6 and ISL-8 (not shown in the main text) are shown in Figure S5.

S5. Relaxation time and grain size distribution of metallic particles

We calculate the relaxation time as the inverse of the angular frequency at which the maximum phase-angle is found, below 10 kHz. Relaxation times can also be determined using Debye superposition or Cole-Cole models but we wished here to avoid using a-priori models, in order to work with laboratory parameters that can be realistically compared to field parameters. The maximum polarization observed in the laboratory is often not reached during field TDIP measurements, given to the limited time-range investigated in the field. However, five samples have relaxation times within the time-range investigated with field measurements (Figure S6). In general, long relaxation times are associated with pyrite-rich samples, while short relaxation times can be associated with both pyrite and iron-oxides (Figure S6).

Based on image analysis of Scanning Electron Microscope photographs, Lévy et al. (2019) determined the grain size distribution of metallic particles for the laboratory samples used in this study. These distributions illustrate that pyrite mineralisations in Krafla cover a wide range of texture and sizes, while iron-oxides are only small and disseminated (Figure S7).

S6. Lithology in borehole KH1

The lithological log of borehole KH1, used to build the lithological resistivity model and achieve temperature corrections in KH1, is given in Figure S8.

S7. Resistivity inversion for profile ISL-13 (KH1 site)

The resistivity inversion model for ISL-13 is shown in Figure S9. Much less data were left in the resistivity pseudo section of profile ISL-13, compared to ISL-10, -11 and -12. This is due to particularly high contact resistance between ground and electrodes in this profile. The problem here is most likely related to the context of the measurements.

REFERENCES

Fiandaca, G., Auken, E., Christiansen, A. V., & Gazoty, A., 2012. Time-domain-induced polarization: Full-decay forward modeling and 1d laterally constrained inversion of cole-cole parameters, *Geophysics*,

77(3), E213–E225.

Gudmundsson, A., 1991. Borun kjarnaholu í Sandabotnaskarð, Report in icelandic, Orkustofnun.

Lévy, L., Gibert, B., Sigmundsson, F., Parat, F., Deldicque, D., & Hersir, G. P., 2019. Tracking magmatic hydrogen sulphur circulations using electrical impedance : complex electrical properties of core samples at the Krafla volcano, Iceland, *Journal of Geophysical Research: Solid Earth*, **124**.

Olsson, P.-I., Fiandaca, G., Dahlin, T., & Auken, E., 2015. Impact of time-domain IP pulse length on measured data and inverted models, in *Near Surface Geoscience 2015-21st European Meeting of Environmental and Engineering Geophysics*.

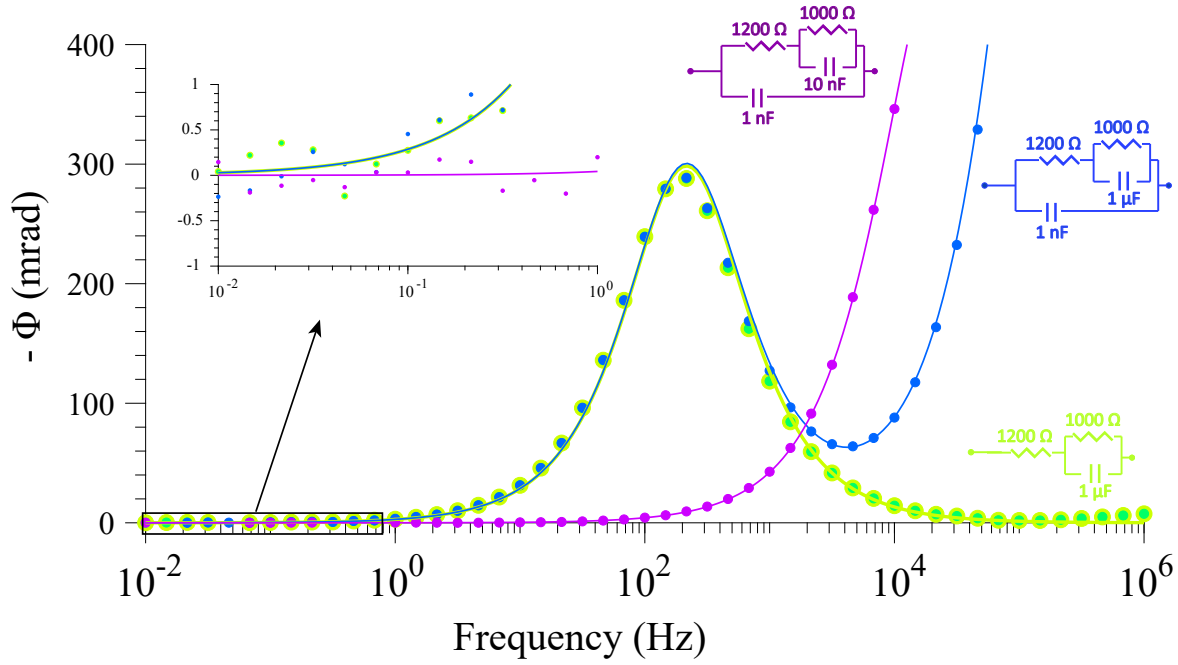

Figure S1. Phase-angle measured spectra versus theoretical predictions for three networks of resistors and capacitors of known impedance. A deviation of 0.5 mrad is observed between measurements and predictions.

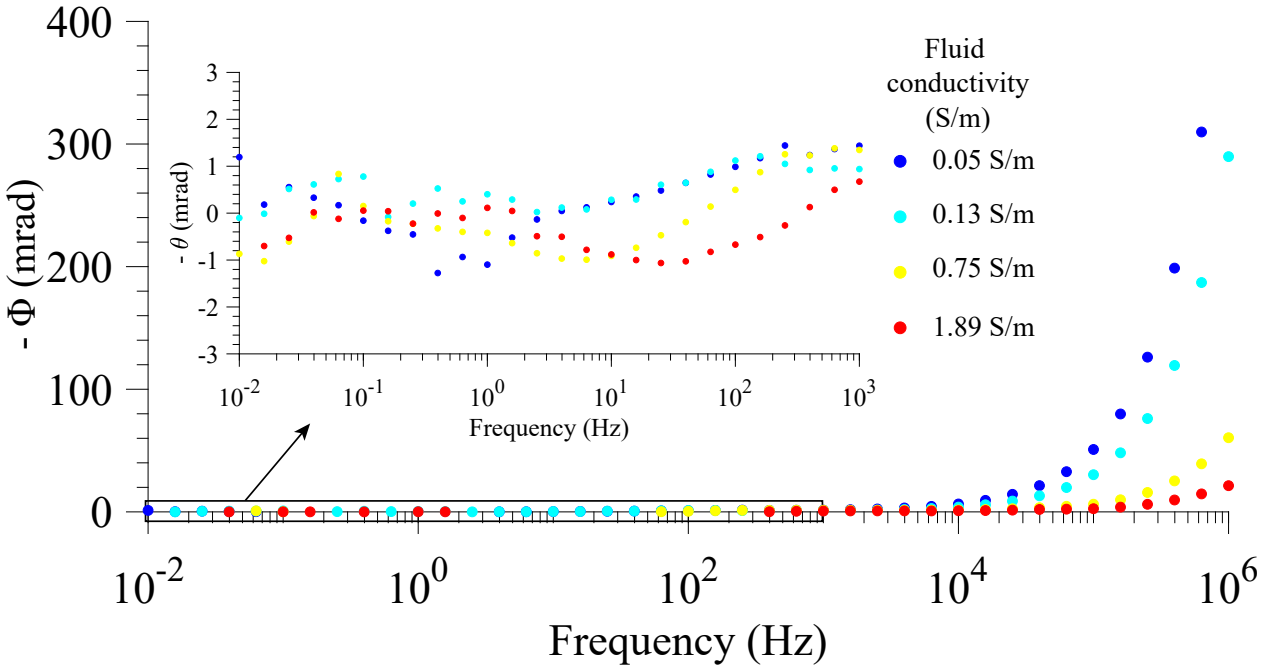

Figure S2. Phase-angle spectra measured with the electrical cell filled with water at different salinities. Deviations of 1 mrad, compared to the supposed absence of polarization response of pure water below 1 kHz, are observed.

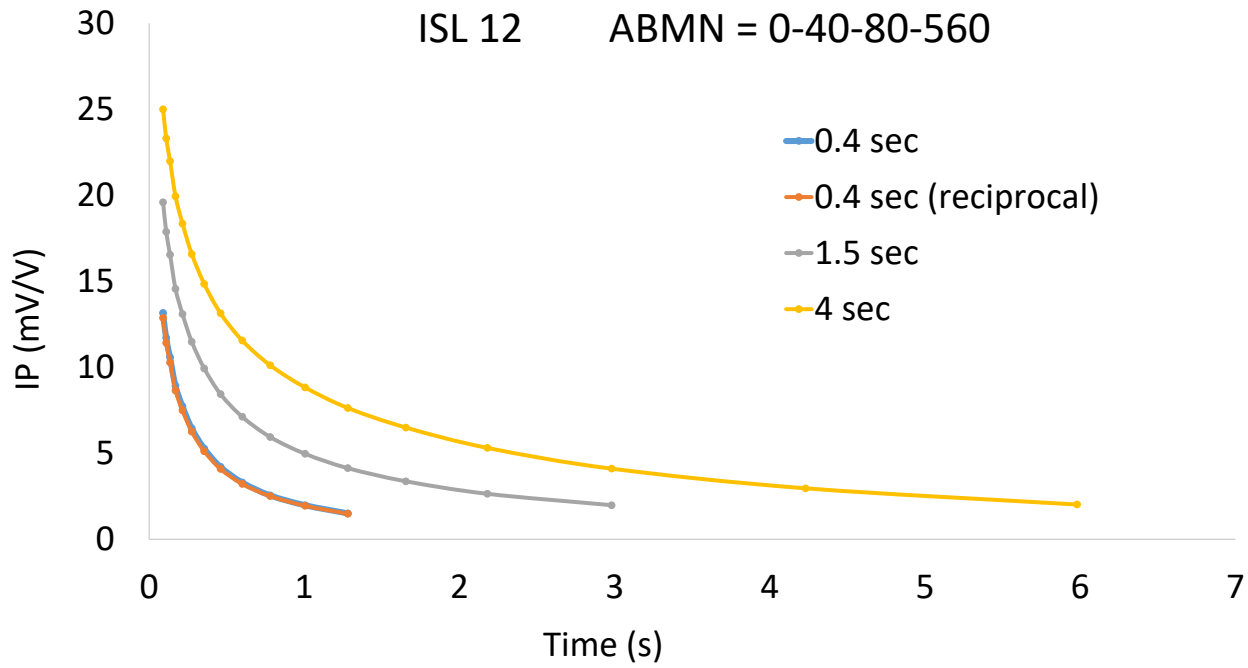

Figure S3. Decay voltage (normalized by the primary voltage) as a function of time, measured during the off-time for on quadrupole of electrodes, corresponding to the positions AMNB = 0-40-80-560. The four different colours correspond to four different sets of measurements: three different current injection times and one reciprocal measurements for the 0.4 s injection (inversion of current and potential cables). The reciprocal measurements are overlapping.

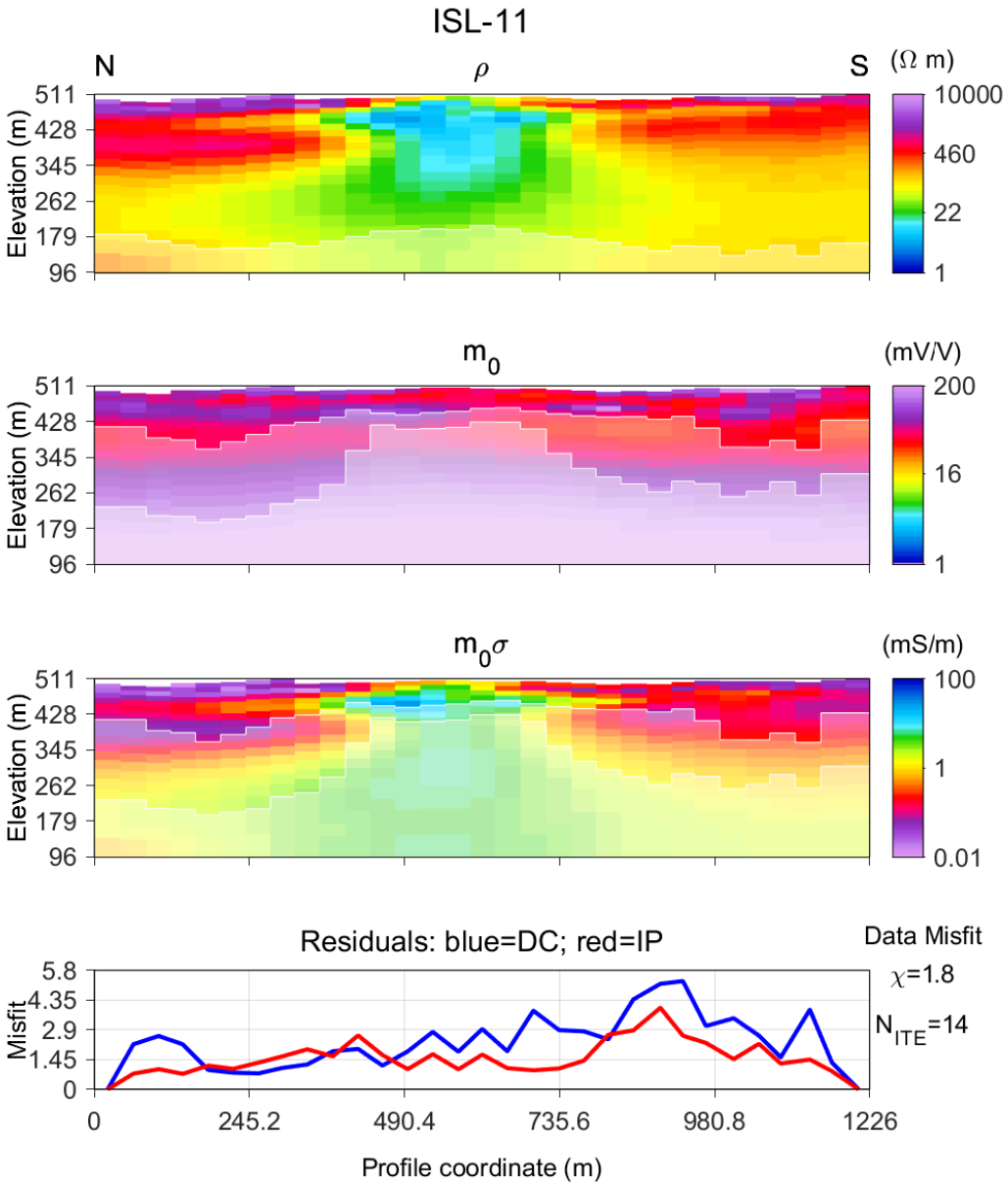

Figure S4. DCIP inversion (resistivity, chargeability and normalized chargeability) for profile ISL-11 (KH1 site), using the "Resistivity Cole-Cole" (RCC) parametrization, instead of the "Maximum Phase Angle" parametrization used in the rest of the study. This RCC parameterization allows to calculate the normalized chargeability.

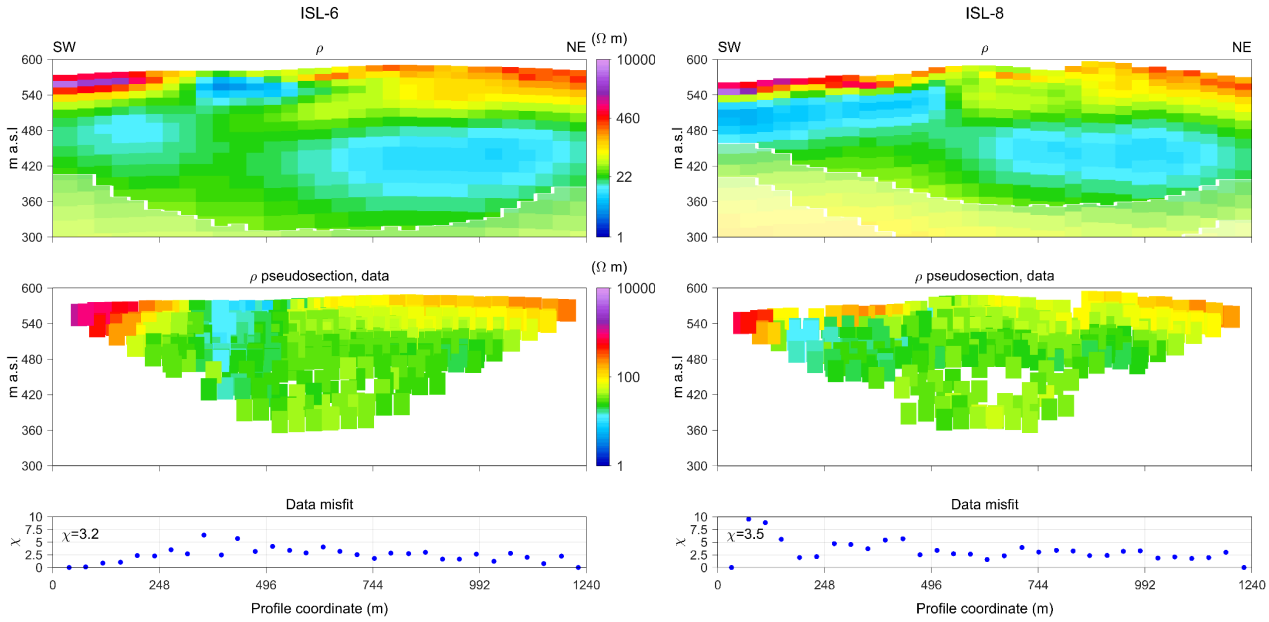

Figure S5. Resistivity inversion for profiles ISL-6 and ISL-8. The upper panels are the inversion models, showing two white lines in the lower part of the figure for the shallow and deep DOI. The middle panels are the apparent resistivity pseudo-sections. The lower panels give the data misfit χ for each vertical section of model (spaced every 40 m).

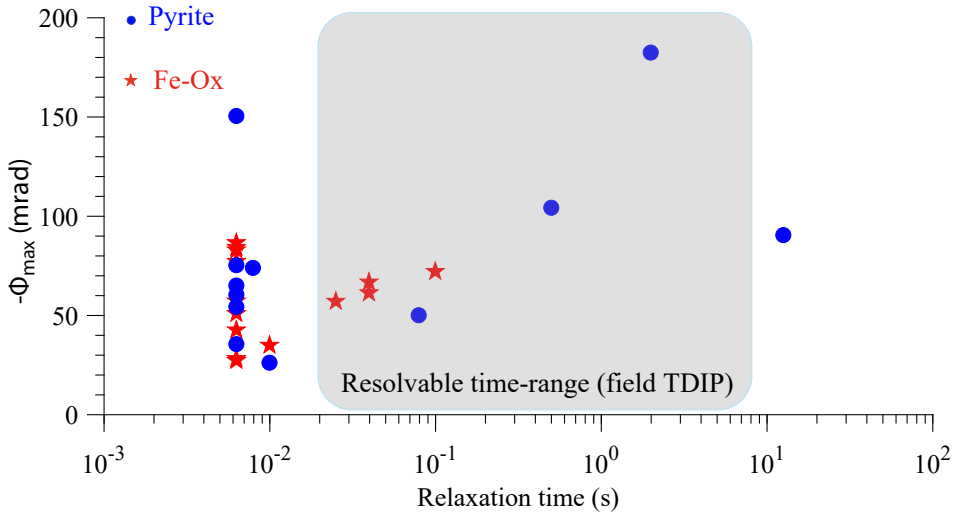

Figure S6. MPA versus relaxation time based on frequency-domain laboratory measurements on core samples. The range of relaxation time that can be resolved with TDIP field measurements is shown in grey.

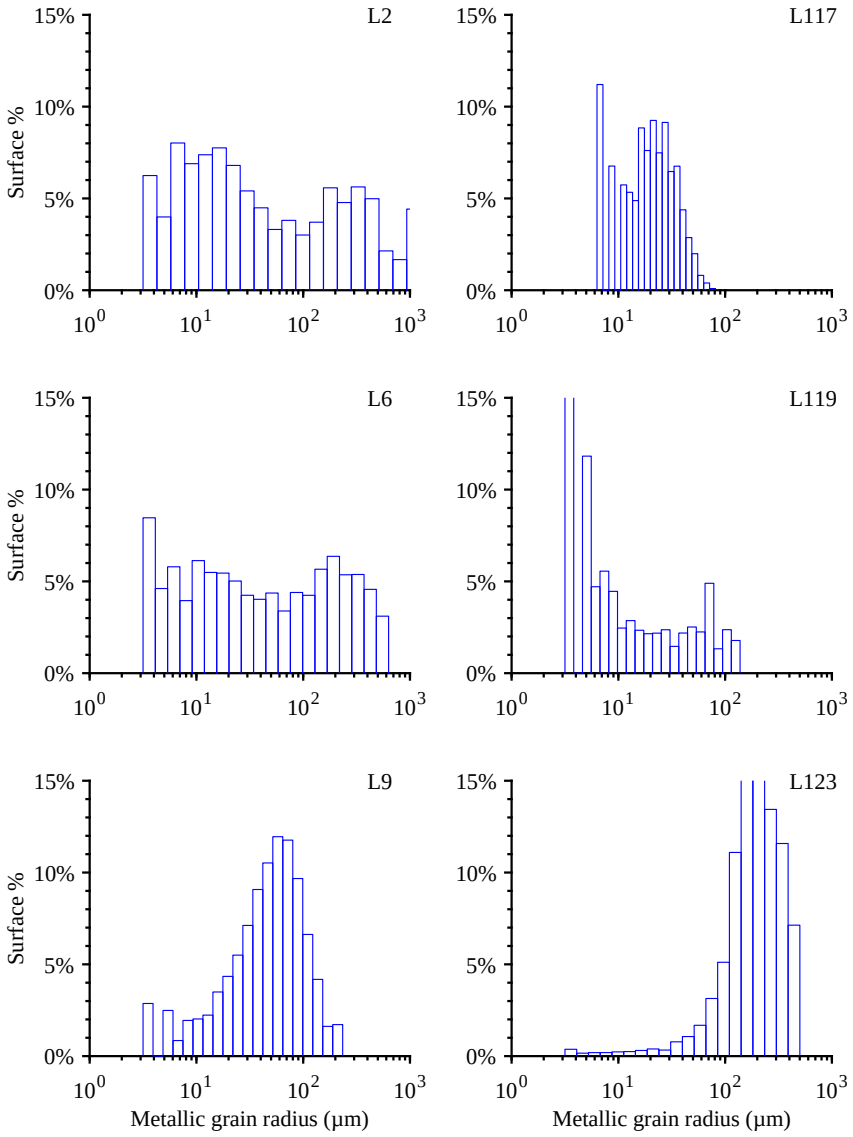

Figure S7. Grain size distribution of metallic particles for the six samples whose phase spectrum are represented in the main text (pyrite for L2, L6, L9, L119 and L123 and magnetite for L117). These distributions are calculated based on image analyses presented by Lévy et al. (2019).

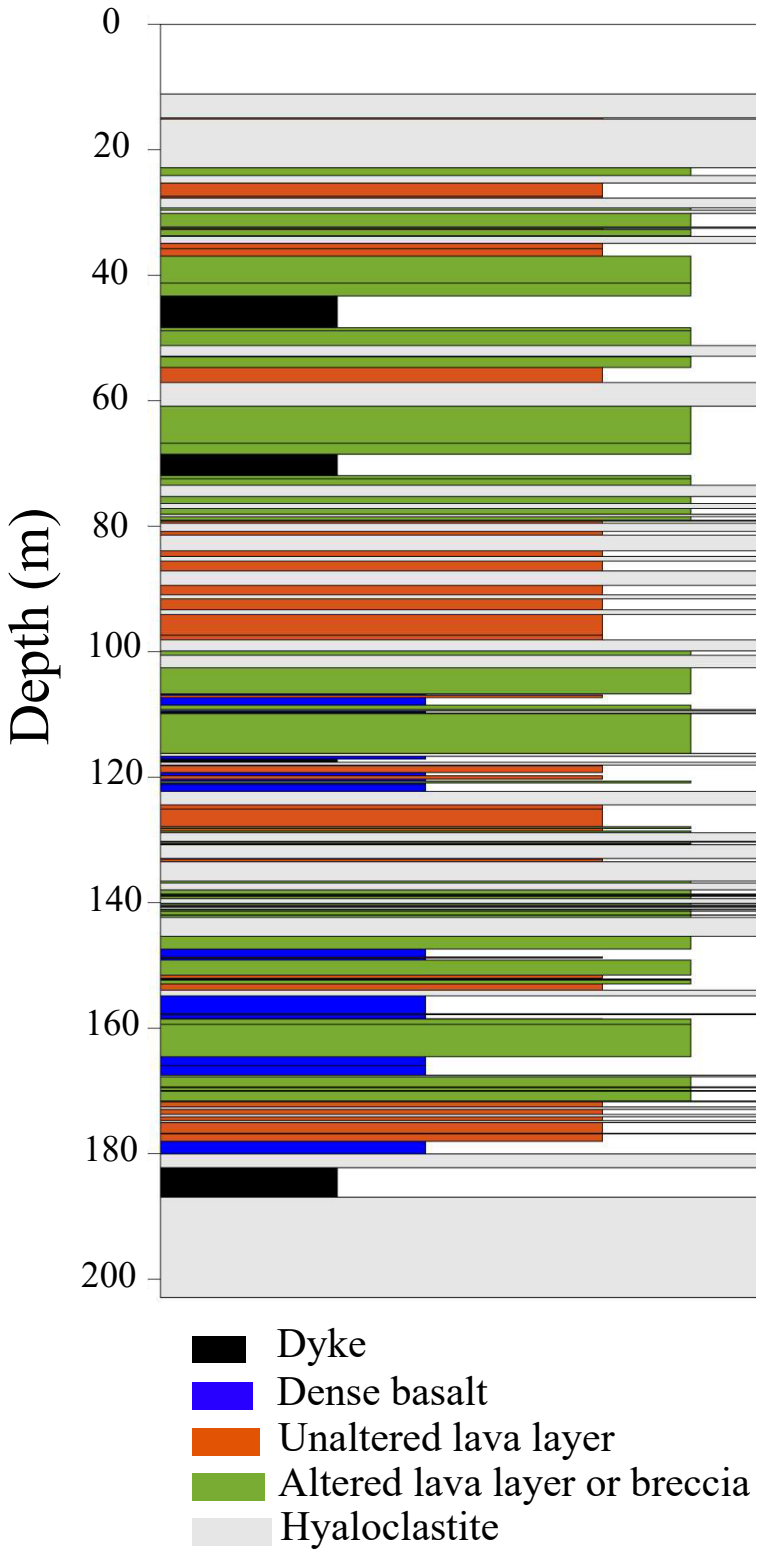

Figure S8. Simplified lithological log in borehole KH1, adapted from Gudmundsson (1991). The lengths of the various lithological layers are different for clarity.

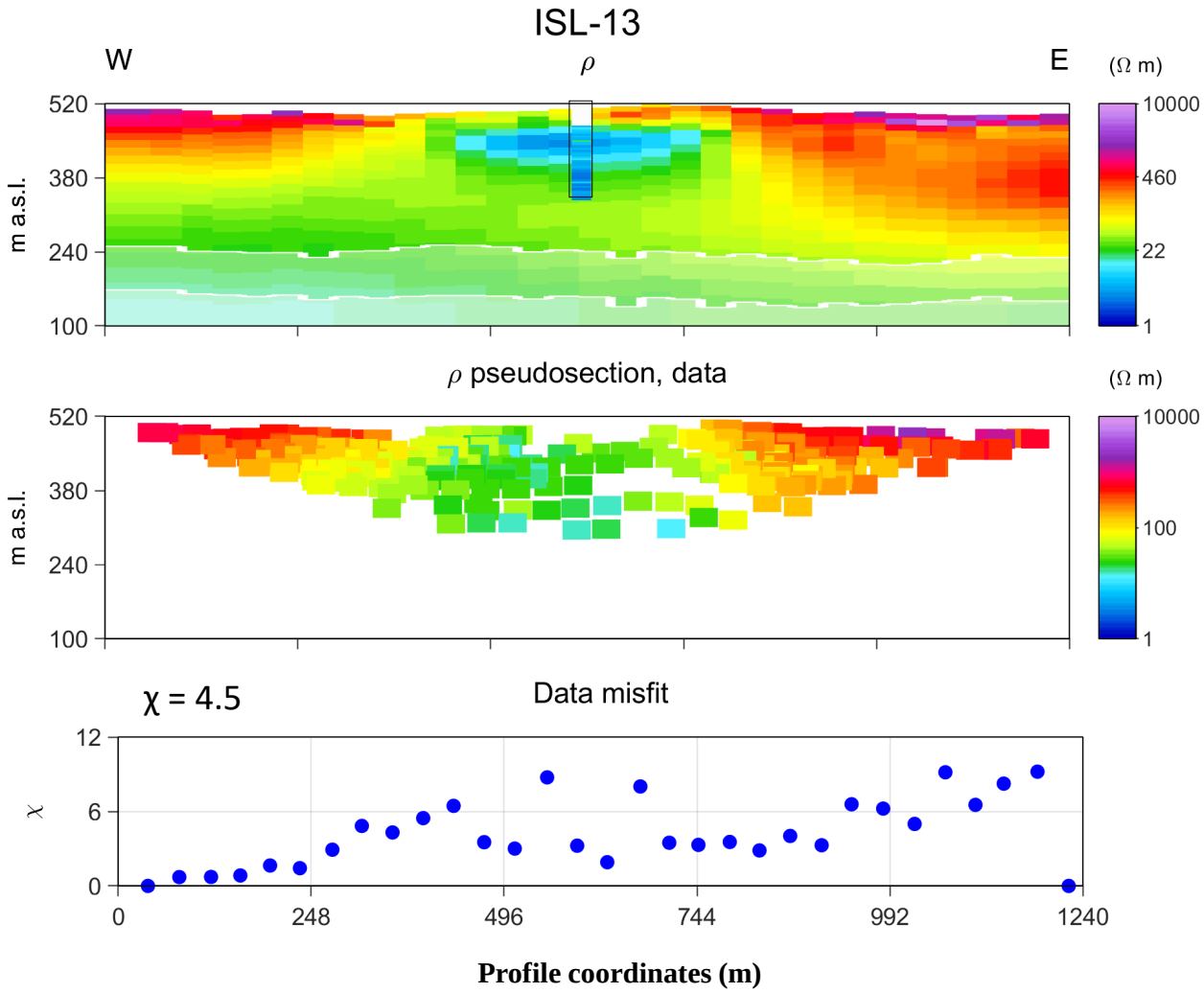

Figure S9. Resistivity inversion model for ISL-13 (perpendicular profile at KH1 site). The data and forward prediction of the model are also shown. The lower panels give the data misfit χ for each vertical section of model (spaced every 40 m).

Smectite quantification in hydrothermally altered volcanic rocks

Léa Lévy[1,2], Thráinn Fridriksson[3], Nathaniel Findling[4], Bruno Lanson[4], Bernard Fraisse[5], and Benoit Gibert[6]

[1]Laboratoire de Géologie, Ecole Normale Supérieure, Paris Sciences et Lettres, UMR8538, CNRS, Paris, France

[2]Nordic Volcanological Center, Institute of Earth Sciences, University of Iceland, 101 Reykjavík, Iceland

[3]ÍSOR - Iceland GeoSurvey, Reykjavík, Iceland

[4]ISTerre - Université Grenoble Alpes, Grenoble, France

[5]Institut Charles Gerhardt Montpellier (ICGM), CNRS, Univ. Montpellier, 34090 Montpellier, France

[6]Géosciences Montpellier, University of Montpellier, France

March 7, 2019

Abstract

In volcanic environments, the presence of smectite can indicate recent hydrothermal circulations. Smectite is also responsible for enhanced rock electrical conductivity, as well mechanical weakening. Therefore, quantifying smectite is important in geothermal exploration. Estimations from

X-ray Diffraction are time-consuming and mostly qualitative. We investigate the use of an optimized unbuffered Cation Exchange Capacity (CEC) measurement, by back-titration of the Copper-triethylenetetramine(II) molecule, to quantify the smectite content of altered volcanic rock samples. We show in particular that a trade-off between two types of measurement uncertainties is theoretically reached for a fraction of reactants consumed of about 30% at the end of the exchange reaction. We suggest a modification to classical protocols to fall in that range.

1 Introduction

Quantifying smectite in altered volcanic rocks is a challenge, due to the presence of a large number of minerals in the same rock formation and in particular to the co-existence of other types of clay minerals, such as chlorite, illite and mixed layer clays. Knowledge of the smectite content is important to better understand the subsurface resistivity structure, due to the large contribution of smectite to the rock electrical conductivity, through Electrical Double Layer mechanisms (Flóvenz et al., 1985; Pezard, 1990; Revil and Glover, 1997; Revil and Glover, 1998; Waxman and Smits, 1968) and interfoliar conduction (Henry, 1997; Lévy et al., 2018; Maraqah et al., 1990). It is also important to predict the mechanical behaviors of altered volcanic rocks, which may be weakened in the presence of secondary minerals, including smectite (Heap et al., 2014; Meller, 2014). Comparison of smectite content in drill-cuttings to in-situ resistivity logs can also provide estimates of the connected porosity (Flóvenz et al., 2005; Pezard, 1990; Revil et al., 1998; Rink and Schopper, 1974; Waxman and Smits, 1968). Moreover, the presence of smectite outside the shallow "clay cap" gives valuable information about the tectonic and convective activity at depth, such as boiling, chemical disequilbrium or recent fault opening (Beaufort et al., 1995;

Bril et al., 1996; Patrier et al., 1996).

Due to its particular crystalline structure, smectite has a much larger Cation Exchange Capacity (CEC) than other clay minerals (Bouchet et al., 2000) and this CEC is mainly located in the interlayer spaces (Lagaly, 1981; Vogt and Köster, 1978). Hower and Mowatt (1966) found a linear correlation between the CEC and the smectite fraction in a series of smectite-illite samples. Kaufhold and Dohrmann (2003) also observed that the CEC measured by back-titration of the Copper-triethylenetetramine(II) "Cu-trien" (Ammann et al., 2005; Bergaya, 1997; Meier and Kahr, 1999) was proportional to the smectite content in bentonites, qualitatively measured by the methylene blue method. Altered volcanic rocks contain a larger variety of minerals than bentonite or smectite-illite series, with often a large fraction of zeolites. Some zeolites, such as clinoptinolite and heulandite, have a higher CEC than smectite, up to 300 meq/100g, thanks to their wide solid solution of extraframework cations (Fridriksson et al., 2004). However, the CEC of clinoptinolite drops to 5 meq/100g measured by the Cu-trien method (Meier and Kahr, 1999), so that the Cu-trien molecule appears to be adequate to measure the CEC and quantify the smectite content in altered volcanic rocks.

Most volcanic rock contain much less smectite than bentonite or smectite-illite series, and thus the uncertainty of the CEC measurement may be very high, due to the small quantity of Cu-trien absorbed. The problem of optimization of the proportion of reactants (Cu-trien and sample) was first addressed by Orsini and Remy (1976) for CEC measurements with the Cobalti-hexamine molecule, "Co-hex", on large masses of soil samples. Orsini and Remy (1976) pointed out that the exchange between Co-hex and soil samples could be considered as total only when the initial quantity of Co-hex was at least three times superior to the CEC but that beyond eight times, the accuracy of the

measurement would significantly decrease. Based on these observations, these authors recommanded to carry out experiments where the initial ratio between Co-hex and rock sample (expressed in CEC units) represents 30% to 80% of the CEC, or equivalently where the fraction of Co-hex consumed during the experiments ranges between 15% and 30%. Further developments of the Co-hex back-titration method (Cieselski, 1997; Ciesielski et al., 1997) have led to extend the latter interval of Co-hex consumed to the range 5%-35%.

In order to determine the optimal experimental conditions for measuring the CEC of altered volcanic samples - where, in particular, the available rock mass may be much more limited than in the case of soils - by the Cu-trien method, we investigate here the theoretical grounds for the ranges suggested by Orsini and Remy (1976) and Ciesielski et al. (1997) and their ability to fit our experimental observations. Furthermore, since the final aim is to quantify the smectite content, we compare the CEC measurements to smectite quantifications based on Rietveld-refinements of X-ray Diffraction (XRD) patterns (Taut et al., 1998). High-quality XRD scans are required for these quantifications, which can be time-consuming. Moreover, the co-existence of different clay minerals with overlapping peaks is a problem in most cases. The need for a simple and cheap method to quantify smectite weight fraction in altered volcanic rocks that may contain different types of clay minerals, motivates our study.

2 Materials and Methods

2.1 Rock samples

Thirty-six samples from the Krafla high-temperature geothermal area are used in this study. Core samples are collected four cored boreholes (KH1, KH3, KH5 and KH6) at varying depths. They present a variety of lithologies and secondary

minerals (Table 1).

Cylindrical plugs (2-3 cm long and 2.5 cm diameter) are prepared from the original core samples for petrophysical measurements, presented by Lévy et al. (2018). From the lateral faces of the plugs, thin sections and powders are prepared. Ten samples are used for optimization of CEC measurements, 22 samples for comparison between quantitative XRD analysis and CEC and 15 samples for chemical analysis by Electron Probe Micro Analysis (EPMA). Some samples are used for more than one type of analysis (Table 1).

A first set of powder is used for the analysis of CEC uncertainty, carried out on 88 samples but presented here for 10 relevant samples. This set of powder is roughly grained to powder size, without any size control.

A second set of powders is used for XRD scans and the CEC measurements that are later compared to XRD mineral quantification, carried out on 21 samples. Powders from the first set are further grained for 10 minutes in ethanol, using an automatic grinder Retsch RM 200. Powders are sieved to ensure a size strictly below 250 μm, and prepared as randomly oriented specimen for subsequent XRD analysis. For each sample, the exact same powder is used later on for CEC measurements.

2.2 Mineral quantification by X-ray Diffraction

The powders are front-loaded onto the sample holder, using a razor blade to smoothen the surface, in order to minimize preferred orientation (PO) and shift displacement of diffraction peaks (Bish and Reynolds, 1989). An example of PO issues when the sample is back-loaded is shown in Appendix B. The XRD scans are carried out in the range 4-75 °2θ (4-65 for a few samples) with a Philips X'Pert Pro (radiation Cu-Kα; 45 kV; 30 mA; step size 0.0167°; time per step 240 s; X'Celerator Scientific high-speed detector; 240

Table 1: Description of the thirty-six samples used in this study (sample name in the first column, ID). The borehole (BH) and depth (in meters) from which the sample are extracted are indicated in Columns 2 and 3. The type of analysis for which the samples are used are indicated in Columns 4 to 6, where "CEC opt" corresponds to the optimization of CEC measurements. The CEC (in meq/100g) is given in Column 7. The lithology (Litho) is given in Column 8: hyalo = hyaloclastite; v. lava = vesicular lava; d. lava = dense lava. The presence of secondary minerals (if more than 1% are quantified by XRD quantification) is indicated in Columns 9 to 16. Sm = smectite; Chl = chlorite; Heu = heulandite (zeolite); Qtz = quartz; Clc = calcite; Pyr = pyrite; Tit = titanite; Oth. = other; Laum = laumontite (zeolite); Act = actinolite; Ep = epidote; Wai = wairakite.

ID	BH	Depth m	XRD	CEC opt	EPMA	CEC meq/100g	Litho	Sm	Chl	Heu	Qtz	Clc	Pyr	Tit	Oth.
L02	KH1	39.5	x			13.21	breccia	x		x	x		x		
L04	KH1	42			x	-	breccia	-	-	-	-	-	-	-	-
L05	KH1	45.3	x		x	5.96	ignimb.	x		x	x				
L06	KH1	48.8	x	x		33.00	breccia	x		x	x	x	x		
L09	KH1	60	x	x		37.00	breccia	x		x	x	x	x		
L10	KH1	66	x			15.24	v. lava	x			x				
L11	KH1	68.7	x			24.34	d. lava	x		x	x			x	
L12	KH1	70	x		x	2.61	d. lava	x				x			
L14	KH1	74.5	x			32.23	hyalo	x		x	x	x	x		
L15	KH1	79.5	x			14.67	d. lava	x			x				
L16	KH1	99	x			4.71	d. lava	x		x	x	x		x	
L19	KH1	120.3	x			14.50	d. lava	x		x	x	x	x	x	
L21	KH1	125.5	x			18.74	d. lava	x			x			x	
L22	KH1	131.1	x			20.63	v. lava	x		x	x	x	x	x	
L26	KH1	157.9	x		x	12.33	v. lava	x			x				
L28	KH1	167.1	x		x	12.55	d. lava	x		x	x		x	x	
L29	KH1	174.3	x		x	9.59	v. lava	x			x	x		x	
L30	KH1	185.1	x		x	7.58	dyke	x			x			x	
L31	KH1	188.5	x		x	20.15	hyalo	x			x	x	x	x	
L119	KH3	60.4	x	x		55.00	hyalo	x		x	x	x	x		
L40	KH5	190			x	10.85	v. lava	x	x		x	x			Laum
L58	KH5	429			x	3.5	dyke	x	x		x	x	x	x	Act
L112	KH6	377.7		x		6.23	dyke	x	x		x	x			
L113	KH6	387		x		3.52	dyke	x	x		x	x			
L114	KH6	394.2		x		2.62	dyke	x	x		x	x			
L81	KH6	461.32	x		x	16.50	d. lava	x			x				Horn
L82	KH6	486.5			x	5.75	d. lava	x	x			x	x	x	
L87	KH6	508.5	x		x	5.6	d. lava	x			x	x	x	x	
L91	KH6	537.2			x	8.4	hyalo	x			x	x	x		
L93	KH6	555			x	1.85	dyke	x	x		x			x	Ep
L99	KH6	587		x		34	hyalo	x	x	x					Wai, Act
L100	KH6	597.5				0.80	hyalo		x		x	x		x	Wai, Act
L80	KH6	448		x		4.80	d. lava	x	x		x				
L86	KH6	501		x		6.33	d. lava	x	x		x				
L89	KH6	515		x		4.98	d. lava	x	x		x				
L95	KH6	560	x			32.25	hyalo	x				x		x	Wai, Act

mm goniometer radius). The diffraction patterns are analyzed quantitatively with the Rietveld program BGMN and the Profex user-interface (Doebelin and Kleeberg, 2015; Taut et al., 1998). The following mineral phases were considered for the refinements: fortserite, labradorite, bytownite, orthoclase, orthose, albite, augite, diopside, kanoite, smectite-tri, smectite-di, zeolite (heulandite, clinoptinolite, philippsite, dachiardite, laumontite, analcime), pyrite, ilmenite, titano-magnetite, hematite, maghemite, anatase, titanite, schorl, chlorite, calcite, quartz, wairakite, prehnite, epidote, actinolite, garnet, grossular. Two examples of refinements are shown, in Figure 1 for a sample containing smectite as the only clay mineral and in Figure 2 for a sample containing smectite, chlorite, and most likely smectite-chlorite.

Smectite content in samples containing a mixture of different clay phases cannot be accurately quantified by Rietveld-refinements, because of strong parameter correlation. The XRD patterns can be fitted (Figure 2) but the software adjusts both the chemical composition of chlorite and the relative quantity of chlorite and smectite to fit the relative intensities of the d(001) peak at 14-15Å and the d(002) peak at 7.2Å. This result in a non-uniqueness of the model parameters related to chlorite chemistry and smectite and chlorite quantity. The chemistry of chlorite can be constrained (especially the relative abundance of Fe and Mg), based on independent chemical analyses, but this requires a large number of electron probe micro-analysis (EPMA) on polished thin sections, to obtain a representative chemical composition of chlorite for the sample, which is time-consuming and expensive. Moreover, assuming the chemistry of chlorite can be properly constrained, the combined presence of smectite and chlorite often implies presence of a smectite-chlorite phase. This smectite-chlorite phase also contributes to the d(001) peak at 14-15Å so that but its contribution cannot be discriminated from that of pure smectite. Therefore, the fitted quantity of

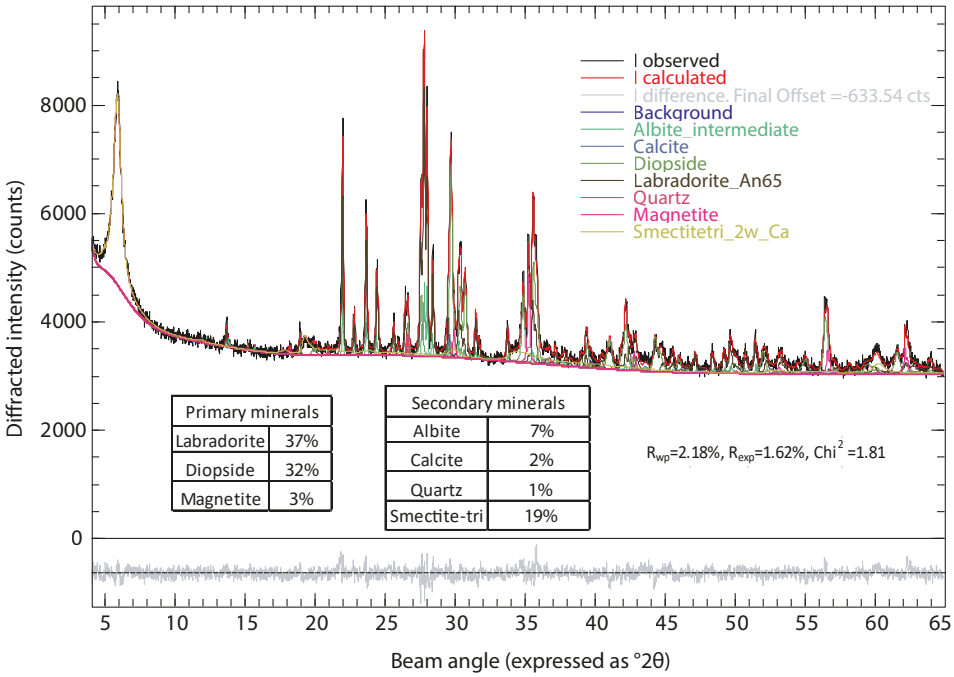

Figure 1: XRD quantitative analysis, using the BGMN software, for sample L15 containing smectite as the only clay mineral. The resulting mineral percentages and fit quality are indicated on the graph.

"smectite" corresponds in reality to a quantity of smectite + smectite-chlorite. Since only the quantity of smectite layers matters for the comparison to the CEC, not the quantitiy "smectite+ smectite-chlorite", this quantification is not appropriate. Therefore in this study, only smectite quantifications for samples containing no other clay phase are used for further comparison to CEC measurements.

Special studies are necessary to determine the exact type of smectite present in each sample, especially regarding the type of interlayer cation (Ca^{2+} or Na^{+}), the number of water layers surrounding interlayer cations and the tri- or dioctahedral character. The tri- or dioctahedral character mainly influences the

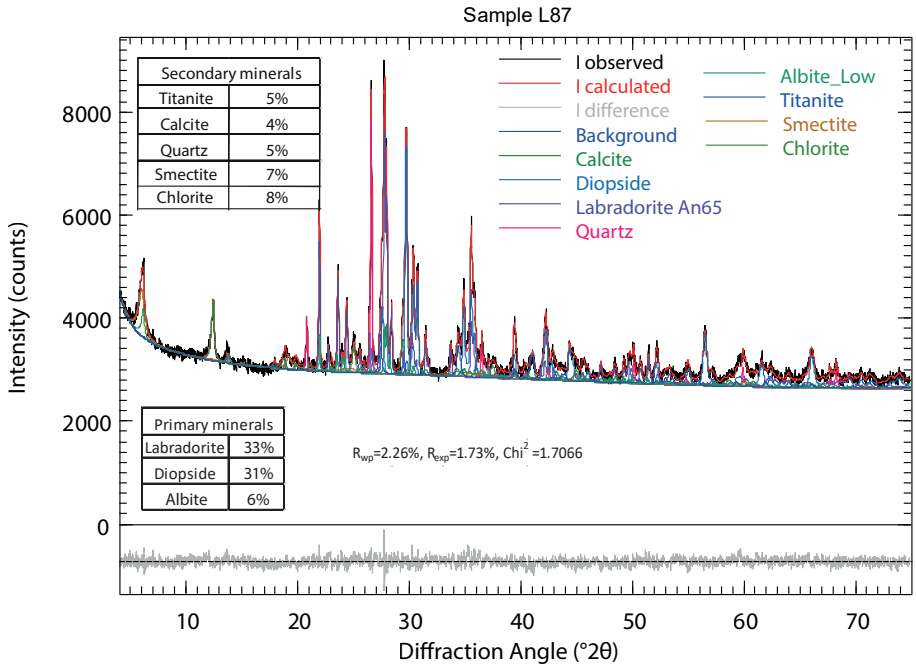

Figure 2: XRD quantitative analysis, using the BGMN software, for a sample containing smectite, chlorite and mixed layer smectite-chlorite.

d(060) diffraction peaks, at high angles, which have a lower intensity and are overlapping with other minerals such as quartz. These high-angles peaks only negligibly affect (if at all) the refinement. On the other hand, low-angle peaks, especially the d(001) around 14-15Å, which is influenced by the composition of the interlayer space, both in terms of cation and water layer, significantly affect the refinement. Therefore, the patterns were fitted with two different types of smectite phases: a phase corresponding to a "tri-octahedral smectite with interfoliar spaces filled with Ca, accompanied by two water layers", and another tri-octahedral smectite "saponite" with more open interlayer distances. An uncertainty on the smectite content was calculated based on the discrepancy between the two fits. The structure files corresponding to these two smectite phases and used for the Rietveld refinements are given in Appendix A. For the

other minerals, the uncertainty was calculated based on the variance of the model parameters given by the software.

2.3 CEC determination

The Copper-triethyletetramine (Cu-trien) molecule was used for back-titration of the CEC, as originally designed by Meier and Kahr (1999) to measure the CEC on pure clay samples and used, for example by Kaufhold and Dohrmann (2003) to measure the CEC of bentonites. First, the powder is mixed with 50 ml of deionized water (measured with a volumetric flask) in an ultrasonic bath for 5 minutes and then 10 ml of Cu-trien at 1.10^{-2} mol/L are added with a pipette. The exchange is considered complete after 3 minutes of magnetic stirring. Next step, the rock and liquid are separated by centrifugation (2000 rounds per minute during 20 minutes). Finaly, the absorbance of the supernatant solution is measured by a spectrophotometer at 578 nm. At the beginning of each series of measurement, the absorbance of the original blank solution (50 ml of deionized water and 10 ml of Cu-trien at 1.10^{-2} mol/L) is measured and the spectrophotometer is calibrated (curves absorbance versus concentration) using reference stock solutions of known concentrations. The CEC (in meq/100g) is then calculated with Equation 1.

$$CEC_{lab} = \frac{2(C_i - C_f)V}{m} \tag{1}$$

where V is the total volume of the solution (60 ml), m is the rock mass in mg and C_i and C_f are the Cu-trien concentrations in the initial and final solutions, respectively, in mol/L. The rock mass suggested by Meier and Kahr (1999) is 200 mg but is a key parameter to be adjusted in the present study: m varies between 100 and 1000 mg in our experiments.

The reference solutions are prepared by mixing about 1.6 g of anhydrous cop-

per sulphate $CuSO_4$ and 1.5 g of the organic compound tri-ethylene-tetramine "trien" in deionized water to obtain a total volume of about 1 L. Other stock solutions with greater initial masses (resulting in higher concentrations) are prepared for calibration of the spectrophotometer. The concentration of the reference and stock solutions are calculated following Equation 2. More details on the stock solutions can be found in Lévy et al. (2016).

$$C_{stock} = \frac{min(\frac{m_{CuSO_4}}{M_{CuSO_4}}; \frac{m_{trien}}{M_{trien}})}{V_{tot}} \quad (2)$$

where m_{CuSO_4} and m_{trien} are the masses of $CuSO_4$ and "trien", in g, M_{CuSO_4} and M_{trien} are the molar masses of $CuSO_4$ and "trien", in g/mol and V_{tot} is the total volume of the solution, in L. The complex "Cu-trien" is formed by stoechiometric reaction between the two compounds, so that the quantity of Cu-trien formed (in mol) corresponds to the quantity of the compound initially present in lesser quantity, the "limiting reactant".

2.4 Chemistry of clay minerals by electron probe micro-analysis

Chemical analyses of clay minerals were carried out on 15 polished thin sections at Géosciences Montpellier, using a CAMECA SX100 electron microprobe (22 keV, 10 nA). The 15 samples used for these measurements are indicated in Table 1.

3 Results and Discussion

3.1 Estimation of the laboratory uncertainty

The laboratory uncertainty is defined in Equation 3.

$$Err_{lab} = \frac{\delta CEC_{lab}}{CEC_{lab}} = \frac{\delta V}{V} + \frac{\delta m}{m} + \frac{\delta C_i + \delta C_f}{|C_i - C_f|} \tag{3}$$

where δV and δm are the relative uncertainty on volume and mass, respectively, and δC_i and δC_f are the relative uncertainty on initial and final concentrations, respectively.

The uncertainty on C_i, δC_i, is taken as the relative difference between the theoretical *a-priori* concentration and the experimental *a-posteriori* concentration. The former is calculated according to the theoretical concentration of the stock solution, which can slightly vary around the recommended value of 1.10^{-2} mol/L (Equation 2). The latter is calculated according to the absorbance measurement of the original blank solution and the calibration curve (Equation 4).

$$\frac{\delta C_i}{C_i} = \frac{C_{i,a-pr} - C_{i,a-post}}{C_{i,a-pr}} = \Delta Cal \tag{4}$$

where $C_{i,a-pr}$ and $C_{i,a-post}$ are the *a-priori* and *a-posteriori* concentrations of the initial Cu-trien solution, in mol/L, and ΔCal is the relative uncertainty on the calibration factor.

In order to simplify the calculations, we consider a constant ratio between absorbance and concentration, although the slope L in Equation 5 may slightly vary from one run of measurements to another, and the y-intercept between concentration and absorbance slightly differs (in the range $10^{-5} - 10^{-3}$ mol/L).

$$C_f = \frac{C_i A_f}{A_i} = \frac{A_f}{L} \tag{5}$$

where L is the constant ratio (slope) between absorbance and concentration. In reality, C_f is calculated with the specific calibration curve of the spectrophotometer at the time of the measurement.

Using Equation 5, the uncertainty on C_f, δC_f, is calculated as shown in Equation 6.

$$\frac{\delta C_f}{C_f} = \frac{\delta C_i}{C_i} + \frac{\delta A_i}{A_i} + \frac{\delta A_f}{A_f} = \Delta_{Cal} + \frac{\delta A_i}{A_i} + \frac{\delta A_f}{A_f} \tag{6}$$

The total laboratory uncertainty is then given in Equation 7.

$$Err_{lab} = \frac{\delta V}{V} + \frac{\delta m}{m} + \frac{C_i \Delta_{Cal} + C_f(\Delta_{Cal} + \frac{\delta_{A_i}}{A_i} + \frac{\delta_{A_f}}{A_f})}{|C_i - C_f|} \tag{7}$$

About 40 series of measurements (and thus calibrations) were carried out, for a total of more than 400 CEC measurements, and ΔCal was found to vary between 0.1 and 1.8%, with an average of 1%. The uncertainty on the volume measurements (by both volumetric flask and pipette) is evaluated to $\delta V = 0.6$ ml, corresponding to 1% of the 60 ml volume. The uncertainty on rock weighting is estimated to $\delta m = 0.5$ mg, based on the variations of the first digit of the scale. The uncertainty on the absorbance measured y the spectrophotometer is taken to 0.001, based on the general variability observed for repeated measurements of fluid samples from the same solution. Since absorbance measurements are given with three digits, this uncertainty of one unit on the last digit is similar to the spectrophotometer uncertainty. Therefore, $\delta A_i = \delta A_f = 0.001$.

3.2 Increasing the rock mass decreases the laboratory uncertainty for low-CEC rocks

Based on Equation 7, we calculate the relative uncertainty of six samples, in CEC measurements using two different initial rock masses and the same initial

Cu-trien solution. We show that the relative uncertainty decreases from up to 350% to less than 20% when increasing the rock mass from the 200 mg, usually found in protocols (Meier and Kahr, 1999) to 1000 mg (Figure 3). Increasing the rock mass from 200 to 1000 mg increases the fraction of Cu-trien consumed from less than 1% to about 13% (Sample L114 in Figure 3). This is particularly true for samples with CEC lower than 7 meq/100g, i.e. with low smectite content, as thos used in the Figure. This effect is due to the limited number of digits, which can be read on the spectrophotometer (only three digits, with values always ≤ 1).

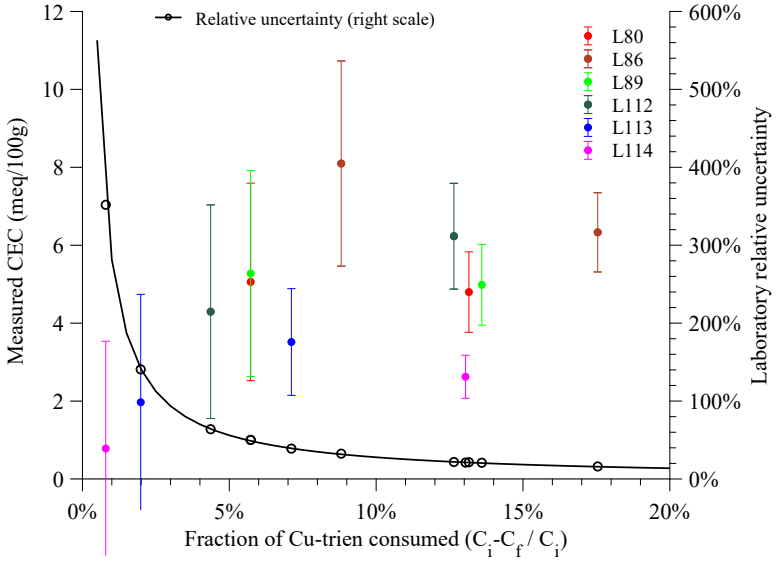

Figure 3: Measured CEC and relative laboratory uncertainty as a function of the fraction of Cu-trien consumed. The circles with errorbars correspond to the measured CEC (left axis) and the stars to the uncertainty, as calculated in Equation 7 (right axis). An increased fraction corresponds to an increased mass of rock initially present. Each color corresponds to one sample. The six samples used in this figure have a CEC inferior to 5 meq/100g. The errorbars (both positive and negative) are calculated as the product of the measured CEC by the relative uncertainty.

Figure 3 also shows that the general relative uncertainty exponentially decreases with the fraction of Cu-trien consumed. This is consistent with Equation 7, where the denominator $|C_i - C_f|$ controls the ovrall value of Err_{lab}, given that $\frac{\delta V}{V}$ and $\frac{\delta m}{m}$ are very small compared to the third term.

3.3 Increasing the rock mass decreases the yield of the exchange reaction for high-CEC rocks

For high-CEC samples, we observe that the measured CEC can decrease by up to 50% when the rock mass is increased, for fixed initial volume and concentration of Cu-trien (Figure 4). A similar observation was also mentioned in Cieselski (1997) and was attributed to a reduced yield of the exchange reaction when the fraction of Cu-trien consumed exceeds a limit.

In order to evaluate how the relative difference between the apparent measured CEC, $CEC_{app} = CEC_{lab}$, and the real CEC, CEC_0, vary with the fraction of Cu-trien consumed, and determine an acceptable threshold of Cu-trien consumption, we write the theoretical relationship between CEC_{app} and CEC_0. For simplification purposes, we consider here only one homovalent exchange reaction, between the Cu-trien(II) cations and the Ca^{2+} cations filling the exchange sites in the rock samples. This reaction is the dominant reaction occurring in these rock samples, as more than half of the interlayer spaces of smectites are filled with Ca^{2+}, according to chemical analyses of the samples (Figure 5). The chemical exchange reaction is written in Equation 8.

$$\mathrm{Cu_{aq}} + \mathrm{Ca_{ads}} \rightleftharpoons \mathrm{Ca_{aq}} + \mathrm{Cu_{ads}} \tag{8}$$

The thermodynamic constant K of this exchange reaction is defined in Equa-

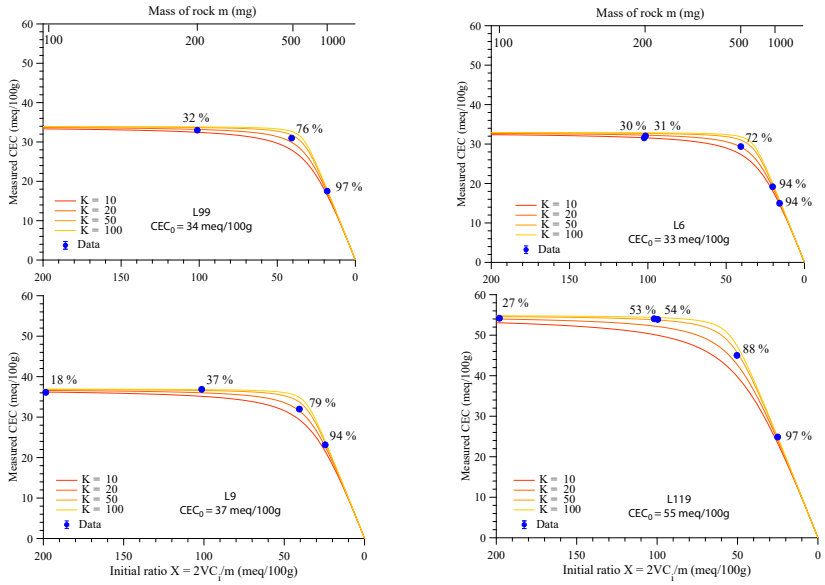

Figure 4: Measured CEC with different initial ratio of reactants (Cu-trien and rocks) for four samples (blue filled circles): L99, L9, L6 and L119. The initial concentration of Cu-trien is more or less constant ($(1.6 \pm 0.1) \cdot 10^{-3}$ mol/L) but the mass of rock varies between 100 and 1000 mg (top x-axes) so that the initial ratio X varies between 20 and 200 meq/100g. The fraction of Cu-trien consumed at the end of the reaction is marked aside each measurement. The laboratory uncertainty is smaller than the symbols. The model predictions for four values of the thermodynamic constant K are also displayed as plain lines with a warm colorscale. The values of K were chosen on a trial-error basis, assuming $K \geq 1$. The value of CEC_0 used for these predictions is marked together with the name of the sample, and corresponds to the measured CEC for the highest initial ratios.

tion 9.

$$K = \frac{X_{Cu,eq} a_{Ca,eq}}{X_{Ca,eq} a_{Cu,eq}} \tag{9}$$

where the subscript "eq" indicates that a chemical equilibrium is reached. $X_{Cu,eq}$ and $X_{Ca,eq}$ are the dimensionless chemical activities of cations Cu-trien(II) and Ca^{2+} filling sites in the rock at the end of the exchange reaction, respectively, and $a_{Cu,eq}$ and $a_{Ca,eq}$ are the dimensionless chemical activities of cations Cu-trien(II) and Ca^{2+} in the aqueous solution at the end of the exchange reaction,

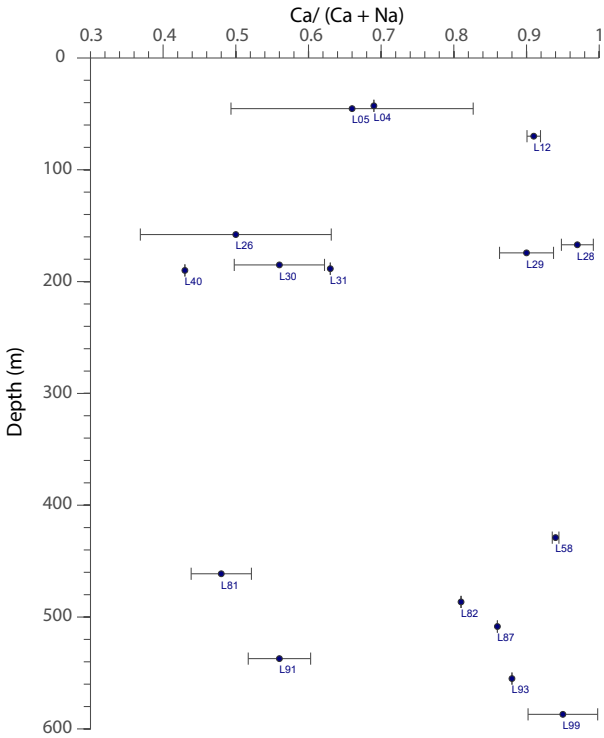

Figure 5: Relative abundance of Ca-ion compared to Na-ion filling the interlayer spaces of smectites, as a function of the depth from which the samples originate. Sixteen samples, where chemical analyses by electron probe where carried out, are reported on this figure: L04 to L31 from KH1, L40-L58 from KH5 and L81-L99 from KH6. The error bar indicates the range of values found for the different smectite measured in each thin section. No particular trend with depth or borehole are evidenced.

respectively. Chemical activities are defined in Equation 10, where the subscript "eq" is removed for clarity purposes, but we assume the thermodynamic equilibrium is reached.

$$\begin{cases} a_{Cu} = [Cu]_{aq} \\ a_{Ca} = [Ca]_{aq} \\ X_{Cu} = \frac{meq(Cu)}{mCEC_0} \\ X_{Ca} = \frac{meq(Ca)}{mCEC_0} \end{cases} \tag{10}$$

where $[Cu]_{aq}$ and $[Ca]_{aq}$ are the chemical concentrations of cations (Cu-trien(II) and Ca^{2+}, respectively) in the aqueous solution, in mol/L, and $meq(Cu)$ and $meq(Ca)$ are the quantities of cations (Cu-trien(II) and Ca^{2+}, respectively) filling sites in the rock, in millimol equivalent "meq". Each mmol of Cu-trien(II) or Ca^{2+} corresponds to 2 meq, given the double positive charge carried by each cation. a_{Cu} and a_{Ca} are normalized by an "infinite" theroretical concentration of 1 mol/L. With CEC_0 being the total CEC of the rock, in meq/g, and m the mass of rock considered in the experiment, in g, $mCEC_0$ is the total number of exchange sites available in the rock, in meq. According to these definition, $[Cu]_{aq}$, $[Ca]_{aq}$, $meq(Cu)$ and $meq(Cu)$ are given in Equation 11.

$$\begin{cases} \left[Cu\right]_{aq} = C_f \\ \left[Ca\right]_{aq} = C_i - C_f \\ meq(Cu) = mCEC_{app} \\ meq(Ca) = m(CEC_0 - CEC_{app}) \end{cases} \tag{11}$$

Combining Equations 9, 10 and 11, the thermodynamic constant, K, can be written as in Equation 12.

$$K = \frac{meq(Cu)}{meq(Ca)} \times \frac{C_i - C_f}{C_f} = \frac{CEC_{app}}{CEC_0 - CEC_{app}} \times \frac{C_i - C_f}{C_f} \tag{12}$$

Given that $CEC_{app} = CEC_{lab}$ and following Equations 1, 11 and 12, $meq(Cu)$

and $meq(Ca)$ can also be written, as in Equation 13.

$$\begin{cases} meq(Cu) = 2V(C_i - C_f) \\ meq(Ca) = \frac{meq(Cu)(C_i - C_f)}{KC_f} = \frac{2V(C_i - C_f)^2}{KC_f} \end{cases} \tag{13}$$

Assuming that all exchange sites are filled with either Cu-trien(II) or Ca^{2+} at the end of the reaction, the total CEC, CEC_0, is described in Equation 14.

$$\begin{aligned} CEC_0 m &= meq(Cu) + meq(Ca) \\ \iff CEC_0 &= \frac{2(C_i - C_f)V}{m}(1 + \frac{(C_i - C_f)}{KC_f}) \\ \iff KC_f CEC_0 &= CEC_{app}(KC_f + C_i - C_f) \\ &= CEC_{app}[(K-1)C_f + C_i] \\ \iff C_f &= C_i \times \frac{CEC_{app}}{KCEC_0 + (1-K)CEC_{app}} \end{aligned} \tag{14}$$

By writing C_f as a function of C_i, m, V and CEC_app (Equation 1), Equation 14 gives Equation 15.

$$\begin{aligned} C_i - \frac{mCEC_{app}}{2V} &= C_i \times \frac{CEC_{app}}{KCEC_0 + (1-K)CEC_{app}} \\ \iff (KCEC_0 + (1-K)CEC_{app}) &\times (2VC_i - mCEC_{app}) \\ &= 2VC_i CEC_{app} \end{aligned} \tag{15}$$

Equation 15 can be re-written as a second-order equation of the variable

$Y = CEC_{app}$ (Equation 16).

$$(1-K)Y^2 + (KCEC_0 + \frac{2VKC_i}{m})Y - \frac{2VKC_iCEC_0}{m} = 0$$

$$\iff aY^2 + bY + c = 0 \begin{cases} a = 1 - K < 0 \\ b = KCEC_0 + \frac{2VKC_i}{m} \\ c = -\frac{2VKC_iCEC_0}{m} \\ \Delta = b^2 - 4ac \end{cases} \quad (16)$$

with $a < 0$ because $K > 1$ (otherwise no exchange would occur). By solving the second-order equation (16) and keeping only the positive solution (which remains positive even if $K < 1$), we obtain an explicit function for CEC_{app} (Equation 17).

$$Y = CEC_{app} = \frac{-b + \sqrt{\Delta}}{2a}$$

$$= \frac{-(\alpha + X) + \sqrt{(\alpha + X)^2 + 2\alpha\beta X}}{\beta} \begin{cases} X = 2V\frac{C_i}{m} \\ \alpha = CEC_0 \\ \beta = 2\frac{1-K}{K} < 0 \end{cases} \quad (17)$$

The function of X presented in Equation 17 increases monotoneously with X and reaches asymptotically the value of CEC_0. Since X is inversely proportional to m, the sequence of equations presented here predicts that an increase of rock mass (all other things being equal) will increase the difference between CEC_{app} and its asymptote CEC_0, which is equivalent to reducing the yield of the exchange reaction. The function presented in Equation 17 reproduces experimental observations on several samples with large smectite volume, provided that CEC_0 is chosen accordingly (Figure 4). Values of K in the range 10-100 are consistent with the observations but the value of K does not affect much the predictions. Given the limited sensitivity of the model to the value of K, we

do not attempt here to evaluate precisely this constant but we suggest that the range 20-50 is appropriate to describe the reaction taking place in the samples shown in Figure 4. In reality, K depends not only on the cation exchanged but also on the type of minerals and of sites involved in the exchange (Tertre, 2014; Reinoso-Maset et al., 2012; Durrant et al., 2018; Robin et al., 2015; Robin et al., 2017).

3.4 Optimization of the CEC measurements

Equations 18 and 19 describe the "partial exchange" and "laboratory" uncertainties, as a function of the fraction $x = \frac{C_i - C_f}{C_i}$ of Cu-trien consumed after the reaction, based on Equations 14 and 7, respectively.

$$Err_{partial} = \frac{CEC_0 - CEC_{app}}{CEC_{app}} = \frac{(C_i - C_f)}{KC_f} = \frac{x}{K(1-x)} \tag{18}$$

$$\begin{aligned} Err_{lab} &= \frac{\delta V}{V} + \frac{\delta m}{m} + \frac{C_i \Delta_{Cal} + C_f(\Delta_{Cal} + \frac{\delta_{A_i}}{A_i} + \frac{\delta_{A_f}}{A_f})}{|C_i - C_f|} \\ &= \frac{\delta V}{V} + \frac{\delta m}{m} + \frac{\Delta_{Cal} + \frac{\delta_{A_f}}{LC_i} + (1-x)(\Delta_{Cal} + \frac{\delta_{A_i}}{A_i})}{x} \end{aligned} \tag{19}$$

Depending on the value of the thermodynamic constant, K, the optimal fraction of Cu-trien consumed to minimize both uncertainties is somewhere between 30% and 80% (Figure 6), as suggested empirically for CEC measurements with Co-hex on soils by Orsini and Remy (1976). Since it is not possible to determine K with these simple measurements, we consider most resonable to aim at 30% consumption (most pessimistic value for K) because the decrease of Err_{lab} beyond 30% is less important.

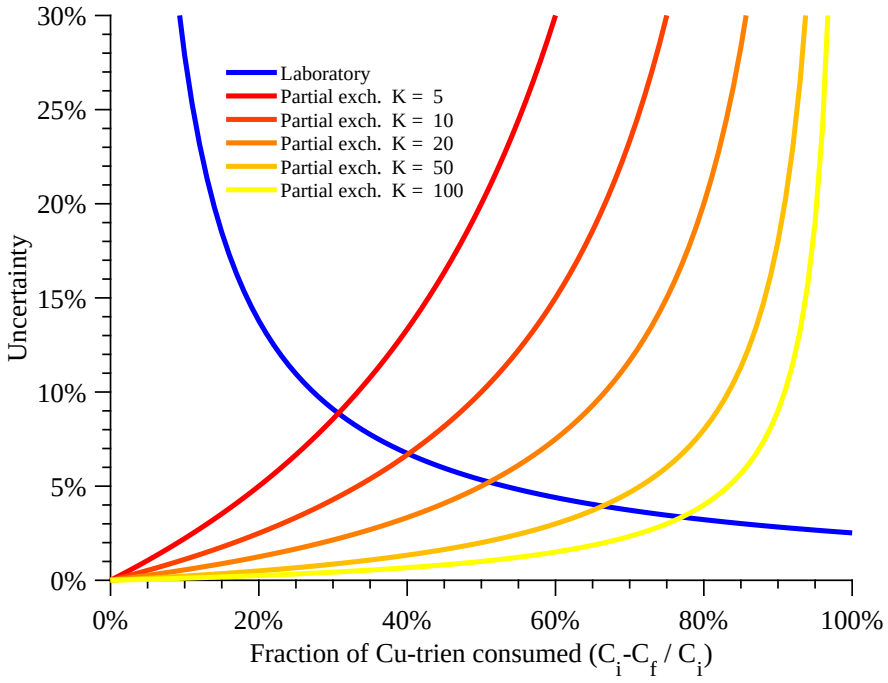

Figure 6: Laboratory and partial exchange uncertainties as a function of fraction of Cu-trien consumed.

3.5 Quantification of smectite weight fraction in altered volcanic rocks

A linear correlation is found between the smectite weight fraction and the CEC of altered volcanic rocks, where the only clay mineral is smectite (Figure 7). Due to the complexity of Rietveld refinements in whole rock samples when several types of clays are involved, only samples where a satisfying fit was obtained using only the clay phase "Smectite tri-octahedral with interlayers filled with Ca and 2 water layers" are reported in this figure. In samples where a peak at 7-7.5Å was observed (typical of chlorite and smectite-chlorite), the smectite quantity derived from the fit was considered to be a mixed-layer clay mineral with an unknown proportion of smectite, which is irrelevant for a quantitative compari-

son to the CEC. An uncertainty on the quantification was calculated by fitting the same diffraction patterns with a different smectite phase: "Saponite with interlayers filled with undetermined cations and 2 water layers". The quantities derived from the fit with the less constrained saponite were systematically lower. The linear fit to the observations shown in Figure 7 has a slope $CEC_{smec} = 88 \pm 6$ meq/100g and a regression coefficient $R^2 = 0.9385$. The slope is consistent with the known range of CEC for smectite 80-120 meq/100g (e.g. Bouchet et al., 2000).

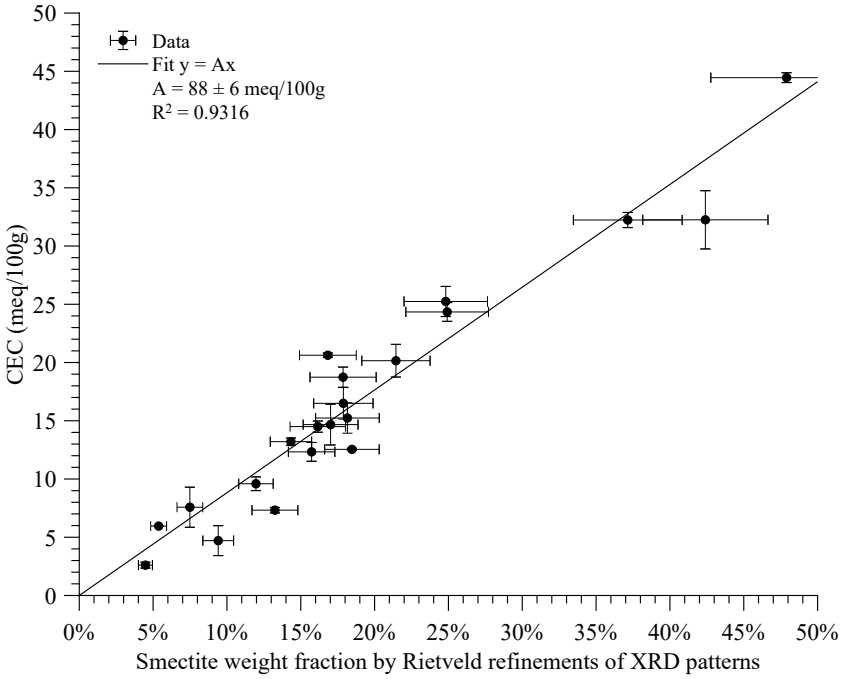

Figure 7: CEC measurements versus smectite quantification by Rietveld refinements of XRD patterns, for samples where smectite is the only clay mineral. The slope and regression coefficient of the fitting line is given in the legend. CEC measurements and XRD scans are carried out on the exact same powders. Modified after Lévy et al. (2018).

The contribution of other minerals to the measured CEC was also investigated, in particular zeolites, illite and chlorite. Zeolites can be divided into

two groups: (i) "rigid" zeolites (e.g. laumontite, mesolite, analcime, natrolite and scolecite), whose chemical formula is well-defined and thus extra-framework cations (other than Al and Si) cannot be replaced but the water content can vary and (ii) "flexible" zeolites (e.g. heulandite, chabazite and clinoptinolite), which exhibit a wide and continuous range of extra-framework cation composition. Although, the CEC of heulandite and clinoptinolite can reach up to 300 meq/100 g (Fridriksson et al., 2004), CEC measurements by the method developed here result in CEC values in the range 0.5-1.5 meq/100g (Lévy et al., 2018). Therefore, the contribution of zeolites to the CEC measured by Cu-trien in altered volcanic samples is negligible. The CEC of pure illite was also measured using the same method (back-titration by Cu-trien), yielding 4 meq/100g, which confirms that the CEC of pure illite is negligible compared to that of pure smectite (Hower and Mowatt, 1966). Moreover, the CEC of samples, which contain large amounts of chlorite, as well as in some cases wairakite and other "high-temperature" alteration minerals (epidote, actinolite), but no hint of smectite, is always inferior to 0.5 meq/100g (Lévy et al., 2018). We conclude that the linear trend presented in Figure 7 can be used to estimate the weight fraction of smectite in altered volcanic samples containing wide range of minerals. This weight fraction also includes smectite sheets in mixed-layer smectite/chlorite or smectite/illite.

As mentioned in Section 2, the grain size of rock powders used for measurements presented in Figure 7 was strictly below 250 μm. This is a condition to transform the CEC measurement in absolute smectite weight fraction. Indeed, the presence of larger grains (e.g. millimetric size) will have less surface exposed during the exchange reaction and result in smaller measured CEC. We observe a discrepancy of 20% for a high-CEC sample, L99, between the CEC measured with the same initial and optimal conditions but grained at two different sizes.

These two measurements were carried out by the Institut National de Recherche en Agronomie in Arras (France), which performs accredited measurements of CEC on soil: (i) using their standard size ($\leq$ 2 mm) and (ii) using a smaller size ($\leq$ 250 μm) on our request. Finally, heterogeneity of core samples from geothermal areas may cause significantly different CEC values depending on which lateral face of the cylindrical plug is used for the powder. Therefore, crushing and mixing together as much rock sample as possible (e.g. from the two lateral faces) is recommended.

4 Conclusions

In this study, we have suggested a modified protocol to minimize the uncertainty of CEC measurements by the Cu-trien method and thus quantify the smectite content in complex volcanic rocks. We have observed that classical CEC measurement protocols by Cu-trien have a relative uncertainty of up to 350% for samples with low smectite contents and that XRD on randomly oriented powders is not sufficient for smectite quantification in samples containing other clay minerals. We have shown that the fraction of Cu-trien consumed at the end of the reaction needs to be optimized in order to minimize the total uncertainty of the CEC measurement. Indeed two types of uncertainties are anti-correlated with varying fraction of Cu-trien consumed. We suggest that a value of 30% for this fraction is, in general, optimal. Finally, we show a linear correlation between the CEC, adequately measured, and the smectite weight fraction determined by XRD, for 20 samples containing smectite as the only clay mineral. Therefore, the method suggested in this study provides to geothermal industry a simple method to quantify the smectite weight fraction (pure smectite or expandable layers in mixed-layer clays) of powders from all kinds of altered volcanic rocks. Different spectrophotometric back-titration methods, using for

example the Cobalti-hexamine (III) molecule, can be used in the same manner for smectite quantification, since a whole range of thermodynamic constants were considered for the cation exchange reaction.

5 Acknowledgments

L.L. thanks Sigurdur Sveinn Jónsson, Helga Margrét Helgadóttir and Bjarni Gautason for their help with identifying primary and alteration minerals in XRD patterns, thin sections and microscopic observations. L.L. also thanks Heimir Ingimarsson, Christina Guenther and Ester Inga Eyjólfsdóttir for their valuable help with the CEC measurements. The authors thank Christophe Nevado, Doriane Delmas and Khaled Oubellouch for high-quality polished thin sections. Finally, the authors are grateful to Landsvirkjun, and especially Ásgrímur Gudmundsson, for providing the material for this work.

Funding: this work was supported by the IMAGE FP7 EC project (Integrated Methods for Advanced Geothermal Exploration, grant agreement No. 608553) and by a PhD grant from Paris Sciences et Lettres granted to Léa Lévy.

Data availability: the .xrdml files (X-ray diffraction patterns) used for Rietveld quantitative analysis are available as Supplementary Material.

References

Ammann, L., Bergaya, F., and Lagaly, G. (2005). "Determination of the cation exchange capacity of clays with copper complexes revisited." In: *Clay Minerals* 40, pp. 441–453.

Beaufort, D., Papapanagiotou, P., Patrier, P., Fujimoto, K., and Kasai, K. (1995). "High-temperature smectites in active geothermal systems". In: *Proceedings 8th Water-Rock Interaction Symposium, Vladivostok*. Ed. by Y. Kharaka and O. Chudaev. Balkema, Rotterdam., pp. 1071 –1076.

Bergaya F., V. M. (1997). "CEC of clays: Measurement by adsorption of a copper ethylenediamine complex". In: *Applied Clay Science* 12, pp. 275–280.

Bish, D. L. and Reynolds, R. C. (1989). "Sample preparation for X-ray diffraction". In: *Reviews in Mineralogy and Geochemistry* 20.1, pp. 73–99.

Bouchet, A., Meunier, A., and Sardini, P. (2000). *Minéraux argileux: structure cristalline, identification par diffraction de rayons X*. Vol. 23. Editions Elf Exploration.

Bril, H., Papapanagiotou, P., Patrier, P., Lenain, J.-F., and Beaufort, D. (1996). "Fluid-rock interaction in the geothermal field of Chipilapa (El Salvador): contribution of fluid-inclusion data". In: *European Journal of Mineralogy*, pp. 515–532.

Cieselski H., S. T.S.M.W. J. (1997). "A comparison between three methods for the determination of cation exchange capacity and exchangeable cations in soils". In: *Agronomie, EDP Sciences* 17.1, pp. 9–16.

Ciesielski, H., Sterckeman, T., Santerne, M., and Willery, J. P. (1997). "Determination of cation exchange capacity and exchangeable cations in soils by means of cobalt hexamine trichloride. Effects of experimental conditions". In: *Agronomie* 17.1, pp. 1–7.

Doebelin, N. and Kleeberg, R. (2015). "Profex: a graphical user interface for the Rietveld refinement program BGMN". In: *Journal of applied crystallography* 48.5, pp. 1573–1580.

Durrant, C. B., Begg, J. D., Kersting, A. B., and Zavarin, M. (2018). "Cesium sorption reversibility and kinetics on illite, montmorillonite, and kaolinite". In: *Science of the Total Environment* 610, pp. 511–520.

Flóvenz, O., Georgsson, L., and Árnason, K. (1985). "Resistivity structure of the upper crust in Iceland". In: *Journal of Geophysical Research* 90.B12, pp. 10136–10150.

Flóvenz, O., Spangenberg, E., Kulenkampf, J., Árnason, K., Karlsdóttir, R., and Huenges, E. (2005). "The role of electrical interface conduction in geothermal exploration". In: *World Geothermal Congress*.

Fridriksson, T., Neuhoff, P. S., Vinani, B. E., and Bird, D. K. (2004). "Experimental determination of thermodynamic properties of ion-exchange in heulandite: binary ion-exchange experiments at 55 and 85° involving Ca2+, Sr2+, Na+ and K+". In: *American Journal of Science* 304, pp. 287–332.

Heap, M., Lavallée, Y., Petrakova, L., Baud, P., Reuschle, T., Varley, N., and Dingwell, D. B. (2014). "Microstructural controls on the physical and mechanical properties of edifice-forming andesites at Volcán de Colima, Mexico". In: *Journal of Geophysical Research: Solid Earth* 119.4, pp. 2925–2963.

Henry, P. (1997). "10. Relationship between porosity, electrical conductivity, and cation exchange capacity in Barbados wedge sediments". In: *Proceedings of the Ocean Drilling Program. Scientific Results*. Vol. 156, pp. 183–195.

Hower, J. and Mowatt, T. C. (1966). "The mineralogy of illites and mixed-layer illite/montmorillonites". In: *American Mineralogist* 51.5-6, pp. 825–854.

Kaufhold, S. and Dohrmann, R. (2003). "Beyond the Methylene Blue Method: Determination of the Smectite Content using the Cutriene Method". In: *Zeitschrift für Angewandte Geologie* 49, pp. 13–17.

Lagaly, G. (1981). "Characterization of clays by organic compounds". In: *Clay Minerals* 16.1, p. 1.

Lévy, L., Flóvenz, O., and Hersir, G. (2016). *IMAGE Task 3.3 - Physical Properties of Rock at Reservoir Conditions. Quantitative Impact of Hydrothermal Alteration on Electrical Resistivity, based on cores from Krafla.* Report ISOR-2016/043. Iceland GeoSurvey (ISOR).

Lévy, L., Gibert, B., Sigmundsson, F., Flóvenz, O. G., Hersir, G. P., Briole, P., and Pezard, P. A. (2018). "The role of smectites in the electrical conductivity of active hydrothermal systems: electrical properties of core samples from Krafla volcano, Iceland". In: *Geophysical Journal International* 215.3, pp. 1558–1582.

Maraqah, H., Li, J., and Whittingham, M. S. (1990). "Ion transport in single crystals of the clay-like aluminosilicate, vermiculite". In: *MRS Online Proceedings Library Archive* 210.

Meier, L. and Kahr, G. (1999). "Determination of the Cation Exchange Capacity (CEC) of Clay Minerals Using the Complexes of Copper(II) Ion with Triethylenetetramine and Tetraethylenepentamine". In: *Clays and Clay Minerals* 47.3, pp. 386–388.

Meller, C. (2014). "Localization and Characterization of Hydrothermal Alteration Zones in a Geothermal Reservoir and Their Significance for Rock Mechanics". PhD thesis. KIT-Bibliothek.

Orsini, L and Remy, J. (1976). "Utilisation du chlorure de cobaltihexamine pour la détermination simultanée de la capacité d'échange et des bases échangeables des sols". In: *Sci. Sol* 4, pp. 269–275.

Patrier, P., Papapanagiotou, P., Beaufort, D., Traineau, H., Bril, H., and Rojas, J. (1996). "Role of permeability versus temperature in the distribution of the fine ($\leq$ 0.2 μ m) clay fraction in the Chipilapa geothermal system (El Salvador, Central America)". In: *Journal of Volcanology and Geother-*

mal Research 72.1, pp. 101–120. DOI: https://doi.org/10.1016/0377-0273(95)00078-X.

Pezard, P. A. (1990). "Electrical properties of mid-ocean ridge basalt and implications for the structure of the upper oceanic crust in Hole 504B". In: *Journal of Geophysical Research* 95.B6, p. 9237. DOI: 10.1029/JB095iB06p09237.

Reinoso-Maset, E., Hainos, D., and Ly, J. (2012). "Sorption of uranium (VI) and radium (II) at trace level onto kaolinite and montmorillonite". In: *VM Goldschmidt Conference*.

Revil, A. and Glover, P. W. J. (1997). "Theory of ionic-surface electrical conduction in porous media". In: *Physical Review B* 55.3, pp. 1757–1773.

— (1998). "Nature of surface electrical conductivity in natural sands, sandstones, and clays". In: *Geophysical Research Letters* 25.5, pp. 691–694.

Revil, A., Cathles, L. M., Losh, S., and Nunn, J. A. (1998). "Electrical conductivity in shaly sands with geophysical applications". In: *Journal of Geophysical Research: Solid Earth* 103.B10, pp. 23925–23936.

Rink, M. and Schopper, J. R. (1974). "Interface conductivity and its implications to electric logging". In: *Society of Petrophysicists and Well-Log Analysts*. Society of Petrophysicists and Well-Log Analysts.

Robin, V., Tertre, E., Beaufort, D., Regnault, O., Sardini, P., and Descostes, M. (2015). "Ion exchange reactions of major inorganic cations (H+, Na+, Ca2+, Mg2+ and K+) on beidellite: Experimental results and new thermodynamic database. Toward a better prediction of contaminant mobility in natural environments". In: *Applied Geochemistry* 59, pp. 74–84.

Robin, V., Tertre, E., Beaucaire, C., Regnault, O., and Descostes, M. (2017). "Experimental data and assessment of predictive modeling for radium ion-exchange on beidellite, a swelling clay mineral with a tetrahedral charge". In: *Applied Geochemistry* 85, pp. 1–9.

Taut, T., Kleeberg, R., and Bergmann, J. (1998). “Seifert Software: The new Seifert Rietveld program BGMN and its application to quantitative phase analysis”. In: *Materials Structure* 5.1, pp. 57–66.

Tertre, E. (2014). “Modélisation des propriétés d’adsorption des minéraux argileux gonflants vis-à-vis de cations inorganiques. Interfaces continentales, environnement.” Habilitation à diriger des recherches. Université de Poitiers.

Vogt, K. and Köster, H. M. (1978). “Zur mineralogie, kristallchemie und geochemie einiger montmorillonite aus bentoniten”. In: *Clay Minerals* 13.1, pp. 25–43.

Waxman, M. H. and Smits, L. J. M. (1968). “Electrical conductivities in oil-bearing shaly sands”. In: *Soc. Pet. Eng. J.* 8, pp. 107–122.

A Structure files for smectite and chlorite

A.1 Chlorite with Fe/Mg ratios constrained

```
PHASE=CHLORITE_Lea //
SpacegroupNo=12 HermannMauguin=C12/m1 //
PARAM=pa=0.6_0.5^0.8
PARAM=pb=0.6_0.5^0.8
PARAM=pc=0.6_0.5^0.8
PARAM=A=0.52558_0.51^0.55 PARAM=B=0.945_0.91^0.98
PARAM=C=1.42543_1.38^1.44
PARAM=BETA=95.587_94.5^98 //
RP=4 PARAM=B1=0_0^0.01 PARAM=k1=0_0^0.1 // PARAM=k2=0_0^0.00001 GEWICHT=SPHAR2
GOAL: chlorite2b=GEWICHT*ifthenelse(ifdef(d),exp(my*d*3/4),1)
E=(MG+2,FE+2(pa)) Wyckoff=a TDS=0.01
E=(MG+2,FE+2(pb)) Wyckoff=g y=0.6678 TDS=0.01
```

```
E=O-2 Wyckoff=i x=0.3150 z=0.9257 TDS=0.01
E=O-2 Wyckoff=j x=0.1890 y=0.1667 z=0.0774 TDS=0.01
E=(SI+4(0.6560),AL+3(0.3440)) Wyckoff=j x=0.2248 y=0.1669 z=0.1937 TDS=0.01
E=O-2 Wyckoff=i x=0.8030 z=0.7643 TDS=0.01
E=O-2 Wyckoff=j x=0.5110 y=0.2280 z=0.2363 TDS=0.01
E=O-2 Wyckoff=i x=0.8280 z=0.5711 TDS=0.01
E=O-2 Wyckoff=j x=0.1310 y=0.3463 z=0.4285 TDS=0.01
E=(MG+2,FE+2(pc)) Wyckoff=h y=0.8336 TDS=0.01
E=AL+3(0.9650) Wyckoff=d TDS=0.01
E=H Wyckoff=i x=0.2887 z=0.8552 TDS=0.02
E=H Wyckoff=i x=0.8377 z=0.6339 TDS=0.02
E=H Wyckoff=j x=0.1586 y=0.3359 z=0.3698 TDS=0.02
pMg=1- (pa+pb+pc)
GOAL=pMg
```

A.2 Saponite loosely constrained

```
PHASE=Saponite2wTest SpacegroupNo=5 HermannMauguin=C121
PARAM=A=0.53_0.525^0.535 B=A*sqrt(3) PARAM=c0=1.5_1.2^1.58
// old PARAM=c0=1.28_1.15^1.35
BETA=100.1
pi==2*acos(0)
RP=4
layer==10 // layer: factor for elongation in c direction
C=c0*layer // C: lattice parameter c for supercell
PARAM=b10=0.002_0^0.015 // isotropic broadening of hkl reflections
PARAM=b11=0.08_0^0.15 // separate broadening of 00l reflections
B1=ifthenelse(and(eq(h,0),eq(k,0)),b10+b11,b10)
```

```
// K20: strain broadening of hkl lines
PARAM=K20=0.000026_0.00001^0.0001
// K21: strain broadening of 001 lines
// changer pour ressembler nontronite de 0.001 a 0.002
PARAM=K21=0_0^0.002
breit2=1/sqr(C) // additional l-dependent broadening to avoid "ripples"
PARAM=GEWICHT=0.0_0 // refining the scale factor
// definition of the helper variable "Saponite..."
// for calculation of phase abundances
GOAL:Saponite2wTest=GEWICHT
// squared lorentzian (Gauss-like) broadening
B2=cat(R2==sqr(h/A)+sqr(k/B),Z2==max(sqr(sk)-R2,0),
orientierung2==Z2/sqr(sk),
ifthenelse(and(eq(h,0),eq(k,0)),K21*sqr(sk),K20*sqr(sk)+breit2*orientierung2))
//
// scaling of classes (001 und hkl) and removal of redundant 001 reflections
GEWICHT[1]=GEWICHT*ifthenelse(and(eq(h,0),eq(k,0)),
ifthenelse(mod(l,layer),0,layer),1)
//
// === occupancies ========================
//
// --- interlayer ----------------
PARAM=pINT=0.3_0.2^0.4
pOZ=pINT
//
// ===== rigid body of the interlayer complex ====================
//    cation, squared surrounded by 4 oxygen (water)
```

```
596 // definition of the positions in cartesian co-ordinates
597 //
598 dCAO=0.241          // distance cation - oxygen
599 //
600 set(ECA,0,0,0)        // cation in the middle of the interlayer
601 // ajout de EOZ1 et EOZ2 comme dans nontronite15
602 set(EOZ1,0,0,dCAO)    // O above
603 set(EOZ2,0,0,-dCAO)    // O below
604 set(EOZ3,dCAO,0,0)
605 set(EOZ4,-dCAO,0,0)
606 set(EOZ5,0,dCAO,0)
607 set(EOZ6,0,-dCAO,0)
608 xx=0.69 // shifting parameter of the interlayer complex in x, fixed
609 yy=0.21 // shifting parameter of the interlayer complex in y, fixed
610 fi1=0 // the 3 Eulerian angles for rotation of the interlayer complex, fixed
611 fi2=0
612 fi3=-18
613 T(xx,yy,0.5*c0*sin(pi*BETA/180),fi1,fi2,fi3,ECA,EOZ1,EOZ2,EOZ3,EOZ4,EOZ5,EOZ6)
614 // shifting and rotation of the rigid body
615 //
616 // --- isotropic temperature factors (nm^2), estimated ----------------------
617 //
618 tdsint=0.01
619 tdsH2O=0.02
620 tdsoct=0.005
621 tdstet=0.003
622 tdso=0.007
```

```
623 //
624 // --- positions ------------------------------
625 // trioctahedral coordinates from phlogopite ICSD 6259
626 //  absolute positions in c-direction [nm]
627 //  to avoid a stretching/shortening of the TOT layer by varying c0
628 //
629 zT=0.2708
630 zO11=0.112
631 zO12=0.104
632 zO2=0.328
633 //
634 E=MG+2 Wyckoff=a y=0.0 TDS=tdsoct  // trans
635 E=MG+2 Wyckoff=a y=0.6673 TDS=tdsoct // cis
636 E=MG+2 Wyckoff=a y=0.3327 TDS=tdsoct  // cis
637 E=(SI+4(0.93),AL+3(0.07)) Wyckoff=c x=0.9238 y=0.8335 z=zT/(layer*c0) TDS=tdstet
638 E=(SI+4(0.93),AL+3(0.07)) Wyckoff=c x=0.9238 y=0.1665 z=zT/(layer*c0) TDS=tdstet
639 E=O-1 Wyckoff=c x=0.979 y=0.0 z=zO2/(layer*c0) TDS=tdso
640 E=O-1 Wyckoff=c x=0.671 y=0.2315 z=zO2/(layer*c0) TDS=tdso
641 E=O-1 Wyckoff=c x=0.871 y=0.1668 z=zO11/(layer*c0) TDS=tdso
642 E=O-1 Wyckoff=c x=0.871 y=0.8332 z=zO11/(layer*c0) TDS=tdso
643 E=O-1 Wyckoff=c x=0.363 y=0.0 z=zO12/(layer*c0) TDS=tdso
644 E=O-1 Wyckoff=c x=0.6710 y=0.7685 z=zO2/(layer*c0) TDS=tdso
645 //
646 // list of interlayer positions
647 // change NA to CA et 1(pINT) to 2(pINT) + ajout de 2 ligne EOZ1 et EOZ2
648 E=CA+2(pINT) Wyckoff=c x=X(ECA) y=Y(ECA) z=Z(ECA)   TDS=tdsint
649 E=O-2(pOZ)  Wyckoff=c x=X(EOZ1) y=Y(EOZ1) z=Z(EOZ1)   TDS=tdsH2O
```

```
E=O-2(pOZ)   Wyckoff=c  x=X(EOZ2)  y=Y(EOZ2)  z=Z(EOZ2)    TDS=tdsH2O
E=O-2(pOZ)   Wyckoff=c  x=X(EOZ3)  y=Y(EOZ3)  z=Z(EOZ3)    TDS=tdsH2O
E=O-2(pOZ)   Wyckoff=c  x=X(EOZ4)  y=Y(EOZ4)  z=Z(EOZ4)    TDS=tdsH2O
E=O-2(pOZ)   Wyckoff=c  x=X(EOZ5)  y=Y(EOZ5)  z=Z(EOZ5)    TDS=tdsH2O
E=O-2(pOZ)   Wyckoff=c  x=X(EOZ6)  y=Y(EOZ6)  z=Z(EOZ6)    TDS=tdsH2O
```

A.3 Tri-octahedral smectite, interlayer spaces filled with Ca and two water layers

```
PHASE=Smectitetri_2w_Ca
SpacegroupNo=5 HermannMauguin=C121
PARAM=B=0.93_0.900^0.930 A=B/sqrt(3)-0.0015 PARAM=c0=1.50_1.42^1.6
BETA=100.2
pi==2*acos(0)
RP=4
layer==10  // layer: factor for elongation in c direction
C=c0*layer // C: lattice parameter c for supercell
PARAM=b10=0.002_0^0.015 // isotropic broadening of hkl reflections
PARAM=b11=0.03_0^0.1  // separate broadening of 001 reflections
B1=ifthenelse(and(eq(h,0),eq(k,0)),b10+b11,b10)
// K20: strain broadening of hkl lines
PARAM=K20=0.000026_0.00001^0.0001
// K21: strain broadening of 001 lines
PARAM=K21=0_0^0.001
breit2=1/sqr(C) // additional l-dependent broadening to avoid "ripples"
PARAM=GEWICHT=0_0 // refining the scale factor
// definition of the helper variable "smectite..."
// for calculation of phase abundances
```

```
676 GOAL: Smectitetri2wCa=GEWICHT*ifthenelse(ifdef(d),exp(my*d*3/4),1) //
677 // squared lorentzian (Gauss-like) broadening
678 B2=cat(R2==sqr(h/A)+sqr(k/B),Z2==max(sqr(sk)-R2,0),orientierung2==Z2/sqr(sk),
679 ifthenelse(and(eq(h,0),eq(k,0)),K21*sqr(sk),K20*sqr(sk)+breit2*orientierung2))
680 //
681 // scaling of classes (00l und hkl) and removal of redundant 00l reflections
682 GEWICHT[1]=GEWICHT*ifthenelse(and(eq(h,0),eq(k,0)), ...
683       ...ifthenelse(mod(l,layer),0,layer),1)
684 //
685 // === occupancies ====================
686 // --- octahedra position -------
687 pMG=0.15_0.1^0.3 PARAM=pFE=0.06_0^0.3 pAL=(1-pMG-pFE)
688 PARAM=ptrans=1.0_0.0^1.0
689 // mixing parameter for cis- and trans-vacancy; 0 => trans-vacant
690 //
691 // --- interlayer ----------------
692 PARAM=pCA=0.15_0.1^0.3
693 pOZ=pCA
694 //
695 // ==== rigid body of the interlayer complex ====================
696 //    cation, octahedrally surrounded by 6 oxygen (water)
697 // definition of the positions in cartesian co-ordinates
698 //
699 dCAO=0.241          // distance cation - oxygen
700 //
701 set(ECA,0,0,0)        // cation in the middle of the interlayer
702 set(EOZ1,0,0,dCAO)    // O above
```

```
703 set(EOZ2,0,0,-dCAO)     // O below
704 set(EOZ3,dCAO,0,0)
705 set(EOZ4,-dCAO,0,0)
706 set(EOZ5,0,dCAO,0)
707 set(EOZ6,0,-dCAO,0)
708 xx=0.7 // shifting parameter of the interlayer complex in x
709 yy=0.2 // shifting parameter of the interlayer complex in y
710 // the first two Eulerian angles for rotation of the interlayer complex,
711 // fixed
712 fi1=45
713 fi2=180*acos(1/sqrt(3))/pi
714 // fi3 (3th eulerian angle) is a rotation around the cartesian z-axis
715 // which is perpendicular to the xy-plane
716 fi3=-20
717 T(xx,yy,0.5*c0*sin(pi*BETA/180),fi1,fi2,fi3,ECA,EOZ1,EOZ2,EOZ3,EOZ4,EOZ5,EOZ6)
718 // shifting and rotation of the rigid body
719 //
720 // --- isotropic temperature factors (nm^2), estimated ------------------------
721 //
722 tdsint=0.015
723 tdsH2O=0.025
724 tdsoct=0.01
725 tdstet=0.01
726 tdso=0.015
727 //
728 // --- positions ---------------------------
729 //  absolute positions in c-direction [nm]
```

```
730 //  to avoid a stretching/shortening of the TOT layer by varying c0
731 //
732 zT=0.271350
733 zO11=0.10955
734 zO12=0.10553
735 zO2=0.33668
736 //
737 E=MG+2 Wyckoff=a y=0.0 TDS=tdsoct
738 E=MG+2 Wyckoff=a y=0.6673 TDS=tdsoct
739 E=MG+2 Wyckoff=a y=0.3327 TDS=tdsoct
740 E=(SI+4(0.93),AL+3(0.07)) Wyckoff=c x=0.9238 y=0.8335 z=zT/C TDS=tdstet
741 E=(SI+4(0.93),AL+3(0.07)) Wyckoff=c x=0.9238 y=0.1665 z=zT/C TDS=tdstet
742 E=O-1 Wyckoff=c x=0.979 y=0.0 z=zO2/C TDS=tdso
743 E=O-1 Wyckoff=c x=0.671 y=0.2315  z=zO2/C TDS=tdso
744 E=O-1 Wyckoff=c x=0.871 y=0.1668  z=zO11/C TDS=tdso
745 E=O-1 Wyckoff=c x=0.871 y=0.8332  z=zO11/C TDS=tdso
746 E=O-1 Wyckoff=c x=0.363 y=0.0     z=zO12/C TDS=tdso
747 E=O-1 Wyckoff=c x=0.6710 y=0.7685 z=zO2/C TDS=tdso
748 //
749 // list of interlayer positions
750 E=CA+2(pCA) Wyckoff=c x=X(ECA) y=Y(ECA) z=Z(ECA)   TDS=tdsint
751 E=O-2(pOZ)  Wyckoff=c x=X(EOZ1) y=Y(EOZ1) z=Z(EOZ1)   TDS=tdsH2O
752 E=O-2(pOZ)  Wyckoff=c x=X(EOZ2) y=Y(EOZ2) z=Z(EOZ2)   TDS=tdsH2O
753 E=O-2(pOZ)  Wyckoff=c x=X(EOZ3) y=Y(EOZ3) z=Z(EOZ3)   TDS=tdsH2O
754 E=O-2(pOZ)  Wyckoff=c x=X(EOZ4) y=Y(EOZ4) z=Z(EOZ4)   TDS=tdsH2O
755 E=O-2(pOZ)  Wyckoff=c x=X(EOZ5) y=Y(EOZ5) z=Z(EOZ5)   TDS=tdsH2O
756 E=O-2(pOZ)  Wyckoff=c x=X(EOZ6) y=Y(EOZ6) z=Z(EOZ6)   TDS=tdsH2O
```

B Effect of preferred orientation on X-ray diffraction patterns: the case of heulandite

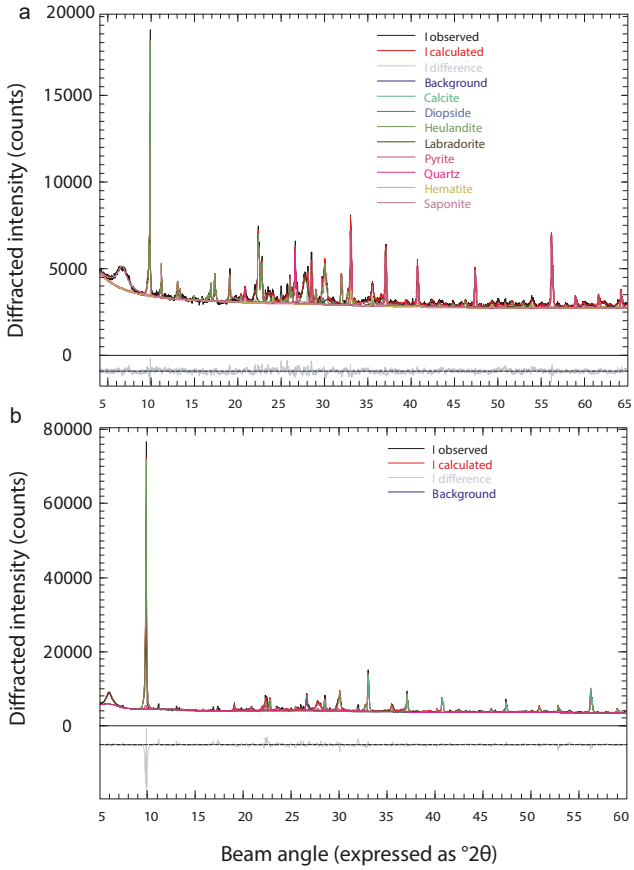

Figure B.1: Illustration of the effect of preferred orientation on X-ray diffraction pattern for a sampl (L02) containing a large amount of heulandite (zeolite). The upper pannel shows the diffraction pattern when the powder is carefully grained and front-loaded. The lower pannel shows the diffraction pattern for the exact same powder but back-loaded. The diffraction peak of heulandite at angle 10 $^{\circ}2\theta$ is four times higher in the lower panel and cannot be correctly fitted.

BIBLIOGRAPHY

Abdulsamad, F., Florsch, N., Schmutz, M., and Camerlynck, C. (2016). "Assessing the high frequency behavior of non-polarizable electrodes for spectral induced polarization measurements." In: *Journal of Applied Geophysics* 135, pp. 449–455.

Abdulsamad, F., Florsch, N., and Camerlynck, C. (2017). "Spectral induced polarization in a sandy medium containing semiconductor materials: experimental results and numerical modelling of the polarization mechanism." In: *Near Surface Geophysics* 15.6, pp. 669–683.

Abramoff, M. D., Magalhaes, P. J., and Ram, S. J. (2004). "Image processing with ImageJ. Biophotonics Int. 11: 36-42." In: *Google Scholar*.

Agarwal, A. and Lang, J. (2005). *Foundations of analog and digital electronic circuits*. Elsevier.

Alt, J. C. (1999). "Hydrothermal alteration and mineralization of oceanic crust: mineralogy, geochemistry, and processes." In: *Reviews in Economic Geology* 8, pp. 133–155.

Ames, L. L. (1966). "Cation exchange properties of wairakite and analcime(Cation exchange properties of wairakite and analcime)." In: *THE AMERICAN MINERALOGIST* 51, pp. 903–909.

Anderson, A. (1975). "Some basaltic and andesitic gases." In: *Reviews of Geophysics* 13.1, pp. 37–55.

Ármannsson, H., Gudmundsson, A., and Steingrímsson, B. S. (1987). "Exploration and development of the Krafla geothermal area." In: *Jökull* 37, pp. 13–30.

Árnason, K. and Magnússon, I. T. (2001). *Niðurstöður við námsmælinga í Kröflu*. Report OS-2001/062. Orkustofnun.

Árnason, K., Vilhjálmsson, A., and Björnsdóttir, T. (2007). *A study of the Krafla volcano using gravity, micro earthquake and MT data*. KenGen, Lake Naivasha, Kenya. 14 pp.

Árnason, K., Karlsdóttir, R., Eysteinsson, H., Flóvenz, O. G., and Gudlaugsson, S. T. (2000). "The resistivity structure of high-temperature geothermal systems in Iceland." In: *World Geothermal Congress*, pp. 923–928.

Ashcroft, N. W. and Mermin, N. D. (1976). "Solid state physics." In: Philadelphia, Pa.: Saunders College. Chap. 12, pp. 225–227.

Auken, E., Christiansen, A. V., Kirkegaard, C., Fiandaca, G., Schamper, C., Behroozmand, A. A., Binley, A., Nielsen, E., Effersø, F., Christensen, N. B., et al. (2014). "An overview of a highly versatile forward and stable inverse algorithm for airborne, ground-based

and borehole electromagnetic and electric data." In: *Exploration Geophysics* 46.3, pp. 223–235.

Axelsson, G. (2008). "Production capacity of geothermal systems." In: *Proceedings of the Workshop for Decision Makers on the Direct Heating Use of Geothermal Resources in Asia*, p. 14.

Bailey, J. C. and Noe-Nygaard, A (1976). "Chemistry of Miocene plume tholeiites from northwest Iceland." In: *Lithos* 9.3, pp. 185–201.

Barsoukov, E. and Macdonald, J. R. (2018). *Impedance spectroscopy: theory, experiment, and applications*. John Wiley & Sons.

Beaufort, D, Patrier, P, Meunier, A, and Ottaviani, M. (1992). "Chemical variations in assemblages including epidote and/or chlorite in the fossil hydrothermal system of Saint Martin (Lesser Antilles)." In: *Journal of Volcanology and Geothermal Research* 51.1-2, pp. 95–114.

Beaufort, D., Papapanagiotou, P., Patrier, P., Fujimoto, K., and Kasai, K. (1995). "High-temperature smectites in active geothermal systems." In: *Proceedings 8th Water-Rock Interaction Symposium, Vladivostok*. Ed. by Y. Kharaka and O. Chudaev. Balkema, Rotterdam., pp. 1071 –1076.

Beaufort, D., Rigault, C., Billon, S., Billault, V., Inoue, A., Inoue, S., and Patrier, P. (2015). "Chlorite and chloritization processes through mixed-layer mineral series in low-temperature geological systems - a review." In: *Clay Minerals* 50.4, pp. 497–523.

Berger, G., Beaufort, D., and Antoine, R. (2018). "Clay minerals related to the late magmatic activity of the Piton des Neiges (Réunion island). Consequence for the primitive crusts." In: *Clay Minerals*, 1–34.

Berger, G. and Velde, B. (1992). "Chemical parameters controlling the propylitic and argillic alteration process." In: *Eur. J. Mineral.* Pp. 1439–1456.

Berger, G., Meunier, A., and Beaufort, D. (2014). "Clay mineral formation on Mars: Chemical constraints and possible contribution of basalt out-gassing." In: *Planetary and Space Science* 95, pp. 25–32.

Bertani, R. (2005). "World geothermal power generation in the period 2001–2005." In: *Geothermics* 34.6, pp. 651–690.

— (2016). "Geothermal power generation in the world 2010–2014 update report." In: *Geothermics* 60, pp. 31–43.

Bertin, J. and Loeb, J. (1976). *Experimental and Theoretical aspects of induced polarization, Vol. 1*. Ed. by R. G. van Nostrand and S. Saxov. Stuttgart, Germany: Schweizerbart Science Publishers.

Binley, A. and Kemna, A. (2005). "DC resistivity and induced polarization methods." In: *Hydrogeophysics*. Springer, pp. 129–156.

Binley, A., Slater, L. D., Fukes, M., and Cassiani, G. (2005). "Relationship between spectral induced polarization and hydraulic properties of saturated and unsaturated sandstone." In: *Water resources research* 41.12.

Björnsson, A. (1985). "Dynamics of crustal rifting in NE Iceland." In: *Journal of Geophysical Research: Solid Earth* 90.B12, pp. 10151–10162.

Bouchet, A., Meunier, A., and Sardini, P. (2000). *Minéraux argileux: structure cristalline, identification par diffraction de rayons X*. Vol. 23. Editions Elf Exploration.

Bourdelle, F., Parra, T., Beyssac, O., Chopin, C., and Vidal, O. (2013). "Clay minerals as geo-thermometer: A comparative study based on high spatial resolution analyses of illite and chlorite in Gulf Coast sandstones (Texas, U.S.A.)" In: *American Mineralogist* 98.5-6, pp. 914–926.

Bril, H., Papapanagiotou, P., Patrier, P., Lenain, J.-F., and Beaufort, D. (1996). "Fluid-rock interaction in the geothermal field of Chipilapa (El Salvador): contribution of fluid-inclusion data." In: *European Journal of Mineralogy*, pp. 515–532.

Bücker, M., Flores Orozco, A., and Kemna, A. (2018). "Electro-chemical polarization around metallic particles–Part 1: The role of diffuse-layer and volume-diffusion relaxation." In: *Geophysics* 83.4, pp. 1–53.

Cannon, K. M., Parman, S. W., and Mustard, J. F. (2017). "Primordial clays on Mars formed beneath a steam or supercritical atmosphere." In: *Nature* 552.7683, p. 88.

Carson, G. L. (2015). "Hydrothermal Acid-sulfate Alteration at Krafla and Námafjall, NE Iceland: Implications for Gusev Crater and Meridiani Planum, Mars." MA thesis. University of Wisconsin-Milwaukee.

Chelidze, T. L. and Gueguen, Y. (1999). "Electrical spectroscopy of porous rocks: A review–I. Theoretical models." In: *Geophysical Journal International* 137.1, pp. 1–15.

Chelidze, T. L., Gueguen, Y., and Ruffet, C. (1999). "Electrical spectroscopy of porous rocks: A review–II. Experimental results and interpretation." In: *Geophysical Journal International* 137.1, pp. 16–34.

Cole, K. S. and Cole, R. H. (1941). "Dispersion and absorption in dielectrics. I. Alternating current characteristics." In: *J. Chem. Phys.* 9, pp. 341–351.

Couto, M., Fiandaca, G, Auken, E, Christiansen, A., and Porsani, J. (2018). "1D AEMIP Inversion Using MPA Reparameterization for HTEM Survey at Lamego Gold Mine, Quadrilátero Ferrífero, MG, Brazil." In: *2nd Conference on Geophysics for Mineral Exploration and Mining*.

Dahlin, T. and Leroux, V. (2012). "Improvement in time-domain induced polarization data quality with multi-electrode systems by separating current and potential cables." In: *Near Surface Geophysics* 10.6, pp. 545–565.

Dahlin, T. and Zhou, B. (2006). "Multiple-gradient array measurements for multichannel 2D resistivity imaging." In: *Near Surface Geophysics* 4.2, pp. 113–123.

DeMets, C., Gordon, R., Argus, D. F., and Stein, S. (1990). "Current plate motions." In: *Geophysical journal international* 101.2, pp. 425–478.

Denk, T., Grimsson, F., Zetter, R., and Simonarson, L. (2011). "Late Cainozoic Floras of Iceland - 15 Million Years of Vegetation and Climate History in the Northern North Atlantic." In: *Topics in Geology, Volume 35*. Ed. by N. H. Landman and P. J. Harries. Vol. 35. Springer, p. 854.

Doebelin, N. and Kleeberg, R. (2015). "Profex: a graphical user interface for the Rietveld refinement program BGMN." In: *Journal of applied crystallography* 48.5, pp. 1573–1580.

Dyer, A., Gawad, A. S. A., Mikhail, M., Enamy, H., and Afshang, M. (1991). "The natural zeolite, laumontite, as a potential material for the treatment of aqueous nuclear wastes." In: *Journal of radioanalytical and nuclear chemistry* 154.4, pp. 265–276.

Edwards, L. (1977). "A modified pseudosection for resistivity and IP." In: *Geophysics* 42.5, pp. 1020–1036.

Einarsson, P. (1978). "S-wave shadows in the Krafla caldera in NE-Iceland, evidence for a magma chamber in the crust." In: *Bulletin Volcanologique* 41.3, pp. 187–195.

— (1991). "Earthquakes and present-day tectonism in Iceland." In: *Tectonophysics* 189.1-4, pp. 261–279.

Elders, W. A. et al. (2011). "Origin of a rhyolite that intruded a geothermal well while drilling at the Krafla volcano, Iceland." In: *Geology* 39.3, pp. 231–234.

Elders, W., Nielson, D, Schiffman, P, and Schriener Jr, A (2014). "Investigating ultra high-enthalpy geothermal systems: a collaborative initiative to promote scientific opportunities." In: *Scientific Drilling* 18, pp. 35–42.

Engel, A. J., Engel, C. G., and Havens, R. (1965). "Chemical characteristics of oceanic basalts and the upper mantle." In: *Geological Society of America Bulletin* 76.7, pp. 719–734.

Ferrage, E. (2016). "Investigation of the interlayer organization of water and ions in smectite from the combined use of diffraction experiments and molecular simulations. A review of methodology, applications, and perspectives." In: *Clays and Clay Minerals* 64.4, pp. 348–373.

Ferrage, E., Lanson, B., Sakharov, B. A., and Drits, V. A. (2005). "Investigation of smectite hydration properties by modeling experimental X-ray diffraction patterns: Part I. Montmorillonite hydration properties." In: *American Mineralogist* 90.8-9, pp. 1358–1374.

Fiandaca, G., Auken, E., Christiansen, A. V., and Gazoty, A. (2012). "Time-domain-induced polarization: Full-decay forward model-

ing and 1D laterally constrained inversion of Cole-Cole parameters." In: *Geophysics* 77.3, E213–E225.

Fiandaca, G., Ramm, J., Binley, A., Gazoty, A., Christiansen, A. V., and Auken, E. (2013). "Resolving spectral information from time domain induced polarization data through 2-D inversion." In: *Geophys. J. Int* 192, pp. 631–646.

Flis, M. F., Newman, G. A., and Hohmann, G. W. (1989). "Induced-polarization effects in time-domain electromagnetic measurements." In: *Geophysics* 54.4, pp. 514–523.

Flores Orozco, A., Velimirovic, M., Tosco, T., Kemna, A., Sapion, H., Klaas, N., Sethi, R., and Bastiaens, L. (2015). "Monitoring the injection of microscale zerovalent iron particles for groundwater remediation by means of complex electrical conductivity imaging." In: *Environmental science & technology* 49.9, pp. 5593–5600.

Florsch, N., Camerlynck, C., and Revil, A (2012). "Direct estimation of the distribution of relaxation times from induced-polarization spectra using a Fourier transform analysis." In: *Near Surface Geophysics* 10.6, pp. 517–531.

Flóvenz, O. G., Hersir, G. P., Sæmundsson, K., Ármannsson, H., and Friðriksson, T. (2012). "7.03 - Geothermal Energy Exploration Techniques." In: *Comprehensive Renewable Energy*. Ed. by A. Sayigh. Oxford: Elsevier, pp. 51 –95.

Flóvenz, Ó. G. and Saemundsson, K. (1993). "Heat flow and geothermal processes in Iceland." In: *Tectonophysics* 225.1-2, pp. 123–138.

Franzson, H (1998). "Reservoir geology of the Nesjavellir high-temperature field in SW-Iceland." In: *Proceedings 19th Annual PNOC-EDC Geothermal Conference*, pp. 13–20.

Fridriksson, T., Neuhoff, P. S., Vinani, B. E., and Bird, D. K. (2004). "Experimental determination of thermodynamic properties of ion-exchange in heulandite: binary ion-exchange experiments at 55 and 85°C involving Ca2+, Sr2+, Na+ and K+." In: *American Journal of Sciences* 304, pp. 287–332.

Gaillard, F. (2004). "Laboratory measurements of electrical conductivity of hydrous and dry silicic melts under pressure." In: *Earth and Planetary Science Letters* 218.1-2, pp. 215–228.

Gast, P. W. (1968). "Trace element fractionation and the origin of tholeiitic and alkaline magma types." In: *Geochimica et Cosmochimica Acta* 32.10, pp. 1057–1086.

Gautason, B., Egilson, T., Blishke, A., and Danielsen, P. E. (2007). *Krafla: Borun tveggja kjarnahola, KH5 og KH6, veturinn 2006-2007.* Report in Icelandic. ISOR.

Gazoty, A, Fiandaca, G., Pedersen, J, Auken, E., and Christiansen, A. V. (2013). "Data repeatability and acquisition techniques for time-domain spectral induced polarization." In: *Near Surface Geophysics* 11.4, pp. 391–406.

Gudmundsson, A. (1991). *Borun kjarnaholu í Sandabotnaskarð*. Report in Icelandic. Orkustofnun.

— (1993). *Lithology cross section through wells BJ-11 and BJ-12 in Bjarnarflag*. Report in Icelandic OS-93071/JHD-35. Orkustofnun.

Gudmundsson, A., Egilson, T., and Haraldson, K. (2007). *Krafla - Hola KS-01. Forborun og 1. áfangi.* Tech. rep. LV-2007/055. Landsvirkjun.

Gudmundsson, A. (2005). "Geothermal Data Collection and Consultancy at Drill Site." In: *zeolites* 40, p. 120.

Gudmundsson, A., Mortensen, A. K., Hjartarson, A., Karlsdóttir, R., and Ármannsson, H. (2010). "Exploration and utilization of the Namafjall high temperature area in North Iceland." In: *World Geothermal Congress*.

Gurin, G., Tarasov, A., Ilyin, Y., and Titov, K. (2013). "Time domain spectral induced polarization of disseminated electronic conductors: Laboratory data analysis through the Debye decomposition approach." In: *Journal of Applied Geophysics* 98, pp. 44–53.

Gurin, G., Titov, K., Ilyin, Y., and Tarasov, A. (2015). "Induced polarization of disseminated electronically conductive minerals: a semi-empirical model." In: *Geophysical Journal International* 200.3, pp. 1555–1565.

Gurin, G., Ilyin, Y., Nilov, S., Ivanov, D., Kozlov, E., and Titov, K. (2018). "Induced polarization of rocks containing pyrite: Interpretation based on X-ray computed tomography." In: *Journal of Applied Geophysics* 154, pp. 50–63.

Haggerty, S. E. (1991). "Oxide textures; a mini-atlas." In: *Reviews in Mineralogy and Geochemistry* 25.1, pp. 129–219.

Hallof, P. and Klein, J. (1983). "Characterization of electrical properties of metallic mineral deposits." In: *Ontario Geological Survey Open File Report* 5468.

Hedenquist, J. W., Arribas, A., and Reynolds, T. J. (1998). "Evolution of an intrusion-centered hydrothermal system; Far Southeast-Lepanto porphyry and epithermal Cu-Au deposits, Philippines." In: *Economic Geology* 93.4, pp. 373–404.

Henley, R. W. and Ellis, A. J. (1983). "Geothermal systems ancient and modern: a geochemical review." In: *Earth-science reviews* 19.1, pp. 1–50.

Henry, P. (1997). "10. Relationship between porosity, electrical conductivity, and cation exchange capacity in Barbados wedge sediments." In: *Proceedings of the Ocean Drilling Program. Scientific Results*. Vol. 156, pp. 183–195.

Hersir, G. P. and Björnsson, A. (1991). *Geophysical exploration for geothermal resources: principles and application.* Report. Orkustofnun.

Hjartardóttir, Á. R., Einarsson, P., Bramham, E., and Wright, T. J. (2012). "The Krafla fissure swarm, Iceland, and its formation by rifting events." In: *Bulletin of Volcanology* 74.9, pp. 2139–2153.

Hjartarson, Á., Erlendsson, Ö., and Blischke, A. (2017). "The Greenland–Iceland–Faroe Ridge Complex." In: *Geological Society, London, Special Publications* 447, SP447–14.

Hoisé, E. (2011). "Contribution a l'etude du message magnetique porte par la lithosphere oceanique: l'altération des mineaux magnétiques-les anomalies magnétiques de haute résolution." PhD thesis. Université Paris Sud-Paris XI.

Hower, J. and Mowatt, T. C. (1966). "The mineralogy of illites and mixed-layer illite/montmorillonites." In: *American Mineralogist* 51.5-6, pp. 825–854.

Huebner, J. S. and Dillenburg, R. G. (1995). "Impedance spectra of hot, dry silicate minerals and rock: Qualitative interpretation of spectra." In: *American Mineralogist* 80.1-2, pp. 46–64.

Huisman, J. A., Zimmermann, E., Esser, O., Haegel, F.-H., Treichel, A., and Vereecken, H. (2016). "Evaluation of a novel correction procedure to remove electrode impedance effects from broadband SIP measurements." In: *Journal of Applied Geophysics* 135, pp. 466–473.

IEA (International Energy Agency) (2011). "Geothermal heat and power." In: *Technology Roadmaps*. OECD/IEA, Paris.

— (2015). "Nuclear Energy." In: *Technology Roadmaps*. OECD/IEA, Paris.

Ingeman-Nielsen, T. and Baumgartner, F. (2006). "Numerical modelling of complex resistivity effects on a homogenous half-space at low frequencies." In: *Geophysical prospecting* 54.3, pp. 261–271.

Ito, G, Lin, J., and Graham, D (2003). "Observational and theoretical studies of the dynamics of mantle plume–mid-ocean ridge interaction." In: *Reviews of Geophysics* 41.4.

Ito, G., Shen, Y., Hirth, G., and Wolfe, C. J. (1999). "Mantle flow, melting, and dehydration of the Iceland mantle plume." In: *Earth and Planetary Science Letters* 165.1, pp. 81–96.

Jónasson, K (1994). "Rhyolite volcanism in the Krafla central volcano, north-east Iceland." In: *Bulletin of Volcanology* 56.6-7, pp. 516–528.

Jónasson, K. (2007). "Silicic volcanism in Iceland: Composition and distribution within the active volcanic zones." In: *Journal of Geodynamics* 43.1, pp. 101–117.

Jónsson, S. S., Gudmundsson, A., and Thordarson, S. (2003). *Krafla borun kjarnaholu KH3 milli Jörundar og Háganga.* Report in Icelandic. ISOR.

Joseph, S., Ingham, M., and Gouws, G. (2015). "Spectral induced polarization measurements on New Zealand sands-dependence on fluid conductivity." In: *Near Surface Geophysics* 13.2, pp. 169–177.

Kaminski, V. and Viezzoli, A. (2017). "Modeling induced polarization effects in helicopter time-domain electromagnetic data: Field case studies." In: *Geophysics* 82.2, B49–B61.

Kang, S. and Oldenburg, D. W. (2016). "On recovering distributed IP information from inductive source time domain electromagnetic data." In: *Geophysical Journal International* 207.1, pp. 174–196.

— (2018). "Time domain electromagnetic-induced polarisation: extracting more induced polarisation information from grounded source time domain electromagnetic data." In: *Geophysical Prospecting* 66.S1, pp. 74–86.

Karlsdóttir, R., Johnsen, G., Björnsson, A., Sigurðsson, A., and Hauksson, E. (1978). *Jarðhitasvæðið við Kröflu - Áfangaskýrsla um jarðeðlisfræðilegar rannskóknir 1976-1978*. Report in Icelandic OS-JHD-7847. Reykjavík: Orkustofnun jarðhitadeild.

Kemna, A., Binley, A., Cassiani, G., Niederleithinger, E., Revil, A., Slater, L., Williams, K. H., Orozco, A. F., Haegel, F.-H., Hoerdt, A., et al. (2012). "An overview of the spectral induced polarization method for near-surface applications." In: *Near Surface Geophysics* 10.6, pp. 453–468.

Ketilsson, J., Björnsson, A., Sveinbjörnsdóttir, A. E., Pálsson, B., Björnsson, G., Axelsson, G., and Sæmundsson, K. (2010). *Nature of geothermal energy and its sustainable utilisation.* In Icelandic. OS-2010/05. Orkustofnun.

Klein, J. D. and Sill, W. R. (1982). "Electrical properties of artificial clay-bearing sandstone." In: *Geophysics* 47.11, pp. 1593–1605.

Kohlrausch, R. (1854). "Theorie des elektrischen Rückstandes in der Leidener Flasche." In: *Annalen der Physik* 167.2, pp. 179–214.

Kristmannsdottir, H. (1975). "Clay minerals formed by hydrothermal alteration of basaltic rocks in Icelandic geothermal fields." In: *GFF* 97.3, pp. 289–292.

— (1979). "Alteration of basaltic rocks by hydrothermal activity at 100-300°C." In: *Developments in sedimentology* 27, pp. 359–367.

Kristmannsdóttir, H. and Tómasson, J. (1978). *Zeolite zones in geothermal areas in Iceland*. Report OS JHD 7649. Orkustofnun, Jarðhita deild.

Kruschwitz, S., Binley, A., Lesmes, D., and Elshenawy, A. (2010). "Textural controls on low-frequency electrical spectra of porous media." In: *Geophysics* 75.4, WA113–WA123.

Lagaly, G. (1981). "Characterization of clays by organic compounds." In: *Clay Miner. Clay Miner.* 16.1, p. 1.

Larsen, H. C. and Saunders, A. D. (1998). "Tectonism and volcanism at the Southeast Greenland rifted margin: a record of plume impact and later continental rupture." In: *Proceedings of the Ocean Drilling Program, Scientific Results*. Vol. 152, pp. 503–533.

Larsen, H. C. (1978). "Offshore continuation of East Greenland dyke swarm and North Atlantic Ocean formation." In: *Nature* 274.5668, p. 220.

Laumonier, M., Farla, R., Frost, D. J., Katsura, T., Marquardt, K., Bouvier, A.-S., and Baumgartner, L. P. (2017). "Experimental determi-

nation of melt interconnectivity and electrical conductivity in the upper mantle." In: *Earth and Planetary Science Letters* 463, pp. 286–297.

Leroux, V., Dahlin, T., and Svensson, M. (2007). "Dense resistivity and induced polarization profiling for a landfill restoration project at Härlöv, Southern Sweden." In: *Waste Management & Research* 25.1, pp. 49–60.

Leroy, P., Weigand, M., Mériguet, G., Zimmermann, E., Tournassat, C., Fagerlund, F., Kemna, A., and Huisman, J. A. (2017). "Spectral induced polarization of Na-montmorillonite dispersions." In: *Journal of colloid and interface science* 505, pp. 1093–1110.

Lesmes, D. P. and Frye, K. M. (2001). "Influence of pore fluid chemistry on the complex conductivity and induced polarization responses of Berea sandstone." In: *Journal of Geophysical Research: Solid Earth* 106.B3, pp. 4079–4090.

Lévy, L., Flóvenz, O., and Hersir, G. (2016). *IMAGE Task 3.3 - Physical Properties of Rock at Reservoir Conditions. Quantitative Impact of Hydrothermal Alteration on Electrical Resistivity, based on cores from Krafla.* Report ISOR-2016/043. Iceland GeoSurvey (ISOR).

Loke, M. H. (2004). *Tutorial: 2-D and 3-D electrical imaging surveys*. Set of notes available online.

Loke, M. H. and Barker, R. (1996). "Rapid least-squares inversion of apparent resistivity pseudosections by a quasi-Newton method 1." In: *Geophysical prospecting* 44.1, pp. 131–152.

Lyklema, J. (2001). *Fundamentals of Interface and Colloid Science. Volume II Solid-Liquid Interfaces*. Academic Press.

Macdonald, J. R. (2000). "Comparison of the universal dynamic response power-law fitting model for conducting systems with superior alternative models." In: *Solid State Ionics* 133.1-2, pp. 79–97.

Maclennan, J (2008). "Concurrent mixing and cooling of melts under Iceland." In: *Journal of Petrology* 49.11, pp. 1931–1953.

Macnae, J (2015). "Comment on: Tarasov, A. & Titov, K., 2013, On the use of the Cole–Cole equations in spectral induced polarization." In: *Geophysical Journal International* 195, pp. 352–356.

Maraqah, H., Li, J., and Whittingham, M. S. (1990). "Ion transport in single crystals of the clay-like aluminosilicate, vermiculite." In: *MRS Online Proceedings Library Archive* 210.

— (1991). "The ionic conductivity of hydrogen vermiculite." In: *Journal of the Electrochemical Society* 138.11, pp. L61–L63.

Markússon, S. H. and Stefánsson, A. (2011). "Geothermal surface alteration of basalts, Krísuvík Iceland - Alteration mineralogy, water chemistry and the effects of acid supply on the alteration process." In: *Journal of Volcanology and Geothermal Research* 206.1-2, pp. 46–59.

Marshall, D. J. and Madden, T. R. (1959). "Induced polarization, a study of its causes." In: *Geophysics* 24.4, pp. 790–816.

Maurya, P., Fiandaca, G, Christiansen, A., and Auken, E (2018a). "Field-scale comparison of frequency-and time-domain spectral induced polarization." In: *Geophysical Journal International*.

Maurya, P. K., Balbarini, N., Møller, I., Rønde, V., Christiansen, A. V., Bjerg, P. L., Auken, E., and Fiandaca, G. (2018b). "Subsurface imaging of water electrical conductivity, hydraulic permeability and lithology at contaminated sites by induced polarization." In: *Geophysical Journal International* 213.2, pp. 770–785.

McKelvey Jr, J., Southwick, P., Spiegler, K., and Wyllie, M. (1955). "The application of a three-element model to the SP and resistivity phenomena evinced by dirty sands." In: *Geophysics* 20.4, pp. 913–931.

Meier, L. and Kahr, G. (1999). "Determination of the Cation Exchange Capacity (CEC) of Clay Minerals Using the Complexes of Copper(II) Ion with Triethylenetetramine and Tetraethylenepentamine." In: *Clays and Clay Minerals* 47.3, pp. 386–388.

Menke, W. (2012). "Chapter 9 - Nonlinear inverse problems." In: *Geophysical Data Analysis: Discrete Inverse Theory (Third Edition)*. Ed. by W. Menke. Third Edition. Boston: Academic Press, pp. 163 – 188.

Merle, R., Caroff, M., Girardeau, J., Cotten, J., and Guivel, C. (2005). "Segregation vesicles, cylinders, and sheets in vapor-differentiated pillow lavas: examples from Tore-Madeira Rise and Chile Triple Junction." In: *Journal of Volcanology and Geothermal Research* 141.1-2, pp. 109–122.

Meunier, A. (2013). *Les argiles par la pratique*. Vuibert.

Meunier, A. (2005). *Clays*. Springer Science & Business Media.

Meunier, A., Mas, A., Beaufort, D., Patrier, P., and Dudoignon, P. (2008). "Clay minerals in basalt-hawaiite rocks from Mururoa atoll (French Polynesia). II. Petrography and geochemistry." In: *Clays and Clay Minerals* 56.6, pp. 730–750.

Meunier, A., Petit, S., Cockell, C. S., El Albani, A., and Beaufort, D. (2010). "The Fe-rich clay microsystems in basalt-komatiite lavas: importance of Fe-smectites for pre-biotic molecule catalysis during the Hadean eon." In: *Origins of Life and Evolution of Biospheres* 40.3, pp. 253–272.

Meunier, A., Petit, S., Ehlmann, B. L., Dudoignon, P., Westall, F., Mas, A., El Albani, A., and Ferrage, E. (2012). "Magmatic precipitation as a possible origin of Noachian clays on Mars." In: *Nature Geoscience* 5.10, pp. 739–743.

Misra, S., Torres-Verdín, C., Revil, A., Rasmus, J., and Homan, D. (2016). "Interfacial polarization of disseminated conductive minerals in absence of redox-active species–Part 1: Mechanistic model and validation." In: *Geophysics* 81.2, E139–E157.

Moorbath, S, Sigurdsson, H, and Goodwin, R (1968). "KAr ages of the oldest exposed rocks in Iceland." In: *Earth and Planetary Science Letters* 4.3, pp. 197–205.

Morgan, W. J. (1971). "Convection plumes in the lower mantle." In: *Nature* 230.5288, p. 42.

Mortensen, A. K., Grönvold, K., Gudmundsson, Á., Steingrímsson, B., and Egilson, T. (2010). "Quenched silicic glass from well K-39 in Krafla, North-Eastern Iceland." In: *World Geothermal Congress*.

Ni, H., Keppler, H., and Behrens, H. (2011). "Electrical conductivity of hydrous basaltic melts: implications for partial melting in the upper mantle." In: *Contributions to Mineralogy and Petrology* 162.3, pp. 637–650.

Nilsen, T. H. (1978). "Lower Tertiary laterite on the Iceland–Faeroe ridge and the Thulean land bridge." In: *Nature* 274.5673, p. 786.

Nono, F., Gibert, B., Parat, F., Loggia, D., Cichy, S. B., and Violay, M. (2018). "Electrical conductivity of Icelandic deep geothermal reservoirs up to supercritical conditions: Insight from laboratory experiments." In: *Journal of Volcanology and Geothermal Research*.

Nordsiek, S. and Weller, A. (2008). "A new approach to fitting induced-polarization spectra." In: *Geophysics* 73.6, F235–F245.

OECD/IEA (2015). *Projected costs of generating electricity - 2015 Edition*. IEA Publishing. Licence: www.iea.org/t&c.

Ohm, G. S. (1827). *Die galvanische Kette, mathematisch bearbeitet*. TH Riemann.

Okpoli, C. C. (2013). "Sensitivity and resolution capacity of electrode configurations." In: *International Journal of Geophysics* 2013.

Oldenburg, D. W. and Li, Y. (1994). "Inversion of induced polarization data." In: *Geophysics* 59.9, pp. 1327–1341.

Oliva-Urcia, B., Kontny, A., Vahle, C., and Schleicher, A. M. (2011). "Modification of the magnetic mineralogy in basalts due to fluid-rock interactions in a high-temperature geothermal system (Krafla, Iceland)." In: *Geophysical Journal International* 186.1, pp. 155–174.

Olsson, P.-I., Fiandaca, G., Dahlin, T., and Auken, E. (2015a). "Impact of time-domain IP pulse length on measured data and inverted models." In: *Near Surface Geoscience 2015-21st European Meeting of Environmental and Engineering Geophysics*.

Olsson, P.-I. (2016). "Optimization of time domain induced polarization data acquisition and spectral information content." PhD thesis. Lund University.

Olsson, P.-I., Dahlin, T., Fiandaca, G., and Auken, E. (2015b). "Measuring time-domain spectral induced polarization in the on-time: decreasing acquisition time and increasing signal-to-noise ratio." In: *Journal of Applied Geophysics* 123, pp. 316–321.

Olsson, P.-I., Fiandaca, G., Larsen, J. J., Dahlin, T., and Auken, E. (2016). "Doubling the spectrum of time-domain induced polarization by harmonic de-noising, drift correction, spike removal,

tapered gating and data uncertainty estimation." In: *Geophysical Supplements to the Monthly Notices of the Royal Astronomical Society* 207.2, pp. 774–784.

Orsini, L and Remy, J. (1976). "Utilisation du chlorure de cobaltihexamine pour la détermination simultanée de la capacité d'échange et des bases échangeables des sols." In: *Sci. Sol* 4, pp. 269–275.

Pabalan, R. T. and Bertetti, F. P. (2001). "Cation-exchange properties of natural zeolites." In: *Reviews in mineralogy and geochemistry* 45.1, pp. 453–518.

Parkhomenko, E. I. (2013). *Electrification phenomena in rocks*. Springer Science & Business Media.

Patrier, P., Papapanagiotou, P., Beaufort, D., Traineau, H., Bril, H., and Rojas, J. (1996). "Role of permeability versus temperature in the distribution of the fine ($\leqslant$ 0.2 μ m) clay fraction in the Chipilapa geothermal system (El Salvador, Central America)." In: *Journal of Volcanology and Geothermal Research* 72.1, pp. 101–120.

Peacock, M. A. and Fuller, R. (1928). "Chlorophaeite, sideromelane and palagonite from the Columbia River Plateau." In: *Amer. Min* 13, pp. 360–382.

Pelton, W. H., Ward, S. H., Hallof, P. G., Sill, W. R., and Nelson, P. H. (1978). "Mineral discrimination and removal of inductive coupling with multifrequency IP." In: *Geophysics* 43.3, pp. 588–609.

Pelton, W., Sill, W., and Smith, B. (1983). "Interpretation of complex resistivity and dielectric data. Part I." In: *Geophysical Transactions* 29.4, pp. 297–330.

Pezard, P. A. (1990). "Electrical properties of mid-ocean ridge basalt and implications for the structure of the upper oceanic crust in Hole 504B." In: *Journal of Geophysical Research* 95.B6, p. 9237.

Placencia-Gómez, E. and Slater, L. D. (2014). "Electrochemical spectral induced polarization modeling of artificial sulfide-sand mixtures." In: *Geophysics* 79.6, pp. 91–106.

— (2016). "On the pore water chemistry effect on spectral induced polarization measurements in the presence of pyrite." In: *Journal of Applied Geophysics* 135, pp. 474–485.

Placencia-Gómez, E., Parviainen, A., Slater, L., and Leveinen, J. (2015). "Spectral induced polarization (SIP) response of mine tailings." In: *Journal of contaminant hydrology* 173, pp. 8–24.

Pommier, A., Gaillard, F., Pichavant, M., and Scaillet, B. (2008). "Laboratory measurements of electrical conductivities of hydrous and dry Mount Vesuvius melts under pressure." In: *Journal of Geophysical Research: Solid Earth* 113.B5.

Pommier, A., Gaillard, F., and Pichavant, M. (2010). "Time-dependent changes of the electrical conductivity of basaltic melts with redox state." In: *Geochimica et Cosmochimica Acta* 74.5, pp. 1653–1671.

Presnall, D., Simmons, C., and Porath, H (1972). "Changes in electrical conductivity of a synthetic basalt during melting." In: *Journal of Geophysical Research* 77.29, pp. 5665–5672.

Pridmore, D. and Shuey, R. (1976). "The electrical resistivity of galena, pyrite, and chalcopyrite." In: *American Mineralogist* 61.3-4, pp. 248–259.

Revil, A and Florsch, N. (2010). "Determination of permeability from spectral induced polarization in granular media." In: *Geophysical Journal International* 181.3, pp. 1480–1498.

Revil, A. and Glover, P. W. J. (1997). "Theory of ionic-surface electrical conduction in porous media." In: *Physical Review B* 55.3, pp. 1757–1773.

Revil, A and Glover, P. (1998). "Nature of surface electrical conductivity in natural sands, sandstones, and clays." In: *Geophysical Research Letters* 25.5, pp. 691–694.

Revil, A., Cathles, L. M., Losh, S., and Nunn, J. A. (1998). "Electrical conductivity in shaly sands with geophysical applications." In: *Journal of Geophysical Research: Solid Earth* 103.B10, pp. 23925–23936.

Revil, A., Breton, M. L., Niu, Q., Wallin, E., Haskins, E., and Thomas, D. M. (2017a). "Induced polarization of volcanic rocks. 2. Influence of pore size and permeability." In: *Geophysical Journal International* 208.2, pp. 814–825.

Revil, A., Le Breton, M., Niu, Q., Wallin, E., Haskins, E., and Thomas, D. M. (2017b). "Induced polarization of volcanic rocks.1. Surface versus quadrature conductivity." In: *Geophysical Journal International* 208.2, pp. 826–844.

Revil, A. and Skold, M. (2011). "Salinity dependence of spectral induced polarization in sands and sandstones." In: *Geophysical Journal International* 187.2, pp. 813–824.

Revil, A., Florsch, N., and Mao, D. (2015a). "Induced polarization response of porous media with metallic particles - Part 1: a theory for disseminated semiconductors." In: *Geophysics*.

Revil, A., Abdel Aal, G. Z., Atekwana, E. A., Mao, D., and Florsch, N. (2015b). "Induced polarization response of porous media with metallic particles - Part 2: comparison with a broad database of experimental data." In: *Geophysics* 80.5, pp. D539–D552.

Revil, A., Coperey, A., Deng, Y., Cerepi, A., and Seleznev, N. (2017c). "Complex conductivity of tight sandstones." In: *Geophysics* 83.2, E55–E74.

Revil, A., Sleevi, M. F., and Mao, D. (2017d). "Induced polarization response of porous media with metallic particles–Part 5: Influence of the background polarization." In: *Geophysics* 82.2, E77–E96.

Richman, D. and Thomas, H. C. (1956). "Self-diffusion of Sodium in a Cation Exchange Resin." In: *The Journal of Physical Chemistry* 60.2, pp. 237–239.

Rosenkjaer, G. K., Gasperikova, E., Newman, G. A., Árnason, K., and Lindsey, N. J. (2015). "Comparison of 3D MT inversions for geothermal exploration: case studies for Krafla and Hengill geothermal systems in Iceland." In: *Geothermics* 57, pp. 258–274.

Sæmundsson, K. (1991). "Náttúra Mývatns." In: ed. by A. Garðarson and A. Einarsson. Reykjavík: Hið íslenska náttúrufræðifélag. Chap. Jarðfræði Kröflukerfisins. Pp. 25–95.

— (2015). *Catalogue of Icelandic volcanoes - Krafla*. Icelandic Volcanoes.

Sæmundsson, K. and Sigmundsson, F. (2013). "Náttúruvá á Íslandi: Eldgos og jarðskjálftar." In: ed. by J. Sólnes, F. Sigmundsson, and B. Bessason. Viðlagatrygging Íslands og Háskólaútgáfan. In Icelandic. Chap. Norðurgosbelti, pp. 319–357.

Sæmundsson, K, Pringle, M., and Hardarson, B. (2000). "About the age of strata in the Krafla volcanic system." In: *Geoscience Society of Iceland, Spring Meeting*, pp. 26–27.

Saemundsson, K. (1974). "Evolution of the axial rifting zone in northern Iceland and the Tjornes fracture zone." In: *Geological Society of America Bulletin* 85.4, pp. 495–504.

Saemundsson, K. (1978). "Fissure swarms and central volcanoes of the neovolcanic zones of Iceland." In: *Geol. J. Spec* 10, pp. 415–432.

Sæmundsson, K. (1979). "Outline of the geology of Iceland." In: *Jokull* 29, pp. 7–28.

Sæmundsson, K. (1983). "The eruption history of the Krafla volcano during the last 3000 years." In: *Ravens Congregations*, pp. 1–2.

Saemundsson, K., Hjartarson, A., Kaldal, I., Sigurgeirsson, M. A., Kristinsson, S. G., and Víkingsson, S. (2012). *Geological map of the northern volcanic zone, Iceland. Northern part 1:100 000*. Reykjavík: Iceland Geosurvey and Landsvirkjun.

Salles, F., Devautour-Vinot, S., Bildstein, O., Jullien, M., Maurin, G., Giuntini, J.-C., Douillard, J.-M., and Van Damme, H. (2008). "Ionic mobility and hydration energies in montmorillonite clay." In: *The Journal of Physical Chemistry C* 112.36, pp. 14001–14009.

Sanders, I. (1986). "Gas filter-pressing origin for segregation vesicles in dykes." In: *Geological Magazine* 123.1, pp. 67–72.

Schaefer, L. (2017). "planetary Science: A steamy proposal for Martian clays." In: *Nature* 552.7683, pp. 37–38.

Schenato, F., Formoso, M. L. L., Dudoignon, P., Meunier, A., Proust, D., and Mas, A. (2003). "Alteration processes of a thick basaltic lava flow of the Paraná basin (Brazil): petrographic and mineralogical studies." In: *Journal of South American Earth Sciences* 16.5, pp. 423–444.

Schilling, J. and Noe-Nygaard, A. (1974). "Faeroe-Iceland plume: Rare-earth evidence." In: *Earth and Planetary Science Letters* 24.1, pp. 1–14.

Schuler, J., Greenfield, T., White, R. S., Roecker, S. W., Brandsdóttir, B., Stock, J. M., Tarasewicz, J., Martens, H. R., and Pugh, D. (2015). "Seismic imaging of the shallow crust beneath the Krafla central volcano, NE Iceland." In: *Journal of Geophysical Research: Solid Earth* 120.10, pp. 7156–7173.

Shao, J.-J., Raidongia, K., Koltonow, A. R., and Huang, J. (2015). "Self-assembled two-dimensional nanofluidic proton channels with high thermal stability." In: *Nature communications* 6, p. 7602.

Shuey, R. (2012). *Semiconducting ore minerals*. Vol. 4. Elsevier.

Sigmarsson, O. and Steinthórsson, S. (2007). "Origin of Icelandic basalts: A review of their petrology and geochemistry." In: *Journal of Geodynamics* 43.1, pp. 87–100.

Sigmarsson, O., Maclennan, J., and Carpentier, M. (2008). "Geochemistry of igneous rocks in Iceland: a review." In: *Jökull* 58, pp. 139–160.

Sigmundsson, F. (2006). *Iceland geodynamics: crustal deformation and divergent plate tectonics*. Springer Science & Business Media.

Sigmundsson, F., Einarsson, P., Hjartardóttir, Á. R., Drouin, V., Jónsdóttir, K., Árnadóttir, T., Geirsson, H., Hreinsdóttir, S., Li, S., and Ófeigsson, B. G. (2018). "Geodynamics of Iceland and the signatures of plate spreading." In: *Journal of Volcanology and Geothermal Research*.

Singer, A. and Banin, A. (1990). "Characteristics and mode of palagonite-A review." In: *Sciences Géologiques, bulletins et mémoires* 88.1, pp. 173–181.

Slade, R. C. T., Barker, J., Hirst, P. R., Halstead, T. K., and Reid, P. I. (1987). "Conduction and diffusion in exchanged montmorillonite clays." In: *Solid State Ionics* 24.4, pp. 289–295.

Slater, L. D. and Lesmes, D. P. (2002a). "Electrical-hydraulic relationships observed for unconsolidated sediments." In: *Water Resources Research* 38.10, pp. 31–1–31–13.

Slater, L. D. and Lesmes, D. (2002b). "IP interpretation in environmental investigations." In: *Geophysics* 67.1, pp. 77–88.

Slater, L. D. and Sandberg, S. K. (2000). "Resistivity and induced polarization monitoring of salt transport under natural hydraulic gradients." In: *Geophysics* 65.2, pp. 408–420.

Stefansson, V. (2000). "The renewability of geothermal energy." In: *Proceedings of the World Geothermal Congress 2000*, pp. 883–888.

Steiner, A (1968). "Clay minerals in hydrothermally altered rocks at Wairakei, New Zealand." In: *Clays and Clay Minerals* 16.3, pp. 193–213.

Sumner, J. S. (2012). *Principles of induced polarization for geophysical exploration*. Vol. 5. Elsevier.

Sun, P., Ma, R., and Sasaki, T. (2018). "Recent progress on exploring exceptionally high and anisotropic H+/OH- ion conduction in two-dimensional materials." In: *Chemical science* 9.1, pp. 33–43.

Tarasov, A. and Titov, K. (2013). "On the use of the Cole–Cole equations in spectral induced polarization." In: *Geophysical Journal International* 195.1, pp. 352–356.

Taut, T., Kleeberg, R., and Bergmann, J. (1998). "Seifert Software: The new Seifert Rietveld program BGMN and its application to quantitative phase analysis." In: *Materials Structure* 5.1, pp. 57–66.

Telford, W. M., Geldart, L. P., and Sheriff, R. E. (1990). *Applied Geophysics*. 2nd. Cambridge University Press.

Thorsteinsdóttir, U. (2017). "A 3D geological static field model of the Krafla geothermal area; constructing a workflow for the Pico Alto geothermal area." Master's thesis. Faculty of Earth's sciences, University of Iceland.

Tuffen, H. and Castro, J. M. (2009). "The emplacement of an obsidian dyke through thin ice: Hrafntinnuhryggur, Krafla Iceland." In: *Journal of Volcanology and Geothermal Research* 185.4, pp. 352–366.

Tyburczy, J. A. and Waff, H. S. (1983). "Electrical conductivity of molten basalt and andesite to 25 kilobars pressure: Geophysical significance and implications for charge transport and melt structure." In: *Journal of Geophysical Research: Solid Earth* 88.B3, pp. 2413–2430.

Utada, M (1980). "Hydrothermal alterations related to igneous activity in Cretaceous and Neogene formations in Japan." In: *Mining Geol., Spec. Issue* 8, pp. 67–83.

Vanhala, H. (1997). "Mapping oil-contaminated sand and till with the spectral induced polarization (SIP) method." In: *Geophysical prospecting* 45.2, pp. 303–326.

Vergara, M, Levi, B, and Villarroel, R (1993). "Geothermal-type alteration in a burial metamorphosed volcanic pile, central Chile." In: *Journal of Metamorphic Geology* 11.3, pp. 449–454.

Vernier, R., Laplaige, P., Desplan, A., and Boissavy, C. (2015). "France country update." In: *Proceedings to World Geothermal Congress*.

Vidal, O., Baldeyrou, A., Beaufort, D., Fritz, B., Geoffroy, N., and Lanson, B. (2012). "Experimental Study of the Stability and Phase Relations of Clays at High Temperature in a Thermal Gradient." In: *Clays and Clay Minerals* 60.2, pp. 200–225.

Vinegar, H. and Waxman, M. (1984). "Induced polarization of shaly sands." In: *Geophysics* 49.8, pp. 1267–1287.

Vink, G. E. (1984). "A hotspot model for Iceland and the Vøring Plateau." In: *Journal of Geophysical Research: Solid Earth* 89.B12, pp. 9949–9959.

Vogt, K. and Köster, H. M. (1978). "Zur mineralogie, kristallchemie und geochemie einiger montmorillonite aus bentoniten." In: *Clay Minerals* 13.1, pp. 25–43.

Volkmann, J. and Klitzsch, N. (2015). "Wideband impedance spectroscopy from 1 mHz to 10 MHz by combination of four-and two-

electrode methods." In: *Journal of Applied Geophysics* 114, pp. 191–201.

Waff, H. S. and Weill, D. F. (1975). "Electrical conductivity of magmatic liquids: effects of temperature, oxygen fugacity and composition." In: *Earth and Planetary Science Letters* 28.2, pp. 254–260.

Wait, J. R. (1987). "Physical model for the complex resistivity of the earth." In: *Electronics letters* 23.19, pp. 979–980.

Wait, J. R. (1958). "A phenomenological theory of induced electrical polarization." In: *Canadian Journal of Physics* 36.12, pp. 1634–1644.

Walker, G. P. L. (1960). "Zeolite zones and dike distribution in relation to the structure of the basalts of eastern Iceland." In: *The Journal of Geology* 68.5, pp. 515–528.

Walker, G. P. (1966). "Acid volcanic rocks in Iceland." In: *Bulletin Volcanologique* 29.1, pp. 375–402.

— (1974). "Eruptive mechanisms in Iceland." In: *Geodynamics of Iceland and the North Atlantic area*. Springer, pp. 189–201.

Ward, S. H. (1988). "The resistivity and induced polarization methods." In: *Symposium on the Application of Geophysics to Engineering and Environmental Problems 1988*. Society of Exploration Geophysicists, pp. 109–250.

Waxman, M. H. and Smits, L. J. M. (1968). "Electrical conductivities in oil-bearing shaly sands." In: *Soc. Pet. Eng. J.* 8, pp. 107–122.

Weigand, M and Kemna, A (2016a). "Debye decomposition of time-lapse spectral induced polarisation data." In: *Computers & Geosciences* 86, pp. 34–45.

Weigand, M. and Kemna, A. (2016b). "Relationship between Cole-Cole model parameters and spectral decomposition parameters derived from SIP data." In: *Geophysical Journal International* 205.3, pp. 1414–1419.

Weller, A. and Slater, L. (2012). "Salinity dependence of complex conductivity of unconsolidated and consolidated materials: Comparisons with electrical double layer models." In: *Geophysics* 77.5, pp. D185–D198.

Weller, A., Slater, L., and Nordsiek, S. (2013). "On the relationship between induced polarization and surface conductivity: Implications for petrophysical interpretation of electrical measurements." In: *Geophysics* 78.5, pp. D315–D325.

Whittingham, M. S. (1987). "Sodium ion conduction in single crystal vermiculite." In: *Solid State Ionics* 25.4, pp. 295–300.

Williams, G. and Watts, D. C. (1970). "Non-symmetrical dielectric relaxation behaviour arising from a simple empirical decay function." In: *Transactions of the Faraday society* 66, pp. 80–85.

Wong, J. (1979). "An electrochemical model of the induced-polarization phenomenon in disseminated sulfide ores." In: *Geophysics* 44.7, pp. 1245–1265.

Wong, J. and Strangway, D. W. (1981). "Induced polarization in disseminated sulfide ores containing elongated mineralization." In: *Geophysics* 46.9, pp. 1258–1268.

Wyllie, M. R. J. and Southwick, P. F. (1954). "An experimental investigation of the SP and resistivity phenomena in dirty sands." In: *Journal of Petroleum Technology* 6.02, pp. 44–57.

Zierenberg, R., Schiffman, P, Barfod, G., Lesher, C., Marks, N., Lowenstern, J. B., Mortensen, A., Pope, E. C., Bird, D., Reed, M., et al. (2013). "Composition and origin of rhyolite melt intersected by drilling in the Krafla geothermal field, Iceland." In: *Contributions to Mineralogy and Petrology* 165.2, pp. 327–347.

DECLARATION

I close this dissertation with a somewhat *philosophical* declaration about research in general, which I figured would be appropriate to deserve the status of Doctor of Philosophy.

The last months of my Ph.D. have been associated with intensive watching of murder investigation series after long working days (efficient anti-social distracting activity). I have been thinking: "wow they investigate cases, pretty much in the same rational way as scientists do, but their work is so much more impressive and directly useful for society". Why on earth do I do scientific research and not murder investigation then? I could not be at peace with this question until recently. Indeed, the excitement scientists can feel when they understand a new phenomenon or witness the realization of their prediction is similar to that of detectives cracking a case. And this excitement is the very reason why both enjoy their job, I believe. For scientists, there is some magic in connecting with nature, understanding how it works, while for detectives, there is a satisfaction of being "smarter than the killer". But what is the outcome for the society? For detectives it is quite clear: arrest killers, put them in jail, decrease the criminality on Earth and make the society happier (is it true, let's not get into that). The outcomes for society of scientific research are less clear. Do I really believe my research is important for society because it will help find more geothermal reservoirs? Honestly, I am not sure. Then what? Is this excitement pointless for the society? Not if it can be shared.

And here is the trick. I believe most human beings want to understand how nature works and what their role in the big universe is - unless they think they already know. Religions would have failed spreading their "enlightening" messages if that was not the case. Therefore, a clear outcome of research, especially for scientific disciplines which can be grouped under the general "physics" term, is to educate the society about how nature works. Not only it empowers people but it makes them dream, feel the magic. What could be better for the society than that? The challenge is to do it right, so that people feel the magic when they listen, but are not fooled. This is where scientific communication should differ from marketing or propaganda, which pursue other goals than genuinely educating and empowering people. The point is: it is too easy to fool people who cannot verify what you tell them and it has more to do with faith than education. That's why scientific communication is a challenge. It has to be accessible to the targeted public but not oversimplified or embellished to a point where the truth of the up-to-date knowledge has disappeared.

Sharing excitement and magic can be thrilling if a connection is established with the public. Despite that, truly educating the society is not a priority for many scientists, who sometimes let this part of the job to unqualified (but convincing) people. It could be considered as a responsibility for scientists, as handing in the case to the district attorney after solving it is a responsibility for detectives. I hope I will remember that whenever I have the opportunity to tell others about my research.

Grund, Iceland, January 2019

Léa Lévy

COLOPHON

This document was typeset using the typographical look-and-feel `classicthesis` developed by André Miede. The style was inspired by Robert Bringhurst's seminal book on typography "*The Elements of Typographic Style*". `classicthesis` is available for both LaTeX and LyX:

https://bitbucket.org/amiede/classicthesis/

RÉSUMÉ

Afin de cartographier la structure souterraine des volcans et détecter des ressources géothermiques de haute température, on utilise souvent l'imagerie de résistivité électrique. La résistivité électrique des volcans est affectée par plusieurs facteurs: volume et salinité de l'eau interstitielle, abondance de minéraux conducteurs, température de la roche et présence de magma. Ce travail de thèse tente de contraindre l'interprétation des structures de résistivité électrique autour des volcans actifs, afin de développer des outils innovants pour l'exploration des ressources géothermiques. La contribution des minéraux conducteurs est au cœur de la thèse: conducteurs ioniques solides (minéraux argileux, en particulier la smectite) ou semi-conducteurs électroniques (pyrite, oxydes de fer), mais l'influence de la porosité, de la salinité, de la température et de la présence de magma est aussi étudiée. La thèse utilise le volcan Krafla comme terrain d'étude pour affiner les interprétations des structures de résistivité électriques, du fait de la disponibilité de carottes, de données, de bibliographie et d'infrastructure. La smectite et la pyrite sont formées par altération hydrothermale des roches volcaniques et témoignent ainsi des convections hydrothermales. Les oxydes de fer en revanche sont plutôt formés lors de la cristallisation du magma et sont dissous lors des circulations hydrothermales. La contribution de la smectite à la conductivité électrique de roches volcaniques, saturées en eau à différentes salinités, est d'abord étudiée en laboratoire (à température ambiante) par spectroscopie d'impédance électrique « résistivité complexe ». Des variations non linéaires de la conductivité électrique à 1 kHz avec la salinité sont observées et discutées. La conduction interfoliaire est suggérée comme un mécanisme important par lequel la smectite conduit le courant électrique. L'influence de la pyrite et des oxydes de fer sur les effets de polarisation provoquée est ensuite analysée en utilisant l'angle de phase de l'impédance, qui dépend de la fréquence. Un angle de phase maximal supérieur à 20 mrad est attribué à la pyrite si la roche est conductrice et aux oxydes de fer si la roche est résistive. L'angle de phase maximal augmente d'environ 22 mrad pour chaque pourcent de pyrite ou d'oxyde de fer. Ces résultats de laboratoire en domaine fréquentiel sont appliqués à l'interprétation de tomographies de résistivité complexe sur le terrain en domaine temporel. Smectite, pyrite et oxydes de fer ont pu être identifiés jusqu'à 200 m de profondeur. La température in-situ, plus élevées qu'en laboratoire, semble augmenter la conductivité de la smectite. De manière générale, la tomographie de résistivité complexe est recommandée comme méthode complémentaire aux sondages électromagnétiques pour l'exploration géothermique.

MOTS CLÉS

Géothermie, conductivité électrique, smectite, pyrite, polarisation provoquée, inversion géophysique

ABSTRACT

Electromagnetic soundings are widely used to image the underground structure of volcanoes and look for high-temperature geothermal resources, The electrical resistivity of volcanoes is affected by several characteristics of rocks: volume and salinity of pore fluid, abundance of conductive minerals, rock temperature and presence of magma. This thesis aims at improving the interpretation of electrical resistivity structures around active volcanoes, in order to develop innovative tools for the assessment of geothermal resources. I focus on conductive minerals, which can either be solid ionic conductors (clay minerals, in particular smectite) or electronic semi-conductors (pyrite and iron-oxides), but I also investigate the effects of porosity, salinity, temperature and presence of magma. I use Krafla volcano as a laboratory area, where extensive literature, borehole data, core samples, surface soundings and infrastructures are available. Smectite and pyrite are formed upon hydrothermal alteration of volcanic rocks and thus witness hydrothermal convection. On the other hand, iron-oxides are mostly formed during the primary crystallization of magma and dissolved by hydrothermal fluids. The contribution of smectite to the electrical conductivity of volcanic rocks saturated with pore water at different salinity is first investigated in the laboratory (room temperature) by electrical impedance spectroscopy "complex resistivity". Non-linear variations of the conductivity at 1 kHz with salinity are observed and discussed. Interfoliar conduction is suggested as an important mechanism by which smectite conducts electrical current. The influence of pyrite and iron-oxides on induced polarization effects is then analyzed, using the frequency-dependent phase-angle of the impedance. A maximum phase-angle higher than 20 mrad is attributed to pyrite if the rock is conductive and to iron-oxides if the rock is resistive. The maximum phase-angle increases by about 22 mrad for each additional per cent of pyrite or iron-oxide. These laboratory frequency-domain findings are partly upscaled to interpret field time-domain complex resistivity tomography at Krafla: smectite, pyrite and iron-oxides can be identified down to 200 m. The in-situ temperature, higher than in laboratory conditions, appears to significantly increase the conductivity associated to smectite. In general, time-domain complex resistivity measurements are recommended as a complementary method to electromagnetic soundings for geothermal exploration.

KEYWORDS

Geothermal energy, electrical conductivity, smectite, pyrite, induced polarization, geophysical inversion